Electron-nuclear dynamics in noble metal nanoparticles

by

Ravithree Dhaneeka Senanayake

B.S., University of Colombo, 2011

AN ABSTRACT OF A DISSERTATION

submitted in partial fulfillment of the requirements for the degree

DOCTOR OF PHILOSOPHY

Department of Chemistry
College of Arts and Sciences

KANSAS STATE UNIVERSITY
Manhattan, Kansas

2018

Abstract

Thiolate-protected noble metal nanoparticles (~2 nm size) are efficient solar photon harvesters, as they favorably absorb within the visible region. Clear mechanistic insights regarding the photo-physics of the excited state dynamics in thiolate-protected noble metal nanoclusters are important for future photocatalytic, light harvesting and photoluminescence applications. Herein, the core and higher excited states lying in the visible range are investigated using the time-dependent density functional theory method for different thiolate-protected nanoclusters. Nonadiabatic molecular dynamics simulations are performed using the fewest switches surface hopping approach with a time-dependent Kohn-Sham (FSSH-TDKS) description of the electronic states with decoherence corrections to study the electronic relaxation dynamics. Calculations on the $[Au_{25}(SH)_{18}]^{-1}$ nanocluster showed that relaxations between core excited states occur on a short time scale (2-18 ps). No semiring or other states were observed at an energy lower than the core-based S_1 state, which suggested that the experimentally observed picosecond time constants could be core-to-core transitions rather than core-to-semiring transitions. Electronic relaxation dynamics on $[Au_{25}(SR)_{18}]^{-1}$ with different R ligands (R = CH_3, C_2H_5, C_3H_7, MPA) [MPA = mercaptopropanoic acid] showed that all ligand clusters including the simplest SH model follow a similar trend in decay within the core states. In the presence of higher excited states, R= H, CH_3, C_2H_5, C_3H_7 demonstrated similar relaxations trends, whereas R=MPA showed a different relaxation of core states due to a smaller LUMO+1-LUMO+2 gap. Overall, the S_1 state gave the slowest decay in all ligated clusters. An examination of separate electron and hole relaxations in the $[Au_{25}(SCH_3)_{18}]^{-1}$ nanocluster showed how the independent electron and hole relaxations contribute to its overall relaxation dynamics. Relaxation dynamics in the $Au_{18}(SH)_{14}$ nanocluster revealed that the S_1 state has the slowest decay, which is a semiring to core charge transfer state. Hole relaxations are faster than electron relaxations in the $Au_{18}(SH)_{14}$ cluster due its closely packed HOMOs. The dynamics in the $Au_{38}(SH)_{24}$ nanocluster predicted that the slowest decay, the decay of S_{11} or the combined S_{11}-S_{12}, S_1-S_2-S_6-S_7 and S_4-S_5-S_9-S_{10} decay, involves intracore relaxations. The phonon spectral densities and vibrational frequencies suggested that the low frequency (25 cm^{-1}) coherent phonon emission reported experimentally could be the bending of the bi-icosahedral Au_{23} core or the “fan blade twisting” mode of two icosahedral units. Relaxation dynamics of the silver nanoparticle $[Ag_{25}(SR)_{18}]^{-1}$

showed that both $[Ag_{25}(SH)_{18}]^{-1}$ and $[Au_{25}(SH)_{18}]^{-1}$ follow a common decay trend within the core states and the higher excited states.

A real-time TDDFT investigation on a set of linear gold nanowires Au_m (m = 4, 6, 8, 10, 12) indicated that the longitudinal peak splits due to the involvement of interband transitions. Time-dependent occupation numbers and their Fourier transformed spectra revealed a dominant single particle transition ($\Sigma_n \rightarrow \Sigma_{n+1}$) in the longitudinal peaks that is coupled with less probable d-band transitions ($d \rightarrow \Sigma$). The transverse modes are constructed from a coupling of two or more single particle transitions with $\Sigma_n \rightarrow \Pi_n$ character.

Electron-nuclear dynamics in noble metal nanoparticles

by

Ravithree Dhaneeka Senanayake

B.S., University of Colombo, 2011

A DISSERTATION

submitted in partial fulfillment of the requirements for the degree

DOCTOR OF PHILOSOPHY

Department of Chemistry
College of Arts and Sciences

KANSAS STATE UNIVERSITY
Manhattan, Kansas

2018

Approved by:

Major Professor
Christine M. Aikens

Copyright

Abstract

Thiolate-protected noble metal nanoparticles (~2 nm size) are efficient solar photon harvesters, as they favorably absorb within the visible region. Clear mechanistic insights regarding the photo-physics of the excited state dynamics in thiolate-protected noble metal nanoclusters are important for future photocatalytic, light harvesting and photoluminescence applications. Herein, the core and higher excited states lying in the visible range are investigated using the time-dependent density functional theory method for different thiolate-protected nanoclusters. Nonadiabatic molecular dynamics simulations are performed using the fewest switches surface hopping approach with a time-dependent Kohn-Sham (FSSH-TDKS) description of the electronic states with decoherence corrections to study the electronic relaxation dynamics. Calculations on the $[Au_{25}(SH)_{18}]^{-1}$ nanocluster showed that relaxations between core excited states occur on a short time scale (2-18 ps). No semiring or other states were observed at an energy lower than the core-based S_1 state, which suggested that the experimentally observed picosecond time constants could be core-to-core transitions rather than core-to-semiring transitions. Electronic relaxation dynamics on $[Au_{25}(SR)_{18}]^{-1}$ with different R ligands (R = CH_3, C_2H_5, C_3H_7, MPA) [MPA = mercaptopropanoic acid] showed that all ligand clusters including the simplest SH model follow a similar trend in decay within the core states. In the presence of higher excited states, R= H, CH_3, C_2H_5, C_3H_7 demonstrated similar relaxations trends, whereas R=MPA showed a different relaxation of core states due to a smaller LUMO+1-LUMO+2 gap. Overall, the S_1 state gave the slowest decay in all ligated clusters. An examination of separate electron and hole relaxations in the $[Au_{25}(SCH_3)_{18}]^{-1}$ nanocluster showed how the independent electron and hole relaxations contribute to its overall relaxation dynamics. Relaxation dynamics in the $Au_{18}(SH)_{14}$ nanocluster revealed that the S_1 state has the slowest decay, which is a semiring to core charge transfer state. Hole relaxations are faster than electron relaxations in the $Au_{18}(SH)_{14}$ cluster due its closely packed HOMOs. The dynamics in the $Au_{38}(SH)_{24}$ nanocluster predicted that the slowest decay, the decay of S_{11} or the combined S_{11}-S_{12}, S_1-S_2-S_6-S_7 and S_4-S_5-S_9-S_{10} decay, involves intracore relaxations. The phonon spectral densities and vibrational frequencies suggested that the low frequency (25 cm^{-1}) coherent phonon emission reported experimentally could be the bending of the bi-icosahedral Au_{23} core or the “fan blade twisting” mode of two icosahedral units. Relaxation dynamics of the silver nanoparticle $[Ag_{25}(SR)_{18}]^{-1}$

showed that both $[Ag_{25}(SH)_{18}]^{-1}$ and $[Au_{25}(SH)_{18}]^{-1}$ follow a common decay trend within the core states and the higher excited states.

A real-time TDDFT investigation on a set of linear gold nanowires Au_m (m = 4, 6, 8, 10, 12) indicated that the longitudinal peak splits due to the involvement of interband transitions. Time-dependent occupation numbers and their Fourier transformed spectra revealed a dominant single particle transition ($\Sigma_n \rightarrow \Sigma_{n+1}$) in the longitudinal peaks that is coupled with less probable d-band transitions (d $\rightarrow \Sigma$). The transverse modes are constructed from a coupling of two or more single particle transitions with $\Sigma_n \rightarrow \Pi_n$ character.

Table of Contents

List of Figures

List of Tables

Acknowledgements

Foremost, I would like to express my sincere gratitude to my advisor, Professor Christine M. Aikens for having me in her group and for the continuous guidance, support, motivation and patience throughout the past five years of my graduate studies. Thank you so much for the vast knowledge, opportunities and for improving my confidence as a researcher. I learnt a lot being a member of the Aikens group, not only the subject matters but also improved my interpersonal skills. I am truly grateful for shaping me as a better scientist and I am hoping to pursue my studies with all that experience in the future.

I would like to thank my advisory committee, Professor Daniel Higgins, Professor Ryszard Jankowiak, Professor Bin Liu and Professor Douglas McGregor for their valuable time, support and input. I also like to thank Professor Carlos Trallero for being in my committee for four years and for his support.

I want to acknowledge the Department of Chemistry, Kansas State University for accepting me as a graduate student.

I would like to thank the research collaborators Professor Alexey Akimov, Professor Xiaosong Li, Dr. David Lingerfelt and Professor Di Sun for their knowledge, support and input.

I am grateful to Dr. Dave Turner for his continuous support with the Beocat technical expertise.

I would like to thank all the past and present Aikens' group members for their support and sharing their knowledge with me. I would also like to extend my gratitude for all the past and present Liu group members for their valuable input. It was a great experience to work with you all.

I would like to express my gratitude to my undergraduate advisor Professor Dhammike Dissanayake and Professor Samantha Weerasinghe and other Professors in the Department of Chemistry, University of Colombo for their knowledge, enormous support and motivation to pursue my graduate studies. I am truly thankful to all my teachers from grade 1 to 13 in Visakha Vidyalaya - Colombo, my high school for laying the foundation for my higher studies.

Special thanks go to Ms. Mary Dooley and Ms. Kimberly Ross for their support during my graduate studies in the department of Chemistry.

I am thankful to all my friends in Manhattan, specially Dimuthu Weerawardene, Nilusha Kariyawasam, Madumali Kalubowila and Medha Gunaratna for being there for me in all the good and bad times. I would like to extend my gratitude to all my friends back in Sri Lanka.

Special thanks go to my aunt, Dr. Thulani Senanayake for the motivation and her enormous support during the past five years. I am truly grateful to you.

I am truly thankful to my grandfather and grandmother for their endless love and care since my childhood. I would like to extend my sincere gratitude to my sister, brother-in-law and my nephew for their love and support. Finally, I want to express my sincere gratitude from the bottom of my heart to my loving father and mother for their endless love, support and strength to come this far. This would not be possible without you.

Dedication

To my dearest father and mother

For their endless love, care and strength

To my grandfather, grandmother and sister

For their endless love and support

.

Chapter 1 - Introduction

1.1 Noble metal nanoparticles

"Noble metals" are metals that are resistant to oxidation occurring under normal environmental conditions. These metals are considered precious due to their low abundance. Among the various noble metals, gold and silver have drawn an enormous interest since ancient times. According to historical reports, gold and silver have been used in coloration of ceramics and glasses[1] and for medicinal field applications as an antimicrobial agent.[2] However, their nanoscale structures were not known in ancient times. Since then, gold and silver noble metal nanoparticles have contributed to major advances in science through their applications in optics, biomedical sensing,[3-5] energy conversion and storage[6-7] and catalysis.[8-11]

1.1.1 Monolayer protected noble metal clusters

The discovery of the gas phase clusters[12] has lead the foundation to the early monolayer protected clusters (MPC). The synthesis of the noble metal nanoparticles using protecting ligands has evolved over time. In the early days, there were several reports on phosphine-protected noble metal clusters.[13-18] Among MPCs, gold has been studied extensively due to its high stability under ambient conditions. In this thesis, I will mainly discuss thiolate-protected noble metal clusters. Significant developments have occurred to understand the correlation between the geometric structures of the MPC and their optical properties. In 2007, the first X-ray crystal structure of a MPC, specifically $Au_{102}(SR)_{44}$ [SR = p-mercaptobenzoic acid (p-MBA)], was determined[19] and it was shown that a small gold core is protected by $Au(SR)_2$ and $Au_2(SR)_3$ semiring motifs rather than a large gold core protected with thiolate ligands. A similar observation occurred with the determination of the crystal structure of $Au_{25}(SR)_{18}^{-1}$ in 2008.[20-21] These types of semiring motifs have been suggested in the "divide and protect" concept introduced in 2006.[22]

The electronic stability of the MPC can be explained in terms of the superatom model.[23] In the superatomic model, stability is decided based on the ligand-core interactions of the nanoparticle. If the MPC is defined as $Au_N X_M L_S^Z$,[24] where X is a one-electron withdrawing or

localizing ligand and L is a Lewis base type ligand, then the electron count *n* of this cluster can be calculated as,

$$n = Nv_A - M - z \quad \textbf{(1.1)}$$

Here, *N* is the number of the gold or silver atoms. v_A is the atomic valence, which is 1 for both gold and silver. *M* is the number of localizing ligands and *S* is the number of Lewis base type ligands in the MPC. *z* is the total charge of the system. For an approximately spherical system, the Aufbau rule for filling the superatomic orbitals are in the order of $1S^2|1P^6|1D^{10}|2S^21F^{14}|2P^61G^{18}|...$, where S-P-D-F-G- denote the angular momentum quantum number. When *n* corresponds to a shell closing "magic number" such as 2, 8, 18, 34, 58, … the spherical MPC is electronically stable. When *n* does not correspond to a magic number, that MPC should be non-spherical. However, the stabilities of the Au_{144} and larger thiolate-protected gold nanoclusters can be decided based on the geometric shell closure rather than the electronic shell filling.[25-27]

1.1.2 Optical properties of thiolate-protected gold and silver nanoparticles

Gold and silver nanoparticles in the 10-100 nm size regime demonstrate unique optical properties[28-31] including the surface plasmon resonance (SPR) phenomenon. The SPR is the collective oscillation of conduction electrons in the presence of an electric field.[32] Classical electromagnetic theory can be used to explain the plasmonic properties of these larger nanoparticles.[33] The ultra-small size (2–3 nm in diameter of the metal core) of MPC nanoparticles places them in between small molecules (e.g. metal–ligand complexes) and plasmonic metal nanoparticles. These ultra-small nanoparticles have strong quantum size effects due to the discrete energy levels of electrons and hence result in multiple absorption bands in the optical absorption spectra.[34-35] Therefore, quantum mechanical calculations are required to understand their optical properties.

1.1.2.1 $Au_{25}(SR)_{18}$

The $Au_{25}(SR)_{18}$ nanocluster has been extensively studied both experimentally and theoretically due to its exceptional stability[36-37] and interesting optical properties. $Au_{25}(SR)_{18}$ has crystallographically resolved charge states of -1, 0, +1[20-21, 38-39] that are stable irrespective of

their charge.[40] The cluster consists of a Au_{13} icosahedral core surrounded by six "V-shaped" −SR−Au−SR−Au−SR− semiring motifs as shown in Figure 1.[20-21]

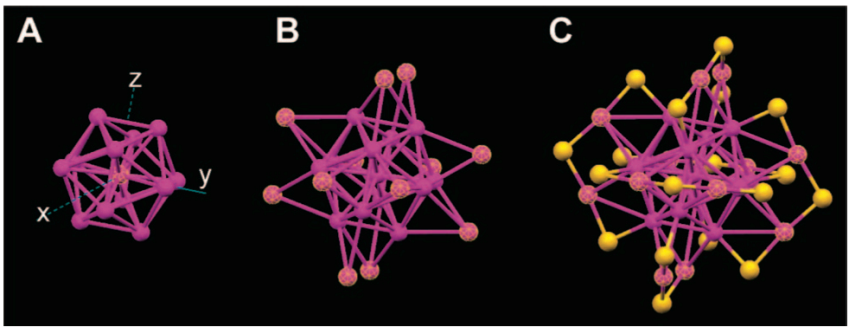

Figure 1.1 Crystal structure of a $Au_{25}(SR)_{18}$ cluster, where R=phenylethyl group (R groups are not shown here) (A) the icosahedral Au_{13} core (B) Au_{13} core and the exterior 12 gold atoms (C) Au_{25} cluster protected by 18 thiolate ligands (magenta-Au; yellow-S) (Reprinted with permission from *J. Am. Chem. Soc.* 2008, *130*, 5883-5885. Copyright 2008 American Chemical Society).

Time-dependent density functional theory (TDDFT) calculations have been performed on the $[Au_{25}(SR)_{18}]^{-1}$ cluster to correlate the optical properties with its cluster geometry. The experimental UV-vis spectrum has revealed three well defined bands at 1.8, 2.75 and 3.1 eV for $[Au_{25}(SR)_{18}]^{-1}$. The theoretical spectrum for $[Au_{25}(SR)_{18}]^{-1}$ agreed quite well with the experiment especially in the spectral shape.[21] Figure 1.2A shows the Kohn-Sham orbital energy level diagram for a model compound $[Au_{25}(SR)_{18}]^{-1}$ and Figure 1.2B shows its theoretical absorption spectrum. The a, b, c labels in the Figure 1.2B refer to the peaks corresponding to the experimentally observed peaks. According to the $[Au_{25}(SR)_{18}]^{-1}$ electronic structure, the *sp*-band is comprised of the HOMO to LUMO+2 orbitals (Figure 1.2A), which has a higher contribution from the 6*sp* atomic orbitals of gold (shown in green). Here, the HOMO is the highest occupied molecular orbital and LUMO is the lowest unoccupied molecular orbital. The HOMO-1 to HOMO-5 orbitals are made up of 5*d* atomic orbitals of gold and *p* orbitals from sulfur, which is known as the *d*-band. The HOMO orbital of $[Au_{25}(SR)_{18}]^{-1}$ is approximately triply degenerate and has the shape of a superatom P orbital, whereas the LUMO orbital is approximately doubly degenerate. The first peak at 1.52 eV corresponds to a HOMO → LUMO transition, which is an intraband, *sp* → *sp* transition. The next peak at 2.63 eV arises from mixed intraband *sp* → *sp* and

interband *sp* → *d* transitions. The peak at 2.91 eV arises mainly from an interband transition sp → d.

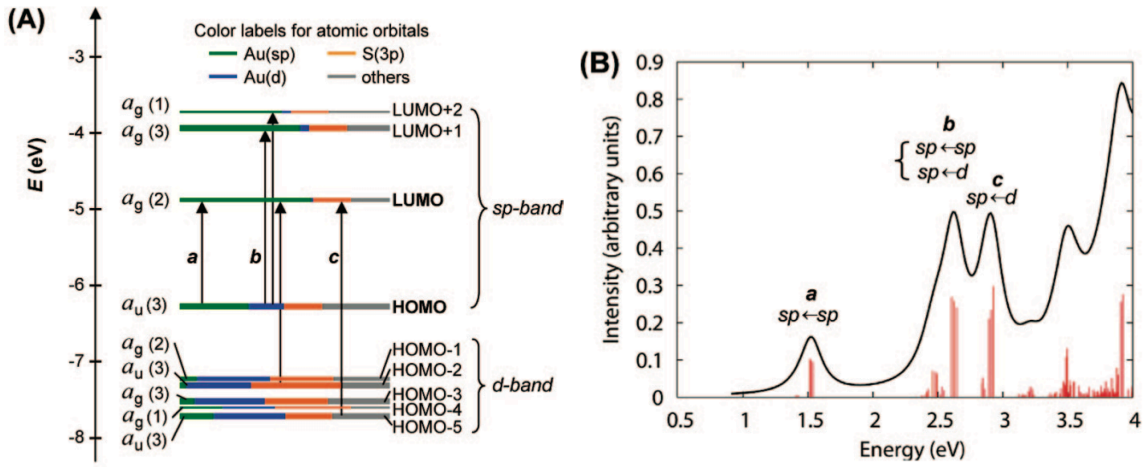

Figure 1.2 (A) Kohn-Sham orbital energy level diagram for $Au_{25}(SH)_{18}^{-1}$ (B) The theoretical absorption spectrum of $Au_{25}(SH)_{18}^{-1}$ (Reprinted with permission from *J. Am. Chem. Soc.* 2008, *130*, 5883-5885. Copyright 2008 American Chemical Society).

It has been shown that the HOMO-LUMO gap of $[Au_{25}(SR)_{18}]^{-1}$ is not significantly affected by the thiolate ligand (R) attached.[40-41] Both theoretical and experimental work have been performed on the $[Au_{25}(SR)_{18}]^{-1}$ cluster to discover the ligand effects on its optical properties. The first absorption peak redshifts less than the second peak for R = CH_3, CH_2CH_3 compared to R = H in a density functional theory (DFT) study.[42] In an experimental study, the para-substituted phenyl groups in the $Au_{25}(SCH_2CH_2Ph)_{18}^{-}$ have shown similar optical absorption spectra with slight blueshifts in the second and third peaks.[41] A double peak has been observed instead of the first main peak in the optical absorption spectra of $[Au_{25}(SR)_{18}]^{-1}$ theoretically[43] and experimentally[44] when different ligands are used. The double peaks are attributed to splitting of the superatom P orbitals due to longer ligands. In a theoretical study, as the charge *q* of the $Au_{25}(SR)_{18}^{q}$ cluster goes from -1 to +1, an increase in the splitting of superatomic P orbitals has been observed.[45] A TDDFT investigation showed that the absorption spectrum of $[Au_{25}(SR)_{18}]^{-1}$ is slightly affected in the presence of a solvent.[42]

The photoluminescence of the $[Au_{25}(SR)_{18}]^{-1}$ nanocluster has been widely investigated both experimentally and theoretically. Various experimental investigations have been carried out to understand the temperature,[46] ligand,[46-47] and charge state dependence and the

photoluminescence mechanism of $Au_{25}(SR)_{18}$ nanocluster.[48-49] The experimental emission of the $Au_{25}(SR)_{18}$ cluster has been observed in the 1.15–1.55 eV range. Diverse photoluminescence mechanisms proposed by the experimental groups have raised the question whether the involved excited states arise from core-based orbitals, charge-transfer states, or from ligand-based states. However, a recent theoretical investigation has proposed that the photoluminescence based states arise from core-based orbitals and that there is no involvement of the semiring states.[50]

1.1.2.2 Other thiolate-protected gold and silver nanoparticles

TDDFT investigations have been carried to along with the crystal structure determinations to understand the optical properties, their origin and to link the structure property relations for various other thiolate-protected nanoparticles.[51-59]

Various sizes of thiolate-protected gold nanoclusters with different core:ligand ratios have been determined by X-ray crystallography.[21, 60-62] Extensive TDDFT calculations have been used to predict cluster structures using theoretical absorption spectra. The $Au_{18}(SR)_{14}$ nanocluster is the smallest stable member of an "isoelectronic" 4 electron family.[62] Tlahuice and Garzon theoretically predicted a $Au_{18}(SR)_{14}$ structure[63] that has a prolate bi-tetrahedral Au_8 core protected by two dimers ($Au_2(SR)_3$) and two trimer ($Au_3(SR)_4$) semiring motifs. In 2014, Kamat and co-workers showed that $Au_{18}(GSH)_{14}$ absorbs strongly in the visible range,[64] which matched with the UV-vis spectra reported by Xie and co-workers in 2013[65] for a similar cluster. Notable peaks appeared at 580 nm and 620 nm.[65] In 2015, two experimental groups of Jin and Zhu crystallized the $Au_{18}(SR)_{14}$ nanocluster in separate experiments. They obtained a similar geometry despite different ligands used.[62, 66] They found that $Au_{18}(SR)_{14}$ is charge neutral cluster with a face-fused Au_9 bi-octahedral core. The core is protected by semiring motifs consisting of one $Au_4(SR)_5$ tetramer, one $Au_2(SR)_3$ dimer, and three $Au(SR)_2$ monomers. The Au_9 core has a +5 charge. The Au_9 core is larger than the Au_7 and Au_8 cores of $Au_{20}(SR)_{16}$ and $Au_{24}(SR)_{20}$, respectively.[62, 66] The $Au_{20}(SR)_{16}$ and $Au_{24}(SR)_{20}$ are other members of "isoelectronic" 4e nanocluster family. In $Au_{18}(SR)_{14}$, strong interactions between the core and the semirings (strong Au_{core}-$Au_{semiring}$ bonds) have been reported. Similar strong core-semiring bonds have been reported in $Au_{20}(SR)_{16}$.[62] Also, the ligand does not affect the geometric structure of this cluster.[62] The experimental UV-vis absorption spectrum of $Au_{18}(SC_6H_{11})_{14}$ showed peaks around 1.97, 2.18 and 2.76 eV[66] and the Zhu and co-workers have shown main peaks at 1.94, 2.14, 2.70 and

3.26 eV on a similar cluster.[62] TDDFT calculations on these geometries have shown similar peaks but with a redshift despite the different level of theories used (BP86/double-ζ valence and PBE/TZP with ZORA level of theories).[62, 66] The first peak at ~ 1.9 eV was assigned to the HOMO → LUMO transition which is a semiring to core charge transfer.[66]

$Au_{38}(SR)_{24}$ is one of the earliest theoretically predicted nanoclusters.[67] Aikens and co-workers[68] found several lower energy geometries for the $Au_{38}(SR)_{24}$ nanocluster by considering the structure of the protective gold-thiolate layer. They showed that the D_3 isomer geometries are stable than the C_{3h} isomer. This cluster consists of a faced fused bi-icosahedral Au_{23} core protected by six $Au_2(SR)_3$ dimeric semirings and three Au(SR) monomeric semirings.[68] Due to its elongated gold core structure, the electronic structure of the Au_{38} can be explained through the particle-in-a-cylinder (PIC) model and the orbitals can be expressed with Σ, Π, Δ symmetries. The core-shell structure of the $Au_{38}(SR)_{24}$ nanocluster results in interesting optical properties. There are four main peaks appearing in the visible region of the optical absorption spectrum. The peaks up to 1.36 eV arise from intraband transitions and the peaks that lie in the 1.59-1.72 eV range arise from a combination of intraband and interband transitions. The transitions out of the ligand-based *d*-band into the *sp*-band are responsible for the fourth peak.[68] A theoretical investigation on the luminescence origin of the $Au_{38}(SR)_{24}$ nanocluster suggested that the two lowest energy fluorescence bands of the $Au_{38}(SH)_{24}$ nanoparticle arise predominantly due to a HOMO → LUMO transition that involves core-based orbitals[50] rather than the core-to-semiring relaxations as predicted in experimental luminescence work.[69]

Similar to thiolate-protected gold nanoclusters, experimental and theoretical work has also been performed to understand the structures and optical properties of thiolate-protected silver clusters. Experimental observation of discrete optical absorption spectra for silver nanoparticles with diameters less than 3 nm[70] suggested that these nanoparticles could behave similar to their gold counterparts. $Ag_{44}(SR)_{30}$ was the first thiolate-protected silver nanoparticle synthesized[71] and its crystal structure has been resolved.[72] It is composed of a Ag_{12} icosahedral core surrounded by a Ag_{20} decahedral outer core. The core is protected by six $Ag_2(SR)_5$ semirings. The HOMO of this cluster is a superatomic D orbital.[72]

Total structure determination of $[Au_{25}(SR)_{18}]^{-1}$ lead to investigation of its silver analog $[Ag_{25}(SR)_{18}]^{-1}$ and two other silver doped Au_{25} clusters. Aikens performed TDDFT calculations on these predicted silver clusters to understand their optical and electronic properties.[73]

$[Ag_{25}(SR)_{18}]^{-1}$ showed an electronic structure similar to its gold analog where the HOMO is nearly triply degenerate and the LUMO is nearly doubly degenerate. The HOMO→LUMO transition has been observed around 1.64 eV with the SAOP/TZP level of theory. The HOMO-LUMO gap of both silver and gold clusters are similar. However, the gap between the LUMO and LUMO+1 is smaller for silver compared to the gold analog. Thus, the second peak in the silver nanoparticle originated from a HOMO→LUMO+1 transition. Later, the "golden" silver nanoparticle, $[Ag_{25}(SR)_{18}]^{-1}$ was synthesized and characterized,[74] and its experimental UV-vis absorption spectrum agrees well with the spectrum predicted by Aikens.

1.1.3 Optical properties of noble metal nanowires

Apart from the ligand-protected noble metal nanoclusters, bare nanoparticles of noble metals also demonstrate unique optical properties. The surface plasmon resonances in these gold and silver nanoparticles can be tuned depending on the size, shape, dielectric function and the environment of the nanoparticle.[75] During the past years, various shapes of gold and silver nanoparticles have been synthesized such as nanorods, nanobars and nanowires.[76-78] Among the various shapes of nanoparticles available, nanorods and nanowires have drawn significant attention due the high sensitivity of their optical properties to their aspect ratios.[79-81] TDDFT theoretical investigations have been performed on nanorods/nanowires with various sizes and shapes[82-87] to understand their interesting optical properties. The plasmon excitations in small nanowires have been investigated using the linear response TDDFT method.[84] This method has also been used to explore the optical properties of silver nanorods.[82] Real time TDDFT has been used to study the end and central plasmon modes in linear sodium and silver chains.[85-86] Later, the size dependence of electronic excitations in copper, silver and gold chains up to 26 atoms was investigated.[87] Recently, the coherent plasmonic behavior of silver nanowires Ag_m (m= 4, 6, 8, 10, 12) was studied using a real time TDDFT method.[88]

1.2 Excited state behavior of noble metal systems

Noble metal nanoclusters demonstrate features specific to their structures that could lead to different relaxations. Precise interpretations of the excited state behavior of monolayer protected gold and silver nanoclusters has been debated over time. The excited state relaxations

of the gold nanoclusters can be described based on several representations. The energy gap law is one of the models used to explain the excited state relaxations; this law states that the excited state lifetimes increase with the decrease in nanoparticle size.[89] In other words, there is an inverse relationship between the HOMO-LUMO energy gap and the non-radiative decay in these systems.[90] It has been shown that the relaxations of gold nanoclusters that arise due to electron-phonon interactions are less significant due to their discontinuous energy states.[64, 91] A common view of the excited state relaxations in monolayer protected gold nanoclusters is that two processes occur, including an ultra-fast relaxation that happens in the gold core (< 200fs) and a subsequent internal relaxation of core-semiring charge transfer (~1ps).[92-97] These long lived semiring states can be responsible for the photoluminescence of the gold nanoclusters. The semiring states have been suggested as the main contributor in the relaxation dynamics of the gold nanoclusters.[91-92, 98] The excited state relaxation dynamics of the gold nanoclusters can also depend on the charge states, dopants, ligands and the solvent.[99-103]

A photoinduced electron transfer study on glutathione-protected gold nanoclusters has suggested that a semiring state with a relatively long lifetime is responsible for the electron transfer, which is of interest for light harvesting applications.[64] A different study has shown that the charge transfer in glutathione-protected gold nanoclusters is dependent on the size of the cluster.[64] $Au_{18}(SR)_{14}$ showed the highest electron transfer yield of ~4% among other gold clusters in that photo-induced electron transfer investigation. In a different gold nanocluster-sensitized solar cell experiment, $Au_{18}(SR)_{14}$ was identified as a better sensitizer based on its power conversion efficiency.[104]

Plasmonic-based solar water splitters have been developed over the past years to produce solar fuels. In a plasmon-enhanced photocatalysis system, a semiconductor material (TiO_2) is in contact with a noble metal nanoparticle (gold/silver) that has a surface plasmon resonance (SPR). This combined noble metal-semiconductor composite system has shown enhanced photocatalytic yields upon visible light irradiation (Figure 1.3)[105-108]

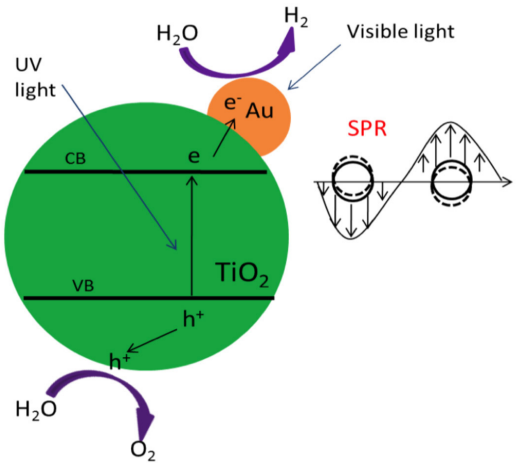

Figure 1.3 The combined noble metal-semiconductor composite system. Electrons (e) in the valence band (VB) are excited to the conduction band (CB) in titanium oxide (TiO_2) by UV light irradiation. The excited electrons migrate to the gold particles (Au) to facilitate hydrogen production. The holes (h^+) created in the VB promote oxygen production. (Reprinted with permission from *SPIE Newsroom*. DOI: 10.1117/2.1201201.00407).

Recently, the research groups of Tatsuma, Kamat, and Jin have shown that even the traditionally non-plasmonic noble metal nanoclusters such as $Au_{25}(SR)_{18}^-$ can also create a photocatalytic enhancement upon visible light irradiation.[6, 109-110] These smaller noble metal nanoparticles are of great interest for photocatalysis due to several reasons. These noble metal nanoparticles can have quantized double layer charging which can promote charge storage within the nanoparticle.[111] Also, these smaller nanoparticles can create a larger shift of the apparent Fermi level than larger particles.[112] More importantly, these small thiolate-stabilized nanoparticles can greatly absorb visible light from the solar spectrum. Despite of many studies, the direction of the electron flow within the noble metal-semiconductor composite system is not fully understood. It has been suggested that the mechanism of electron flow can vary depending on whether visible light or UV light is used. Experimentally, several different interfaces between the noble metal and TiO_2 have been studied since the interface is an important factor that affects the rates of charge migration and recombination. The mercaptopropionic acid (MPA) linker can be used to covalently attached the gold nanoparticle to the TiO_2 surface.[112] Generating solar fuels from photocatalysis is an interesting concept, but more development is needed due to the inadequate current understanding of the fundamental physical principles involved.

1.2.1 Nonradiative relaxations of thiolate-protected noble metal nanoparticles

It is vital to investigate the excited state relaxations of thiolate-protected noble metal clusters upon visible light irradiation to understand their photo-physics. Precise knowledge of the photo-physics of thiolate-protected noble metal nanoparticles can eventually lead to further development of its potential applications as mentioned in the previous section. Energy relaxation dynamics investigations on different sizes and structures of thiolate-protected noble metal nanocluster will allow us to elucidate their physical and chemical properties for the advanced development of catalytic applications.[96-97, 103, 113-116] Experimental work on thiolate-protected gold clusters reported that fluorescence could arise from charge transfer (CT) interactions between the ligands and the metal core.[92] Hence, understanding the role played by CT and core transitions in defining the excited state behavior of the thiolate-protected gold clusters is crucial.

1.2.1.1 $[Au_{25}(SR)_{18}]^{-1}$

In the literature, various experimental depictions of electron relaxation dynamics from excited states lying near the HOMO−LUMO gap and from higher excited states of the $[Au_{25}(SR)_{18}]^{-1}$ cluster are available. Very distinct time scales that range from the femtosecond to nanosecond scale and different mechanisms for relaxation have been reported experimentally for nonradiative relaxation dynamics of the $[Au_{25}(SR)_{18}]^{-1}$ cluster.

Whetten, El-Sayed and co-workers[117] have performed studies on a thiolate-stabilized gold cluster which was later identified as the Au_{25} cluster. Their transient absorption studies revealed the luminescence lifetime to be on a nanosecond time scale or longer. At the same time, a fast relaxation (750 fs) was observed and was attributed to relaxation from higher excited state(s) to the lowest singlet excited state through internal conversion. The femtosecond relaxation dynamics performed on the $[Au_{25}(SCH_2CH_2Ph)_{18}]^{-1}$ anion by Moran and co-workers[93] showed an extremely rapid internal conversion process, ~200 fs, which they attributed to the transitions in the multilevel electronic structure of the Au_{13} core. A significant wave function overlap of the states localized in the core atoms has been recognized as the reason for the ultrafast relaxation. These core states include the HOMO−LUMO which is approximately 6-fold degenerate and the HOMO−LUMO+1, which is approximately 9-fold degenerate. They observed another decay channel with a 1.2 ps internal conversion time scale, which they identified as a relaxation from

the core to the semirings. Femtosecond time-resolved luminescence measurements on $Au_{25}L_{18}$ clusters (L = hexanethiol and glutathione) by Ramakrishna and co-workers suggested that higher excited states have decay lifetimes of 200 fs to a few picoseconds and are relatively long-lived compared to molecular excited states and excited states in larger nanoparticles.[92]

Jin and co-workers studied the ultrafast electron relaxation dynamics of anionic and neutral $Au_{25}(SR)_{18}$ nanoclusters.[113] They reported that in both clusters, photoexcitation occurs into two nondegenerate states near the HOMO-LUMO gap that are derived from the core orbitals. A large difference between the lifetimes of the core excitations was observed for the two clusters where the anion gives a decay rate more than 1000 times slower than the neutral cluster. Knappenberger and co-workers studied the excited state relaxation dynamics in the $Au_{25}L_{18}$ cluster in its anion and neutral forms using time-resolved near-infrared transient absorption spectroscopy.[99] A nonradiative core-to-ligand energy transfer process following the internal conversion, on a few picosecond time scale, was identified as the main relaxation mechanism. A ∼100 ps relaxation was reported for the anion where the relaxation starts from the excitation to LUMO+1 and not LUMO. Different excited state lifetimes have been identified for states as core and CT type states for $Au_{25}(SR)_{18}$ clusters by Goodson and co-workers.[97] The core states are made of the HOMO−LUMO transitions, whereas the CT states are the core−shell transitions. They suggested that core states have a lifetime below 5 ps and the CT states had lifetimes above 1 ns.

The excited states of glutathione-protected gold nanoclusters have been studied by Kamat and co-workers.[98] They reported a 780 ns long-lived excited state, which they assigned to a ligand-to-metal transition. A 3 ps short-lived state has been ascribed to a metal core transition in the reduced glutathione-stabilized gold cluster. In a different study, the size-dependence of the excited state dynamics in glutathione-protected gold clusters was investigated. The $Au_{25}(GS)_{18}$ cluster has shown a rapid ca. 1 ps decay which was assigned to a metal−metal transition and a slower decay of ca. 200 ns was identified which they identified as a ligand-to-metal charge transfer.[64] A femtosecond two-dimensional electronic spectroscopy (2DES) study was performed to understand the electronic relaxation dynamics on the superatom P and D states of the $[Au_{25}(SC_8H_9)_{18}]^{-1}$ cluster by Knappenberger and co-workers.[95] Two distinct transitions around 1.90 and 2.20 eV were identified, which are believed to arise from the HOMO−1; HOMO−2 → LUMO+1;LUMO and HOMO−1;HOMO−2 → LUMO+2;LUMO+3 respectively.

The hot electrons created in the excitations to LUMO+2 and LUMO+3 in the 2.20 eV excitation rapidly relax to the LUMO within 200 fs via internal conversion. These higher LUMOs arise from the Au *sp* conduction band. A rapid 85 fs decay has been reported for the 1.90 eV excitation, which is assigned to an internal conversion of electron from LUMO+1 to LUMO. A common decay to both the 1.90 and 2.20 eV excitations, which has a time constant of 300 fs for the decay, was attributed to internal conversion of holes between the HOMO−2 and HOMO states. A very recent theoretical study on the $[Au_{25}(SH)_{18}]^{-1}$ cluster proposed a mechanism considering relaxations mainly within the core states. They supported the idea that the relaxations are a sum of ring and core contributions.[118] Recently, Knappenberger, Jin and co-workers studied the ligand and solvent dependent electronic relaxation dynamics of $Au_{25}(SR)_{18}^{-}$ clusters.[102] This study concluded that intraband relaxation among the MPC superatom states is mediated by low-frequency vibrations of the gold core.

In addition to the undoped $[Au_{25}(SR)_{18}]^{-1}$ nanocluster, nonradiative relaxation experiments have also been performed on doped versions of the $[Au_{25}(SR)_{18}]^{-1}$ nanocluster. In 2010, Moran and co-workers studied the relaxation dynamics of the $Au_{24}Pd(SCH_2CH_2Ph)_{18}$ cluster. They reported relaxation within the core within 50 fs and core-to-ligand internal conversion with a decay constant of 500 fs which was similar to their relaxation dynamics on $Au_{25}(SCH_2CH_2Ph)_{18}^{-}$.[94] Jin and co-workers investigated the effects of single atom doping on the ultrafast electron dynamics of the $M_1Au_{24}(SR)_{18}$ (M=Pd, Pt) nanoclusters. Similar relaxation pathways were observed for both Pt and Pd doped systems. However, the Pt dopant showed an accelerated coupling between the metal core and the surface ligands compared to the Pd dopant.[100] A temperature dependent absorption and ultrafast exciton relaxation dynamics study was performed on $MAu_{24}(SR)_{18}$ clusters (M = Pt, Hg) to understand the role of the central metal atom. Ultrafast transient absorption results have shown that Pt-doping leads to faster excited state relaxation while the Hg-doping and undoped Au_{25} relax to shell gold in a much longer time.[101]

1.2.1.2 Other thiolate-protected gold nanoparticles

Various excited state relaxation dynamic experiments have been conducted on other thiolate-protected gold nanoclusters such as $Au_{10-12}(GSH)_{10-12}$, $Au_{15}(GSH)_{13}$, $Au_{18}(GSH)_{14}$,[64] and $Au_{38}(SC_2H_4Ph)_{24}$.[119] In 2014, Kamat and co-workers carried out ultrafast (femtosecond) transient absorption spectroscopy and nanosecond transient absorption spectroscopy to

investigate the excited state behavior of glutathione-protected clusters $Au_{25}(GSH)_{18}$, $Au_{18}(GSH)_{14}$, $Au_{15}(GSH)_{13}$, and $Au_{10-12}(GSH)_{10-12}$. They were able to determine the quantum yield of electron transfer between the excited metal clusters and methyl viologen (MV^{2+}) to find the size dependent properties. The study showed a rapid (< 1 ps) and a slower (~200 ns) relaxation for larger sized clusters with core metal atoms while only a slower relaxation was observed for the homoleptic ($Au_{10-12}(GSH)_{10-12}$) clusters. The decay components were identified as metal−metal transition and ligand-to-metal charge transfer, respectively. An increasing photocatalytic reduction yield with decreasing cluster size ($Au_{25} < Au_{18} < Au_{15} < Au_{10-12}$) was found. However, $Au_{18}(GSH)_{14}$ was identified as the highest potential photosensitizer based on the quantum yield of electron transfer and good visible light absorption properties.[64] Similar observations have been found by Bang and co-workers. They reported a power conversion efficiency of 3.8% for $Au_{18}(GSH)_{14}$ cluster used in a gold nanocluster-sensitized solar cell.[104]

A very recent experiment by Jin and co-workers reports the ultrafast relaxation dynamics of $Au_{38}(SC_2H_4Ph)_{24}$ nanoclusters and the effects of structural isomerism.[119] The study found a correlation between ultrafast relaxation dynamics and atomic structures of two isomers of thiolate-protected $Au_{38}(SC_2H_4Ph)_{24}$. The bi-icosahedral Au_{38} with a Au_{23} inner core showed a rapid decay (1.5 ps) followed by nanosecond relaxation to the ground state. The isomer with a core composed of mono-icosahedral Au_{13} capped by a Au_{12} tri-tetrahedron by sharing two atoms revealed similar relaxation processes, but with the rapid decay being accelerated (1 ps). Here, the picosecond relaxations were assigned to core–shell charge transfer or to electronic rearrangement within the metal core.

Experimental work has also been done on a rod shaped 25-atom gold nanocluster to understand its ultrafast relaxation dynamics.[114] The 25-atom rod is protected by 10 triphenylphosphines, 5 phenylethylthiolates, and 2 chloride electron-withdrawing ligands which is different from the conventional ligand arrangement of the $[Au_{25}(SR)_{18}]^{-1}$ nanocluster. Their femtosecond transient absorption studies revealed two lifetimes, with the 0.8 ps component attributed to the fast internal conversion process from LUMO+n to LUMO and the long component to electron relaxation to the ground state.

A series of *n*-hexanethiolate-protected gold clusters (Au_{25}, Au_{38}, Au_{67}, Au_{102}, Au_{144}, Au_{333}) were studied to understand the excited state relaxation. It has found that excited state dynamics of the nanoclusters are governed by the energy gap law.[89] In a recent investigation, the

size dependent excited state dynamics in a periodic series of face-centered cubic gold nanoclusters (including $Au_{28}(SR)_{20}$, $Au_{36}(SR)_{24}$, $Au_{44}(SR)_{28}$, $Au_{52}(SR)_{32}$) have been studied. The excited state behavior of these nanoparticles showed a different behavior compared to the rest of the nanoclusters studied so far. This study suggested that core-semiring relaxations are not involved in the relaxations, and relaxation of the excited states slows down with an increase in nanoparticle size.[120]

1.2.1.3 Silver thiolate-protected nanoparticles

In the literature, no experimental work has been performed yet on the relaxation dynamics of thiolate-protected silver nanoclusters that are an exact analog of the thiolate-protected gold nanoclusters mentioned in the previous section. However, transient spectroscopy experiments have been done on a ligand-stabilized silver cluster, $[Ag_{44}(SR)_{30}]^{4-}$, to understand its time-dependent optical properties.[115] Furthermore, an investigation has been done on a rod-shaped, silver-doped Ag_xAu_{25-x} nanocluster to compare the relaxation dynamics in the doped structures with the undoped cluster. This study observed faster nuclear relaxation in doped systems compared to undoped.[121]

1.3 Objectives and overview of the thesis

A clear interpretation of excited state relaxation dynamics in thiolate-protected noble metal nanoparticles has drawn much attention in research due the applicability of these systems as a potential photosensitizer in metal cluster-sensitized solar cells, in light harvesting, and in photoluminescence applications. Various experimental work has been done to characterize the electron relaxation dynamics of the excited states in noble metal nanoparticles. Despite the widespread experiments, very distinct time scales that range from the femtosecond to nanosecond scale have been reported experimentally for nonradiative relaxation dynamics. Also, several different mechanisms for relaxation have been proposed. The primary objective of this thesis is to explore the excited state relaxation dynamics of thiolate-protected noble metal clusters upon visible light irradiation to understand their photo-physics. The relaxation dynamics will be assessed on various noble metal nanoparticles based on ligand effects, size effects and the noble metals. A secondary objective of this thesis to investigate the optical absorption in a set of

gold nanowires using the real time TDDFT method, which is a model system that will aid in understanding the electron dynamics in larger plasmonic nanoparticles.

Chapter 2 explains the theory and the computational methods used in this research. Chapter 3 (Senanayake, R. D.; Akimov, A. V.; Aikens, C. M., *J. Phys. Chem. C*. **2017**, 121, 10653−10662.) delivers a theoretical investigation of electron and nuclear dynamics in the $[Au_{25}(SH)_{18}]^{-1}$ thiolate-protected gold nanocluster. Chapter 4 gives insights on the electronic relaxation dynamics in the thiolate-protected nanocluster series $[Au_{25}(SR)_{18}]^{-1}$ (R = CH_3, C_2H_5, C_3H_7, MPA) [MPA = mercaptopropionic acid] to understand the ligand effects on relaxation dynamics as well as to examine separate electron and hole relaxations in the $[Au_{25}(SCH_3)_{18}]^{-1}$ nanocluster. Chapter 5 provides a theoretical investigation of relaxation dynamics in the $Au_{18}(SH)_{14}$ gold nanocluster. Chapter 6 explains a theoretical investigation of relaxation dynamics in the $Au_{38}(SH)_{24}$ thiolate-protected gold nanocluster. Chapter 7 explores the relaxation dynamics of the $[Ag_{25}(SH)_{18}]^{-1}$ nanocluster compared to its exact gold analog, $[Au_{25}(SH)_{18}]^{-1}$. Chapter 8 gives a real-time TDDFT investigation of optical absorption in gold nanowires. Finally, Chapter 9 summarizes this thesis and provides possible directions for future work.

1.4 References

1. Hunt, L., The True Story of Purple of Cassius. *GOLD BULL* **1976,** *9* (4), 134-139.

2. Vajtai, R., *Springer Handbook of Nanomaterials*. Springer Science & Business Media: 2013.

3. Jiang, S.; Win, K. Y.; Liu, S.; Teng, C. P.; Zheng, Y.; Han, M.-Y., Surface-functionalized Nanoparticles for Biosensing and Imaging-guided Therapeutics. *Nanoscale* **2013,** *5* (8), 3127-3148.

4. Mahmoud, M. A.; El-Sayed, M. A., Different Plasmon Sensing Behavior of Silver and Gold Nanorods. *J. Phys. Chem. Lett.* **2013,** *4* (9), 1541-1545.

5. Saha, K.; Agasti, S. S.; Kim, C.; Li, X.; Rotello, V. M., Gold Nanoparticles in Chemical and Biological Sensing. *Chem. Rev.* **2012,** *112* (5), 2739-2779.

6. Chen, Y.-S.; Choi, H.; Kamat, P. V., Metal-cluster-sensitized Solar Cells. A New Class of Thiolated Gold Sensitizers Delivering Efficiency Greater than 2%. *J. Am. Chem. Soc.* **2013,** *135* (24), 8822-8825.

7. Hirakawa, T.; Kamat, P. V., Photoinduced Electron Storage and Surface Plasmon Modulation in Ag@ TiO_2 Clusters. *Langmuir* **2004,** *20* (14), 5645-5647.

8. Sun, Y., Conversion of Ag Nanowires to AgCl Nanowires Decorated with Au Nanoparticles and their Photocatalytic Activity. *J. Phys. Chem. C* **2010,** *114* (5), 2127-2133.

9. Rashid, M. H.; Bhattacharjee, R. R.; Kotal, A.; Mandal, T. K., Synthesis of Spongy Gold Nanocrystals with Pronounced Catalytic Activities. *Langmuir* **2006,** *22* (17), 7141-7143.

10. Sarina, S.; Waclawik, E. R.; Zhu, H., Photocatalysis on Supported Gold and Silver Nanoparticles Under Ultraviolet and Visible Light Irradiation. *Green Chem.* **2013,** *15* (7), 1814-1833.

11. Shahbazali, E.; Hessel, V.; Noël, T.; Wang, Q., Metallic Nanoparticles Made in Flow and their Catalytic Applications in Organic Synthesis. *Nanotechnology Reviews* **2014,** *3* (1), 65-86.

12. Pradeep, T., *Nano: The Essentials*. Tata McGraw-Hill Education: 2007.

13. Albano, V.; Bellon, P.; Manassero, M.; Sansoni, M., Intermetallic Pattern in Metal-Atom Clusters. Structural Studies on $Au_{11}X_3(PR_3)_7$ Species. *Journal of the Chemical Society D: Chemical Communications* **1970,** (18), 1210-1211.

14. McPartlin, M.; Mason, R.; Malatesta, L., Novel Cluster Complexes of Gold(0)–Gold(I). *Journal of the Chemical Society D: Chemical Communications* **1969,** (7), 334-334.

15. Bellon, P.; Manassero, M.; Sansoni, M., Crystal and Molecular Structure of Tri-iodoheptakis (tri-p-fluorophenylphosphine) Undecagold. *J. Chem. Soc., Dalton Trans.* **1972,** (14), 1481-1487.

16. van der Velden, J. W.; Bour, J. J.; Bosman, W. P.; Noordik, J. H., Synthesis and X-ray Crystal Structure Determination of the Cationic Gold Cluster Compound $[Au_8(PPh_3)_7](NO_3)_2$. *J. Chem. Soc., Chem. Commun.* **1981,** (23), 1218-1219.

17. Bellon, P.; Cariati, F.; Manassero, M.; Naldini, L.; Sansoni, M., Novel Gold Clusters. Preparation, Properties, and X-ray Structure Determination of Salts of Octakis (triarylphosphine) Enneagold,$[Au_9L_8]X_3$. *Journal of the Chemical Society D: Chemical Communications* **1971,** (22), 1423-1424.

18. Li, J.; Wang, S.-G., Phosphane-stabilized Gold Clusters: Investigation of the Stability of $[Au_{13}(PMe_2Ph)_{10}Cl_2]^{3+}$. *J. Mol. Model.* **2010,** *16* (3), 505-512.

19. Jadzinsky, P. D.; Calero, G.; Ackerson, C. J.; Bushnell, D. A.; Kornberg, R. D., Structure of a Thiol Monolayer-Protected Gold Nanoparticle at 1.1 Å Resolution. *Science* **2007,** *318* (5849), 430-433.

20. Heaven, M. W.; Dass, A.; White, P. S.; Holt, K. M.; Murray, R. W., Crystal Structure of the Gold Nanoparticle $[N(C_8H_{17})_4][Au_{25}(SCH_2CH_2Ph)_{18}]$. *J. Am. Chem. Soc.* **2008,** *130* (12), 3754-3755.

21. Zhu, M.; Aikens, C. M.; Hollander, F. J.; Schatz, G. C.; Jin, R., Correlating the Crystal Structure of a Thiol-protected Au_{25} Cluster and Optical Properties. *J. Am. Chem. Soc.* **2008,** *130* (18), 5883-5885.

22. Häkkinen, H.; Walter, M.; Grönbeck, H., Divide and Protect: Capping Gold Nanoclusters with Molecular Gold−thiolate Rings. *J. Phys. Chem. B* **2006,** *110* (20), 9927-9931.

23. Khanna, S.; Jena, P., Assembling Crystals From Clusters. *Phys. Rev. Lett.* **1992,** *69* (11), 1664.

24. Aikens, C. M., Electronic Structure of Ligand-Passivated Gold and Silver Nanoclusters. *J. Phys. Chem. Lett.* **2010,** *2* (2), 99-104.

25. Lopez-Acevedo, O.; Akola, J.; Whetten, R. L.; Grönbeck, H.; Häkkinen, H., Structure and Bonding in the Ubiquitous Icosahedral Metallic Gold Cluster $Au_{144}(SR)_{60}$. *J. Phys. Chem. C* **2009,** *113* (13), 5035-5038.

26. Dass, A., Faradaurate Nanomolecules: A Superstable Plasmonic 76.3 kDa Cluster. *J. Am. Chem. Soc.* **2011,** *133* (48), 19259-19261.

27. Wong, O. A.; Heinecke, C. L.; Simone, A. R.; Whetten, R. L.; Ackerson, C. J., Ligand Symmetry-equivalence on Thiolate Protected Gold Nanoclusters Determined by NMR Spectroscopy. *Nanoscale* **2012,** *4* (14), 4099-4102.

28. Halas, N. J.; Lal, S.; Chang, W.-S.; Link, S.; Nordlander, P., Plasmons in Strongly Coupled Metallic Nanostructures. *Chem. Rev.* **2011,** *111* (6), 3913-3961.

29. Chen, H.; Shao, L.; Li, Q.; Wang, J., Gold Nanorods and their Plasmonic Properties. *Chem. Soc. Rev.* **2013,** *42* (7), 2679-2724.

30. Yang, H.; Wang, Y.; Chen, X.; Zhao, X.; Gu, L.; Huang, H.; Yan, J.; Xu, C.; Li, G.; Wu, J., Plasmonic Twinned Silver Nanoparticles with Molecular Precision. *Nat. Commun.* **2016,** *7*, 12809.

31. Amendola, V.; Pilot, R.; Frasconi, M.; Maragò, O. M.; Iatì, M. A., Surface Plasmon Resonance in Gold Nanoparticles: A Review. *J. Phys. Condens. Matter* **2017,** *29* (20), 203002.

32. Willets, K. A.; Van Duyne, R. P., Localized Surface Plasmon Resonance Spectroscopy and Sensing. *Annu. Rev. Phys. Chem.* **2007,** *58*, 267-297.

33. Mie, G., Beiträge Zur Optik Trüber Medien, Speziell Kolloidaler Metallösungen. *Ann. Phys. (Berl.)* **1908,** *330* (3), 377-445.

34. Harbich, W.; Fedrigo, S.; Buttet, J., The Optical Absorption Spectra of Small Silver Clusters (n= 5–11) Embedded in Argon Matrices. *Chem. Phys. Lett.* **1992,** *195* (5-6), 613-617.

35. Harb, M.; Rabilloud, F.; Simon, D.; Rydlo, A.; Lecoultre, S.; Conus, F.; Rodrigues, V.; Félix, C., Optical Absorption of Small Silver Clusters: Ag_n,(n= 4–22). *J. Chem. Phys.* **2008,** *129* (19), 194108.

36. Negishi, Y.; Nobusada, K.; Tsukuda, T., Glutathione-protected Gold Clusters Revisited: Bridging the Gap Between Gold(I)−Thiolate Complexes and Thiolate-Protected Gold Nanocrystals. *J. Am. Chem. Soc.* **2005,** *127* (14), 5261-5270.

37. Shichibu, Y.; Negishi, Y.; Tsukuda, T.; Teranishi, T., Large-scale Synthesis of Thiolated Au_{25} Clusters via Ligand Exchange Reactions of Phosphine-stabilized Au_{11} Clusters. *J. Am. Chem. Soc.* **2005,** *127* (39), 13464-13465.

38. Zhu, M.; Eckenhoff, W. T.; Pintauer, T.; Jin, R., Conversion of Anionic $[Au_{25}(SCH_2CH_2Ph)_{18}]^-$ Cluster to Charge Neutral Cluster via Air Oxidation. *J. Phys. Chem. C* **2008,** *112* (37), 14221-14224.

39. Tofanelli, M. A.; Salorinne, K.; Ni, T. W.; Malola, S.; Newell, B.; Phillips, B.; Häkkinen, H.; Ackerson, C. J., Jahn–Teller Effects in $Au_{25}(SR)_{18}$. *Chem. Sci.* **2016,** *7* (3), 1882-1890.

40. Negishi, Y.; Chaki, N. K.; Shichibu, Y.; Whetten, R. L.; Tsukuda, T., Origin of Magic Stability of Thiolated Gold Clusters: A Case Study on $Au_{25}(SC_6H_{13})18$. *J. Am. Chem. Soc.* **2007,** *129* (37), 11322-11323.

41. Guo, R.; Murray, R. W., Substituent Effects on Redox Potentials and Optical Gap Energies of Molecule-like $Au_{38}(SPhX)_{24}$ Nanoparticles. *J. Am. Chem. Soc.* **2005,** *127* (34), 12140-12143.

42. Aikens, C. M., Effects of Core Distances, Solvent, Ligand, and Level of Theory on the TDDFT Optical Absorption Spectrum of the Thiolate-protected Au_{25} Nanoparticle. *J. Phys. Chem. A* **2009,** *113* (40), 10811-10817.

43. Aikens, C. M., Geometric and Electronic Structure of $Au_{25}(SPhX)_{18}^-$(X= H, F, Cl, Br, CH_3, and OCH_3). *J. Phys. Chem. Lett.* **2010,** *1* (17), 2594-2599.

44. Akola, J.; Kacprzak, K. A.; Lopez-Acevedo, O.; Walter, M.; Grönbeck, H.; Häkkinen, H., Thiolate-protected Au_{25} Superatoms as Building Blocks: Dimers and Crystals. *J. Phys. Chem. C* **2010,** *114* (38), 15986-15994.

45. Antonello, S.; Perera, N. V.; Ruzzi, M.; Gascón, J. A.; Maran, F., Interplay of Charge State, Lability, and Magnetism in the Molecule-like $Au_{25}(SR)_{18}$ Cluster. *J. Am. Chem. Soc.* **2013,** *135* (41), 15585-15594.

46. Shibu, E. S.; Pradeep, T., Photoluminescence and Temperature Dependent Emission Studies of Au_{25} Clusters in Solid State. *Int. J. Photoenergy* **2007,** *1*, 1-4.

47. Shibu, E.; Muhammed, M. H.; Tsukuda, T.; Pradeep, T., Ligand Exchange of $Au_{25}SG_{18}$ Leading to Functionalized Gold Clusters: Spectroscopy, Kinetics, and Luminescence. *J. Phys. Chem. C* **2008,** *112* (32), 12168-12176.

48. Link, S.; Beeby, A.; FitzGerald, S.; El-Sayed, M. A.; Schaaff, T. G.; Whetten, R. L., Visible to Infrared Luminescence from a 28-atom Gold Cluster. *J. Phys. Chem. B* **2002,** *106* (13), 3410-3415.

49. Lee, D.; Donkers, R. L.; Wang, G.; Harper, A. S.; Murray, R. W., Electrochemistry and Optical Absorbance and Luminescence of Molecule-like Au_{38} Nanoparticles. *J. Am. Chem. Soc.* **2004,** *126* (19), 6193-6199.

50. Weerawardene, K. D. M.; Aikens, C. M., Theoretical Insights into the Origin of Photoluminescence of $Au_{25}(SR)_{18}^-$Nanoparticles. *J. Am. Chem. Soc.* **2016,** *138* (35), 11202-11210.

51. Zhu, M.; Qian, H.; Jin, R., Thiolate-protected Au_{20} Clusters with a Large Energy Gap of 2.1 eV. *J. Am. Chem. Soc.* **2009,** *131* (21), 7220-7221.

52. Weerawardene, K. D. M.; Aikens, C. M., Effect of Aliphatic versus Aromatic Ligands on the Structure and Optical Absorption of $Au_{20}(SR)_{16}$. *J. Phys. Chem. C* **2016,** *120* (15), 8354-8363.

53. Yu, Y.; Luo, Z.; Chevrier, D. M.; Leong, D. T.; Zhang, P.; Jiang, D.-e.; Xie, J., Identification of a Highly Luminescent $Au_{22}(SG)_{18}$ Nanocluster. *J. Am. Chem. Soc.* **2014,** *136* (4), 1246-1249.

54. Das, A.; Li, T.; Li, G.; Nobusada, K.; Zeng, C.; Rosi, N. L.; Jin, R., Crystal Structure and Electronic Properties of a Thiolate-protected Au_{24} Nanocluster. *Nanoscale* **2014,** *6* (12), 6458-6462.

55. Das, A.; Li, T.; Nobusada, K.; Zeng, C.; Rosi, N. L.; Jin, R., Nonsuperatomic $[Au_{23}(SC_6H_{11})_{16}]^-$ Nanocluster Featuring Bipyramidal Au_{15} Kernel and Trimeric $Au_3(SR)_4$ Motif. *J. Am. Chem. Soc.* **2013,** *135* (49), 18264-18267.

56. Crasto, D.; Malola, S.; Brosofsky, G.; Dass, A.; Häkkinen, H., Single Crystal XRD Structure and Theoretical Analysis of the Chiral $Au_{30}S$ (S-t-Bu)$_{18}$ Cluster. *J. Am. Chem. Soc.* **2014,** *136* (13), 5000-5005.

57. Zhu, M.; Qian, H.; Jin, R., Thiolate-protected $Au_{24}(SC_2H_4Ph)_{20}$ Nanoclusters: Superatoms or Not? *J. Phys. Chem. Lett.* **2010,** *1* (6), 1003-1007.

58. Nimmala, P. R.; Knoppe, S.; Jupally, V. R.; Delcamp, J. H.; Aikens, C. M.; Dass, A., $Au_{36}(SPh)_{24}$ Nanomolecules: X-ray Crystal Structure, Optical Spectroscopy, Electrochemistry, and Theoretical Analysis. *J. Phys. Chem. B* **2014,** *118* (49), 14157-14167.

59. Knoppe, S.; Malola, S.; Lehtovaara, L.; Bürgi, T.; Häkkinen, H., Electronic Structure and Optical Properties of the Thiolate-Protected $Au_{28}(SMe)_{20}$ Cluster. *J. Phys. Chem. A* **2013,** *117* (40), 10526-10533.

60. Qian, H.; Eckenhoff, W. T.; Zhu, Y.; Pintauer, T.; Jin, R., Total Structure Determination of Thiolate-protected Au_{38} Nanoparticles. *J. Am. Chem. Soc.* **2010,** *132* (24), 8280-8281.

61. Zeng, C.; Liu, C.; Chen, Y.; Rosi, N. L.; Jin, R., Gold–thiolate Ring as a Protecting Motif in the $Au_{20}(SR)_{16}$ Nanocluster and Implications. *J. Am. Chem. Soc.* **2014,** *136* (34), 11922-11925.

62. Chen, S.; Wang, S.; Zhong, J.; Song, Y.; Zhang, J.; Sheng, H.; Pei, Y.; Zhu, M., The Structure and Optical Properties of the $[Au_{18}(SR)_{14}]$ Nanocluster. *Angew. Chem. Int. Ed.* **2015,** *54* (10), 3145-3149.

63. Tlahuice, A.; Garzón, I. L., On the Structure of the $Au_{18}(SR)_{14}$ Cluster. *Phys. Chem. Chem. Phys.* **2012,** *14* (11), 3737-3740.

64. Stamplecoskie, K. G.; Kamat, P. V., Size-dependent Excited State Behavior of Glutathione-capped Gold Clusters and their Light-Harvesting Capacity. *J. Am. Chem. Soc.* **2014,** *136* (31), 11093-11099.

65. Yu, Y.; Chen, X.; Yao, Q.; Yu, Y.; Yan, N.; Xie, J., Scalable and Precise Synthesis of Thiolated $Au_{10–12}$, Au_{15}, Au_{18}, and Au_{25} Nanoclusters via pH Controlled CO Reduction. *Chem. Mater.* **2013,** *25* (6), 946-952.

66. Das, A.; Liu, C.; Byun, H. Y.; Nobusada, K.; Zhao, S.; Rosi, N.; Jin, R., Structure Determination of $[Au_{18}(SR)_{14}]$. *Angew. Chem. Int. Ed.* **2015,** *127* (10), 3183-3187.

67. Pei, Y.; Gao, Y.; Zeng, X. C., Structural Prediction of Thiolate-Protected Au_{38}: A Face-fused Bi-icosahedral Au Core. *J. Am. Chem. Soc.* **2008,** *130* (25), 7830-7832.

68. Lopez-Acevedo, O.; Tsunoyama, H.; Tsukuda, T.; Hakkinen, H.; Aikens, C. M., Chirality and Electronic Structure of the Thiolate-protected Au_{38} Nanocluster. *J. Am. Chem. Soc.* **2010,** *132* (23), 8210-8218.

69. Devadas, M. S.; Thanthirige, V. D.; Bairu, S.; Sinn, E.; Ramakrishna, G., Temperature-dependent Absorption and Ultrafast Luminescence Dynamics of Bi-icosahedral Au_{25} Clusters. *J. Phys. Chem. C* **2013,** *117* (44), 23155-23161.

70. Bakr, O. M.; Amendola, V.; Aikens, C. M.; Wenseleers, W.; Li, R.; Dal Negro, L.; Schatz, G. C.; Stellacci, F., Silver Nanoparticles with Broad Multiband Linear Optical Absorption. *Angew. Chem. Int. Ed.* **2009,** *121* (32), 6035-6040.

71. Harkness, K. M.; Tang, Y.; Dass, A.; Pan, J.; Kothalawala, N.; Reddy, V. J.; Cliffel, D. E.; Demeler, B.; Stellacci, F.; Bakr, O. M., $Ag_{44}(SR)_{30}^{4-}$: A Silver–thiolate Superatom Complex. *Nanoscale* **2012,** *4* (14), 4269-4274.

72. Yang, H.; Wang, Y.; Huang, H.; Gell, L.; Lehtovaara, L.; Malola, S.; Häkkinen, H.; Zheng, N., All-thiol-stabilized Ag_{44} and Au_{12} Ag_{32} Nanoparticles with Single-crystal Structures. *Nat. Commun.* **2013,** *4*, 2422.

73. Aikens, C. M., Origin of Discrete Optical Absorption Spectra of $M_{25}(SH)_{18}^{-}$ Nanoparticles (M= Au, Ag). *J. Phys. Chem. C* **2008,** *112* (50), 19797-19800.

74. Joshi, C. P.; Bootharaju, M. S.; Alhilaly, M. J.; Bakr, O. M., $[Ag_{25}(SR)_{18}]^-$: The "golden" Silver Nanoparticle. *J. Am. Chem. Soc.* **2015,** *137* (36), 11578-11581.

75. Kelly, K. L.; Coronado, E.; Zhao, L. L.; Schatz, G. C., The Optical Properties of Metal Nanoparticles: The Influence of Size, Shape, and Dielectric Environment. ACS Publications: 2003.

76. Szymańska-Chargot, M.; Gruszecka, A.; Smolira, A.; Bederski, K.; Głuch, K.; Cytawa, J.; Michalak, L., Formation of Nanoparticles and Nanorods via UV Irradiation of $AgNO_3$ Solutions. *J. Alloys Compd.* **2009,** *486* (1-2), 66-69.

77. Wiley, B. J.; Chen, Y.; McLellan, J. M.; Xiong, Y.; Li, Z.-Y.; Ginger, D.; Xia, Y., Synthesis and Optical Properties of Silver Nanobars and Nanorice. *Nano Lett.* **2007,** *7* (4), 1032-1036.

78. Sun, Y.; Gates, B.; Mayers, B.; Xia, Y., Crystalline Silver Nanowires by Soft Solution Processing. *Nano Lett.* **2002,** *2* (2), 165-168.

79. Schmucker, A. L.; Harris, N.; Banholzer, M. J.; Blaber, M. G.; Osberg, K. D.; Schatz, G. C.; Mirkin, C. A., Correlating Nanorod Structure with Experimentally Measured and Theoretically Predicted Surface Plasmon Resonance. *ACS Nano* **2010,** *4* (9), 5453-5463.

80. Al-Sherbini, E.-S. A., UV–visible Light Reshaping of Gold Nanorods. *Mater. Chem. Phys.* **2010,** *121* (1-2), 349-353.

81. Ni, W.; Ambjornsson, T.; Apell, S. P.; Chen, H.; Wang, J., Observing Plasmonic− Molecular Resonance Coupling on Single Gold Nanorods. *Nano Lett.* **2009,** *10* (1), 77-84.

82. Johnson, H. E.; Aikens, C. M., Electronic Structure and TDDFT Optical Absorption Spectra of Silver Nanorods. *J. Phys. Chem. A* **2009,** *113* (16), 4445-4450.

83. López-Lozano, X.; Barron, H.; Mottet, C.; Weissker, H.-C., Aspect-ratio-and Size-dependent Emergence of the Surface-Plasmon Resonance in Gold Nanorods–an Ab initio TDDFT Study. *Phys. Chem. Chem. Phys.* **2014,** *16* (5), 1820-1823.

84. Guidez, E. B.; Aikens, C. M., Theoretical Analysis of the Optical Excitation Spectra of Silver and Gold Nanowires. *Nanoscale* **2012,** *4* (14), 4190-4198.

85. Yan, J.; Yuan, Z.; Gao, S., End and Central Plasmon Resonances in Linear Atomic Chains. *Phys. Rev. Lett.* **2007,** *98* (21), 216602.

86. Yan, J.; Gao, S., Plasmon Resonances in Linear Atomic Chains: Free-electron Behavior and Anisotropic Screening of d Electrons. *Phys. Rev. B* **2008,** *78* (23), 235413.

87. Gao, B.; Ruud, K.; Luo, Y., Plasmon Resonances in Linear Noble-metal Chains. *J. Chem. Phys.* **2012,** *137* (19), 194307.

88. Ding, F.; Guidez, E. B.; Aikens, C. M.; Li, X., Quantum Coherent Plasmon in Silver Nanowires: A Real-time TDDFT Study. *J. Chem. Phys.* **2014,** *140* (24), 244705.

89. Kwak, K.; Thanthirige, V. D.; Pyo, K.; Lee, D.; Ramakrishna, G., Energy Gap Law for Exciton Dynamics in Gold Cluster Molecules. *J. Phys. Chem. Lett.* **2017,** *8* (19), 4898-4905.

90. Englman, R.; Jortner, J., The Energy Gap Law for Radiationless Transitions in Large Molecules. *Mol. Phys* **1970,** *18* (2), 145-164.

91. Yau, S. H.; Varnavski, O.; Gilbertson, J. D.; Chandler, B.; Ramakrishna, G.; Goodson III, T., Ultrafast Optical Study of Small Gold Monolayer Protected Clusters: A Closer Look at Emission. *J. Phys. Chem. C* **2010,** *114* (38), 15979-15985.

92. Devadas, M. S.; Kim, J.; Sinn, E.; Lee, D.; Goodson III, T.; Ramakrishna, G., Unique Ultrafast Visible Luminescence in Monolayer-Protected Au_{25} Clusters. *J. Phys. Chem. C* **2010,** *114* (51), 22417-22423.

93. Miller, S. A.; Womick, J. M.; Parker, J. F.; Murray, R. W.; Moran, A. M., Femtosecond Relaxation Dynamics of $Au_{25}L_{18}^-$ Monolayer-protected Clusters. *J. Phys. Chem. C* **2009,** *113* (22), 9440-9444.

94. Miller, S. A.; Fields-Zinna, C. A.; Murray, R. W.; Moran, A. M., Nonlinear Optical Signatures of Core and Ligand Electronic States in $Au_{24}PdL_{18}$. *J. Phys. Chem. Lett.* **2010,** *1* (9), 1383-1387.

95. Stoll, T.; Sgrò, E.; Jarrett, J. W.; Réhault, J.; Oriana, A.; Sala, L.; Branchi, F.; Cerullo, G.; Knappenberger Jr, K. L., Superatom state-resolved Dynamics of the $Au_{25}(SC_8H_9)_{18}^-$ Cluster from Two-dimensional Electronic Spectroscopy. *J. Am. Chem. Soc.* **2016,** *138* (6), 1788-1791.

96. Mustalahti, S.; Myllyperkiö, P.; Lahtinen, T.; Malola, S.; Salorinne, K.; Tero, T.-R.; Koivisto, J.; Häkkinen, H.; Pettersson, M., Photodynamics of a Molecular Water-Soluble Nanocluster Identified as Au_{130}(p MBA)$_{50}$. *J. Phys. Chem. C* **2015,** *119* (34), 20224-20229.

97. Yau, S. H.; Varnavski, O.; Goodson III, T., An Ultrafast Look at Au Nanoclusters. *Acc. Chem. Res.* **2013,** *46* (7), 1506-1516.

98. Stamplecoskie, K. G.; Chen, Y.-S.; Kamat, P. V., Excited-state Behavior of Luminescent Glutathione-Protected Gold Clusters. *J. Phys. Chem. C* **2014,** *118* (2), 1370-1376.

99. Green, T. D.; Knappenberger, K. L., Relaxation Dynamics of $Au_{25}L_{18}$ Nanoclusters Studied by Femtosecond Time-resolved Near Infrared Transient Absorption Spectroscopy. *Nanoscale* **2012,** *4* (14), 4111-4118.

100. Zhou, M.; Qian, H.; Sfeir, M. Y.; Nobusada, K.; Jin, R., Effects of Single Atom Doping on the Ultrafast Electron Dynamics of $M_1Au_{24}(SR)_{18}$ (M= Pd, Pt) Nanoclusters. *Nanoscale* **2016,** *8* (13), 7163-7171.

101. Thanthirige, V. D.; Kim, M.; Choi, W.; Kwak, K.; Lee, D.; Ramakrishna, G., Temperature-Dependent Absorption and Ultrafast Exciton Relaxation Dynamics in $MAu_{24}(SR)_{18}$ Clusters (M= Pt, Hg): Role of the Central Metal Atom. *J. Phys. Chem. C* **2016,** *120* (40), 23180-23188.

102. Yi, C.; Zheng, H.; Herbert, P. J.; Chen, Y.; Jin, R.; Knappenberger Jr, K. L., Ligand-and Solvent-Dependent Electronic Relaxation Dynamics of $Au_{25}(SR)_{18}^-$Monolayer-Protected Clusters. *J. Phys. Chem. C* **2017,** *121* (44), 24894-24902.

103. Zhou, M.; Vdović, S.; Long, S.; Zhu, M.; Yan, L.; Wang, Y.; Niu, Y.; Wang, X.; Guo, Q.; Jin, R., Intramolecular Charge Transfer and Solvation Dynamics of thiolate-protected $Au_{20}(SR)_{16}$ Clusters Studied by Ultrafast Measurement. *J. Phys. Chem. A* **2013,** *117* (40), 10294-10303.

104. Abbas, M. A.; Kim, T.-Y.; Lee, S. U.; Kang, Y. S.; Bang, J. H., Exploring Interfacial Events in Gold-Nanocluster-Sensitized Solar Cells: Insights into the Effects of the Cluster Size and Electrolyte on Solar Cell Performance. *J. Am. Chem. Soc.* **2015,** *138* (1), 390-401.

105. Mubeen, S.; Lee, J.; Singh, N.; Krämer, S.; Stucky, G. D.; Moskovits, M., An Autonomous Photosynthetic Device in which All Charge Carriers Derive from Surface Plasmons. *Nat. Nanotechnol.* **2013,** *8* (4), 247.

106. Hou, W.; Cronin, S. B., A Review of Surface Plasmon Resonance-enhanced Photocatalysis. *Adv. Funct. Mater.* **2013,** *23* (13), 1612-1619.

107. Liu, Z.; Hou, W.; Pavaskar, P.; Aykol, M.; Cronin, S. B., Plasmon Resonant Enhancement of Photocatalytic Water Splitting Under Visible Illumination. *Nano Lett.* **2011,** *11* (3), 1111-1116.

108. Primo, A.; Corma, A.; García, H., Titania Supported Gold Nanoparticles as Photocatalyst. *Phys. Chem. Chem. Phys.* **2011,** *13* (3), 886-910.

109. Kogo, A.; Sakai, N.; Tatsuma, T., Photocatalysis of Au_{25}-modified TiO_2 Under Visible and Near Infrared Light. *Electrochem. Commun.* **2010,** *12* (7), 996-999.

110. Yu, C.; Li, G.; Kumar, S.; Kawasaki, H.; Jin, R., Stable $Au_{25}(SR)_{18}/TiO_2$ Composite Nanostructure with Enhanced Visible Light Photocatalytic Activity. *J. Phys. Chem. Lett.* **2013,** *4* (17), 2847-2852.

111. Chen, S.; Ingram, R. S.; Hostetler, M. J.; Pietron, J. J.; Murray, R. W.; Schaaff, T. G.; Khoury, J. T.; Alvarez, M. M.; Whetten, R. L., Gold Nanoelectrodes of Varied Size: Transition to Molecule-like Charging. *Science* **1998,** *280* (5372), 2098-2101.

112. Subramanian, V.; Wolf, E. E.; Kamat, P. V., Catalysis with TiO_2/Gold Nanocomposites. Effect of Metal Particle Size on the Fermi Level Equilibration. *J. Am. Chem. Soc.* **2004,** *126* (15), 4943-4950.

113. Qian, H.; Sfeir, M. Y.; Jin, R., Ultrafast Relaxation Dynamics of $[Au_{25}(SR)_{18}]^{q}$ Nanoclusters: Effects of Charge State. *J. Phys. Chem. C* **2010,** *114* (47), 19935-19940.

114. Sfeir, M. Y.; Qian, H.; Nobusada, K.; Jin, R., Ultrafast Relaxation Dynamics of Rod-shaped 25-atom Gold Nanoclusters. *J. Phys. Chem. C* **2011,** *115* (14), 6200-6207.

115. Pelton, M.; Tang, Y.; Bakr, O. M.; Stellacci, F., Long-lived Charge-separated States in Ligand-stabilized Silver Clusters. *J. Am. Chem. Soc.* **2012,** *134* (29), 11856-11859.

116. Mustalahti, S.; Myllyperkiö, P.; Lahtinen, T.; Salorinne, K.; Malola, S.; Koivisto, J.; Häkkinen, H.; Pettersson, M., Ultrafast Electronic Relaxation and Vibrational Cooling Dynamics of $Au_{144}(SC_2H_4Ph)_{60}$ Nanocluster Probed by Transient Mid-IR spectroscopy. *J. Phys. Chem. C* **2014,** *118* (31), 18233-18239.

117. Link, S.; El-Sayed, M. A.; Schaaff, T. G.; Whetten, R. L., Transition from Nanoparticle to Molecular Behavior: A Femtosecond Transient Absorption Study of a Size-Selected 28 Atom Gold Cluster. *Chem. Phys. Lett.* **2002,** *356* (3-4), 240-246.

118. Chen, X.; Prezhdo, O. V.; Ma, Z.; Hou, T.; Guo, Z.; Li, Y., Ab initio Phonon-coupled Nonadiabatic Relaxation Dynamics of $[Au_{25}(SH)_{18}]^{-}$ Clusters. *Phys. Status Solidi B* **2016,** *253* (3), 458-462.

119. Zhou, M.; Tian, S.; Zeng, C.; Sfeir, M. Y.; Wu, Z.; Jin, R., Ultrafast Relaxation Dynamics of $Au_{38}(SC_2H_4Ph)_{24}$ Nanoclusters and Effects of Structural Isomerism. *J. Phys. Chem. C* **2017,** *121* (20), 10686-10693.

120. Zhou, M.; Zeng, C.; Sfeir, M. Y.; Cotlet, M.; Iida, K.; Nobusada, K.; Jin, R., Evolution of Excited-State Dynamics in Periodic Au_{28}, Au_{36}, Au_{44}, and Au_{52} Nanoclusters. *J. Phys. Chem. Lett.* **2017,** *8* (17), 4023-4030.

121. Zhou, M.; Zhong, J.; Wang, S.; Guo, Q.; Zhu, M.; Pei, Y.; Xia, A., Ultrafast Relaxation Dynamics of Luminescent Rod-Shaped, Silver-Doped Ag_xAu_{25-x} Clusters. *J. Phys. Chem. C* **2015,** *119* (32), 18790-18797.

Chapter 2 - Theory and computational methods

2.1 Quantum mechanics

2.1.1 The Schrödinger equation

Classical mechanics can only be applied to macroscopic particles, which is not satisfactory to explain the motion of electrons in atoms and molecules. Therefore, one requires quantum mechanics to explain the nature of the microscopic particles.

The Schrödinger equation is considered to be the master equation of quantum mechanics. Ψ is called the state function or wavefunction of the quantum mechanical system, and it can provide all possible information about a system. The wavefunction can depend on both the position (x) of the particle as well as the time (t), and can describe the state of a particular quantum mechanical system. Therefore, for a one particle, one dimensional system, the time-dependent Schrödinger equation (TDSE) can be defined as,

$$-\frac{\hbar}{i}\frac{\partial\Psi(x,t)}{\partial t} = -\frac{\hbar^2}{2m}\frac{\partial^2\Psi(x,t)}{\partial x^2} + V(x,t)\Psi(x,t) \qquad \textbf{(2.1)}$$

This equation will describe how the state function changes with time. In other words, it will allow one to calculate the future wavefunction at any time if the wavefunction at time t_0 is known. In this equation, the constant $\hbar$ (h-bar) is defined as $h/2\pi$, $i = \sqrt{-1}$, and m is the mass of the particle. $V(x,t)$ is the potential energy function of the system. The wavefunction gives a measurement of the x coordinates (the position) of the particle as well. The probability density gives the probability of finding a particle in a region of the x axis from x to $x+dx$. It is defined as,

$$|\Psi(x,t)|^2\, dx \qquad \textbf{(2.2)}$$

If a system does not experience any time-dependent external forces, the time-independent Schrödinger equation can be used, which is,

$$E\Psi(x) = -\frac{\hbar^2}{2m}\frac{d^2\Psi(x)}{dx^2} + V(x)\Psi(x) \qquad \textbf{(2.3)}$$

Here, the potential energy V only depends on x and is independent of time t. Hence, the probability density, $|\Psi(x)|^2$, is also independent of time. In this case, $\Psi(x)$ known as a stationary state and E is the energy of the system.

2.1.2 The Born-Oppenheimer approximation

The molecular Hamiltonian for non-relativistic and field-free conditions is given by the equation,

$$\hat{\mathrm{H}} = -\frac{\hbar^2}{2}\sum_{\alpha}\frac{1}{m_\alpha}\nabla_\alpha^2 - \frac{\hbar^2}{2m_e}\sum_{i}\nabla_i^2 + \sum_{\alpha}\sum_{\beta>\alpha}\frac{Z_\alpha Z_\beta\, e'^2}{r_{\alpha\beta}} - \sum_{\alpha}\sum_{i}\frac{Z_\alpha e'^2}{r_{i\alpha}} + \sum_{j}\sum_{i>j}\frac{e'^2}{r_{ij}} \qquad \textbf{(2.4)}$$

The α and β refer to nuclei and i and j refer to electrons. The operators for the kinetic energy of the nuclei and electrons are given by the first and the second terms respectively. The third and fifth terms give the potential energy of repulsion between nuclei and electrons respectively, with $r_{\alpha\beta}$ being the distance between the nuclei α and β with atomic numbers Z_α and Z_β and r_{ij} being the distance between electrons i and j. The potential energy of the attraction between the electrons and the nuclei is given by the fourth term where $r_{i\alpha}$ is the distance between electron i and nucleus α.

Use of the full Hamiltonian (2.4) in solving the Schrödinger equation can be complex. Therefore, one can use the Born-Oppenheimer approximation to simplify the Hamiltonian. The nuclei are much heavier than the electrons ($m_\alpha >> m_e$). Therefore, the electrons move faster than the nuclei and to a good approximation, one can consider the nuclei to be fixed while the electrons have motion. The change in the nuclear configuration is negligible during the electronic motion. Considering the nuclei as fixed, the nuclear kinetic energy term can be omitted to get the Schrödinger equation for the electronic motion only,

$$\left(\hat{\mathrm{H}}_{el} + V_{NN}\right)\Psi_{el} = U\Psi_{el} \qquad \textbf{(2.5)}$$

Now, $\hat{\mathrm{H}}_{\mathrm{el}}$ is the purely electronic Hamiltonian which is given by,

$$\hat{\mathrm{H}}_{el} = -\frac{\hbar^2}{2m_e}\sum_{i}\nabla_i^2 - \sum_{\alpha}\sum_{i}\frac{Z_\alpha e'^2}{r_{i\alpha}} + \sum_{j}\sum_{i>j}\frac{e'^2}{r_{ij}} \qquad \textbf{(2.6)}$$

When the nuclear repulsion, V_{NN}, is added to the electronic Hamiltonian we get $\hat{\mathrm{H}}_{\mathrm{el}} + V_{NN}$.
V_{NN} is given by,

$$V_{NN} = \sum_{\alpha}\sum_{\beta>\alpha}\frac{Z_\alpha Z_\beta e'^2}{r_{\alpha\beta}} \qquad \textbf{(2.7)}$$

Then, the electronic energy including the internuclear repulsion is given by the U term (2.5), which has a value of,

$$U = E_{el} + V_{NN} \quad \textbf{(2.8)}$$

The electronic coordinates are the variables in the electronic Schrödinger equation (2.5), whereas V_{NN} is independent of the electronic coordinates. V_{NN} is a constant for a given nuclear configuration. Hence, omission of the V_{NN} constant from the Hamiltonian will not affect the wavefunction and will result purely in the electronic energy E_{el},

$$\hat{\mathrm{H}}_{el}\Psi_{el} = E_{el}\Psi_{el} \quad \textbf{(2.9)}$$

However, E_{el} depends parametrically on the nuclear coordinates.

2.1.3 Mixed quantum-classical dynamics

Computationally it is not feasible to carry out accurate quantum mechanical calculations on the dynamics of molecular processes which involve more than 2-3 atoms. Conventional molecular dynamics (MD) has been used to simplify this problem over the years. However, the the electrons are not accounted for in classical MD which is a limitation. The MD calculations are done based on two main approximations. The first approximation is the Born-Oppenheimer approximation mentioned in section 2.1.2 above, which separates the electronic and atomic motions and reduce the dynamics to atomic motion on a single adiabatic potential energy surface. The treatment of the atomic motions by classical mechanics is the second approximation. However, these approximations can be invalid for processes of interest in applications, such as electron transfer, radiationless processes in molecules, and photoinduced chemistry. To address these issues, mixed quantum-classical dynamics methods have been introduced. The aim of these calculations is to maintain a multi-dimensional classical mechanical treatment for most atoms while having the important degrees of freedom computed with quantum mechanics. Self-consistency in the mixed quantum-classical dynamics is vital, where the quantum mechanical degrees of freedom must progress accurately under the influence of the surrounding classical motions and then in return, the classical degrees of freedom should respond accurately to the quantum mechanics (called the quantum back reaction problem).[1]

2.1.3.1 Nonadiabatic dynamics

The adiabatic processes where the nuclear and the electronic motions are decoupled can be treated with the Born-Oppenheimer (BO) *ab initio* molecular dynamics (AIMD). However, when the nuclear and electronic degrees of freedom are strongly coupled such as in many photochemical processes, the BO-AIMD approximation breaks down. For example, in metal nanoparticles the density of states is high and multiple electronic states can be populated during an excitation. Therefore, it is vital to treat the transitions between these states during the nuclear dynamics simulations, and these transitions are treated by applying nonadiabatic (NA) dynamics. The NA dynamics will attempt to treat the interactions between the quantum and classical systems in a self-consistent way while accounting for the NA effects. There are two main approaches to treat the NA effects: the mean-field method and the surface-hopping method.

2.1.3.1.1 The mean-field method

The mean-field method is also known as the Ehrenfest method.[2-9] It is based on a mean-field separation of classical and quantum motions.[2] The quantum variable r, is considered as fast and the classical variable R, is considered slow. The fast particles are moving in the average field of the slow particles and *vice versa*. There is feedback between the fast and slow degrees of freedom in an average manner. The Ehrenfest method[2-9] can be obtained as a classical limit of the time-dependent self-consistent field method.[10-13] In this method the total wavefunction is factorized into the product of fast and slow particle functions $\Xi(r,t)$ and $\Omega(R,t)$ as,[1]

$$\Psi(r,R,t) = \Xi(r,t)\Omega(R,t)exp\left[\frac{i}{\hbar}\int E_r(t')\,dt'\right] \tag{2.10}$$

$\Xi(r,t)$ and $\Omega(R,t)$ are normalized at every time t with respect to integration over r and R, respectively. $E_r(t')$ is called the phase factor which is given by,

$$E_r(t) = \iint \Xi^*(r,t)\,\Omega^*(R,t)H_r(r,R)\Xi(r,t)\Omega(R,t)drdR \tag{2.11}$$

$H_r(r,R)$ is the Hamiltonian of the fast system for slow particles fixed at position R, which is given by,

$$H_r(r,R) = -\frac{\hbar^2}{2}\sum_b \frac{\nabla_{rb}^2}{m_b} + V_{rR}(r,R) \tag{2.12}$$

In this equation, m_b is the mass of the fast particle b and $V_{rR}(r,R)$ contains all the inter-particle interactions such as fast-fast, slow-slow and fast-slow. Then, the mean-field Ehrenfest method can be defined using the equation,

$$i\hbar \frac{\partial \Xi(r,R,t)}{\partial t} = H_r(r,R)\Xi(r,R,t) \quad \textbf{(2.13)}$$

Here, the total energy is conserved[14] through the energy transfer between the quantum and classical coordinates. This method does not change based on the choice of quantum representation (adiabatic or diabatic). The classical particles evolve subject to a single effective potential corresponding to an average over quantum states. Therefore, this method neglects the correlation between the classical and quantum motions. However, the mean-field method can provide accurate quantum transition probabilities and is computationally manageable especially for systems with a dense manifold of excited states such as metal nanoparticles.

2.1.3.1.2 Surface-hopping method

The surface-hopping method has been developed to introduce the classical-quantum correlation that is absent in the mean-field method.[1] The approximations used by the surface-hopping method may not be as transparent as the in the mean-field method. However, the surface-hopping approach can be obtained from a multi-configuration expansion of the Schrödinger equation with approximations analogous to the mean-field method. In the surface-hopping approach, a given trajectory can be divided into different branches, each corresponding to a particular quantum state and weighted by the amplitude of the state. Thus, it includes the classical-quantum correlations. The total energy is conserved in the surface-hopping method and it also provides accurate quantum transition probabilities. A hopping algorithm can be used for the surface-hopping which decides the microscopic reversibility. Unlike the mean-field method, the surface-hopping can be changed depending on the choice of quantum representation. The surface-hopping based on the adiabatic representation will adequately explain the back reaction of the quantum transitions on the classical trajectories.

Different hopping algorithms can be utilized for the surface-hopping method.[9, 15-21] The 'fewest switches surface-hopping' (FSSH) algorithm is one of the most commonly used algorithms.[19] It is a variationally-based hopping algorithm that maintains the correct populations

$|c_i(t)|$ of each state with a minimum number of hops between states. For a case of two states, the probability of a switch from state 1 to state 2 during the time interval *dt* is given by,

$$P_{1\to 2} = -\frac{d[log|c_1(t)|^2]}{dt} \quad \textbf{(2.14)}$$

A hop will not occur if this probability is less than zero. In this case the fewest switches algorithm will not exactly reproduce the populations $|c_i(t)|$. If a hop is possible, the hop will be followed by a change in the velocity in the direction of the local nonadiabatic coupling vector to conserve the total energy of the quantum-classical system.[22-24]

The surface-hopping methods will not be appropriate for cases with non-vanishing coupling between states.[25] Also the method requires excited state wavefunctions for each state of interest,[26-27] which will make it more computationally expensive.

2.2 Computational methods

2.2.1 Density functional theory

The electronic wavefunction for an *n*-electron molecule will depend on *3n* spatial and *n* spin coordinates. The main idea of the density functional theory (DFT) is to replace the wavefunction with its *3n* spatial and *n* spin coordinates with fewer variables. Therefore, DFT will not calculate the molecular wavefunction; instead, the molecular electron probability density ρ is calculated and the molecular electronic energy *E* is calculated from ρ. The density only depends on *x, y* and *z* coordinates.

The ground state electronic energy E_0 is a functional of the ground state density ρ_0 as,

$$E_0 = E_0[\rho_0] \quad \textbf{(2.15)}$$

DFT will calculate E_0 and other ground state molecular properties from the ground state electron density ρ_0. Since DFT is associated with a fewer number of variables (i.e. only three variables), a higher computational efficiency can potentially be achieved.

2.2.1.1 Hohenberg-Kohn theorem

The purely electronic Hamiltonian (2.6) in atomic units can be rewritten as,

$$\hat{\mathrm{H}}_{el} = -\frac{1}{2}\sum_{i=1}^{n}\nabla_i^2 + \sum_{i=1}^{n}\upsilon(r_i) + \sum_{j}\sum_{i>j}\frac{1}{r_{ij}} \tag{2.16}$$

where,

$$\upsilon(r_i) = -\sum_{\alpha}\frac{Z_\alpha}{r_{i\alpha}} \tag{2.17}$$

The ground state electronic wavefunction Ψ_0 of an n-electron molecule is an eigenfunction of the purely electronic Hamiltonian (2.16). $\upsilon(r_i)$ is the potential energy of interaction between electron i and the nuclei which depends on the coordinates x_i, y_i, z_i of electron i and on the nuclear coordinates. $\upsilon(r_i)$ in the electronic Schrödinger equation is a function of only x_i, y_i, z_i because the Schrödinger equation is solved for fixed locations of nuclei. The term $\upsilon(r_i)$ is produced by the charges external to the system and hence it is called the external potential acting on electron i. The electronic wavefunction and the allowed energies of the molecule can be found as the solutions to the electronic Schrödinger equation once $\upsilon(r_i)$ and number of electrons n are specified.

According to the Hohenberg and Kohn theorem,[28] the ground state electron probability density $\rho_0(r)$ for a system with a nondegenerate ground state determines the external potential and the number of electrons, which is given by the relation,

$$\int \rho_0(r)dr = n \tag{2.18}$$

Thus, the relation between the ground state electronic energy E_0 and $\rho_0(r)$ is given by,

$$E_0 = E_\upsilon(\rho_0) \tag{2.19}$$

E_0 is a functional of the function $\rho_0(r)$, where the υ subscript denotes the dependence of E_0 on the external potential $\upsilon(r_i)$, which will be different for various molecules.

The sum of electronic kinetic-energy, electron-nuclear attraction, and electron-electron repulsion terms is given by the purely electronic Hamiltonian (2.6). When we take the average of (2.6) for the ground state, we get,

$$E = \bar{T} + \bar{V}_{Ne} + \bar{V}_{ee} \tag{2.20}$$

The overbars denote the averages. These average values of molecular properties are determined by the ground state electronic wavefunction, which is then dependent on $\rho_0(r)$. Thus, equation (2.20) can be written as a functional of ρ_0.

$$E_0 = E_v(\rho_0) = \bar{T}[\rho_0] + \bar{V}_{Ne}[\rho_0] + \bar{V}_{ee}[\rho_0] \quad \textbf{(2.21)}$$

The $\bar{V}_{Ne}$ term is given by,

$$\bar{V}_{Ne} = \int \rho_0(r)v(r)\,dr \quad \textbf{(2.22)}$$

where *v(r)* is the nuclear attraction potential energy function for an electron located at point *r*. Therefore, the $\bar{V}_{Ne}[\rho_0]$ is known. However, the functionals $\bar{T}[\rho_0]$ and $\bar{V}_{ee}[\rho_0]$ are not known. Equation (2.21) can be rewritten as,

$$E_0 = E_v(\rho_0) = \int \rho_0(r)v(r)\,dr + F[\rho_0] \quad \textbf{(2.23)}$$

Therefore, the Hohenberg-Kohn theorem does not allow the calculation of E_0 from ρ_0 because the $F[\rho_0] = \bar{T}[\rho_0] + \bar{V}_{ee}[\rho_0]$ functional is unknown.

2.2.1.2 Kohn-Sham method

Since the Hohenberg and Kohn theorem does not show how to calculate E_0 from ρ_0 or how to find ρ_0 without finding the wavefunction, Kohn and Sham introduced a key step forward to find ρ_0 and then find E_0 from ρ_0. The Kohn-Sham theory[29] is developed based on a fictitious reference system of *n* noninteracting electrons. The noninteracting system is denoted by the subscript *s* throughout the text. The *n* noninteracting electrons experience the same external potential energy function $v_s(r_i)$ such that,

$$\rho_s(r) = \rho_0(r) \quad \textbf{(2.24)}$$

where $\rho_s(r)$ is the ground state electron probability density of the reference system and $\rho_0(r)$ is the exact ground state electron density of the molecule we are interested in. The Hohenberg and Kohn theorem proved that the external potential is determined by the ground state probability density function.[28] Therefore, one can determine the $v_s(r_i)$ of the reference system once $\rho_s(r)$ is defined for the reference system. We can write the Hamiltonian of the reference system as,

$$\hat{\mathrm{H}}_s = \sum_{i=1}^{n} \hat{h}_i^{KS} \quad \textbf{(2.25)}$$

where,

$$\hat{h}_i^{KS} = -\frac{1}{2}\nabla_i^2 + v_s(r_i) \quad \textbf{(2.26)}$$

$\hat{h}_i^{KS}$ is the one-electron Kohn-Sham Hamiltonian. There is no interaction between the electrons in the reference system. Thus, the ground state wavefunction $\Psi_{s,0}$ of the reference system is a Slater determinant of the lowest energy Kohn-Sham spin orbitals u_i^{KS} of the reference system.

$$\Psi_{s,0} = |u_1 u_2 \ldots\ldots u_n| \tag{2.27}$$

$$u_i = \theta_i^{KS}(r_i)\sigma_i \tag{2.28}$$

$\theta_i^{KS}(r_i)$ is the spatial part of each spin orbital and σ_i is a spin function (α or β). In a closed shell system, the electrons are paired in the Kohn-Sham orbitals. The two electrons will have opposite spin α and β in the same spatial Kohn-Sham orbital. Each spin orbital is an eigenfunction of the one electron operator $\hat{h}_i^{KS}$ such that,

$$\hat{h}_i^{KS}\theta_i^{KS} = \varepsilon_i^{KS}\theta_i^{KS} \tag{2.29}$$

The ε_i^{KS} are the Kohn-Sham orbital energies. Kohn-Sham theorem rewrites the components of the Hohenberg-Kohn equation (2.21). $\Delta\bar{T}$ is defined as,

$$\Delta\bar{T}[\rho_0] = \bar{T}[\rho_0] - \bar{T}_s[\rho_0] \tag{2.30}$$

which is the difference in the average ground state electronic kinetic energy between the molecule and the reference system of noninteracting electrons where the electron density is equal to that of the molecule. It also defines the following term,

$$\Delta\bar{V}_{ee}[\rho_0] = \bar{V}_{ee}[\rho_0] - \frac{1}{2}\iint \frac{\rho(r_1)\rho(r_2)}{r_{12}} dr_1 dr_2 \tag{2.31}$$

r_{12} is the distance between the points x_1, y_1, z_1 and x_2, y_2, z_2 and the second term in (2.31) is the classical expression for the electrostatic interelectronic repulsion energy given that the electrons are smeared out into a continuous distribution of charge with electron density ρ. Thus, we can substitute (2.30) and (2.31) into equation (2.21) to get,

$$E_0 = E_v(\rho_0) = \int \rho_0(r)v(r)\,dr + \bar{T}_s[\rho_0] + \frac{1}{2}\iint \frac{\rho(r_1)\rho(r_2)}{r_{12}} dr_1 dr_2 + E_{xc}[\rho_0] \tag{2.32}$$

where,

$$E_{xc}[\rho_0] = \Delta\bar{T}[\rho_0] + \Delta\bar{V}_{ee}[\rho_0] \tag{2.33}$$

$E_{xc}[\rho_0]$ is called the exchange-correlation energy functional. However, the $\Delta\bar{T}$ and $\Delta\bar{V}_{ee}$ are not known. The common practice it to apply a good approximation for the $E_{xc}[\rho_0]$ which will be discussed in the next section. The rest of the terms in the (2.32) can be evaluated through the ground state electron density. The ground state electron density can be obtained from the Kohn-Sham orbitals as follows,

$$\rho_0(r) = \rho_s(r) = \sum_{i=1}^{n} \left|\theta_i^{KS}\right|^2 \tag{2.34}$$

The first term in (2.32) can be evaluated through $\rho_0(r)$. The $\bar{T}_s[\rho_0]$, kinetic energy of the noninteracting system with wavefunction Ψ_s, and the Slater-Condon rules result in the following relation,

$$\bar{T}_s[\rho_0] = -\frac{1}{2}\left\langle \Psi_s \middle| \sum_i \nabla_i^2 \middle| \Psi_s \right\rangle = -\frac{1}{2}\sum_i \left\langle \theta_i^{KS}(1) \middle| \nabla_1^2 \middle| \theta_i^{KS}(1) \right\rangle \tag{2.35}$$

Therefore, one can find E_0 (2.32) from $\rho_0(r)$ if we know the Kohn-Sham orbitals θ_i^{KS} and the $E_{xc}[\rho_0]$.

2.2.1.3 Exchange-correlation energy functional

The $E_{xc}[\rho_0]$ is known as the exchange-correlation energy functional. In DFT calculations, various approximate functionals $E_{xc}[\rho_0]$ are used. A common procedure is to compare the calculated molecular properties in DFT to the experimental values to validate a functional.

In the procedure of developing approximate Kohn-Sham DFT functionals, the $E_{xc}[\rho_0]$ is written as the sum of an exchange energy functional and E_x and the correlation energy functional E_c which is,

$$E_{xc} = E_x + E_c \tag{2.36}$$

E_x is defined using the exchange energy in Hartree-Fock theory, where the Hartree-Fock orbitals are replaced by the Kohn-Sham orbitals and for a closed-shell molecule the equation is given by,

$$E_x = -\frac{1}{4}\sum_{i=1}^{n}\sum_{j=1}^{n}\left\langle \theta_i^{KS}(1)\theta_j^{KS}(2)\right| 1/r_{12} \left|\theta_j^{KS}(1)\theta_i^{KS}(2)\right\rangle \quad \textbf{(2.37)}$$

The currently available models (e.g. Local density approximation) are used to evaluate the E_c (2.36). The exchange-correlation functionals that are currently used can be explained using the Jacob's ladder analogy.[30] The Jacob's ladder of DFT list the functionals that go from less accurate to more accurate while climbing the ladder. However, the computational cost of using each functional will also rise while climbing up. The Jacob's ladder in the ascending order of the accuracy is given by,

1. Local density approximation (LDA) – Depends only on the local density (ρ)
   Ex: Vosko, Wilk, Nusair (VWN)[31]
2. Generalized Gradient approximation (GGA) - Depends on the local density and the gradient of the density (∇ρ)
   Ex: BP86[32-33], PBE[34]
3. Meta-GGA – Include either (or both) of the second derivative of density ($\nabla^2\rho$) or orbital kinetic energy density (τ)
   Ex: TPSS[35]
4. Hybrid GGA – Mixes LDA, GGA, meta-GGA and exact exchange formulas (ρ, ∇ρ, $\nabla^2\rho$ or τ, E_x)
   Ex: B3LYP[33, 36]
5. Generalized random phase – Both the occupied and virtual orbitals used and optimized effective potential (OEP) is used

2.2.2 Basis sets

The wavefunction can be represented as a linear combination of the basis functions χ_r. The molecular orbitals (MOs) ϕ_i can be written as,

$$\phi_i = \sum_i c_{ri}\chi_r \quad \textbf{(2.38)}$$

where the basis functions χ_r are usually considered as atomic orbitals (AOs). The basis sets are constructed to have enough flexibility to represent "real" wavefunctions.

2.2.2.1 Atomic basis sets

When atomic basis sets are used, AOs are considered as the basis functions and are represented as a linear combination of one or more slater type orbitals (STOs) or Gaussian type orbitals (GTOs). The STOs have the form,

$$\chi_{\zeta,n,l,m} = NY_l^m(\theta,\phi)r^{n-1}e^{-\zeta r} \tag{2.39}$$

where Y_l^m are spherical harmonic functions. N is the normalization constant.

The GTOs in Cartesian coordinates have the form,

$$g_{ijk} = Nx^i y^i z^k e^{-\zeta r^2} \tag{2.40}$$

The i, j and k are nonnegative integers. ζ is a positive orbital exponent and x, y, z are Cartesian coordinates.

A STO approximates a 1s hydrogen orbital and it describes the electron density near nucleus better than a GTO. The GTO does not have the proper cusp at the nucleus, therefore the AOs are represented poorly. Also, GTOs do not represent the tail of the wavefunction properly since it falls off quickly at distances far away from the nucleus. However, GTOs are normally used in calculations since the integrals associated with GTOs can be calculated analytically as opposed to the STOs which need to be solved numerically. Hence, contracted Gaussian functions (CGF) have been introduced to fit Gaussians to approximate a STO. The CGF has the form,

$$\phi_\mu^{CGF} = \sum_{p=1}^{L} d_{p\mu}\, \phi_p^{GF} \tag{2.41}$$

which gives linear combination of multiple GTOs. The ϕ_p^{GF} called a primitive Gaussian and $d_{p\mu}$ are the contracted coefficients.

STOs are used in the Amsterdam density functional (ADF)[37] calculations mentioned in this thesis. A minimal basis set is composed of one STO for each inner shell and valence shell AO of each atom. When each STO of a minimal basis set is replaced by two STOs that are different in their orbital exponents ζ(zeta), a double-zeta (DZ) basis set is obtained. Similarly, the triple-zeta (TZ) basis set replaces each STO by three STOs that differ in their orbital exponents. As the basis set gets larger, the accuracy and the computational cost of the calculation increases.

Upon molecule formation, the AOs can change their shape and their centers tend to shift. Therefore, polarization functions are added with *l* quantum numbers that are greater than the maximum *l* of the valence shell of the ground state atom. A polarization function added to a DZ basis set is called DZP. Here, a set of five 3*d* functions on each "first row" and "second row" atom and a set of three 2*p* functions on each hydrogen atom is added. Diffuse functions are used for calculations on anions to correctly model the spread-out electron density.

The Gaussian software[38] calculations use Gaussian orbitals and CGF functions. The Gaussian calculations performed in this thesis used the LANL2DZ (Los Alamos National Laboratory basis sets) basis set which has been developed through a fitting procedure of pseudo-orbitals with Gaussian functions.[39]

2.2.2.2 Plane wave basis sets

Plane wave basis sets are used for the periodic calculations.[40-41] Unlike in the atomic basis sets, plane wave basis sets are not centered on atoms. Many elements with periodic structures have band structures that can be explained in terms of plane wave basis sets. For periodic systems, the one-electron Kohn-Sham orbital becomes,

$$\theta_i \rightarrow \theta_k \tag{2.42}$$

Then a second index, *n*, is added to represent the one-electron band which is $\theta_{n,k}(r)$. In this basis set, the plane waves are used as the basis functions. According to the Bloch theorem,[40] a Kohn-Sham orbital can be given by plane waves in the presence of a periodic potential, in the form,

$$\theta_{n,k}(\vec{r}+\tau) = \theta_{n,k}(\vec{r})e^{ik\tau} \tag{2.43}$$

In real space, τ is a translational vector ($\vec{\tau} = u_1\vec{a}_1 + u_2\vec{a}_2 + u_3\vec{a}_3$) that makes the Hamiltonian invariant. The $\theta_{n,k}(\vec{r})$ is the basis set whereas the $e^{ik\tau}$ is the phase factor. In reciprocal space, the real space vectors will be replaced by a *k* vector. In the smallest cell in the reciprocal space (Brillouin Zone), the plane wavefunction is given by,

$$\theta_k(\vec{r}) = u_{\vec{k}}(\vec{r})e^{i\vec{k}.\vec{r}} \tag{2.44}$$

Fourier transform operations can establish a relation between the reciprocal and the real space. The plane wave basis set's total energy expression and the Hamiltonian are simple to

implement. Also, the Fast Fourier Transform (FFT) makes the evaluation of the $\widehat{H}\theta$ very efficient.

In the (2.44) equation each electron occupied a *k* state. Then charge density *ρ(r)* is given by,

$$\rho(r) = \sum_{k} \left|\theta_{\vec{k}}(\vec{r})\right|^2 \tag{2.45}$$

The plane wavefunction can be expanded into a discrete summation,

$$\theta_{n\vec{k}}(\vec{r}) = \sum_{G} c_{n\vec{k}}(\vec{G}) e^{i(\vec{k}+\vec{G}).\vec{r}} \tag{2.46}$$

where $\vec{G}$ is the lattice vector in the reciprocal space, ($\vec{G} = v_1\vec{b}_1 + v_2\vec{b}_2 + v_3\vec{b}_3$), and $c_{n\vec{k}}$ is the expansion co-efficient. An infinite number of states will be required to give a full description of the plane wave function. Therefore, the number of plane waves used in the basis set will be described by the energy cutoff E_{cut}, according to the following relation,

$$E_{cut} = \frac{\hbar^2}{2m}\left|\vec{G}_{cut}\right|^2 \tag{2.47}$$

2.2.2.2.1 Pseudopotential

The wavefunctions show a rapid varying behavior near the non-valence electrons (core electrons) near the nucleus. However, these non-valence electrons do not affect the physical and chemical properties directly. Therefore, an effective potential known as the "pseudopotential" is composed to replace the all electron potential. The valence electrons are described by "pseudo wavefunctions". A pseudopotential reduces the size of the basis set. There are different types of pseudopotentials available to use. All of these methods are frozen core methods where the core electrons are pre-calculated in an atomic environment and kept frozen.

Projector augmented wave (PAW) method[42] is one of the pseudopotentials available which is used in the Vienna Ab initio Simulation Package (VASP)[43] calculations performed for the calculations in this thesis. In the PAW method, the wavefunctions are decomposed into three terms such as,

$$exact\ wavefunction \quad \textbf{(2.48)}$$
$$= pseudo\ plane\ waves - pseudo\ onsite\ radial\ grids$$
$$+ exact\ onsite\ radial\ grids$$

This considers no interaction between the different radial grids and plane waves; hence the computational efficiency is increased. The PAW method will be able to obtain an accuracy similar to the all electron calculations.

2.2.3 Relativistic effects

The scalar relativistic effects play a major role in the chemistry of the heaviest main group elements. These effects originate from energy changes among the electronic levels that can be explained through the Einstein's theory of relativity to electrons within an atom. Einstein's theory of relativity states that the relativistic mass *m* of a moving object increases as its velocity *v* increases according to the relation,

$$m = \frac{m_0}{\sqrt{(1 - (v/c)^2)}} \quad \textbf{(2.49)}$$

where m_0 is the rest mass and *c* is the speed of light (137 au). The electron velocity can be calculated using the expression, $(2\pi e^2/n'h)Z$ where e is electron charge, *n'* is a quantum number and *Z* is the atomic number.[44] The average velocity of a 1*s* electron in an atom is approximately *Z* au when *n*=1 (ground state). Hence, the average velocity of a 1*s* electron in a heavy atom (higher *Z* value) is significantly higher. At this higher speed, the value for the electron mass *m* (the relativistic mass) is higher than the rest mass m_0. Thus, the magnitude of the relativistic corrections increases with the value of *Z*. Also, the *s* orbital shrinks at a higher electron speed since the radius of a hydrogen-like 1*s* orbital (Bohr radius) is inversely proportional to electron mass. The relative energy levels of atomic orbitals also change due to the relativistic effects. The *s* orbital energies decrease substantially and *p* orbitals decrease to a lesser extent. This creates an increased shielding of the inner *s* electrons, In contrast, the *d* and *f* orbitals are expanded and their energies are increased due to the increased shielding of the inner *s* electrons.[44] The optical and electronic properties and geometries can be affected due the relativistic effects in heavy elements such as gold and silver. Therefore, the calculations performed for this thesis have included the relativistic effects since the projects involve gold and silver nanoparticles.

The zeroth order regular approximation (ZORA)[45] is used in the ADF program to include the relativistic effects. The zeroth order of the regular expansion of the Dirac equation[37, 46] is given as the ZORA equation. In Gaussian program calculations, the relativistic effects are included through the LANL2DZ basis set used for gold and silver nanoparticles. In the LANL2DZ basis set, effective core potentials (ECP) are used to replace the innermost core electron. The ECPs for the fourth and fifth row elements include the mass-velocity relativistic effects into the potentials.[39] The scalar relativistic effects are included in the VASP software calculations through the pseudopotentials. Here, the valence electrons are treated in a scalar relativistic approximation.[47]

2.2.4 Time-dependent density functional theory

Time-dependent density functional theory (TDDFT) is an extension of the DFT. The DFT method is a static ground state theory that cannot be used to treat the excited states and photo-absorption spectra and the dynamical nature of systems. Thus, TDDFT has been introduced to investigate the properties and dynamics of molecular systems in the presence of the electric or magnetic fields.

2.2.4.1 Runge-Gross Theorem

The foundation for TDDFT was developed through the Runge-Gross theorem (1984). Runge and Gross[48] introduced the time dependent analogue of the Hohenberg-Kohn theorem (2.2.1.1). The Runge-Gross theorem states that there is a unique one-to-one mapping between the time-dependent external potential, $V_{ext}(r,t)$, of a system and its time-dependent density, $\rho(r,t)$, for a given initial wavefunction Φ_0. Thus, $V_{ext}(r,t)$ and the time-dependent many-body wavefunction are both functionals of the density that are given as,

$$V_{ext}(r,t) = V_{ext}[\rho, \Phi_0](r,t) \quad \textbf{(2.50)}$$

$$\Phi(t) = \Phi[\rho\,, \Phi_0](t) \quad \textbf{(2.51)}$$

Hence, this will allow one to calculate all the properties of a system.

2.2.4.2 Time-dependent Kohn-Sham (TDKS) equations

The time-dependent density, *ρ(r,t)* of an interacting system could be equivalent to the time-dependent density of a noninteracting system evolving in a different potential.[49] This is true when the initial noninteracting wavefunction, Φ_s, (Ψ_s in section 2.2.1.2 was the noninteracting wavefunction without the time dependence) reproduces the initial density and its first time-derivative. The potential that describes this noninteracting system is unknown as in ground state DFT, hence approximations must be utilized. Similar to ground state DFT, the noninteracting system is described by a single Slater determinant of Kohn–Sham one-electron orbitals. For TDDFT, the orbitals become time-dependent orbitals, $\phi_j(r,t)$,

$$\Phi_s(r,t) = \left|\phi_1(r,t)\phi_2(r,t)\ldots\phi_j(r,t)\right| \tag{2.52}$$

Then, the time-dependent density is given by the sum over these occupied orbitals,

$$\rho(r,t) = \sum_{j=1}^{N}\left|\phi_j(r,t)\right|^2 \tag{2.53}$$

The set of time-dependent effective single-particle Kohn–Sham equations is given by,

$$i\frac{\partial\phi_j(r,t)}{\partial t} = H(r,t)\phi_j(r,t) = \left[-\frac{\nabla^2}{2} + \int dr'\,\frac{\rho(r',t)}{|r-r'|} + V_{xc}[\rho,\Phi_0,\Phi_s](r,t) + V_{ext}(r,t)\right]\phi_j(r,t) \tag{2.54}$$

where the kinetic energy of an electron in a Kohn–Sham orbital is given by the first term on the right-hand side in (2.54). The next term is the Coulomb repulsion which depends only on the density at a given time *t*. The time-dependent single-particle external potential, $V_{ext}(r,t)$, includes both the external time-dependent perturbation and the Coulombic attractive potential of the nuclei. $V_{xc}[\rho,\Phi_0,\Phi_s](r,t)$ is the time-dependent exchange-correlation potential. It includes dependence on the density at all previous points in time and also the initial interacting and noninteracting states. Then, the elements of the Kohn–Sham density matrix P are created from the time-dependent coefficients as,

$$P_{\mu\nu}(t) = \sum_i c^i_{\mu,i}(t)c_{\nu,i}(t) \tag{2.55}$$

because the Kohn–Sham molecular orbitals can be expanded as a linear combination of basis functions, χ_μ, such that $\phi_j(t) = \sum_\mu c_{\mu,i}(t)\chi_\mu$.

In an orthonormal basis, the TDDFT equation for the density matrix, which is also known as the quantum Liouville equation of motion,[50] can be given as,

$$i\hbar \frac{d\mathrm{P}(t)}{dt} = [\mathrm{H}(t), \mathrm{P}(t)] \tag{2.56}$$

The H is the Hamiltonian, which will be the Kohn–Sham operator, given in the matrix form, $\mathrm{H}_{\mu\nu}(t) = \langle \chi_\mu | \hat{\mathrm{H}}(t) | \chi_\nu \rangle$. Equation (2.56) can be used as the starting point to propagate the electron density in time via numerical integration for the real-time-TDDFT (RT-TDDFT) method or applying a small perturbation and retaining only the linear response (LR) of the density to derive the LR matrix formulation of TDDFT. A detailed explanation of the RT-TDDFT and LR-TDDFT methods will be given in the next sections of this chapter.

In TDDFT methods the unknown exchange-correlation potential is approximated and the adiabatic approximation for V_{xc} is used in most of the TDDFT methods. In the adiabatic approximation, the instantaneous electron density is inserted into standard ground state V_{xc} potentials. As mentioned in the previous section, the V_{xc} is a functional of the initial state of the system as well as the entire history of the density as $V_{xc}[\rho, \Phi_0, \Phi_s](r,t)$. This is known as the memory dependence of the exchange-correlation potential and it originates from the reduced nature of the density compared to the full many-body wavefunction that contains the complete information about the system at any given time. It is assumed that the electron density varies slowly within the adiabatic approximation. Thus, all history of the density, as well as initial state dependence, is ignored within the adiabatic approximation, and the exchange-correlation potential is given by,[50]

$$V_{xc}[\rho, \Phi_0, \Phi_s](r,t) = V_{xc}[\rho(t)] \tag{2.57}$$

2.2.4.3 Linear-response (LR) and real-time (RT) time-dependent density functional theories

The field-matter interactions are vital for many photoexcitation applications. Depending on whether the field is weak or strong, the TDDFT method utilized will vary. Section 2.2.4.2 explains the starting point of the LR-TDDFT and RT-TDDFT methods. If there is a smaller interaction with the field than the magnitude of the intermolecular interactions, then the excitation is defined as weak. In such instances, only a small perturbation is induced away from the ground state of the system. LR-TDDFT is a perturbation theory-based method which will describe such weak excitations. In this method, the excitation energies are calculated according

to the Casida equations.[51] They consider solutions to a non-Hermitian eigenvalue equation derived from retaining only the first-order response of the density to a perturbation. This method was used to calculate optical absorption spectra for the gold and silver nanoparticles mentioned in this thesis using both ADF and Gaussian software.

On the other hand, the RT-TDDFT method can go beyond the linear response of the density, where it can capture the field-matter interactions in both weak and strong regimes. In the RT approach, the electron density is observed in time and space which will unveil the dynamical nature of an excitation. RT-TDDFT propagates the electronic density according to equation (2.56). Then, the density matrix is propagated using a unitary time evolution operator, $U(t_n)$, as,[52-53]

$$P(t_{n+1}) = U(t_n) \cdot \mathrm{P}(t_{n+1}) \cdot U^{\dagger}(t_n) \qquad \textbf{(2.58)}$$

where $U(t_n)$ is constructed from the eigenvectors $A(t_n)$ and eigenvalues $\varepsilon(t_n)$ of the Kohn-Sham matrix at time t_n as,

$$U(t_n) = A(t_n) \cdot exp[-i \cdot 2\Delta t \cdot \varepsilon(t_n)] \cdot A^{\dagger}(t_n) \qquad \textbf{(2.59)}$$

with time step Δt. The time dependent response of the systems is probed by applying an external electric field. Then, the time-dependent dipole moment *μ(t)* is calculated at each time step using,

$$\mu(t) = \mathrm{Tr}[\mathrm{DP}(t)] \qquad \textbf{(2.60)}$$

D is the dipole matrix in the orthonormal basis. When the dipole response in real time is known, one can calculate dipole strength function $S(\omega)$, which gives the optical absorption spectra within the RT approach. $S(\omega)$ is given by,[53]

$$S(\omega) = \frac{4\pi\omega}{3c}\mathrm{Tr}[\mathrm{Im}\alpha(\omega)] \qquad \textbf{(2.61)}$$

$\alpha(\omega)$ is the polarizability in the frequency domain which can be obtained by taking the Fourier transform of the μ(t) and dividing by the Fourier transform of the applied electric field according to the following relation,

$$\mu_i(\omega) = \alpha_{ii}(\omega)E_i(\omega) \qquad \textbf{(2.62)}$$

i denotes the *x*, *y*, *z* Cartesian coordinates. The RT-TDDFT calculations mentioned in this thesis were performed using a development version of the Gaussian series of programs.[38]

2.2.5 Trajectory surface hopping in the time-dependent Kohn-Sham approach

The mean-field Ehrenfest method (section 2.1.3.1.1) for electron-nuclear interactions will fail to explain the scattering and nonradiative electron-nuclear relaxations within the TDKS-DFT methodology. Therefore, the trajectory surface hopping (SH) TDKS approach has been introduced as a solution. This method has developed FSSH (section 2.1.3.1.2) for DFT within the Kohn-Sham (KS) representation of the electron density (FSSH-TDKS).[26] The FSSH-TDKS method has been used to calculate the nonradiative relaxation dynamics of the thiolate-protected gold/silver nanoclusters mentioned in this thesis.

The KS energy can be expressed as the expectation value of the Hamiltonian in the basis of Slater determinants constructed with TDKS orbitals, ϕ_i as follows,

$$E = \langle \phi_a \phi_b \ldots . \phi_p | H | \phi_a \phi_b \ldots . \phi_p \rangle \tag{2.63}$$

where H is the Hamiltonian within the generalized gradient approximation. In this method, the time dependence in TDDFT is due to the ionic motion. Therefore, $V_{ext}(r) = V_{ext}\big(r, R(t)\big)$, where this value depends on the time through the nuclear trajectory, $R(t)$. The time dependence of the electron density due to an external field is not considered here. However, $R(t)$ accounts for the quantum backreaction problem. In trajectory SH methods, the nuclear trajectory $R(t)$ responds to electronic forces by stochastically hopping between electronic states. Since the FSSH is suitable within the adiabatic representation as mentioned earlier, the single electron adiabatic KS orbitals (or many electron Slater determinants formed from these orbitals) can be the eigenstates of the KS Hamiltonian (2.54). The time-dependent $\phi_p(r,t)$ KS orbitals can be expanded in the adiabatic KS orbitals $\tilde{\phi}_k(r;R)$ and we get $\phi_p(r,t) = \sum_k^n c_{pk}(t)\,|\tilde{\phi}_k(r;R)\rangle$. n is the number of electrons. Then, the TDKS equation (2.54) transforms to an equation in the coefficients c_{pk} as,

$$i\hbar \frac{\partial}{\partial t} c_{pk}(t) = \sum_m^n c_{pm}(t)\big(\in_m \delta_{km} + d_{km} \cdot \dot{R}\big) \tag{2.64}$$

The NA coupling is given by,

$$d_{km} \cdot \dot{R} = -i\hbar \langle \tilde{\phi}_k(r;R) | \nabla_R | \tilde{\phi}_m(r;R) \rangle \cdot \dot{R} = -i\hbar \left\langle \tilde{\phi}_k \middle| \frac{\partial}{\partial t} \middle| \tilde{\phi}_m \right\rangle \tag{2.65}$$

which is nonzero only if the determinants are different by a single KS orbital. ∇_R is the gradient operator. The Velocity Verlet algorithm[54-55] is used to propagate the nuclei with a time step Δt.

The solution to equation (2.64) gives the coherent time evolution of electronic states that are coupled to evolution of nuclear subsystems. Here, the standard FSSH algorithm (section 2.1.3.1.3) by Tully[19] can determine the fate of the system stochastically on-the-fly, producing different nuclear trajectories. However, the standard FSSH can be computationally expensive because the electronic structure calculations should be performed at each nuclear time step for all trajectories. Hence, as a solution, the FSSH method within the classical path approximation (FSSH-CPA) has been introduced for large systems.

2.2.5.1 FSSH-CPA

In CPA, it is assumed that the nuclear dynamics of the system stays unaffected by the dynamics of the electronic degrees of freedom. However, the electronic dynamics are driven by the nuclear dynamics. The electronic Hamiltonian will parametrically depend on the classical nuclear variable along a MD trajectory. The MD trajectory can be predetermined since it is independent of the electron evolution. Therefore, few MD trajectories will be required and many stochastic realizations of the FSSH algorithm can be calculated on the same trajectory. However, the CPA is valid when there are no significant structural changes to the system upon electronic excitations. In other words, kinetic energy should be the primary source of the nuclear dynamics.

In FSSH-CPA, the hop rejection and velocity rescaling in standard FSSH are replaced by scaling the transition probabilities, $g_{i\to j}(t)$ with the Boltzmann factor[56] as,

$$g_{i\to j}(t) \to g_{i\to j}(t) b_{i\to j}(t) \tag{2.66}$$

$$b_{i\to j}(t) = \begin{cases} exp\left(-\dfrac{E_j - E_i}{k_b T}\right) & E_j > E_i \\ 1 & E_j =< E_i \end{cases} \tag{2.67}$$

The transitions that are up in energy will be less probable due to this Boltzmann scaling and will not affect the rates of the energy loss. Hence, the detailed balance will be retained during the NA dynamics.

2.2.5.2 Decoherence induced surface hopping (DISH)

In mixed quantum-classical dynamics the electrons are treated quantum mechanically (i.e. quantum subsystems) while the nuclei are treated classically. The quantum mechanical wave

packet of the total system that includes all quantum effects of the bath splits into uncorrelated branches. The separation of the nuclear wave packets linked to different electronic states results a loss of coherence within the electronic subsystem. In other words, the microscopic system can evolve quantum mechanically as a superposition quantum states in contact with a bath. The macroscopic bath follows a group of trajectories associated with the components of the quantum state. Diverged bath trajectories lead to a loss of phase relationship among the states of the total system.[57-58] However, this phenomena will not occur if the nuclear motion is treated classically as in the FSSH in mixed quantum-classical dynamics. Therefore, decoherence can be introduced as a correction to the SH method. For the calculations in this thesis, we use the PYXAID program[56, 59] which accounts for the decoherence correction through the DISH[60] algorithm within the CPA implementation.

The decoherence effects should be included if the decoherence time is less than the time of the coherent electronic transition and for materials with well separated energy levels. The time scale of divergence of nuclear wave packets gives the decoherence time which is related to the phonon-induced pure dephasing times. The phonon-induced pure dephasing times are obtained through optical response theory.[61-62] They are obtained through the autocorrelation function of the electronic energy gap changing along the MD trajectory due to the nuclear motion. In DISH, a hop happens because of the decoherence in the electronic subsystem. As the semiclassical nuclear wave packet associated with a given electronic state *i,* moves sufficiently far away from the wave packets that are related to the other states, it should decide to hop to state *i* or to stay in the superposition of the remaining states. This happens when the time since the last decoherence (t_i) event for state *i* is greater than the decoherence time $\tau_i(t)$ for state *i*. The decoherence time $\tau_i(t)$ is defined as,

$$\frac{1}{\tau_i(t)} = \sum_{j=1, j\neq i}^{N} \left|c_j(t)\right|^2 r_{ij} \qquad \textbf{(2.68)}$$

where r_{ij} gives the decoherence rates between the pairs of electronic states which are precomputed before the NA-MD simulation using the optical response theory[63] and $c_j(t)$ are state amplitudes. Then, the trajectory must decide to hop to a new state. Within the CPA, the probability of hops upward in energy are scaled by the Boltzmann factor as mentioned in (2.67).

2.2.5.3 Basis set, initial conditions and time dependent populations for FSSH-TDKS

It is important to decide the electronic state basis and the initial conditions for the FSSH-TDKS calculations. The TD Slater determinant in the basis of the Slater determinants composed of the adiabatic one electron KS orbitals is considered as the basis set. All the KS orbitals obtained from the electronic structure calculations will not be necessary for the TDKS calculations, hence an "active space" is used in the calculations. Once the basis and the initial conditions are decided, the time dependent population for each state can be calculated as,[56]

$$P_i(t) = \frac{M_i(t)}{M} \tag{2.69}$$

M is the total number of trajectories in the ensemble and $M_i(t)$ is the number of surface hopping trajectories in electronic state i at time t.

2.3 References

1. Tully, J., Mixed Quantum–classical Dynamics. *Faraday Discuss.* **1998,** *110*, 407-419.

2. McLachlan, A., A Variational Solution of the Time-Dependent Schrodinger Equation. *Mol. Phys.* **1964,** *8* (1), 39-44.

3. Meyer, H. D.; Miller, W. H., Analysis and Extension of Some Recently Proposed Classical Models for Electronic Degrees of Freedom. *J. Chem. Phys.* **1980,** *72* (4), 2272-2281.

4. Micha, D. A., A self-consistent Eikonal Treatment of Electronic Transitions in Molecular Collisions. *J. Chem. Phys.* **1983,** *78* (12), 7138-7145.

5. Kirson, Z.; Gerber, R. B.; Nitzan, A.; Ratner, M. A., Dynamics of Metal Electron Excitation in Atom-surface Collisions: A Quantum Wave Packet Approach. *Surf. Sci.* **1984,** *137* (2), 527-550.

6. Sawada, S.-I.; Nitzan, A.; Metiu, H., Mean-trajectory Approximation for Charge- and Energy-transfer Processes at Surfaces. *Phys. Rev. B* **1985,** *32* (2), 851-867.

7. Berendsen, H. J. C.; Mavri, J., Quantum Simulation of Reaction Dynamics by Density Matrix Evolution. *J. Phys. Chem. A* **1993,** *97* (51), 13464-13468.

8. Bala, P.; Lesyng, B.; McCammon, J. A., Extended Hellmann-Feynman Theorem for Non-stationary States and its Application in Quantum-classical Molecular Dynamics Simulations. *Chem. Phys. Lett.* **1994,** *219* (3), 259-266.

9. Head-Gordon, M.; Tully, J. C., Molecular Dynamics with Electronic Frictions. *J. Chem. Phys.* **1995,** *103* (23), 10137-10145.

10. Dirac, P. A. M., Note on Exchange Phenomena in the Thomas Atom. *Math. Proc. Camb. Philos. Soc.* **2008,** *26* (3), 376-385.

11. Heller, E. J., Time Dependent Variational Approach to Semiclassical Dynamics. *J. Chem. Phys.* **1976,** *64* (1), 63-73.

12. Gerber, R. B.; Buch, V.; Ratner, M. A., Time‐dependent Self‐consistent Field Approximation for Intramolecular Energy Transfer. I. Formulation and Application to Dissociation of van der Waals Molecules. *J. Chem. Phys.* **1982,** *77* (6), 3022-3030.

13. Jackson, B., Time-Dependent Wave Packet Approach to Quantum Reactive Scattering. *Annu. Rev. Phys. Chem.* **1995,** *46* (1), 251-274.

14. Thompson, D. L., *Modern Methods for Multidimensional Dynamics Computations in Chemistry*. World Scientific: 1998.

15. Tully, J. C.; Preston, R. K., Trajectory Surface Hopping Approach to Nonadiabatic Molecular Collisions: The Reaction of H^+ with D_2. *J. Chem. Phys.* **1971,** *55* (2), 562-572.

16. Stine, J. R.; Muckerman, J. T., On the Multidimensional Surface Intersection Problem and Classical Trajectory ''Surface Hopping''. *J. Chem. Phys.* **1976,** *65* (10), 3975-3984.

17. Blais, N. C.; Truhlar, D. G., Trajectory‐surface‐hopping Study of Na(3p 2P) $+H_2 \rightarrow$ Na(3s 2S)+H_2(v′, j′, θ). *J. Chem. Phys.* **1983,** *79* (3), 1334-1342.

18. Parlant, G.; Gislason, E. A., An Exact Trajectory Surface Hopping Procedure: Comparison with Exact Quantal Calculations. *J. Chem. Phys.* **1989,** *91* (7), 4416-4418.

19. Tully, J. C., Molecular Dynamics with Electronic Transitions. *J. Chem. Phys.* **1990,** *93* (2), 1061-1071.

20. Kuntz, P. J., Classical Path Surface‐hopping Dynamics. I. General Theory and Illustrative Trajectories. *J. Chem. Phys.* **1991,** *95* (1), 141-155.

21. Webster, F.; Rossky, P. J.; Friesner, R. A., Nonadiabatic Processes in Condensed Matter: Semi-classical Theory and Implementation. *Comput. Phys. Commun.* **1991,** *63* (1), 494-522.

22. Coker, D. F.; Xiao, L., Methods for Molecular Dynamics with Nonadiabatic Transitions. *J. Chem. Phys.* **1995,** *102* (1), 496-510.

23. Tully, J. C., Nonadiabatic Molecular Dynamics. *Int. J. Quantum Chem.* **1991,** *40* (S25), 299-309.

24. Herman, M. F., Dynamics by Semiclassical Methods. *Annu. Rev. Phys. Chem.* **1994,** *45* (1), 83-111.

25. Kohen, D.; Stillinger, F. H.; Tully, J. C., Model Studies of Nonadiabatic Dynamics. *J. Chem. Phys.* **1998,** *109* (12), 4713-4725.

26. Craig, C. F.; Duncan, W. R.; Prezhdo, O. V., Trajectory Surface Hopping in the Time-dependent Kohn-Sham Approach for Electron-nuclear Dynamics. *Phys. Rev. Lett.* **2005,** *95* (16), 163001.

27. Tapavicza, E.; Tavernelli, I.; Rothlisberger, U., Trajectory Surface Hopping within Linear Response Time-dependent Density-functional Theory. *Phys. Rev. Lett.* **2007,** *98* (2), 023001.

28. Hohenberg, P.; Kohn, W., Inhomogeneous Electron Gas. *Phys. Rev.* **1964,** *136* (3B), B864.

29. Kohn, W.; Sham, L. J., Self-consistent Equations Including Exchange and Correlation Effects. *Phys. Rev.* **1965,** *140* (4A), A1133.

30. Perdew, J. P.; Schmidt, K. In *Jacob's Ladder of Density Functional Approximations for the Exchange-Correlation Energy*, AIP Conference Proceedings, AIP: 2001; pp 1-20.

31. Vosko, S. H.; Wilk, L.; Nusair, M., Accurate Spin-dependent Electron Liquid Correlation Energies for Local Spin Density Calculations: a Critical Analysis. *Can. J. Phys.* **1980,** *58* (8), 1200-1211.

32. Perdew, J. P., Density-functional Approximation for the Correlation Energy of the Inhomogeneous Electron Gas. *Phys. Rev. B* **1986,** *33* (12), 8822.

33. Becke, A. D., Density-functional Exchange-Energy Approximation with Correct Asymptotic Behavior. *Phys. Rev. A* **1988,** *38* (6), 3098.

34. Perdew, J. P.; Burke, K.; Ernzerhof, M., Generalized Gradient Approximation Made Simple. *Phys. Rev. Lett.* **1996,** *77* (18), 3865.

35. Tao, J.; Perdew, J. P.; Staroverov, V. N.; Scuseria, G. E., Climbing the Density Functional Ladder: Nonempirical Meta–generalized Gradient Approximation Designed for Molecules and Solids. *Phys. Rev. Lett.* **2003,** *91* (14), 146401.

36. Lee, C.; Yang, W.; Parr, R. G., Development of the Colle-Salvetti Correlation-energy Formula into a Functional of the Electron Density. *Phys. Rev. B* **1988,** *37* (2), 785.

37. Te Velde, G. t.; Bickelhaupt, F. M.; Baerends, E. J.; Fonseca Guerra, C.; van Gisbergen, S. J.; Snijders, J. G.; Ziegler, T., Chemistry with ADF. *J. Comput. Chem.* **2001,** *22* (9), 931-967.

38. Frisch, M.; Trucks, G.; Schlegel, H. B.; Scuseria, G.; Robb, M.; Cheeseman, J.; Scalmani, G.; Barone, V.; Mennucci, B.; Petersson, G., Gaussian 09, revision D. 01. Gaussian, Inc., Wallingford CT: 2009.

39. Hay, P. J.; Wadt, W. R., Ab initio Effective Core Potentials for Molecular Calculations. Potentials for K to Au Including the Outermost Core Orbitals. *J. Chem. Phys.* **1985,** *82* (1), 299-310.

40. Hoffman, R. *Solids and Surfaces: A Chemist's View of Bonding in Extended Structures*; CORNELL UNIV ITHACA NY BAKER LAB: 1988.

41. Liu, B., Density Functional Theory for Solids - Lecture 3 on Plane Waves and Lecture 4 on K-points **2017**.

42. Blöchl, P. E., Projector Augmented-wave Method. *Phys. Rev. B* **1994,** *50* (24), 17953.

43. Kresse, G.; Furthmüller, J., Efficiency of Ab-initio Total Energy Calculations for Metals and Semiconductors Using a Plane-wave Basis Set. *Comput. Mater. Sci.* **1996,** *6* (1), 15-50.

44. Thayer, J. S., Relativistic Effects and the Chemistry of the Heaviest Main-group Elements. *J. Chem. Educ* **2005,** *82* (11), 1721.

45. Lenthe, E. v.; Baerends, E.-J.; Snijders, J. G., Relativistic Regular Two‐component Hamiltonians. *J. Chem. Phys.* **1993,** *99* (6), 4597-4610.

46. van Lenthe, E.; Ehlers, A.; Baerends, E.-J., Geometry Optimizations in the Zero Order Regular Approximation for Relativistic Effects. *J. Chem. Phys.* **1999,** *110* (18), 8943-8953.

47. Hafner, J., Ab‐initio Simulations of Materials using VASP: Density‐functional Theory and Beyond. *J. Comput. Chem.* **2008,** *29* (13), 2044-2078.

48. Runge, E.; Gross, E. K., Density-functional Theory for Time-Dependent Systems. *Phys. Rev. Lett.* **1984,** *52* (12), 997.

49. van Leeuwen, R., Mapping from Densities to Potentials in Time-dependent Density-functional Theory. *Phys. Rev. Lett.* **1999,** *82* (19), 3863.

50. Provorse, M. R.; Isborn, C. M., Electron Dynamics with Real‐time time‐dependent Density Functional Theory. *Int. J. Quantum Chem.* **2016,** *116* (10), 739-749.

51. Casida, M. E., Time-dependent Density-Functional Theory for Molecules and Molecular Solids. *Comput. Theor. Chem.* **2009,** *914* (1), 3-18.

52. Yabana, K.; Nakatsukasa, T.; Iwata, J. I.; Bertsch, G., Real‐time, Real‐space Implementation of the Linear Response Time‐Dependent Density‐functional Theory. *Phys. Status Solidi B* **2006,** *243* (5), 1121-1138.

53. Ding, F.; Guidez, E. B.; Aikens, C. M.; Li, X., Quantum Coherent Plasmon in Silver Nanowires: A Real-time TDDFT Study. *J. Chem. Phys.* **2014,** *140* (24), 244705.

54. Allen, M. P.; Tildesley, D. J., *Computer Simulation of Liquids*. Oxford university press: 2017.

55. Swope, W. C.; Andersen, H. C.; Berens, P. H.; Wilson, K. R., A Computer Simulation Method for the Calculation of Equilibrium Constants for the Formation of Physical Clusters of Molecules: Application to Small Water Clusters. *J. Chem. Phys.* **1982,** *76* (1), 637-649.

56. Akimov, A. V.; Prezhdo, O. V., The PYXAID Program for Non-Adiabatic Molecular Dynamics in Condensed Matter Systems. *J. Chem. Theory Comput.* **2013,** *9* (11), 4959-4972.

57. Zurek, W. H., Decoherence, Einselection, and the Quantum Origins of the Classical. *Rev. Mod. Phys* **2003,** *75* (3), 715.

58. Leggett, A. J.; Chakravarty, S.; Dorsey, A.; Fisher, M. P.; Garg, A.; Zwerger, W., Dynamics of the Dissipative Two-state System. *Rev. Mod. Phys* **1987,** *59* (1), 1.

59. Akimov, A. V.; Prezhdo, O. V., Advanced Capabilities of The PYXAID Program: Integration Schemes, Decoherence Effects, Multiexcitonic States, and Field-Matter Interaction. *J. Chem. Theory Comput.* **2014,** *10* (2), 789-804.

60. Jaeger, H. M.; Fischer, S.; Prezhdo, O. V., Decoherence-induced Surface Hopping. *J. Chem. Phys.* **2012,** *137* (22), 22A545.

61. Mukamel, S., *Principles of Nonlinear Optical Spectroscopy*. Oxford University Press on Demand: 1999.

62. Prezhdo, O. V.; Rossky, P. J., Evaluation of Quantum Transition Rates from Quantum-classical Molecular Dynamics Simulations. *J. Chem. Phys.* **1997,** *107* (15), 5863-5878.

63. Madrid, A. B.; Hyeon-Deuk, K.; Habenicht, B. F.; Prezhdo, O. V., Phonon-induced Dephasing of Excitons in Semiconductor Quantum Dots: Multiple Exciton Generation, Fission, and Luminescence. *ACS Nano* **2009,** *3* (9), 2487-2494.

Chapter 3 - Theoretical Investigation of Electron and Nuclear Dynamics in the $[Au_{25}(SH)_{18}]^{-1}$ Thiolate-protected Gold Nanocluster

Reproduced with permission from:

Senanayake, R. D.; Akimov, A. V.; Aikens, C. M., *J. Phys. Chem. C*, **2017**, 121 (20), 10653–10662.

3.1 Abstract

Clear mechanistic insights into excited state dynamics in thiolate-protected gold nanoclusters are vital for understanding the origin of the photocatalytic enhancement via metal nanoparticles in the visible region. Extensive experimental studies on the $[Au_{25}(SR)_{18}]^{-1}$ thiolate-protected gold nanocluster nonradiative relaxation dynamics reported very distinct time constants which span from the femtosecond to nanosecond scale. In this work, the nonradiative excited state relaxations of the $[Au_{25}(SH)_{18}]^{-1}$ cluster are investigated theoretically to characterize the electron relaxation dynamics. The core and higher excited states lying in the energy range 0.0 – 2.2 eV are investigated using time-dependent density functional theory (TD-DFT). The quantum dynamics of these states is studied using a surface hopping method with decoherence correction, augmented with a real-time approach to DFT. Population transfer from the S_1 state to the ground state occurs on the several hundred picoseconds timescale. Relaxation between excited states that arise from core-to-core transitions is found to occur on a much shorter time scale (2-18 ps). No semi-ring or other states are observed at an energy lower than the core-based S_1 state. This observation suggests that the several picosecond time constants observed by Moran and coworkers could arise from core-to-core transitions rather than from a core-to-semi-ring transition. A large energy gap between the S_7 and S_6 states is found to be responsible for a relatively slow decay time for S_7. The S_1 state population decrease demonstrates the slowest decay time due to the large energy gap to the ground state. The spectral densities are calculated to understand the electron-phonon interactions that lead to electronic relaxations.

3.2 Introduction

Thiolate-protected gold clusters in various size regimes have fascinated researchers due to their promising optical, electrochemical, catalytic, and magnetic properties[1-10] which make the clusters useful in photocatalysis, optics, sensing, and medical applications.[11-13] Among these systems, thiolate-protected gold nanoparticles in the 1-2 nm size range demonstrate exceptional optical properties due to quantum confinement leading to a discrete spectrum of electronic energy levels, well-defined HOMO-LUMO transitions, and catalytic behavior that depends on the particle size. The quantization of energy levels occurs when the diameter of the metal nanoparticle is below the Fermi wavelength of the metal.[14] Small thiolate-stabilized nanoparticles have been reported as efficient solar photon harvesters, due to their favorable absorption spectrum that spans throughout the visible region.[15]

Thiolate-protected gold clusters such as the well-defined $[Au_{25}(SR)_{18}]^{-1}$ cluster, which consists of a Au_{13} icosahedral core surrounded by six 'V-shaped' -S-Au-S-Au-S- semi-ring motifs,[16, 17] have gained a lot of attraction in recent years. Recently, several research groups have shown that traditionally non-plasmonic noble metal clusters like $[Au_{25}(SR)_{18}]^{-1}$ can enhance photocatalytic yields upon visible irradiation.[18-21] Therefore, thiolate-protected gold clusters have been proposed as photosensitizers in metal-cluster-sensitized solar cells.[18] Even though there have been many experimental studies on gold nanocluster composite systems up to date, the origin of the photocatalytic enhancement in these systems is still a point of active debate.[18, 22-25] It is essential to study the excited state relaxation of these noble metal nanoparticles alone upon visible light irradiation in order to understand the origin of their photocatalytic enhancement.

It has been reported that fluorescence of thiolate-protected gold clusters could arise from charge transfer (CT) interactions between the ligands and the metal core.[14] Hence, it is important to understand whether the CT and the core transitions a play a major role in defining the excited state behavior of the thiolate-protected gold clusters. Due to the lack of fundamental research related to excited state dynamics in these clusters, such studies will offer new perceptions in understanding the photocatalytic activity of thiolate-stabilized gold nanoparticles in the visible region.

Numerous experimental characterizations of photoluminescence and electron relaxation dynamics from excited states lying near the HOMO-LUMO gap and from higher excited states of the $[Au_{25}(SR)_{18}]^{-1}$ cluster are available. Whetten, El-Sayed, and coworkers[26] have performed a

luminescence study on a thiolate-stabilized gold cluster which was later identified as the Au_{25} cluster. They suggested two mechanisms explaining the origin of two prominent peaks in the emission spectrum at 1.15 eV and 1.55 eV. According to the first mechanism, the peaks could be attributed to intraband and interband transitions, respectively. According to the second one, the peaks are explained by the relaxation from the lowest singlet state S_1 to the ground state and from the lowest triplet state T_1 to the ground state, respectively. The latter proposed mechanism assumes an excitation to higher excited states which is followed by fast relaxation to S_1 due to internal conversion. Then, the fluorescence originates from an electron-hole recombination, bringing the system to the ground state. Phosphorescence would arise due to intersystem crossing to T_1 followed by a radiative relaxation to the ground state. The former mechanism proposed attributes the 1.15 eV peak to an intraband transition within the sp band across the HOMO-LUMO gap, whereas the 1.5 eV peak is due to the radiative interband recombination between the sp and d bands. The luminescence decay times of a few to several hundred nanoseconds as well as microseconds have been observed for the radiative relaxations. The authors also suggested that the luminescence decay dynamics could be complex and may involve several closely spaced energy levels.[27] A transient absorption study performed on the same gold cluster by the same research groups confirmed the luminescence lifetime to be on a nanosecond timescale or longer. At the same time, a fast relaxation with a time constant of 750 fs was observed and was attributed to relaxation from higher excited state(s) to the lowest singlet excited state through internal conversion.[26]

Moran and coworkers studied femtosecond relaxation dynamics in the $[Au_{25}(SCH_2CH_2Ph)_{18}]^{-1}$ anion. In contrast to Whetten et al., they observed an extremely rapid internal conversion process, taking place on the order of 200 fs, which they attributed to the transitions in the multilevel electronic structure of the Au_{13} core.[28] The ultrafast relaxation timescale has been rationalized based on a significant wavefunction overlap of the states localized in the core atoms; the core states include the HOMO-LUMO which is approximately six-fold degenerate and the HOMO-LUMO+1, which is approximately nine-fold degenerate. Another observed decay channel, with the 1.2 ps internal conversion timescale, was suggested to be due to relaxation from the core to the semi-rings. A similar study on the Pd-doped Au_{25} cluster suggested very fast (< 50fs) internal conversion within the core states, a 500 fs internal conversion between core to ligand states, and a relaxation of the semi-ring states of around 25 ps.[29]

An ultrafast luminescence dynamics study has been performed by Ramakrishna and coworkers on $Au_{25}L_{18}$ clusters with two different protecting ligands, L = hexanethiol and glutathione.[14] They observed that the luminescence arises from the Au_{25} core states and that the excited states relaxation time constants are independent of the presence of protecting ligand. The luminescence decay was attributed to relaxation of Au core states to semi-ring states. The researchers found that the relaxation proceeded through a manifold of electronic states and takes several hundreds of femtoseconds to complete. According to their femtosecond time-resolved luminescence measurements, higher excited states have decay lifetimes of 200 fs to a few picoseconds and are relatively long-lived compared to molecular excited states and excited states in larger nanoparticles.[14]

Using time-resolved near infrared transient absorption spectroscopy, Knappenberger and coworkers studied the excited state relaxation dynamics in the $Au_{25}L_{18}$ cluster in its anion and neutral forms.[30] The major relaxation mechanism was identified as a non-radiative core-to-ligand energy transfer process following the internal conversion, on a few picosecond time scale. A relaxation process which had been a previously unnoticed decay channel with a time scale of several hundred picoseconds was observed for the neutral system which had an activation barrier with respect to the HOMO-LUMO energy gap. For the anion, a ~100 ps relaxation was reported, presumably starting from the excitation to LUMO+1. No indication of this relaxation pathway initiated from the LUMO was observed. A radiative decay of a LUMO excitation has been observed to occur on an approximately 5 ns timescale.[30]

Goodson and coworkers[31] have identified different excited state lifetimes for states that they assign as core and CT type states for $Au_{25}(SR)_{18}$ clusters. The core states are comprised by the HOMO–LUMO transitions, whereas the CT states are the core-shell transitions. The core states were suggested to have a lifetime below 5 ps and the CT states had lifetimes above 1 ns.

Kamat and coworkers[32] have studied excited states of glutathione-protected gold nanoclusters. They identified a 780 ns long-lived excited state, which they assigned to a ligand-to-metal transition. An approximately 3 ps short-lived state, also observed in the experiment, was ascribed to a metal core transition in the reduced glutathione-stabilized gold cluster. In a separate report, the size-dependence of the excited state dynamics in glutathione-protected gold clusters was investigated. The $Au_{25}(GS)_{18}$ cluster showed a rapid ca. 1 ps decay and a slower decay of

ca. 200 ns, which were identified as a metal−metal transition and a ligand-to-metal charge transfer, respectively.[15]

Very recently, an electronic relaxation dynamics investigation has been carried out by Knappenberger and coworkers on the superatom P and D states of the $[Au_{25}(SC_8H_9)_{18}]^{-1}$ cluster using femtosecond two-dimensional electronic spectroscopy (2DES) in the visible region.[33] 2DES can distinguish the spectrally overlapped signals in the one-dimensional experiments.[34] In the absorption spectrum, two distinct transitions around 1.9 eV and 2.2 eV were identified, which are believed to arise from the HOMO-1;HOMO-2→LUMO+1;LUMO and HOMO-1;HOMO-2→LUMO+2;LUMO+3 respectively. As per their findings, hot electrons created in the excitations to LUMO+2 and LUMO+3 in the 2.2 eV rapidly relax to the LUMO within 200 fs via internal conversion. These higher LUMOs arise from the Au sp conduction band.[13] Regarding the 1.9 eV excitation, a rapid 85 fs decay was reported which had been attributed to an internal conversion of electron from LUMO+1 to LUMO. A 300 fs decay which is common to 1.9 eV and 2.2 eV was attributed to internal conversion of holes between the HOMO-2 and HOMO states.[33]

A very recent theoretical investigation by Aikens and coworkers[35] proposed the origin of the photoluminescence of $[Au_{25}(SR)_{18}]^{-1}$ cluster capped by different ligands R (R=H, CH_3, CH_2CH_3, $CH_2CH_2CH_3$) in the gas phase. According to this study, the Au-Au bonds expand slightly in the Au_{13} core in the first excited state compared to the ground state geometry. Reduction in the symmetry of the outer shell of the core was observed, which caused an increased splitting among the approximate triply degenerate HOMO, HOMO-1, HOMO-2 and doubly degenerate LUMO, LUMO+1 orbitals. A vibrational breathing mode in the range of 75-80 cm^{-1} was reported for the vibrations responsible for the nuclear relaxation. Several excited states had been suggested to be responsible for the observed emission of the $[Au_{25}(SR)_{18}]^{-1}$ cluster. The excited states were found to arise from the excitations out of the superatom P orbitals into the lowest two superatom D orbitals, which are the core-based transitions.[35]

Overall, very distinct time scales which span from the femtosecond to nanosecond scale have been reported experimentally for non-radiative relaxation dynamics. In addition, several different mechanisms for relaxation were proposed. Theoretical studies can help elucidate the different time scales and relaxation mechanisms. A very recent theoretical study performed nonadiabatic dynamics on the $[Au_{25}(SH)_{18}]^-$ cluster and proposed a mechanism considering relaxations mainly

within the core states.[36] A 30 ps decay was reported for the slowest nonradiative energy transfer from LUMO to HOMO. They support the idea that the relaxations are a sum of ring and core contributions.[36] Further investigations of the core and higher state relaxations are vital to fully understand the electron relaxation dynamics of the Au_{25} cluster. Herein, the main focus of this article is to unveil the physical principles behind the electron-nuclear dynamics and the mechanism of electron relaxation of the thiolate-protected Au_{25} nanoparticle.

3.3 Computational methodology

We have performed ab initio real-time nonadiabatic molecular dynamics (NA-MD) simulations to study the electronic relaxation dynamics in thiolate-protected nanoclusters. The NA-MD simulations allow modeling quantum transitions in a manifold of electronic states coupled to nuclear degrees of freedom. These processes cannot be treated with the Born-Oppenheimer ab initio molecular dynamics, which assumes that only one electronic state is sufficient for accurate modeling of electron-nuclear systems. The NA-MD simulations are performed using the fewest switches surface hopping (FSSH)[37] algorithm. Specifically, we utilize a simplified but computationally efficient approach based on the classical path approximation (CPA) and the Kohn-Sham description of electronic states (FSSH-TDKS).[38] This approximation is valid when the nuclear dynamics is not significantly affected by electronic excitation, which is typical for solid-state systems or structurally rigid blocks, such as quantum dots. The assumption is supported by the previous TD-DFT studies,[35] which suggest only slight changes in Au-Au distances in the core of the nanoparticle, and no significant changes in the geometry of the ligands. The overcoherent nature of the FSSH approach is corrected by the decoherence-induced surface hopping (DISH)[39] scheme. All the NA-MD simulations are performed using the PYXAID program.[40-41]

The computations are organized in several steps. The initial relaxed geometry of $[Au_{25}(SH)_{18}]^{-1}$ was obtained by performing a geometry optimization using a conjugate gradient method as implemented in the Amsterdam Density Functional (ADF)[42] package. The core electrons are treated using a frozen core approximation. Valence electrons are described using the localized atomic triple zeta polarized basis set (TZP). The scalar relativistic effects of electrons in gold are accounted for via a zero order regular approximation (ZORA).[43] The electronic exchange and correlation are treated using the GGA Perdew–Burke–Ernzerhof

exchange-correlation functional (PBE)[44] functional. The vibrational frequency calculations are performed using ADF at the same level of theory. Electronic excitations (including absorption spectra) in the optimized structures were studied using linear response time-dependent density functional theory (TD-DFT) with the same specifications as above.

In the second step, the systems are thermalized and the molecular dynamics (MD) trajectories are computed. These calculations rely on density functional theory (DFT) calculations performed with the Vienna Ab initio Simulation Package (VASP).[45] The core electrons are treated using the pseudopotentials of the projector-augmented wave (PAW)[46] type, whereas the valence electrons are obtained using a plane wave basis set. The plane wave basis is defined by the kinetic energy cutoff value of 400.0 eV. A simulation box with a size of 24 Å was used to avoid contacts between the $[Au_{25}(SH)_{18}]^{-1}$. Only the gamma-point sampling over the Brillouin zone was considered, as appropriate for the finite size systems. A temperature ramping calculation was performed on the relaxed geometry at 0 K in order to heat the system up to 300 K. An MD trajectory was obtained by integrating classical Hamiltonian equations of motion for nuclei using the Verlet algorithm[47] and the 1 fs integration timestep. The trajectories were run under microcanonical ensemble conditions. Valence electron interaction was described using the PBE exchange-correlation functional.[44] The MD trajectory of 5 ps in length was computed.

In the third step, the nonadiabatic coupling (NAC) elements are calculated using the wavefunctions computed along the MD trajectory obtained in the previous step. Specifically, we employ a numerical scheme of Tully and Hammes-Schiffer[48] to calculate NACs as implemented in the PYXAID code. These couplings were precomputed, stored, and used in the subsequent steps to model NA transitions. The precomputed 5 ps trajectory was split into several smaller pieces, each 3.5 ps in length, resulting in 10 different starting geometries. The 3.5 ps sub-trajectories are considered the NA-MD trajectories, determining the maximal time of simulated electronic relaxation. For each NA-MD trajectory, 1000 realizations of the stochastic FSSH/DISH state hopping trajectories are considered, leading to sufficiently well converged statistics of electronic transitions.

Several important electronic excited states that contribute to the two main peaks in the optical absorption spectrum of $[Au_{25}(SH)_{18}]^{-1}$ in the energy range of 0.0 - 2.2 eV are characterized in detail. The excited state decay times are calculated including decoherence both ‘with’ and ‘without’ an energy correction to the calculated excited states. The energy corrections are used to

compensate for underestimation/overestimation in the calculated DFT band gaps compared to the experimental gaps. The decay times of the excited states populations are calculated by fitting to an exponential decay which has the form,

$$f(t) = exp\left(-\frac{t}{\tau}\right) \quad \textbf{(3.1)}$$

The ground state population increase was calculated fitting the data to an exponential rise which has the form,

$$f(t) = 1 - exp\left(-\frac{t}{\tau}\right) \quad \textbf{(3.2)}$$

The fitting was done using Gnuplot fitting implemented in GNUPLOT 5.0.

3.4 Results and discussion

The absorption spectrum calculated at the PBE level of theory (Figure 3.1) shows strong peaks around 1.4 eV, 2.5 eV and 3.3 eV. The peak positions are shifted compared to the three well-defined bands at 1.8, 2.75, and 3.1 eV[16, 17] observed in the experimental UV-vis absorption spectrum of $[Au_{25}(SH)_{18}]^{-1}$, yet the assignment is rather clear. The 1.41 eV peak obtained using DFT calculations arises from the core to core transitions of the Au_{13} core. The energy is slightly below the 1.5 eV value reported elsewhere.[17]

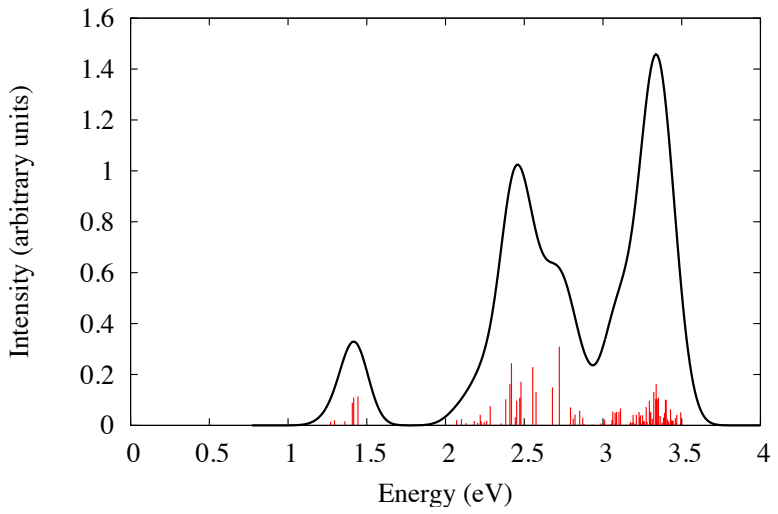

Figure 3.1 Calculated PBE/TZP optical absorption spectrum for $[Au_{25}(SH)_{18}]^{-1}$.

3.4.1 Relaxation dynamics of the first excited state peak.

To understand the electronic relaxation process of the $[Au_{25}(SH)_{18}]^{-1}$ cluster, we have studied the 1.4 eV peak which corresponds to the experimental 1.8 eV peak.[16, 33] According to Aikens and coworkers,[17] the first excited state that occurs at 1.52 eV (1.41 eV in this study) corresponds to the intraband transition of HOMO→ LUMO where the HOMO is triply degenerate and the LUMO is doubly degenerate. In this study we will consider the doubly degenerate LUMO as two separate orbitals, LUMO and LUMO+1, and the triply degenerate HOMO as three separate orbitals, i.e. the HOMO, HOMO-1, and HOMO-2 orbitals. Table 3.1 shows the excitations involved in the 1.4 eV peak. The 1.4 eV peak is mainly constructed from the excited states 4, 5, and 6, which have higher oscillator strengths compared to excitations 1-3. States 4 and 5 have nearly equal oscillator strengths. The single-particle excitations that contribute the highest weights to each excitation are shown in the table. It should be noted that the transitions going from HOMO, HOMO-1 and HOMO-2 → LUMO and LUMO+1 are all core-to-core intraband transitions.

Table 3.1 The transitions with the highest weights for the first six excited states from the TDDFT calculation.

Excitation transitions	Energy (eV)	Oscillator strength	Weight	Most weighted transitions
1	1.270	0.0031	0.8514	HOMO → LUMO
			0.0593	HOMO-2 → LUMO
			0.0426	HOMO-1 → LUMO+1
			0.0357	HOMO → LUMO+1
2	1.296	0.0043	0.7912	HOMO → LUMO+1
			0.1107	HOMO-1 → LUMO
			0.048	HOMO-2 → LUMO+1
			0.0378	HOMO → LUMO
3	1.361	0.0035	0.4518	HOMO-1 → LUMO
			0.1829	HOMO-2 → LUMO+1
			0.1769	HOMO-2 → LUMO
			0.1468	HOMO-1 → LUMO+1
			0.0308	HOMO → LUMO+1
4	1.408	0.0189	0.4127	HOMO-1 → LUMO
			0.2062	HOMO-2 → LUMO
			0.1989	HOMO-1 → LUMO+1
			0.0818	HOMO-2 → LUMO+1

			0.0735	HOMO → LUMO+1
5	1.417	0.0232	0.5656	HOMO-1 → LUMO+1
			0.2718	HOMO-2 → LUMO
			0.0861	HOMO → LUMO
			0.0429	HOMO-2 → LUMO+1
6	1.444	0.0242	0.6276	HOMO-2 → LUMO+1
			0.2618	HOMO-2 → LUMO
			0.0493	HOMO → LUMO+1
			0.0234	HOMO-1 → LUMO+1
			0.0113	HOMO → LUMO

It should be noted that the first six excited states from the TDDFT calculation (Table 3.1) are slightly different from the S_1-S_6 states that we define for use in the FSSH-TDKS calculations to deduce the relaxation dynamics of the 1.4 eV excitation (Table 3.2). They vary in that each of the states in the FSSH-TDKS calculations arise from a single Slater determinant, whereas the TDDFT calculations yield states that are inherently mixed. However, the S_1-S_6 states shown in Table 3.2 roughly correspond to the transitions with the highest weights from the first six excited states in the TDDFT calculation.

Table 3.2 Excited states and corresponding transitions used in the FSSH-TDKS calculations.

Excited state	Transition
S_1	HOMO → LUMO
S_2	HOMO → LUMO+1
S_3	HOMO-1 → LUMO
S_4	HOMO-1 → LUMO+1
S_5	HOMO-2 → LUMO
S_6	HOMO-2 → LUMO+1

The analysis of the orbital energies of the $[Au_{25}(SH)_{18}]^{-1}$ cluster indicates the near-degeneracy of the LUMO and LUMO+1 as well as the near-degeneracy of HOMO, HOMO-1 and HOMO-2 (Figure 3.2). This behavior is consistent with the previous characterization of the nature of these orbitals.[17] As shown in Figure 3.3, the HOMO-2, HOMO-1, and HOMO consist mainly of core gold orbitals which have a mixed 6s and 6p character. The LUMO and LUMO+1 are also composed of 6s orbitals from gold atoms in the core of the nanostructure. The lower

lying orbitals (HOMO-3 to HOMO-6) show mainly 5d character originating from the ligand gold atoms and a small amount of 3p character from sulfur orbitals. The orbitals shown in Figure 3.3 are plotted with the ADF GUI.

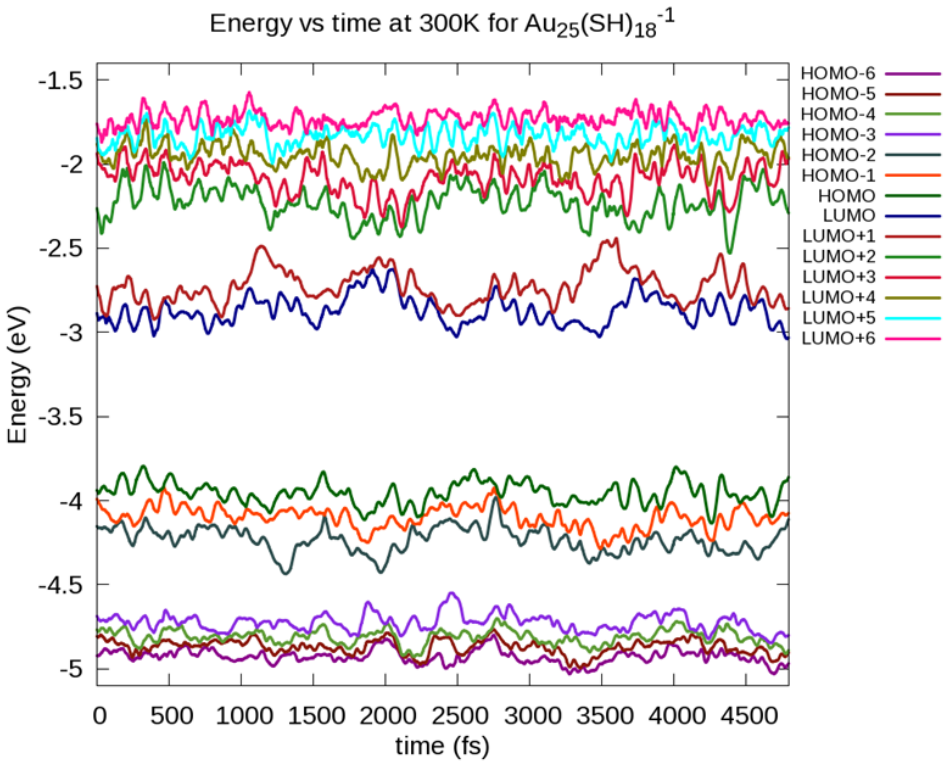

Figure 3.2 Variation of the HOMO-6 to LUMO+6 orbital energies with time.

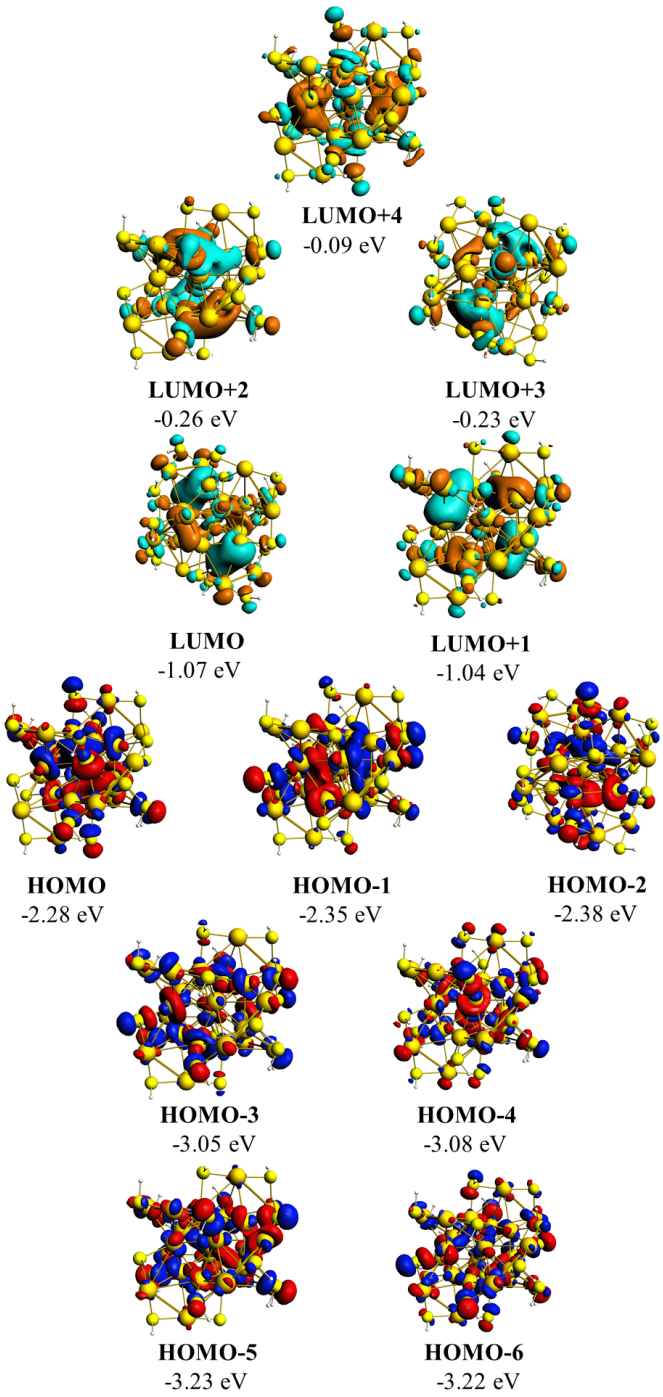

Figure 3.3 The orbitals near the HOMO-LUMO gap and their relative energies in eV.

3.4.1.1 Relaxation dynamics of the S_1 state

A fully coherent relaxation dynamics of the S_1 state was modeled considering electronic transitions from LUMO to HOMO (Figure 3.4). In this initial study, we have considered a

minimal model, including only the S_1 and ground states. Figure 3.4a shows the LUMO population decay, which relates both to the S_1 state population decrease and the ground state (GS) population increase. The S_1 decay time was found to be 5.7 ps, which is much less than the recently reported decay time of 30 ps for S_1 in a similar theoretical work.[36] Increasing the HOMO-LUMO gap by 0.55 eV, to match the corresponding experimental value, only slightly increases the timescale – up to 6.3 ps (Figure 3.4b). To correct the overcoherent nature of the FSSH scheme, we have considered adding decoherence effects via the DISH algorithm (Figure 3.4, panels c and d). Decoherence is included in all remaining calculations we will discuss in the next section. Decay times of 65.0 ps and 349.0 ps were obtained for simulations with decoherence both 'without' and 'with' the energy correction to the S_1 state, respectively. Inclusion of decoherence changes the decay time values considerably. In addition, the inclusion of decoherence amplifies the energy gap correction. We should note that the simulation times obtained with DISH (Figure 3.4, panels c and d) are not long enough to obtain accurate values for these decay times, so the latter rely on extrapolation and the obtained timescales should be considered to be estimates.

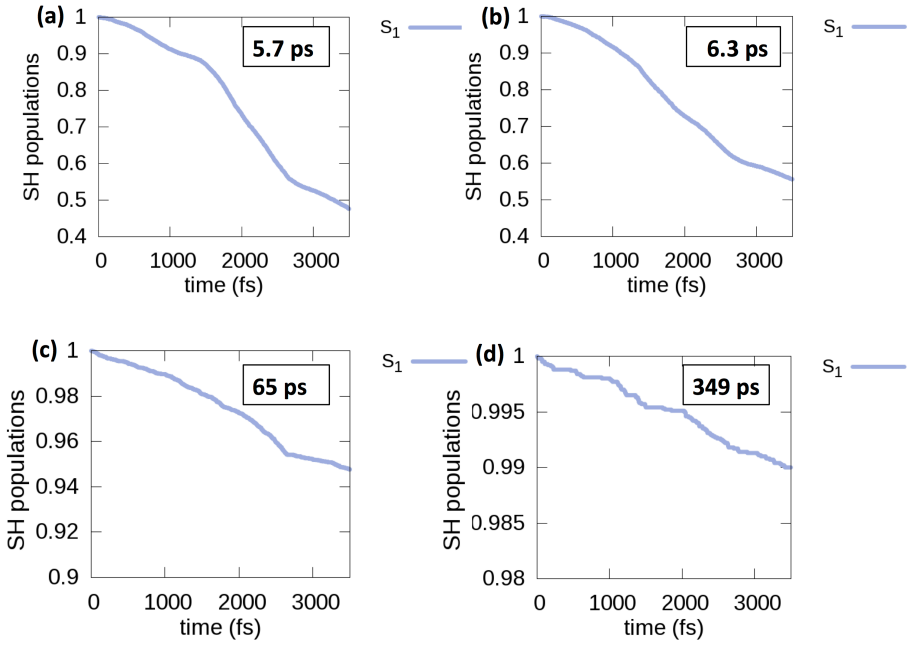

Figure 3.4 Dynamics of the S_1 state relaxation: with energy gap correction (b, d) and with decoherence correction (c, d).

3.4.1.2 Relaxation dynamics of S_1 to S_6 states

In this section, the relaxation of the first six excited states, S_1 to S_6 is discussed. In contrast to the model study discussed in section 3.4.1.1, all six excited states and the ground state are included in the calculations. The computed kinetic curves are shown in Figure 3.5. The corresponding ground state recovery times are shown in Table 3.3. Compared to the minimal 2-state model, the relaxation of the S_1 state in the presence of all six excited states does not significantly change. This is expected, since no lower energy state is involved in this process. The presence of higher energy states does not alter the dynamics significantly, since they remain energetically inaccessible (transitions to them are very infrequent). It should be noted that the ground state growth dynamics should include contributions from multiple relaxation pathways. Whetten and coworkers have also suggested the involvement of several degenerate energy states which leads to complicated decay dynamics.[27] Without the 0.55 eV energy correction, the ground state growth after excitation of S_1 is 73 ps when all six excited states are considered, compared to 65 ps in the presence of only S_1. This could be due to a small electron population transfer to the higher energy S_2 and S_3 states as shown in Figure 3.5a, which may delay the relaxation to the ground state. However, when the energy correction to the excited state is incorporated, the ground state growth time decreases to 313 ps from 349 ps.

Table 3.3 Ground state population increase lifetimes after excitation of the six excited states contributing to the 1.4 eV peak.

Excited state	Ground state growth time (ps) without considering the energy correction	Ground state growth time (ps) with the energy correction
S_1	73	313
S_2	71	365
S_3	81	441
S_4	120	690
S_5	96	750
S_6	158	1429

It is clearly evident that the initial LUMO+1 → HOMO-2 excitation (S_6) leads to the slowest GS recovery regardless of whether an energy correction is used. The LUMO+1 → HOMO-1 excitation (S_4) leads to the second longest GS population growth when no energy correction is

applied. Both S_1 and S_2 decay to the GS much faster. Generally, higher initial excitation leads to slower repopulation of the ground state (Table 3.3). The large initial excitation number implies the presence of a large number of intermediate states. Each additional intermediate state retains the system in the excited state for a longer duration, exerting an effective "friction", and leading to longer GS recovery times. For all states shown in Table 3.3, it is clear that the times for repopulation of the ground state have increased significantly as a result of the addition of the energy correction.

Table 3.4 The decay times of the excited state population decrease of the six excited states contributing to the 1.4 eV peak.

Excited state	Decay time (ps) without considering the energy correction	Decay time (ps) with the energy correction
S_1	15	18
S_2	3.2	3.3
S_3	3.0	3.1
S_4	1.9	1.9
S_5	2.6	2.6
S_6	1.9	1.9

The excited state depopulation times are summarized in Table 3.4. Despite the slow overall ground state population growth dynamics, the decay times of initial excited states are ultrafast. Excited state depopulation occurs quickly between the excited states. It is clear that ground state repopulation times after excitation of the S_1 state are much larger than the decay times of the S_1 state (73 ps vs. 15 ps without energy correction and 313 ps vs. 18 ps with it). We can hypothesize that the S_2 and S_3 states play an important role in the S_1 state relaxation since the S_1 state population transfer to the S_2 and S_3 states is much faster than the population transfer to the GS. In Figure 3.5b the S_2 state quickly transfers some population to the S_1 state and a small amount to the S_3 and S_5 higher energy states while the ground state is populated slowly. The ground state population increase is slightly slower when the energy correction is added as shown in Figure A.1b. When excited to the S_6 state as in Figure 3.5f, the population relaxes to the lower energy S_1-S_5 states, and the populations of all states after 3.5 ps reach an average value of 0.17.

As mentioned in the introduction, the work performed by Moran and coworkers in 2009 identified a 1.2 ps time constant measured with a probe pulse of 620 nm (~1.99 eV) and a time

constant of 4 ps with a lower energy probe pulse of 725-800 nm (~1.55 – 1.71 eV).[28] The probe energy range lies between 1.5 to 1.99 eV, which spans the energy range of the first absorption peak of the $[Au_{25}(SH)_{18}]^{-1}$ cluster[17] which arises from core to core transitions. Therefore, we suggest that the time constants observed by Moran and coworkers could arise from core to core transitions rather than from a core to semi-ring transition. We observe time constants for the near HOMO-LUMO core states (S_1 to S_6 states) in a range of 2 - 18 ps, which is in a good agreement with the picosecond time scale constants observed by Moran and coworkers. Because the initial dynamics for the FSSH-TDKS method are run on the ground state potential, it is possible that excited state nuclear relaxation could decrease some of these time constants.

3.4.2 Relaxation dynamics of higher excited states up to S_{35}

The relaxation of the higher excited states will be discussed in this section. We consider an initial excitation corresponding to the peak at around 2.2 eV. Analysis of the most probable transitions with highest oscillator strengths and transition dipole moments gives the HOMO-6 to LUMO+4 orbitals as the orbitals involved in the main transitions. The detailed analysis of the transitions is shown in Table A.1 in the supporting information in Appendix A.

All possible single particle transitions were considered for orbitals between HOMO-6 and LUMO+4 as shown in Table 3.5; S_1-S_6 have the same transitions as in Table 3.2.

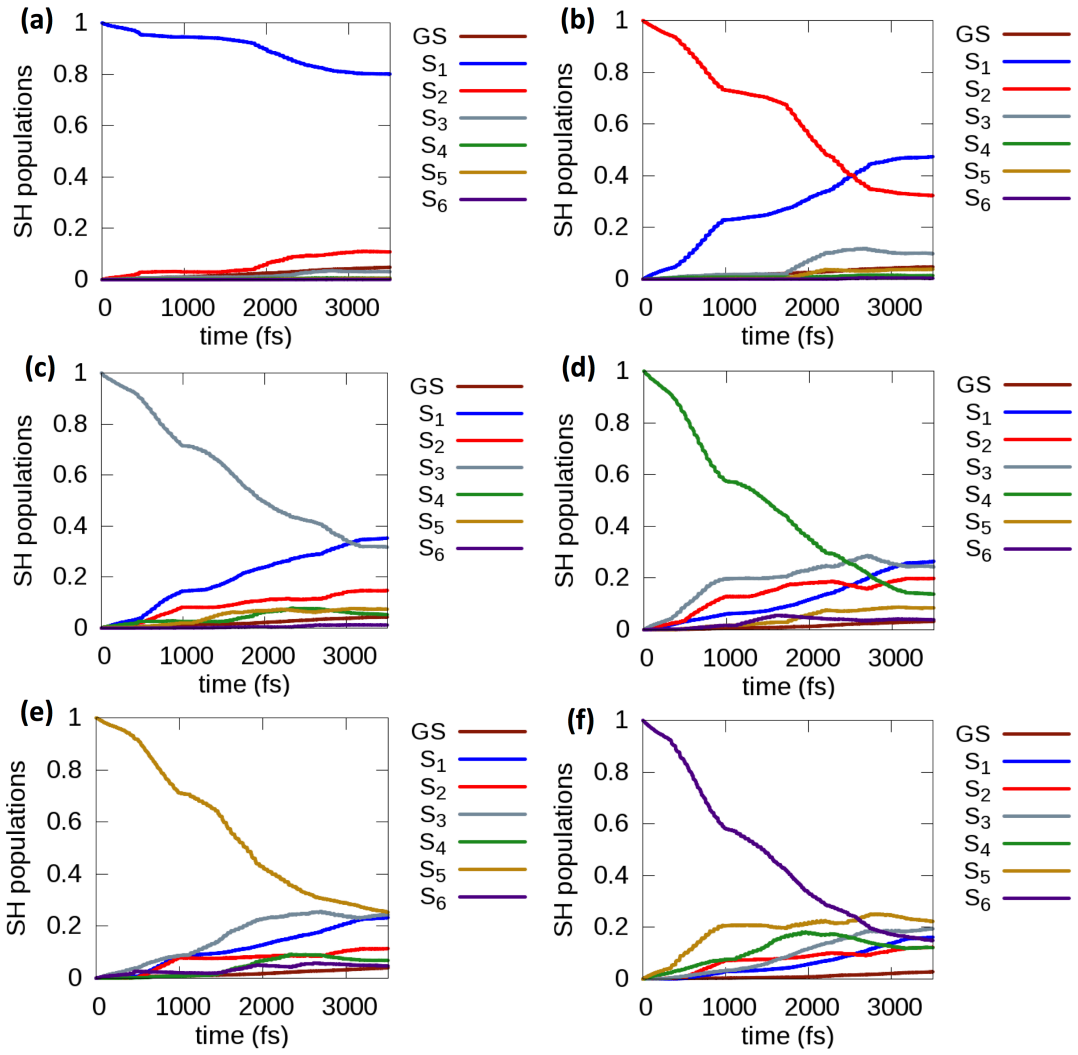

Figure 3.5 Evolution of the populations of S_1, S_2, S_3, S_4, S_5, S_6 states. 5(a) to 5(f) are relaxations from S_1 - S_6, respectively, without the energy correction.

Table 3.5 Transitions considered for higher excited states.

Excited state	Transition
S_7	HOMO → LUMO+2
S_8	HOMO → LUMO+3
S_9	HOMO → LUMO+4
S_{10}	HOMO-1 → LUMO+2
S_{11}	HOMO-1 → LUMO+3
S_{12}	HOMO-1 → LUMO+4
S_{13}	HOMO-2 → LUMO+2
S_{14}	HOMO-2 → LUMO+3

S_{15}	HOMO-2 → LUMO+4
S_{16}	HOMO-3 → LUMO
S_{17}	HOMO-3 → LUMO+1
S_{18}	HOMO-3 → LUMO+2
S_{19}	HOMO-3 → LUMO+3
S_{20}	HOMO-3 → LUMO+4
S_{21}	HOMO-4 → LUMO
S_{22}	HOMO-4 → LUMO+1
S_{23}	HOMO-4 → LUMO+2
S_{24}	HOMO-4 → LUMO+3
S_{25}	HOMO-4 → LUMO+4
S_{26}	HOMO-5 → LUMO
S_{27}	HOMO-5 → LUMO+1
S_{28}	HOMO-5 → LUMO+2
S_{29}	HOMO-5 → LUMO+3
S_{30}	HOMO-5 → LUMO+4
S_{31}	HOMO-6 → LUMO
S_{32}	HOMO-6 → LUMO+1
S_{33}	HOMO-6 → LUMO+2
S_{34}	HOMO-6 → LUMO+3
S_{35}	HOMO-6 → LUMO+4

An excited state energy correction of 0.55 eV was used for the S_1 to S_6 states and no correction was considered for the S_7 to S_{35} states. All relaxation times were calculated with the inclusion of decoherence. The population relaxation of states S_1 to S_6 is shown in Figure A.2 in the supporting information (Appendix A). According to Figure A.2, the population relaxations of states S_1 to S_6 preserve similar relaxation patterns compared to the Figure A.1 plots with only minor changes.

The calculated excited state population decay times for the first six states are shown in Table A.2 in the supporting information. The S_1 state has the slowest decay time of 15 ps compared to the other six states having 3.3 to 1.4 ps decay times. Compared to the decay times observed for the case where only the S_1-S_6 states were considered, these states have similar decay times. A similar trend is followed for the six states except for the S_5 state, which now has a decay time similar to S_4.

The depopulation of the S_8 to S_{35} states occurs much faster than that of the S_1 state, on the timescale ranging from 0.7 to 3.1 ps (Table A.3, in the Supporting Information, Appendix A).

Among all these states, the S_7 state has a distinctively long lifetime of 9.9 ps, comparable to that of the S_1 state. This is likely due to the large energy gap between the S_7 and S_6 states, which makes the population transfer more difficult. Geometrical relaxation of the S_7 state can decrease this energy gap,[35] which may lead to faster decay times.

3.4.3 Electron-phonon interactions in the $[Au_{25}(SH)_{18}]^{-1}$ cluster

Nonadiabatic couplings arise due to interactions between electronic and nuclear degrees of freedom; thus, vibrations in the $[Au_{25}(SH)_{18}]^{-1}$ cluster can lead to non-radiative relaxation of excited states. Therefore, it is vital to understand which nuclear vibrational motions couple most strongly with electronic states in order to understand the dynamics of electronic relaxations in these systems.

In the femtosecond relaxation dynamics study on the $[Au_{25}(SCH_2CH_2Ph)_{18}]^{-1}$ cluster, Moran and coworkers identified a 80 cm^{-1} vibrational mode when the probe pulse was tuned to 660-700 nm (~ 1.8 eV), which they attributed to a radial Au-Au bond stretching mode within the Au_{13} core of the cluster.[28] Similarly, a time dependent photoluminescence study on $Au_{25}(SC_3H_9)^{18}$ by Knappenberger and coworkers identified a Au(0)-Au(I) stretching vibrational mode around 90 cm^{-1} and a Au(I)-S stretching mode around 200 cm^{-1}.[49]

In order to understand electron-phonon interactions in the $[Au_{25}(SH)_{18}]^{-1}$ cluster, Fourier transforms of the normalized autocorrelation function of the energy gap fluctuation for a pair of electronic excited states are computed. The energy gap could be between the GS and an electronic excited state or between two different electronic excited states. This gives the phonon spectral density that shows the vibrational modes that are correlated with the non-radiative relaxations.

Figure 3.6 shows the Fourier transforms of autocorrelation functions of the fluctuations of the energy gaps (phonon spectral density spectra) between the GS and S_1, GS and S_2, GS and S_7, and GS and S_8 separately. Between GS and S_1-S_2, there is a range of intense peaks in the region of 0-100 cm^{-1}, with two intense peaks around 25 cm^{-1} and 62.5 cm^{-1}. These features are also shown in the graphs drawn between the GS and the S_3-S_6 states which are shown in Figure A.3. The 25 cm^{-1} peak is also visible in the GS-S_7 and GS-S_8 plots. Furthermore, a small peak in the range 75-100 cm^{-1} is visible for the GS with S_1, S_2, S_4, S_6 and S_8 which could be attributed to the 80

cm^{-1} vibrational mode observed experimentally. These states arise from core-based transitions. All the plots are drawn with a resolution of ~ 4.8 cm^{-1}.

The phonon spectral densities for the pairs of GS with S_7 and S_8 reveal a different character. Both display a small peak around the 200-225 cm^{-1} range. The S_7 and S_8 states arise from the HOMO → LUMO+2 and HOMO → LUMO+3 transitions, respectively. To investigate further, similar graphs were plotted between the two adjacent excited states instead of the GS-excited state. Figure 3.6 also shows the graphs drawn for S_1-S_2 and S_2-S_3 only while the remainder of the graphs are shown in Figure A.4.

In order to correlate the observed vibrational frequencies to the cluster geometry, we compared the frequency values to the frequency calculation with ADF. According to this comparison, it is possible that the ~ 25 cm^{-1} frequency that we observe could be a Au(core)-Au(semi-ring) stretching frequency and that the ~ 62.5 cm^{-1} mode could be a Au(core)-Au(core) stretch. We observed very clear Au(core)-S stretching vibrations between the 213.3 – 237 cm^{-1} frequencies from the frequency calculation. Therefore, the small peak we see around the 200-225 cm^{-1} range from the spectral density plots could be attributed to a Au(core)-S stretching vibration.

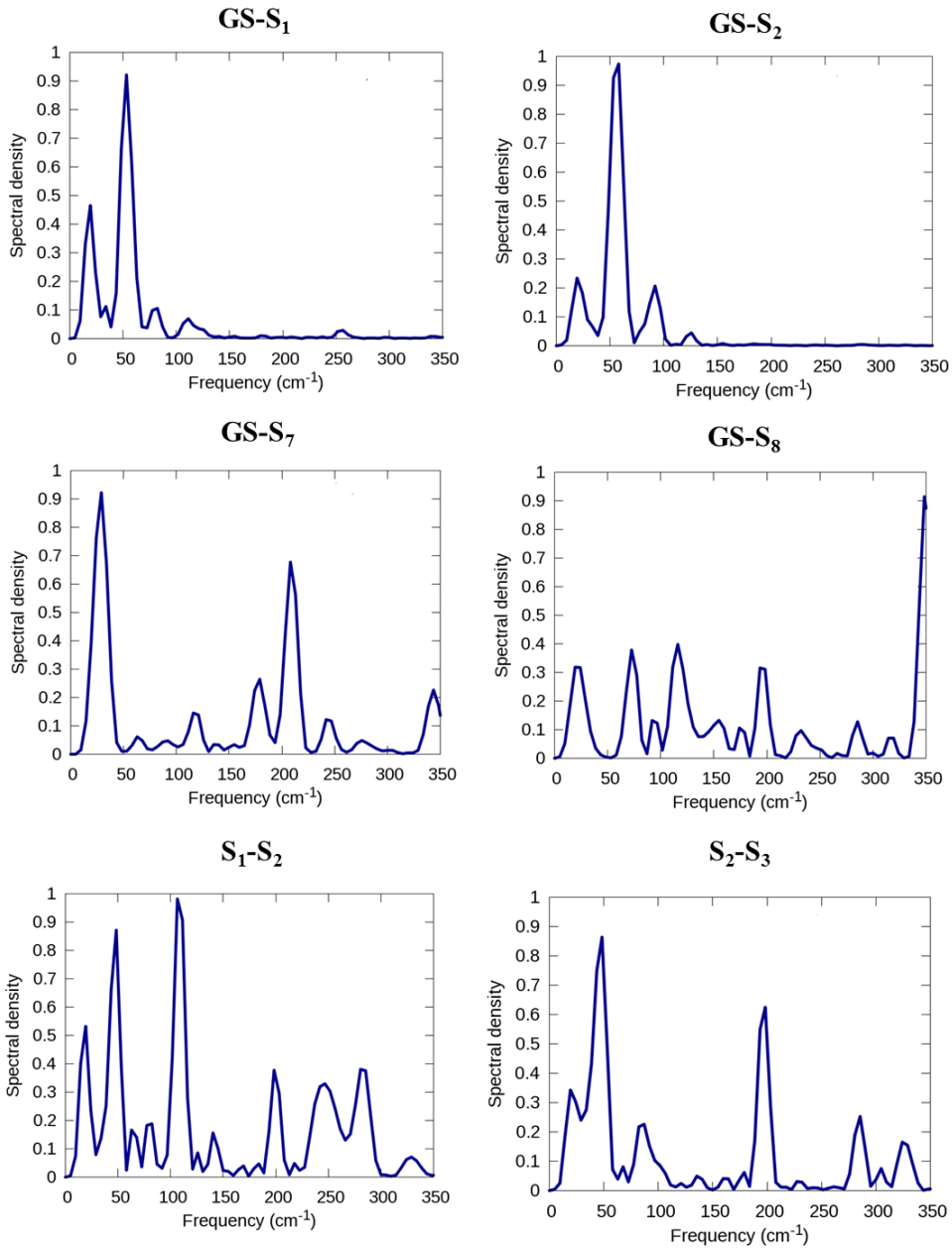

Figure 3.6 Fourier transform of autocorrelation functions of the fluctuations of the energy gaps (phonon spectral density spectra) between GS-S_1, GS-S_2, GS-S_7, GS-S_8, S_1-S_2, and S_2-S_3.

3.5 Conclusion

The nonradiative relaxation dynamics of the $[Au_{25}(SH)_{18}]^{-1}$ cluster excited states have been investigated using TDDFT and KS-DFT based NA-MD methods. The timescales for the ground state recovery were found to be up to two orders of magnitude larger than the relaxation

timescales of the S_1-S_6 excited states. The GS recovery time increases with the initial excitation energy, suggesting that the recovery of the ground state population may be significantly inhibited by the effective "friction" due to the presence of intermediate electronic states, even though the relaxation of the initially-prepared state may occur on the ultrafast timescale. Importantly, the timescales for the GS recovery are increased by a factor of 2-6 by including an energy gap correction.

The S_1-S_6 excited states were found to decay non-radiatively on the timescale of 2.5 to 18 ps, due to fast relaxation to the other excited states as well as to the GS. Our relaxation dynamics calculations of the core states suggest that the time constants observed by Moran and coworkers could arise from core to core transitions rather than from a core to semi-ring transition as they suggested. We predicted time constants for the near HOMO-LUMO core states (S_1 to S_6 states) to be on the picosecond time scale, which is in good agreement with the picosecond time scale constants observed by Moran and coworkers.

The relaxation dynamics of the higher excited states with energy up to ~ 2.2 eV preserve similar relaxation trends. Within the higher excited state relaxations, we observe that S_7 has the slowest decay time of 9.9 ps. This could be due to the large energy gap between the S_7 and S_6 states. The S_1 state population decrease demonstrates the slowest decay time due to the large energy gap to the GS; in our study, no semi-ring or other states were observed at lower energy than the core-based S_1 state.

3.6 Acknowledgements

This material is based on work supported by Department of Energy under grant DE-SC0012273. Some of the computing for this project was performed on the Beocat Research Cluster at Kansas State University, which is funded in part by NSF grants CHE-1726332, CNS-1006860, EPS-1006860, and EPS-0919443. Beocat Application Scientist Dr. Dave Turner provided valuable technical expertise. This work also used the Extreme Science and Engineering Discovery Environment (XSEDE),[50] which is supported by National Science Foundation grant number ACI-1053575. The authors are grateful to Dr. Emilie Guidez for her support and valuable discussions. A.V.A. acknowledges financial support from the University at Buffalo, The State University of New York startup package.

3.7 References

1. Templeton, A. C.; Wuelfing, W. P.; Murray, R. W., Monolayer-Protected Cluster Molecules. *Acc. Chem. Res.* **2000,** *33*, 27-36.

2. Walter, M.; Akola, J.; Lopez-Acevedo, O.; Jadzinsky, P. D.; Calero, G.; Ackerson, C. J.; Whetten, R. L.; Grönbeck, H.; Häkkinen, H., A Unified View of Ligand-Protected Gold Clusters as Superatom Complexes. *Proc. Natl. Acad. Sci. USA* **2008,** *105*, 9157-9162.

3. Jadzinsky, P. D.; Calero, G.; Ackerson, C. J.; Bushnell, D. A.; Kornberg, R. D., Structure of a Thiol Monolayer-Protected Gold Nanoparticle at 1.1 Å Resolution. *Science* **2007,** *318*, 430-433.

4. Chen, S.; Ingram, R. S.; Hostetler, M. J.; Pietron, J. J.; Murray, R. W.; Schaaff, T. G.; Khoury, J. T.; Alvarez, M. M.; Whetten, R. L., Gold Nanoelectrodes of Varied Size: Transition to Molecule-Like Charging. *Science* **1998,** *280*, 2098-2101.

5. Valden, M.; Lai, X.; Goodman, D. W., Onset of Catalytic Activity of Gold Clusters on Titania with the Appearance of Nonmetallic Properties. *Science* **1998,** *281*, 1647-1650.

6. Zhu, M.; Aikens, C. M.; Hendrich, M. P.; Gupta, R.; Qian, H.; Schatz, G. C.; Jin, R., Reversible Switching of Magnetism in Thiolate-Protected Au_{25} Superatoms. *J. Am. Chem. Soc.* **2009,** *131*, 2490-2492.

7. Meng, X.; Liu, Z.; Zhu, M.; Jin, R., Controlled Reduction for Size Selective Synthesis of Thiolate-Protected Gold Nanoclusters Au(n)(n = 20, 24, 39, 40). *Nanoscale Res. Lett.* **2012,** *7*, 277-277.

8. Zhu, Y.; Qian, H.; Drake, B. A.; Jin, R., Atomically Precise $Au_{25}(SR)_{18}$ Nanoparticles as Catalysts for the Selective Hydrogenation of α,β-Unsaturated Ketones and Aldehydes. *Angew. Chem. Int. Ed.* **2010,** *49*, 1295-1298.

9. Ramakrishna, G.; Varnavski, O.; Kim, J.; Lee, D.; Goodson, T., Quantum-Sized Gold Clusters as Efficient Two-Photon Absorbers. *J. Am. Chem. Soc.* **2008,** *130*, 5032-5033.

10. Ramakrishna, G.; Varnavski, O.; Kim, J.; Lee, D.; Goodson, T., Nonlinear Optical Properties of Quantum Sized Gold Clusters. *SPIE* **2008,** *7049*, 70490L-70490L-12.

11. Murray, R. W., Nanoelectrochemistry: Metal Nanoparticles, Nanoelectrodes, and Nanopores. *Chem. Rev.* **2008,** *108*, 2688-2720.

12. Aikens, C. M., Origin of Discrete Optical Absorption Spectra of $M_{25}(SH)_{18}^-$ Nanoparticles (M = Au, Ag). *J. Phys. Chem. C* **2008,** *112*, 19797-19800.

13. Aikens, C. M., Electronic Structure of Ligand-Passivated Gold and Silver Nanoclusters. *J. Phys. Chem. Lett.* **2011,** *2*, 99-104.

14. Devadas, M. S.; Kim, J.; Sinn, E.; Lee, D.; Goodson, T.; Ramakrishna, G., Unique Ultrafast Visible Luminescence in Monolayer-Protected Au_{25} Clusters. *J. Phys. Chem. C* **2010,** *114*, 22417-22423.

15. Stamplecoskie, K. G.; Kamat, P. V., Size-Dependent Excited State Behavior of Glutathione-Capped Gold Clusters and Their Light-Harvesting Capacity. *J. Am. Chem. Soc.* **2014,** *136*, 11093-11099.

16. Heaven, M. W.; Dass, A.; White, P. S.; Holt, K. M.; Murray, R. W., Crystal Structure of the Gold Nanoparticle $[N(C_8H_{17})_4][Au_{25}(SCH_2CH_2Ph)_{18}]$. *J. Am. Chem. Soc.* **2008,** *130*, 3754-3755.

17. Zhu, M.; Aikens, C. M.; Hollander, F. J.; Schatz, G. C.; Jin, R., Correlating the Crystal Structure of a Thiol-Protected Au_{25} Cluster and Optical Properties. *J. Am. Chem. Soc.* **2008,** *130*, 5883-5885.

18. Chen, Y.-S.; Choi, H.; Kamat, P. V., Metal-Cluster-Sensitized Solar Cells. A New Class of Thiolated Gold Sensitizers Delivering Efficiency Greater Than 2%. *J. Am. Chem. Soc.* **2013,** *135*, 8822-8825.

19. Kogo, A.; Sakai, N.; Tatsuma, T., Photocatalysis of Au_{25}-Modified TiO_2 Under Visible and Near Infrared Light. *Electrochem commun* **2010,** *12*, 996-999.

20. Kogo, A.; Sakai, N.; Tatsuma, T., Photoelectrochemical Analysis of Size-Dependent Electronic Structures of Gold Clusters Supported on TiO_2. *Nanoscale* **2012,** *4*, 4217-4221.

21. Yu, C.; Li, G.; Kumar, S.; Kawasaki, H.; Jin, R., Stable $Au_{25}(SR)_{18}/TiO_2$ Composite Nanostructure with Enhanced Visible Light Photocatalytic Activity. *J. Phys. Chem. Lett.* **2013,** *4*, 2847-2852.

22. Subramanian, V.; Wolf, E. E.; Kamat, P. V., Catalysis with TiO_2/Gold Nanocomposites. Effect of Metal Particle Size on the Fermi Level Equilibration. *J. Am. Chem. Soc.* **2004,** *126*, 4943-4950.

23. Qian, K.; Sweeny, B. C.; Johnston-Peck, A. C.; Niu, W.; Graham, J. O.; DuChene, J. S.; Qiu, J.; Wang, Y.-C.; Engelhard, M. H.; Su, D.; Stach, E. A.; Wei, W. D., Surface Plasmon-Driven Water Reduction: Gold Nanoparticle Size Matters. *J. Am. Chem. Soc.* **2014,** *136*, 9842-9845.

24. Gomes Silva, C.; Juárez, R.; Marino, T.; Molinari, R.; García, H., Influence of Excitation Wavelength (UV or Visible Light) on the Photocatalytic Activity of Titania Containing Gold Nanoparticles for the Generation of Hydrogen or Oxygen from Water. *J. Am. Chem. Soc.* **2011,** *133*, 595-602.

25. Primo, A.; Marino, T.; Corma, A.; Molinari, R.; García, H., Efficient Visible-Light Photocatalytic Water Splitting by Minute Amounts of Gold Supported on Nanoparticulate CeO_2 Obtained by a Biopolymer Templating Method. *J. Am. Chem. Soc.* **2011,** *133*, 6930-6933.

26. Link, S.; El-Sayed, M. A.; Gregory Schaaff, T.; Whetten, R. L., Transition from Nanoparticle to Molecular Behavior: A Femtosecond Transient Absorption Study of a Size-Selected 28 Atom Gold Cluster. *Chem. Phys. Lett.* **2002,** *356*, 240-246.

27. Link, S.; Beeby, A.; FitzGerald, S.; El-Sayed, M. A.; Schaaff, T. G.; Whetten, R. L., Visible to Infrared Luminescence from a 28-Atom Gold Cluster. *J. Phys. Chem. B* **2002,** *106*, 3410-3415.

28. Miller, S. A.; Womick, J. M.; Parker, J. F.; Murray, R. W.; Moran, A. M., Femtosecond Relaxation Dynamics of $Au_{25}L_{18}^-$ Monolayer-Protected Clusters. *J. Phys. Chem. C* **2009,** *113*, 9440-9444.

29. Miller, S. A.; Fields-Zinna, C. A.; Murray, R. W.; Moran, A. M., Nonlinear Optical Signatures of Core and Ligand Electronic States in $Au_{24}PdL_{18}$. *J. Phys. Chem. Lett.* **2010,** *1* (9), 1383-1387.

30. Green, T. D.; Knappenberger, K. L., Relaxation Dynamics of $Au_{25}L_{18}$ Nanoclusters Studied by Femtosecond Time-Resolved Near Infrared Transient Absorption Spectroscopy. *Nanoscale* **2012,** *4*, 4111-4118.

31. Yau, S. H.; Varnavski, O.; Goodson, T., An Ultrafast Look at Au Nanoclusters. *Acc. Chem. Res.* **2013,** *46*, 1506-1516.

32. Stamplecoskie, K. G.; Chen, Y.-S.; Kamat, P. V., Excited-State Behavior of Luminescent Glutathione-Protected Gold Clusters. *J. Phys. Chem. C* **2014,** *118*, 1370-1376.

33. Stoll, T.; Sgrò, E.; Jarrett, J. W.; Réhault, J.; Oriana, A.; Sala, L.; Branchi, F.; Cerullo, G.; Knappenberger, K. L., Superatom State-Resolved Dynamics of the $Au_{25}(SC_8H_9)_{18}^-$ Cluster from Two-Dimensional Electronic Spectroscopy. *J. Am. Chem. Soc.* **2016,** *138*, 1788-1791.

34. Mukamel, S., Multidimensional Femtosecond Correlation Spectroscopies of Electronic and Vibrational Excitations. *Annu. Rev. Phys. Chem.* **2000,** *51*, 691-729.

35. Weerawardene, K. L. D. M.; Aikens, C. M., Theoretical Insights into Origin of Photoluminescence of $Au_{25}(SR)_{18}^-$ Nanoparticles *J. Am. Chem. Soc.* **2016,** *138*, 11202–11210.

36. Chen, X.; Prezhdo, O. V.; Ma, Z.; Hou, T.; Guo, Z.; Li, Y., Ab initio Phonon-Coupled Nonadiabatic Relaxation Dynamics of $[Au_{25}(SH)_{18}]^-$ Clusters. *Phys. Status Solidi (b)* **2016,** *253*, 458-462.

37. C. Tully, J., Mixed Quantum-Classical Dynamics. *Farad. Discuss.* **1998,** *110*, 407-419.

38. Craig, C. F.; Duncan, W. R.; Prezhdo, O. V., Trajectory Surface Hopping in the Time-Dependent Kohn-Sham Approach for Electron-Nuclear Dynamics. *Phys. Rev. Lett.* **2005,** *95*, 163001.

39. Jaeger, H. M.; Fischer, S.; Prezhdo, O. V., Decoherence-Induced Surface Hopping. *J. Chem. Phys* **2012,** *137*, 22A545.

40. Akimov, A. V.; Prezhdo, O. V., The PYXAID Program for Non-Adiabatic Molecular Dynamics in Condensed Matter Systems. *J. Chem. Theory Comput.* **2013,** *9*, 4959-4972.

41. Akimov, A. V.; Prezhdo, O. V., Advanced Capabilities of the PYXAID Program: Integration Schemes, Decoherence Effects, Multiexcitonic States, and Field-Matter Interaction. *J. Chem. Theory Comput.* **2014,** *10*, 789-804.

42. te Velde, G.; Bickelhaupt, F. M.; Baerends, E. J.; Fonseca Guerra, C.; van Gisbergen, S. J. A.; Snijders, J. G.; Ziegler, T., Chemistry with ADF. *J. Comput. Chem.* **2001,** *22*, 931-967.

43. Lenthe, E. v.; Baerends, E. J.; Snijders, J. G., Relativistic Regular Two-Component Hamiltonians. *J. Chem. Phys* **1993,** *99*, 4597-4610.

44. Perdew, J. P.; Burke, K.; Ernzerhof, M., Generalized Gradient Approximation Made Simple. *Phys. Rev. Lett.* **1996,** *77*, 3865-3868.

45. Kresse, G.; Furthmüller, J., Efficiency of Ab-Initio Total Energy Calculations for Metals and Semiconductors Using a Plane-Wave Basis Set. *Comput. Mater. Sci.* **1996,** *6*, 15-50.

46. Kresse, G.; Joubert, D., From Ultrasoft Pseudopotentials to the Projector Augmented-wave Method. *Phys. Rev. B* **1999,** *59*, 1758-1775.

47. Verlet, L., Computer "Experiments" on Classical Fluids. I. Thermodynamical Properties of Lennard-Jones Molecules. *Phys. Rev.* **1967,** *159*, 98-103.

48. Hammes-Schiffer, S.; Tully, J. C., Proton Transfer in Solution: Molecular Dynamics with Quantum Transitions. *J. Chem. Phys.* **1994,** *101*, 4657-4667.

49. Green, T. D.; Yi, C.; Zeng, C.; Jin, R.; McGill, S.; Knappenberger, K. L., Temperature-Dependent Photoluminescence of Structurally-Precise Quantum-Confined $Au_{25(}SC_8H_9)_{18}$ and $Au_{38}(SC_{12}H_{25})_{24}$ Metal Nanoparticles. *J. Phys. Chem. A* **2014,** *118*, 10611-10621.

50. John, T., XSEDE: Accelerating Scientific Discovery. **2014**, pp 62-74.

Chapter 4 - The Electronic Relaxation Dynamics in $[Au_{25}(SR)_{18}]^{-1}$ (R = CH_3, C_2H_5, C_3H_7, MPA) [MPA = mercaptopropionic acid ligand] Thiolate-protected Nanocluster Series: Ligand Effects and Separate Electron and Hole Relaxation Dynamics in the $[Au_{25}(SCH_3)_{18}]^{-1}$ Nanocluster

4.1 Abstract

We investigate the excited electron dynamics in $[Au_{25}(SR)_{18}]^{-1}$ (R = CH_3, C_2H_5, C_3H_7, MPA) [MPA = mercaptopropanoic acid] nanoparticles to understand how different ligands affect the excited state dynamics in this system. The population dynamics of the core and higher excited states lying in the energy range 0.00–2.20 eV are studied using a surface hopping method with decoherence correction in a real-time DFT approach. All of the ligated clusters follow a similar trend in decay for the core states (S_1-S_6). The observed time constants are on the picosecond time scale (2-19 ps), which agrees with the experimental time scale, and this study confirms that the time constants observed experimentally could originate from core-to-core transitions and not from core-to-semiring transitions. In the presence of higher excited states, R = H, CH_3, C_2H_5, and C_3H_7 demonstrate similar relaxations trends whereas R = MPA shows slightly different relaxation of the core states due to a smaller gap between LUMO+1 and LUMO+2 gap in its electronic structure. The S_1 (HOMO-LUMO) state gives the slowest decay in all ligated clusters, while S_7 has a relatively long decay. Furthermore, separate electron and hole relaxations were performed on the $[Au_{25}(SCH_3)_{18}]^{-1}$ nanocluster to understand how the independent electron, hole relaxations contribute to the overall relaxation dynamics.

4.2 Introduction

Small thiolate-protected gold clusters in the ~2 nm size regime have been identified as promising efficient solar photon harvesters.[1-2] Their ability to absorb photons in the visible range has been a major reason for their usefulness in photocatalytic applications.[1] Experimental studies have demonstrated that even non-plasmonic clusters such as $[Au_{25}(SR)_{18}]^{-1}$ can contribute to photocatalytic enhancement upon visible light irradiation on a Au_{25}-semiconductor system.[3-6] These observations have suggested that the $[Au_{25}(SR)_{18}]^{-1}$ nanocluster can be a possible

photosensitizer in metal cluster-sensitized solar cells.[3] Also, $[Au_{25}(SR)_{18}]^{-1}$ has shown interesting photoluminescence properties[7-11] that are important for future sensing and imaging applications. Therefore, a thorough understanding of the excited state relaxations in $[Au_{25}(SR)_{18}]^{-1}$ is required for the development of relevant applications.

The $[Au_{25}(SR)_{18}]^{-1}$ cluster is a well-defined thiolate-protected gold nanoparticle with an icosahedral core that consists of thirteen gold atoms. The gold core is surrounded by six "V-shaped" −S−Au−S−Au−S− semiring motifs.[12-13] Several different $[Au_{25}(SR)_{18}]^{-1}$ clusters have been reported experimentally and theoretically depending on the type of the ligand R attached to the sulfur atoms. Some of the SR groups used are alkanethiols such as $-SCH_3$, $-SCH_2CH_3$, $-SC_6H_{13}$, $-SCH_2CH_2Ph$; glutathiones; arylthiols such as -SPhX(X=H, F, Cl, Br, CH_3, OCH_3, NO_2, *t*Bu), and dithiolates.[2, 7, 11-25] In the literature, various experimental characterizations of electron relaxation dynamics from excited states lying near the HOMO−LUMO gap and from higher excited states of the $[Au_{25}(SR)_{18}]^{-1}$ cluster can be found.[2, 9, 11, 23, 26-29] In these experiments, groups have used different ligands in the R group, including SR = glutathiones, hexanethiols, $-SCH_2CH_2Ph$.

In 2002, Whetten and co-workers performed a femtosecond transient absorption study on the glutathione-stabilized Au_{25} cluster and found two relaxation lifetimes: one around 750 fs and the other on the nanosecond time scale.[9] Moran and co-workers studied the femtosecond relaxation dynamics of the Au_{25} cluster when the ligand was R = CH_2CH_2Ph. They proposed a relaxation mechanism involving a relaxation time of ~200 fs for the Au_{13} core and a slower 1.2 ps time constant for the relaxation from core to semiring states.[11] A femtosecond time-resolved luminescence study of $Au_{25}L_{18}$ [L = hexanethiol (C_6S) and glutathione (GS)] by Ramakrishna and co-workers suggested that higher excited state decay constants have lifetimes of 200 fs to a few picoseconds.[26] Kamat and co-workers also studied relaxation dynamics of the glutathione-protected Au_{25} nanocluster. In their study, the $Au_{25}(GS)_{18}$ cluster showed a ~1 ps decay constant for a metal-metal transition and a slower ca. 200 ns decay constant for a ligand-to-metal charge transfer.[1] Overall, experimental studies on nonradiative relaxation dynamics on Au_{25} clusters with different ligand systems have demonstrated varying time constants that span from the femtosecond to nanosecond time scale.

At this point, a systematic theoretical study is needed to explain the different time scales observed for different Au_{25} clusters and provide further insights into the Au_{25} relaxation

mechanism. Recent theoretical studies have been performed on understanding the nonradiative excited state relaxations of the $[Au_{25}(SH)_{18}]^{-1}$ cluster to characterize the electron relaxation dynamics.[30-31] Those investigations considered the smallest possible Au_{25} cluster model with simple SH ligands. In the study by Senanayake et al.,[30] the core and higher excited states lying in the energy range of 0.00−2.20 eV were considered in the relaxation dynamics calculations. It was found that relaxations between excited states that arise from core-to-core transitions occur on a short time scale of around 2-18 ps. This study also supported that idea that no semiring states are involved at an energy lower than the core-based S_1 state. The observation suggests that the several picosecond time constants observed by Moran and co-workers could arise from core-to-core transitions rather than from a core-to-semiring transition.[30] The SH ligand was used in our previous study to capture the relaxation dynamics of the Au_{25} cluster while reducing the complexity of the geometry of the system and minimizing the computational cost. However, it is important to determine how the trends in the relaxation dynamics differ in the Au_{25} cluster with more realistic ligands. Therefore, an analysis of the relaxation dynamics that occur when the ligands are varied will provide better insight to the relaxation dynamics of the Au_{25} cluster.

Herein, the main goal of this study is to investigate the electronic relaxation dynamics in the thiolate-protected nanocluster series $[Au_{25}(SR)_{18}]^{-1}$ (R = CH_3, C_2H_5, C_3H_7, MPA) [MPA = mercaptopropionic acid] to understand the ligand effects on relaxation dynamics compared to the $[Au_{25}(SH)_{18}]^{-1}$ system. The ligands used in this study are closer to common experimentally used ligands such as glutathione and phenylethylthiol. MPA-ligated gold clusters have been used in a photocatalysis study with TiO_2/gold nanocomposites because MPA has a carboxylic functional group (-COOH) that can covalently bind to the TiO_2 surface.[32] Studying the relaxation dynamics of $[Au_{25}(SR)_{18}]^{-1}$ with different R groups will be beneficial for understanding how the ligands affect the dynamics, especially how the core and the higher excited state relaxations will differ based on the ligand used. The findings of this investigation will provide better insights into the photo-physics of the $[Au_{25}(SR)_{18}]^{-1}$ nanocluster, which is necessary for its useful applications.

4.3 Computational methodology

We have performed ab initio real-time nonadiabatic molecular dynamics (NA-MD) simulations to study the electronic relaxation dynamics in the thiolate-protected nanocluster series $[Au_{25}(SR)_{18}]^{-1}$ (R = CH_3, C_2H_5, C_3H_7, MPA). The NA-MD simulations were performed

using the fewest switches surface hopping (FSSH)[33] algorithm with the classical path approximation and a time-dependent Kohn−Sham description of electronic states (FSSH-TDKS).[34] The overcoherent nature of the FSSH approach is corrected by the decoherence-induced surface hopping (DISH)[35] scheme. The FSSH simulations are performed using the PYXAID program.[36-37]

The computational methodology has several steps that are described briefly in this section. A detailed explanation of the method employed is given elsewhere.[30, 36-37] The relaxed geometries of the thiol-protected nanoclusters were obtained by performing a geometry optimization with the PBE[38]/TZP level of theory with the Amsterdam Density Functional (ADF)[39] software package. The zero-order regular approximation (ZORA)[40] was used to treat the scalar relativistic effects in gold. Linear response time-dependent density functional theory (TD-DFT) calculations were performed using the same level of theory to get the electronic excitations and the absorption spectra.

Secondly, the Vienna Ab initio Simulation Package (VASP)[41] is used to perform temperature ramping and molecular dynamics (MD) calculations. The 0K systems are thermalized through a temperature ramping calculation performed at 300K. An MD trajectory of 5 ps in length was computed with a 1 fs integration time step. We used projector-augmented wave[42] pseudopotentials, a kinetic energy cutoff value of 402.4 eV for the temperature ramping calculations and a kinetic energy cutoff value of 301.8 eV for the MD simulations and NA coupling calculations (these values are the same as in the previous R=SH study), gamma points, and the PBE functional in all of our VASP calculations. For R= CH_3, C_2H_5, and C_3H_7, a 24 Å simulation box size was used; for MPA, the simulation box size was set to 30 Å due to its larger size. This bigger box size for R=MPA will minimize the possible interactions between the neighboring images due to the use of periodic boundary conditions.

In the third step, we calculated the nonadiabatic coupling elements following the same approach described in our previous study on $[Au_{25}(SH)_{18}]^{-1}$. The NA-MD calculations were performed considering 3.5 ps length sub-trajectories with 10 different starting geometries. For each NA-MD trajectory, 1000 realizations of the stochastic FSSH/DISH state hopping trajectories are considered.

The important electronic excited states contributing to the two main peaks in the optical absorption spectrum of $[Au_{25}(SR)_{18}]^{-1}$ in the energy range of 0.00−2.20 eV were analyzed both

with and without an energy correction to the calculated excited states. With the PBE level of theory, the first excitation peak (S_1-S_6 states) is underestimated by ~0.55 eV compared to the experimental peak. The second peak has a smaller underestimation. Therefore, an excited state energy correction of 0.55 eV was used for the S_1-S_6 states and no correction was used for higher states. The decay times of the excited states populations and the ground state population increase times were calculated for all of the nanoclusters using the same equations and procedure mentioned in our previous study.[30]

4.4 Results and discussion

The absorption spectra (Figure 4.1) calculated for $[Au_{25}(SR)_{18}]^{-1}$ (R = CH_3, C_2H_5, C_3H_7, MPA) at the PBE level of theory show strong peaks around similar energies compared to $[Au_{25}(SH)_{18}]^{-1}$. $[Au_{25}(SCH_3)_{18}]^{-1}$ exhibits strong peaks around 1.35 and 2.60 eV. Similarly, the absorption spectra for $[Au_{25}(SR)_{18}]^{-1}$ (R = C_2H_5, C_3H_7, MPA) display strong peaks around [1.37, 2.60], [1.37, 2.60], and [1.30, 2.40] eV, respectively. The peak positions are shifted compared to the three well-defined bands at 1.8, 2.75, and 3.1 eV observed in the $[Au_{25}(SR)_{18}]^{-1}$ experimental[12-13] UV−vis absorption spectrum. The first peak of $[Au_{25}(SR)_{18}]^{-1}$ with different ligands is redshifted compared to that of $[Au_{25}(SH)_{18}]^{-1}$. However, the assignment of the first peak in all the clusters studied here is similar to the previous DFT calculations performed on the related $[Au_{25}(SH)_{18}]^{-1}$ cluster.[13, 30] The first peak arises from core-to-core transitions within the Au_{13} core.

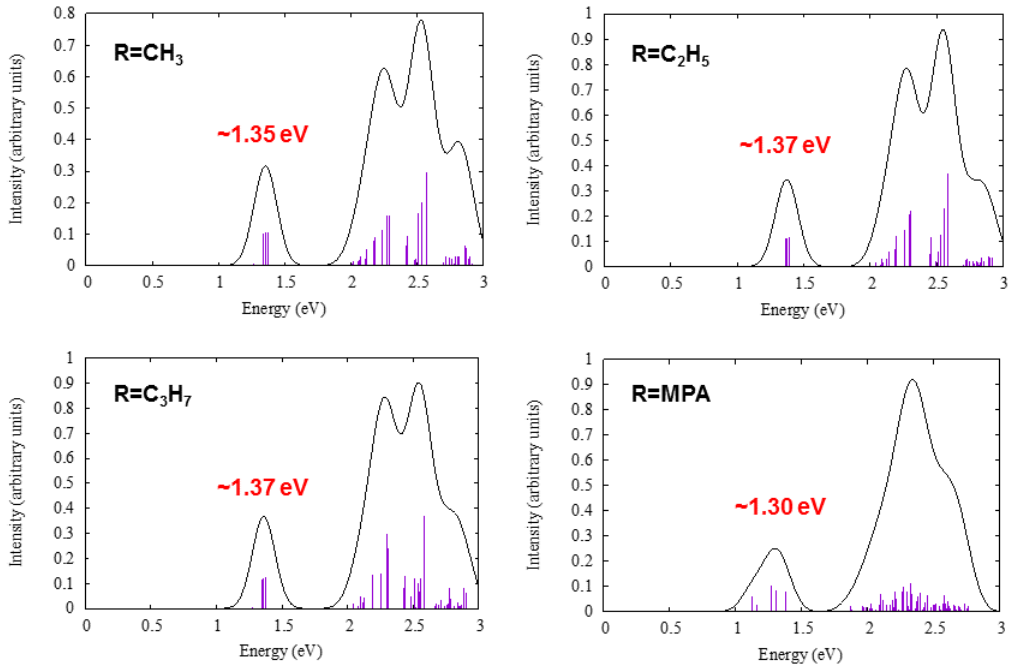

Figure 4.1 Calculated optical absorption spectra for $[Au_{25}(SR)_{18}]^{-1}$ (R = CH_3, C_2H_5, C_3H_7, MPA).

4.4.1 Relaxation dynamics of the first excited state peak in $[Au_{25}(SR)_{18}]^{-1}$

To understand how electronic relaxation dynamics differ when $[Au_{25}(SR)_{18}]^{-1}$ is substituted with various ligands R (R = CH_3, C_2H_5, C_3H_7, MPA), we have studied the first peak in the spectrum that corresponds to the 1.8 eV experimental peak. The first excited state of the clusters with ligands R = CH_3, C_2H_5, C_3H_7, and MPA occurs around 1.35, 1.37, 1.37, and 1.30 eV, respectively. The first excited state peak in these three clusters can be attributed to an intraband transition arising from HOMO → LUMO where the HOMO is nearly triply degenerate and the LUMO is nearly doubly degenerate as in previously reported theoretical investigations.[13, 30] In this work, we discuss the approximately doubly degenerate LUMO as two separate orbitals (LUMO and LUMO+1) and the triply degenerate HOMO as three separate orbitals (HOMO, HOMO-1 and HOMO-2) because the degeneracy is lifted because of nuclear distortions in the *x*, *y*, and *z* directions during the dynamics. The 1.35 eV peak is constructed from excited states 4, 5, and 6, which have higher oscillator strengths compared to excited states 1 to 3. (see Appendix B, Table B.1)

The table also shows the highest weighted single-particle excitations that contribute to the first peak. The transitions going from the HOMO, HOMO-1 and HOMO-2 to the LUMO and

LUMO+1 are all core-to-core intraband transitions. The excitations involved in the other ligated clusters are also in Table B.1. The first peak in all ligated clusters originates from similar core-to-core based transitions. Therefore, we can define the same six excited states for the FSSH-TDKS calculations of the first peak as were defined for the $[Au_{25}(SH)_{18}]^{-1}$ case (Table 4.1). These six excited states used in the FSSH-TDKS calculations (Table 4.1) are slightly different from the first six excited states determined from the TDDFT calculations (Table B.1); the FSSH-TDKS calculations use a single Slater determinant while the TDDFT calculations allow for mixed states. In the FSSH-TDKS calculations, the states shown in Table 4.1 correspond to the six transitions with the highest weights across the first six excited states in the TDDFT calculation.

Table 4.1 The six excited states considered for the FSSH-TDKS calculations responsible for the first absorption peak.

Excited state	Transition
S_1	HOMO → LUMO
S_2	HOMO → LUMO+1
S_3	HOMO-1 → LUMO
S_4	HOMO-1 → LUMO+1
S_5	HOMO-2 → LUMO
S_6	HOMO-2 → LUMO+1

Clusters with ligands R = CH_3, C_2H_5, and C_3H_7 demonstrate near degeneracies of LUMOs and HOMOs similar to the $[Au_{25}(SH)_{18}]^{-1}$ case. The variation of the orbital energies with time during the MD simulations is shown in Figure 4.2 for R = CH_3 while R = C_2H_5, C_3H_7 are shown in the SI in Appendix B, Figure B.1. The orbital energy variation during the MD run for clusters with R = CH_3, C_2H_5, C_3H_7 shows a similar behavior. The HOMO-2, HOMO-1 and HOMO of those clusters are mainly constructed of core gold orbitals (mixed 6s and 6p character), whereas the LUMO and LUMO+1 are also constructed of core gold atomic orbitals (6s character). The lower lying HOMOs are mainly composed from ligand gold (5d character) atoms and from a small amount of sulfur atomic orbitals (3p character). Compared to the other ligated Au_{25} clusters, the electronic structure of the cluster with R=MPA started to indicate a slight difference during the MD simulation (Figure 4.3). Initially (0–400 fs), the electronic structure exhibits an energy gap between the LUMO+1 and higher level LUMOs; after around

400fs, the energy gap between the LUMO+1 and LUMO+2 decreases. The triple degeneracy of the HOMO, HOMO-1, HOMO-2 is preserved and there is a notable gap between the HOMO-2 and lower level HOMOs for the R=MPA cluster as shown in Figure 4.3. However, the LUMO orbital energies are closer in energy to each other in the MPA-ligated cluster compared to the other clusters.

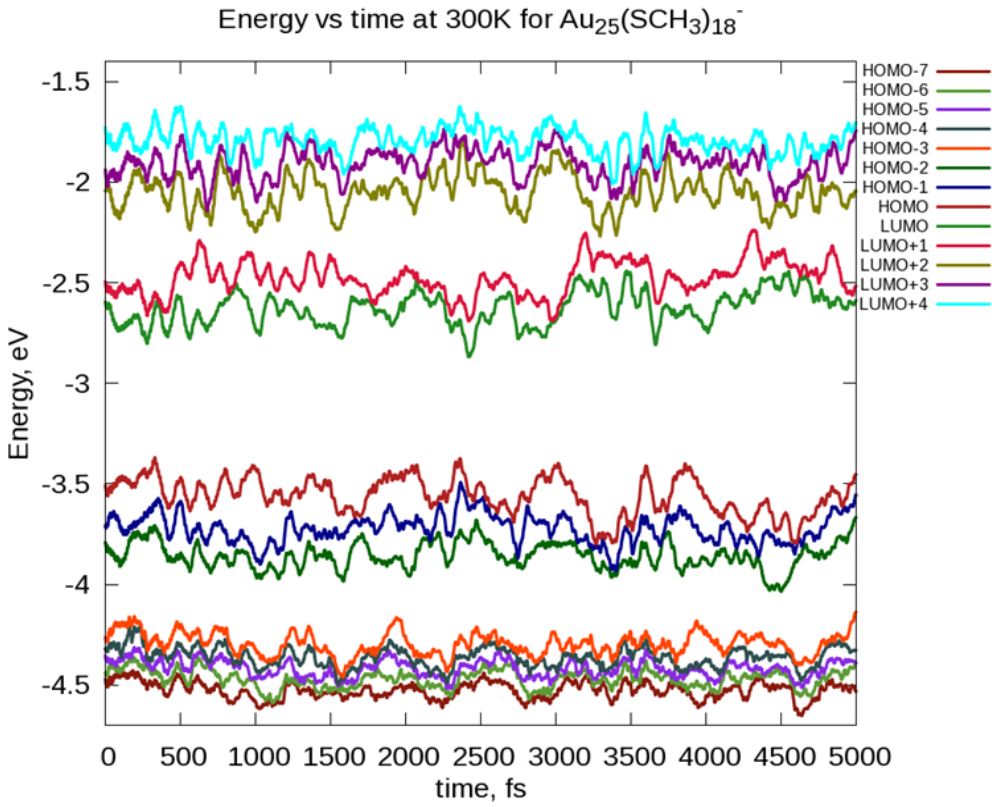

Figure 4.2 Orbital energy variation with time during the MD simulation for $[Au_{25}(SCH_3)_{18}]^{-1}$.

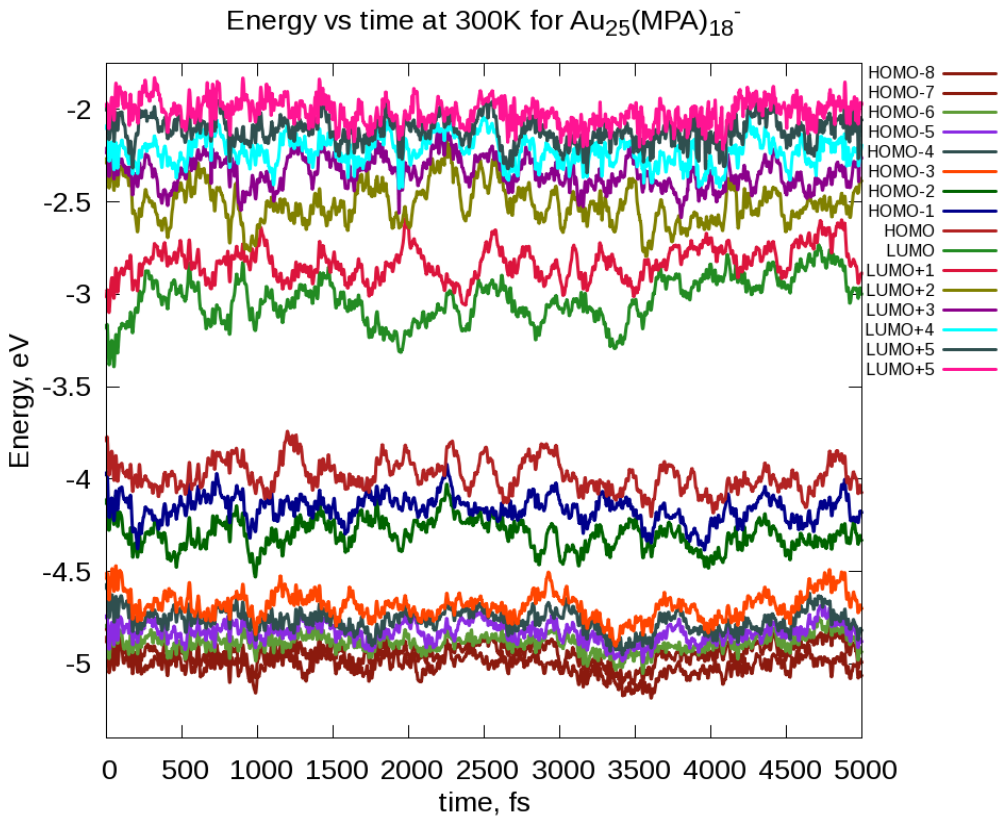

Figure 4.3 Orbital energy variation with time during the MD simulation for $[Au_{25}(MPA)_{18}]^{-1}$.

4.4.1.1 Relaxation dynamics of S_1 to S_6 states in $[Au_{25}(SR)_{18}]^{-1}$

In this section, the electronic relaxation of the first six excited states, S_1 to S_6, of $[Au_{25}(SR)_{18}]^{-1}$ with different ligands are discussed. Similar to the $[Au_{25}(SH)_{18}]^{-1}$ model system studied earlier, all six excited states and the ground state (GS) are included in all the calculations in this section. The overcoherent nature associated with the FSSH calculation was adjusted by adding decoherence effects through the DISH algorithm implemented in the PYXAID program. Inclusion of the decoherence correction in the calculations changes the decay time values considerably, as shown previously in detail for $[Au_{25}(SH)_{18}]^{-1}$.[30] Therefore, the decoherence correction was added in all calculations discussed in this work. In addition, we also added an energy correction of 0.55 eV to the HOMO-LUMO gap of the various clusters considered in the calculations, to provide a better match with the corresponding experimental value. We used the same 0.55 eV energy correction for the excited states in all the clusters due to the similar HOMO-LUMO gaps obtained from the ADF geometry optimizations and to keep the comparison between different clusters consistent. The relaxation dynamics were performed both "without"

and “with” energy corrections to see the implications of this correction on the patterns in the excited state relaxation dynamics in the different clusters. Both the excited state population decays and the GS population increase times are determined in this work.

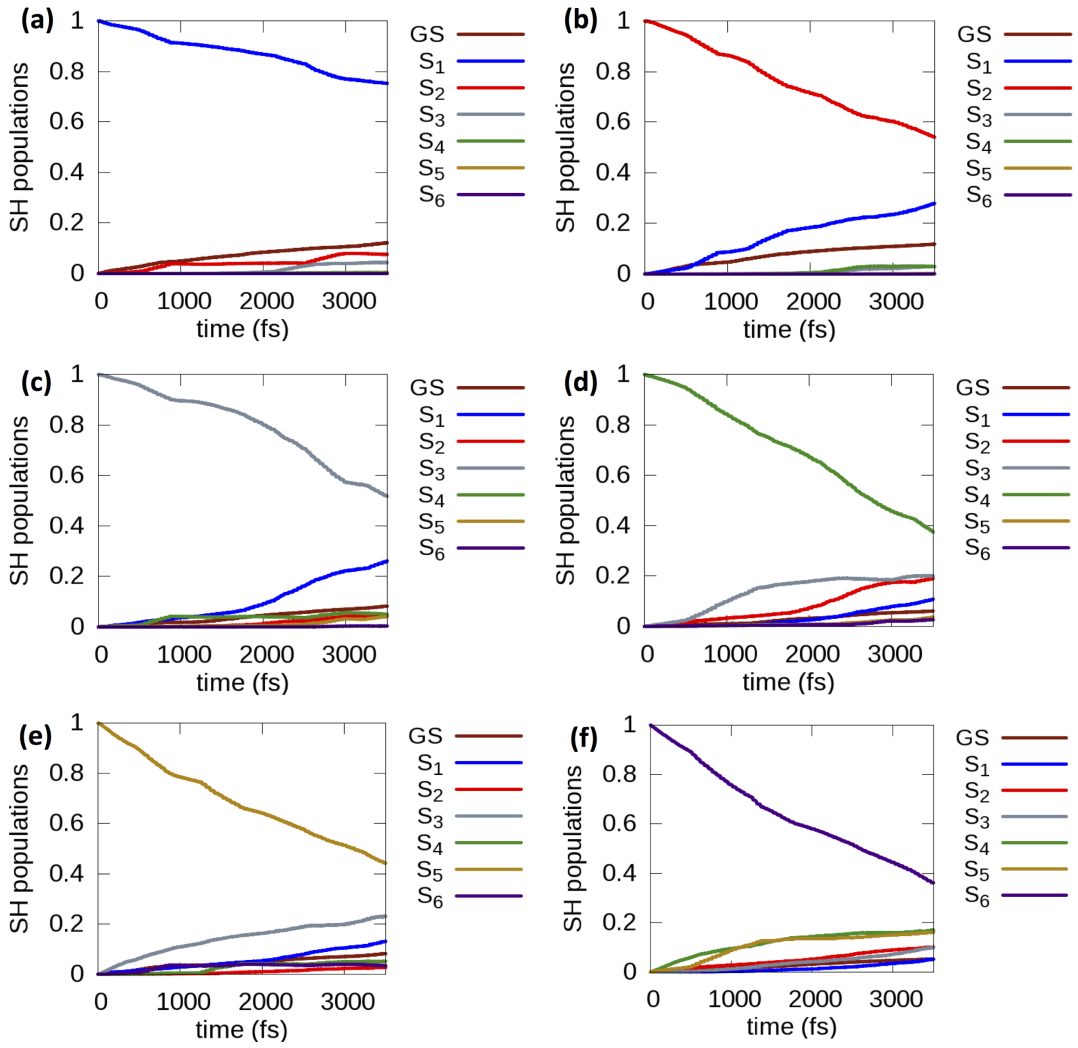

Figure 4.4 Evolution of the populations of S_1, S_2, S_3, S_4, S_5, S_6 states (panels a−f, respectively) for $[Au_{25}(SCH_3)_{18}]^{-1}$ without an energy correction.

The population dynamics computed for the $[Au_{25}(SCH_3)_{18}]^{-1}$ cluster are shown in Figure 4.4. The relaxation patterns observed for the cluster with the methyl ligand demonstrated a similar relaxation pattern for the S_1 to S_6 state relaxations for $[Au_{25}(SH)_{18}]^{-1}$. The relaxation patterns obtained using a 0.55 eV energy correction to the excited states (Figure B.2) preserved a similar pattern to those in Figure 4.4 regardless of whether the correction was added. The

computed GS growth times for the $[Au_{25}(SCH_3)_{18}]^{-1}$ cluster are shown in Table 4.2.

Table 4.2 Ground state population increase time constants after excitation into the six excited states contributing to the 1.35 eV peak of $[Au_{25}(SCH_3)_{18}]^{-1}$.

Excited state	GS growth time (ps) without considering the energy correction	GS growth time (ps) with the energy correction
S_1	25	77
S_2	24	105
S_3	43	168
S_4	58	258
S_5	39	215
S_6	62	477

The GS growth times are influenced by the presence of intermediate states. For example, a small population of S_1 transfers to the S_2 and S_3 states before relaxing to the GS. The R=CH_3 cluster overall demonstrated shorter GS growth times (24-62 ps seconds) compared to the SH ligand model GS growth times (73-158 ps without the energy correction). The trend in GS growth time constants observed for the first six states follows a similar pattern as in the SH ligand model: states S_1 and S_2 decay to the GS quickly while the other four higher energy states require longer times for repopulation of the GS. Among the S_3 to S_6 states, the S_4 (HOMO-1-LUMO+1) state exhibits the slowest GS growth time when no energy correction is used, whereas S_6 (HOMO-2-LUMO+1) is the slowest with the 0.55 eV energy correction. The times for repopulation of the GS increase significantly with the addition of the correction, which is logical because the energy gap between the LUMOs and HOMOs has increased; this was also observed for the SH ligand model system.[30] The results from the GS growth times again confirm that higher initial excitations leads to slower repopulation to the GS due to the presence of a large number of intermediate states and the higher initial excitation energy. Due to the involvement of the intermediate states, the GS growth is non-exponential, and there is always uncertainty in determining the exact relaxation time constants. However, the approach is useful to get an idea about the relaxation pathways involved.

Table 4.3 Decay times for the excited state population decrease of the six excited states contributing to the 1.35 eV peak of $[Au_{25}(SCH_3)_{18}]^{-1}$.

Excited state	Decay time (ps) without considering the energy correction	Decay time (ps) with the energy correction
S_1	13	18
S_2	5.9	7.4
S_3	6.9	7.8
S_4	4.4	4.7
S_5	4.4	4.9
S_6	3.7	3.8

The excited state depopulation time constants are also useful to evaluate as these represent a different process than the GS growth times. $[Au_{25}(SCH_3)_{18}]^{-1}$ yields very short decay constants (<20 fs) for all six states both without and with an energy correction (Table 4.3). Ultrafast decay time constants were also observed for the H ligand model.[30] The GS growth time after S_1 state excitation (24 ps) is twice as large as the decay time constant of the S_1 state (12 ps); this occurs because population in the S_1 state can transfer to the S_2 and higher energy states in addition to returning to the ground state. In the H ligand model, this effect was profound where the GS growth time of S_1 was nearly five times larger than the S_1 state decay time. In Figure 4.4a, the S_1 state transfers a small population to S_2 and S_3 and a larger proportion to the GS. When the energy correction is added, a similar degree of population is transferred to the S_2 and S_3 but a slower population growth is observed for the GS. This could further support the idea that S_2 and S_3 states play a vital role in S_1 relaxation.

After initial excitation to the S_2 state, S_2 transfers population to S_1 and a small amount of electronic population is transferred to S_4 (Figure 4.4b). In the H ligand model, the GS was populated slowly when the S_2 state relaxes, whereas with R=CH_3 the GS is populated much faster when the S_2 state relaxes. However, the GS population increase is slower when the energy correction is added as shown in Figure B.2b. The excitation of the S_6 state will lead the population to relax into the lower energy S_1-S_5 states. The populations of all six excited states reach an average value of ~0.1 after the 3.5 ps trajectories, which is less than in the H ligand model case.

Similar to the methyl ligand cluster calculations, relaxation dynamics were performed on

ethyl-, propyl-, and MPA-stabilized clusters. The relaxation curves ("without" and "with" the energy correction) for the clusters with R=C_2H_5, C_3H_7 are shown in the SI (Figure B.3, B.4, B.5, B.6) and have similar relaxation patterns as observed for R=CH_3. The curves for R=MPA without the energy correction are shown in Figure 4.5.

The ethyl and propyl results show that both S_2 and S_3 could play a role in S_1 state relaxation due to a small amount of population transfer to S_2 and S_3 (Figure B.3a, B.5a), similar to the methyl ligand. However, in MPA, the S_1 state population primarily transfers to S_3 as shown in Figure 4.5a and Figure B.7.

In ethyl and propyl ligated clusters, the S_6 state population relaxes mainly to the S_4 state. Overall, the S_1-S_5 states populations reach an average value of ~0.15 for ethyl and propyl. In the MPA case, initially the S_6 state relaxes to S_4 and then population later transfers to S_2, and the S_1-S_5 states populations eventually reach an average of ~0.18.

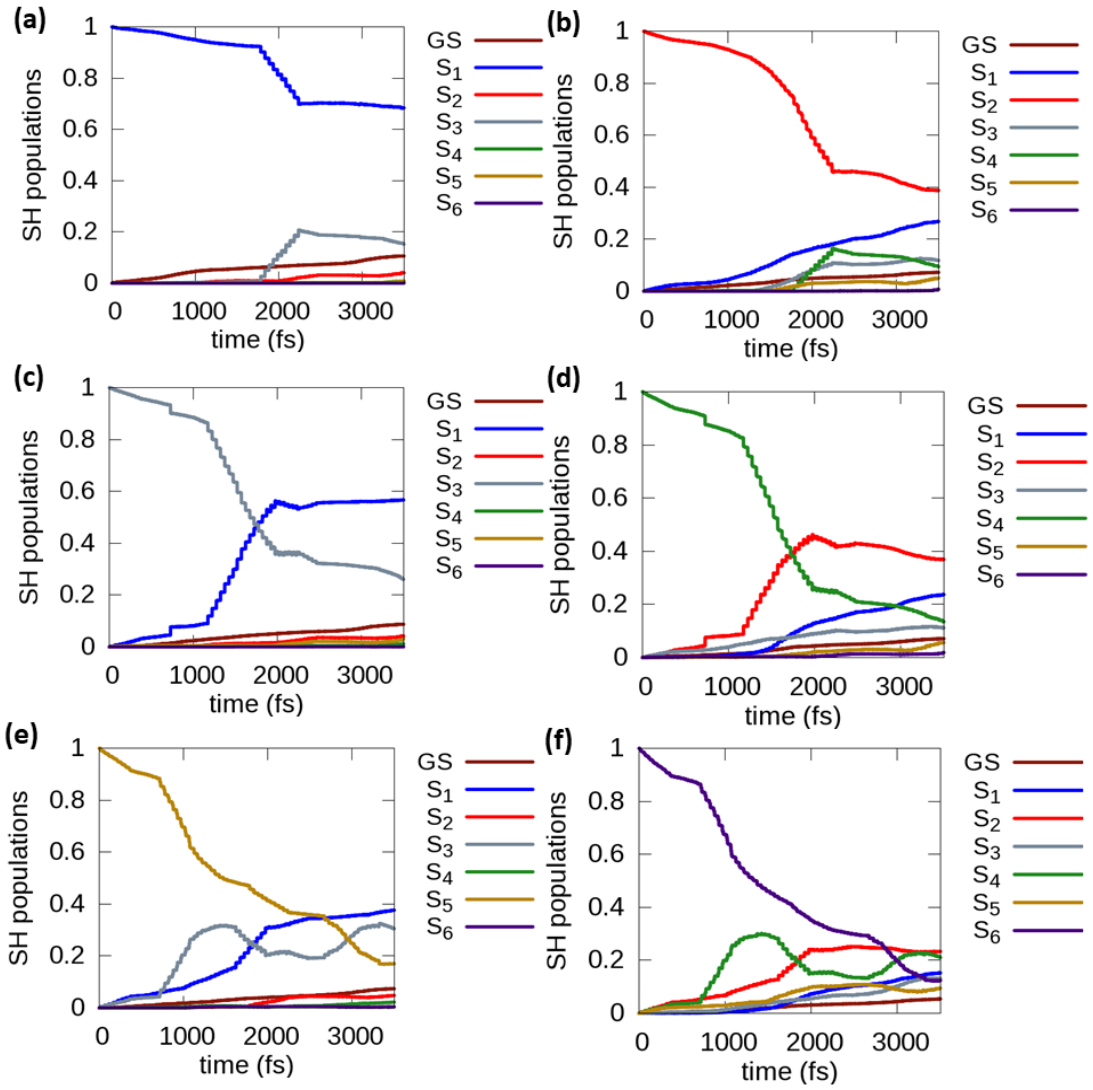

Figure 4.5 Evolution of the populations of the S_1, S_2, S_3, S_4, S_5, S_6 states (panels a-f, respectively) without the energy correction for $[Au_{25}(MPA)_{18}]^{-1}$.

Compared to the other ligated clusters, the MPA S_1-S_6 state relaxations show a "step-like relaxation" behavior as shown in Figure 4.5. In the MPA S_1 state relaxation (Figure 4.5a), the S_1 population relaxes to S_3 rapidly during the 1900-2400 fs time frame. To understand the relaxation further, we ran separate FSSH calculations on the ten different initial conditions for the S_1-S_6 states. The ten initial conditions differ by an offset of 50 fs. All ten relaxations of the S_1 state show a rapid population transfer from S_1 to S_3 at a time corresponding to the 2200-2300 fs time frame of the initial MD run. During the 2200-2300 fs time frame, the HOMO, HOMO-1, and HOMO-2 become close in energy (Figure 4.3). Moreover, the LUMO and LUMO+1 also

become close in energy at the same time. This could facilitate the rapid S_1 state population transfer to the S_3 state because the HOMO and HOMO-1 orbitals are degenerate at that time, so the S_1 and S_3 states are similarly degenerate. A similar explanation can be suggested for the S_3 and S_4 state step-like relaxations, as S_3(HOMO-1-LUMO) relaxes to the S_1(HOMO-LUMO) and S_4(HOMO-1-LUMO+1) relaxes to S_2(HOMO-LUMO+1). In both cases, the relaxation occurs during a similar time frame where one can notice the degenerate nature of the HOMO and HOMO-1 orbitals. The degenerate orbitals make the population transfer easier among the states involved.

4.4.1.2 Comparison of results for different ligands

It is important to note that the GS growth times computed for the ligands R= CH_3, C_2H_5, C_3H_7, MPA are shorter than the corresponding GS growth times from the SH system (Table 4.4 and Table B.2). This could be due to the presence of the S-C bond and its lower vibrational frequencies in the ligand systems instead of the S-H bond. Due to the complexity in determining the exact relaxation time constants using the GS growth times, we mainly focus on the excited state decay time constants.

Table 4.4 GS growth times calculated for ligated clusters "without" the energy correction.

Excited state	GS growth time (ps)				
	H[30]	**CH_3**	**C_2H_5**	**C_3H_7**	**MPA**
S_1	72	24	44	32	30
S_2	71	23	44	34	44
S_3	81	43	50	48	39
S_4	114	55	54	54	49
S_5	95	38	93	37	49
S_6	162	44	83	75	67

Table 4.5 summarizes the excited state decay time constants obtained for all ligated clusters including the H ligand.[30] It is important to note that the decay time constants obtained for e.g. the R=MPA S_1-S_6 states may not give the best values due to inherent error in fitting the "step relaxation" populations to an exponential decay. Very short excited state decay times on the picosecond time scale were observed for all ligated clusters; these excited state decay times

are much smaller than the corresponding GS growth times. Interestingly, all the ligand clusters including the H ligand model follow a similar trend of decay time constant variation with the six states as shown in Figure 4.6. In ethyl and MPA, the S_3 state does not show an increase in time constant compared to S_2. The slowest S_1 state decay time constant is obtained for the ethyl ligand. The decay time constants with the 0.55 eV correction are tabulated in Table B.3. The decay times give similar trends both without and with the energy correction.

Table 4.5 Decay times calculated for the ligated clusters. No energy correction is employed.

Excited state	Decay time (ps)				
	H^{30}	CH_3	C_2H_5	C_3H_7	MPA
S_1	15	12	19	13	9.2
S_2	3.1	5.9	7.3	5.1	4.2
S_3	3.0	7.6	4.3	4.5	2.8
S_4	1.9	4.7	2.9	2.7	2.2
S_5	2.5	4.5	3.6	2.2	2.3
S_6	1.9	4.5	2.8	1.9	2.1

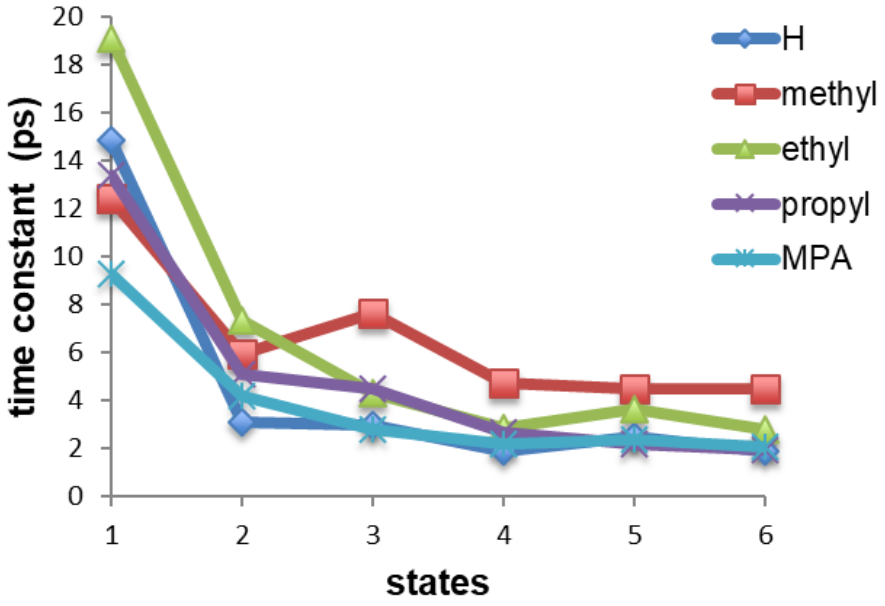

Figure 4.6 The decay time constant variations for six excited states S_N (N=1-6) with different ligands.

The ligated clusters studied in this section exhibit a first excited state peak around 1.30 – 1.41 eV in the calculated optical absorption spectra that falls near the energy range (~1.55 – 1.99

eV) of the probe pulse applied in the experimental work.[11] In the calculations in the current work, the first excited state peak in these ligated clusters arises from core to core transitions similar to the previous H ligand[30] model. This suggests that the time constants observed by Moran and co-workers could originate from core-to-core transitions and not from core-to-semiring transitions. The decay constants of the core states (S_1 to S_6) near the HOMO-LUMO gap in the ligated clusters studied in this section are all on the picosecond time scale which agrees well with the experimentally observed[11] time constants.

4.4.2 Relaxation dynamics of higher excited states in $[Au_{25}(SR)_{18}]^{-1}$

The relaxation dynamics of the higher excited states in the $[Au_{25}(SR)_{18}]^{-1}$ (R = CH_3, C_2H_5, C_3H_7, MPA) nanoclusters are analyzed in this section. Initial excitations corresponding to the peak around 2.20 eV were considered for all ligated clusters. We performed the analysis by identifying the most probable transitions with the highest oscillator strengths and transition dipole moments. The Au_{25} cluster with ligands R = CH_3, C_2H_5, C_3H_7 has HOMO-7 to LUMO+4 orbitals involved in the main transitions. The Au_{25} cluster with the MPA ligand yielded HOMO-9 to LUMO+6 orbitals that are involved in the main transitions.

All possible single particle transitions were considered for orbitals between HOMO-7 to LUMO+4 for the clusters with ligands R = CH_3, C_2H_5, C_3H_7. Even though the R = MPA cluster gave transitions involving HOMO-9 to LUMO+8 orbitals we limited the transitions to transitions involving HOMO-7 to LUMO+4 orbitals similar to the rest of the clusters for consistency. Therefore, we could define the same excited states for all nanoclusters to be considered in the FSSH calculations. These single particle transitions are shown in Table 4.6 while keeping the same transitions for S_1-S_6 in Table 4.1.

Table 4.6 Transitions considered for higher excited states.

Excited state	Transition	Excited state	Transition
S_7	HOMO → LUMO+2	**S_{24}**	HOMO-4 → LUMO+3
S_8	HOMO → LUMO+3	**S_{25}**	HOMO-4 → LUMO+4
S_9	HOMO → LUMO+4	**S_{26}**	HOMO-5 → LUMO
S_{10}	HOMO-1 → LUMO+2	**S_{27}**	HOMO-5 → LUMO+1
S_{11}	HOMO-1 → LUMO+3	**S_{28}**	HOMO-5 → LUMO+2

S_{12}	HOMO-1 → LUMO+4	**S_{29}**	HOMO-5 → LUMO+3
S_{13}	HOMO-2 → LUMO+2	**S_{30}**	HOMO-5 → LUMO+4
S_{14}	HOMO-2 → LUMO+3	**S_{31}**	HOMO-6 → LUMO
S_{15}	HOMO-2 → LUMO+4	**S_{32}**	HOMO-6 → LUMO+1
S_{16}	HOMO-3 → LUMO	**S_{33}**	HOMO-6 → LUMO+2
S_{17}	HOMO-3 → LUMO+1	**S_{34}**	HOMO-6 → LUMO+3
S_{18}	HOMO-3 → LUMO+2	**S_{35}**	HOMO-6 → LUMO+4
S_{19}	HOMO-3 → LUMO+3	**S_{36}**	HOMO-7 → LUMO
S_{20}	HOMO-3 → LUMO+4	**S_{37}**	HOMO-7 → LUMO+1
S_{21}	HOMO-4 → LUMO	**S_{38}**	HOMO-7 → LUMO+2
S_{22}	HOMO-4 → LUMO+1	**S_{39}**	HOMO-7 → LUMO+3
S_{23}	HOMO-4 → LUMO+2	**S_{40}**	HOMO-7 → LUMO+4

The population relaxation of states S_1 to S_6 is shown in the SI for the clusters with R = CH_3, C_2H_5, C_3H_7 (Figures B.8, B.9, B.10). The population relaxations of states S_1 to S_6 preserve similar relaxation patterns to those shown in Figures B.2, B.4, and B.6, respectively, with only minor changes when additional higher states are included in the calculations.

Compared to the decay times from the simulation in which only the S_1−S_6 states were considered, these states have similar decay times when additional higher excited states are considered for R = CH_3, C_2H_5, and C_3H_7 (Table B.4). Similar to the H model, the S_7 state has a distinctively long lifetime, comparable to that of the S_1 state for the R = CH_3, C_2H_5, C_3H_7, MPA cases. This likely arises because of a large energy gap between the S_7 and S_6 states, which makes population transfer more difficult. Depopulation of the other higher states (S_8 – S_{40}) occurs much faster than that of the S_1 state, on a time scale ranging from 0.4 to 4.1 ps (Table B.4).

However, the decay time constants of S_1-S_6 are shorter for the R = MPA cluster compared to the other clusters in the presence of higher excited states (Table B.4). With R = MPA, S_1 state population transfers to S_7 which is different from clusters with R = CH_3, C_2H_5, and C_3H_7. Furthermore, S_2 state population transfers to S_7 and then to S_1. The involvement of the S_7 state in S_1 and S_2 relaxations in the R = MPA cluster could be due to the change in the LUMO orbital energies during the MD run around 400 fs as mentioned earlier. The LUMO orbital energies lie much closer in energy for the MPA cluster compared to the other clusters. The S_1(HOMO-LUMO) population could transfer to S_7(HOMO-LUMO+2) due to the fact that LUMO and LUMO+2 become close in energy as shown by the orbital energy variation in Figure 4.3. In the

presence of the higher excited states, the "step-like relaxation" behavior in the S_1-S_6 states is less significant (Figure B.11). The S_1-S_6 states become closer in energy to the higher states (S_7-S_{11}) with the addition of the excited state correction. For example, with only the S_1-S_6 states present, the S_1 state relaxes to S_3 through a step-like relaxation. In the presence of higher states, the S_1 population transfers to S_7 instead of S_3. However, the energy difference between S_1-S_7 is larger than S_1-S_3. Therefore, the population transfer $S_1 \rightarrow S_7$ occurs less rapidly than $S_1 \rightarrow S_3$, which results in less "step-like" behavior. For R = MPA in the presence of higher excited states, the S_7 state gives a relatively slow decay time constant of 8.6 ps whereas the S_1 state yields the slowest decay of 10.7 ps.

Adding the energy correction to the first six states makes the S_1-S_6 states shift more towards the S_7. However, in R=MPA the energy gap between the LUMO+1 and LUMO+2 is less (Figure 4.3) compared to the other ligand systems considered here. Therefore, the shift in the S_1-S_6 states due to the correction is more sensitive in R=MPA than in the rest of the systems, and the population relaxations reflect this. Thus, we see the S_1 state population transfers mostly to S_7 when the correction is added. This could also be a reason why S_7 has a relatively long decay time constant with the correction. We also performed a relaxation calculation for R = MPA when no correction is added to the first six states in the presence of the higher excited states. There, we observed a similar trend of decay within the first six excited states. The S_1 decay constant is observed to be 17.4 ps and S_7 now yields a shorter decay constant of 5.1 ps. In the S_1 relaxation, the S_1 population is now mainly transferred to S_2 with only a very small amount transferred to S_7.

4.4.3 Separate electron and hole relaxations in $[Au_{25}(SCH_3)_{18}]^{-1}$

In this section we discuss separate electron and hole relaxation dynamics for the $[Au_{25}(SCH_3)_{18}]^{-1}$ nanocluster. The analysis was performed to understand how the electrons and holes could relax independently of each other in $[Au_{25}(SCH_3)_{18}]^{-1}$. In this calculation, we define the excited states for the FSSH-TDKS calculations (Table B.5) in a different order than we defined for the total relaxation dynamics performed in the previous section (Table 4.1, Table 4.6).

The S_1-S_5 states originate by exciting an electron from HOMO to the LUMO-LUMO+4 orbitals, leaving a hole in the HOMO. For clarity, a schematic diagram of orbital levels filled with electrons for the GS and S_1 to S_{40} is shown in Figure 4.7. We consider S_1-S_5 states as one set

of electron relaxations (with the same hole). Thus, the forty states (Table B.5) can be separated into eight different sets of electron relaxations which are: S_1-S_5, S_6-S_{10}, S_{11}-S_{15}, S_{16}-S_{20}, S_{21}-S_{25}, S_{26}-S_{30}, S_{31}-S_{35}, and S_{36}-S_{40}. Similarly, the hole relaxations can be separated into five sets. The first set consists of S_1, S_6, S_{11}, S_{21}, S_{26}, S_{31}, and S_{36}, in which the electron is excited into the same orbital (LUMO) while leaving a hole in the HOMO, HOMO-1, HOMO-2, …, and HOMO-7 orbitals, respectively. In the next four hole relaxation sets, the electron is excited into LUMO+1, LUMO+2, LUMO+3, and LUMO+4, respectively. Separate relaxation calculations were performed for the eight sets of electron relaxations and five sets of hole relaxations.

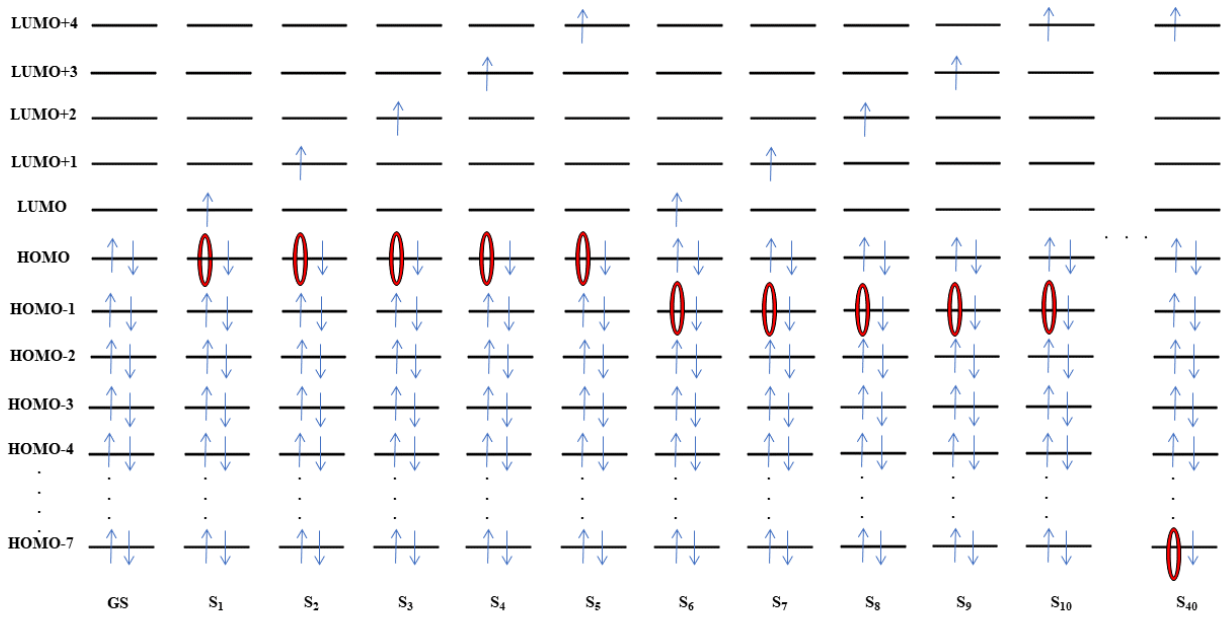

Figure 4.7 A schematic diagram of orbital levels filled with electrons for GS and S_1 to S_{40} states considered during the separate electron and hole relaxations.

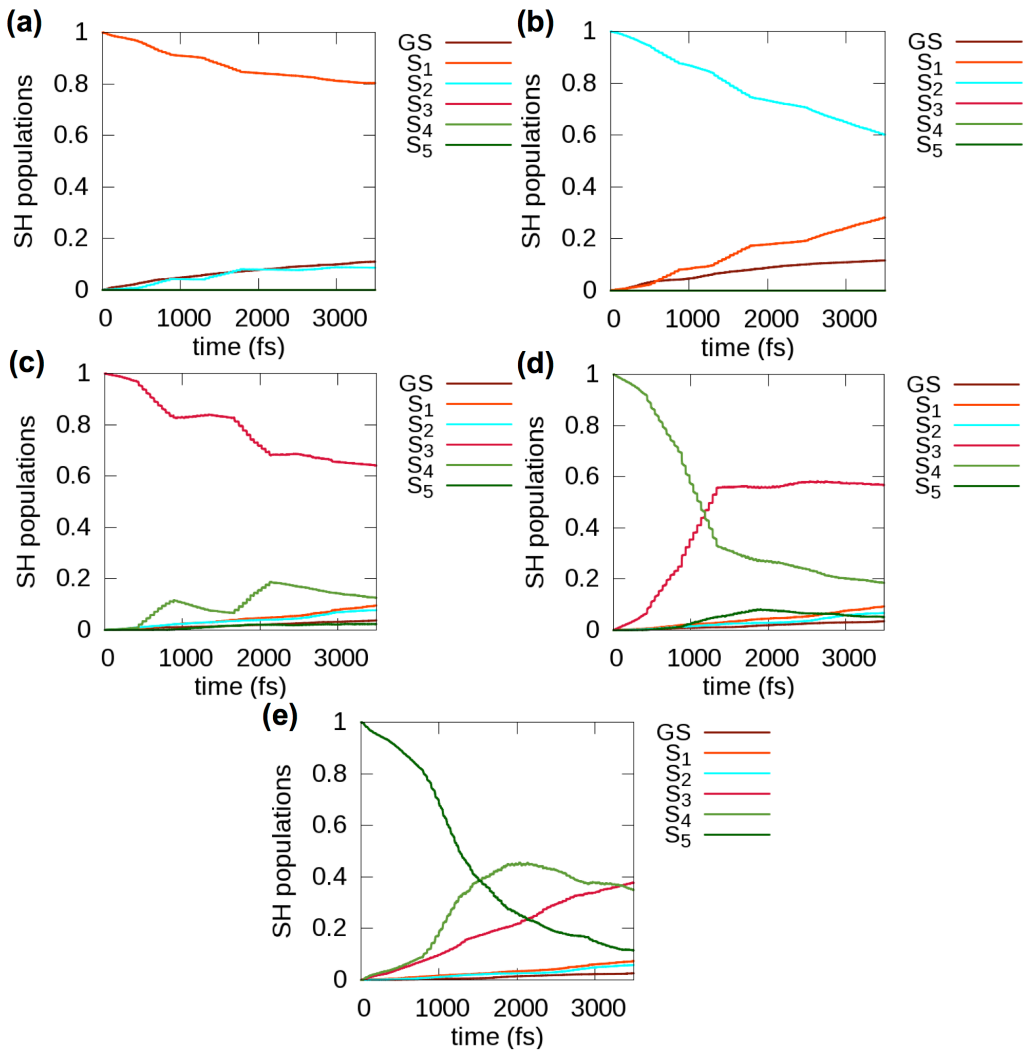

Figure 4.8 Evolution of the population initially excited into (a)S_1 (b)S_2 (c)S_3 (d)S_4 (e)S_5 during the first set of electron relaxations in $[Au_{25}(SCH_3)_{18}]^{-1}$.

The population relaxations of S_1-S_5 states in the first set of electron relaxation are shown in the Figure 4.8. Relaxations of states where the electron is excited to the LUMO (S_1, S_6, S_{11}, S_{16}, S_{21}, S_{26}, S_{31}, S_{36}) while the hole is held constant follow similar population relaxation patterns (Figure 4.8 and Figure B.12). Some of the initially excited S_1 population transfers into the higher energy S_2 state (Figure 4.8a). The S_2 population mainly transfer back to the S_1 state (Figure 4.8b) This can occur because the LUMO+1 and LUMO lie close in energy. Similar transfer of population from LUMO to LUMO+1 can occur regardless of the hole energy level (Figure B.12). One slight difference occurs with repopulation times for the GS. The S_1 state population relaxes to the GS much faster than S_{36} relaxes to the GS, which is expected because the S_1 state

population can easily transfer to the GS (the electron in the LUMO can fill the hole in the HOMO) whereas it is hard for the S_{36} population to transfer to the GS (the electron in the LUMO would need to fill a hole in the HOMO-7) due to the absence of intermediate states between the S_{36} and GS in this electron-only relaxation. Similar explanations can be given for the remainder of the electron relaxation simulations. Likewise, common population relaxation patterns were observed for the relaxations in which the electron is excited into LUMO+1 through LUMO+4 separately (not shown). The calculated decay constants when the electron is excited into LUMO through LUMO+4 for eight different simulations that differ based on the orbital where the hole is created are plotted in Figure 4.9 and the values are given in Table B.6. All eight electron relaxations follow similar relaxation trends regardless of where the hole is created. Decay constants for states where the electron is initially excited into the LUMO+3 and LUMO+4 orbitals are essentially constant because population transfer from these states is dominated by electron transfer into lower energy LUMOs (see Figure 4.8d, e). Their decay is faster (short time constants) as they have electron transfer to their nearby intermediate states. The decay from states where the electron is intially excited into LUMO+2 is also constant but with a slow decay due to the population is being mainly transferred to the next higher state (Figure 4.8c). This could be due to the large energy gap between the LUMO+1 and LUMO+2.

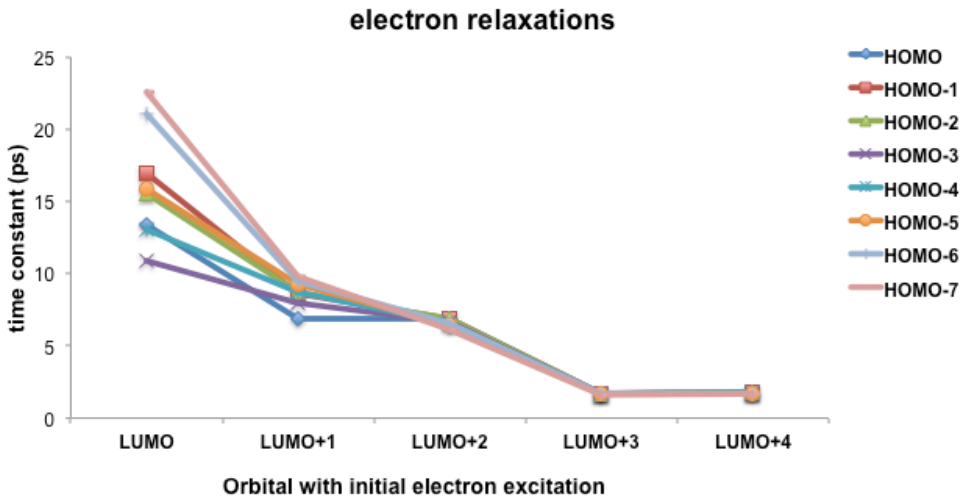

Figure 4.9 The decay constant trend variation among the five states of each electron relaxation. The legend gives the orbitals where the hole is created for each excitation; the hole is kept constant during each simulation.

The states initially excited into the LUMO is dominated by the energy difference between the LUMO and the HOMO-n orbital. The S_1 state can relax to GS faster while [S_6, S_{11}, S_{16}, S_{21}, S_{26}, S_{31}, S_{36}] cannot relax faster due to the absence of intermediate states in each electron relaxation set. Thus, they have different time constants. Same applies to the states where the electron is excited into LUMO+1. However, the time constants do not vary much to each other as they have some intermediate states to relax. Therefore, the electron relaxation trend is mainly decided based on their decay into other LUMOs as opposed to decay across the big HOMO(-n)-LUMO gap.

A similar analysis was performed for the hole relaxations. The population relaxations of states where the hole is created in the HOMO follow a similar population relaxation pattern regardless of the orbital into which the electron is excited (Figure B.13). Some of the initially excited S_1 population transfers into the higher energy S_6 state (Figure B.13). This can occur because the HOMO-1 and HOMO lie close in energy. Similar transfer of population from HOMO to HOMO-1 can occur regardless of the LUMO+n level occupied by the electron (Figure B.13). Similarly, relaxations of states where the hole is created in the HOMO-1 through HOMO-7 have similar relaxation patterns in their population transfer plots (not shown).

For repopulation of the ground state, S_1 and S_2 relax to the GS much faster than states S_3-S_5. It is easier for S_1 to relax to the GS than it is for S_3-S_5 to relax to the GS because an electron in the LUMO has a smaller energy difference for recombination with the hole in the HOMO during the S_1 decay to GS compared to an electron in the LUMO+2 to LUMO+4 recombining with a hole in the HOMO during S_3-S_5 decay to GS.

Figure 4.10 and Table B.7 give the decay constants for the simulations in which the hole is initially created in HOMO through HOMO-7; these simulations differ based on the orbital into which the electron is excited. The five hole relaxation simulations follow the same trends regardless of where the electron is excited into.

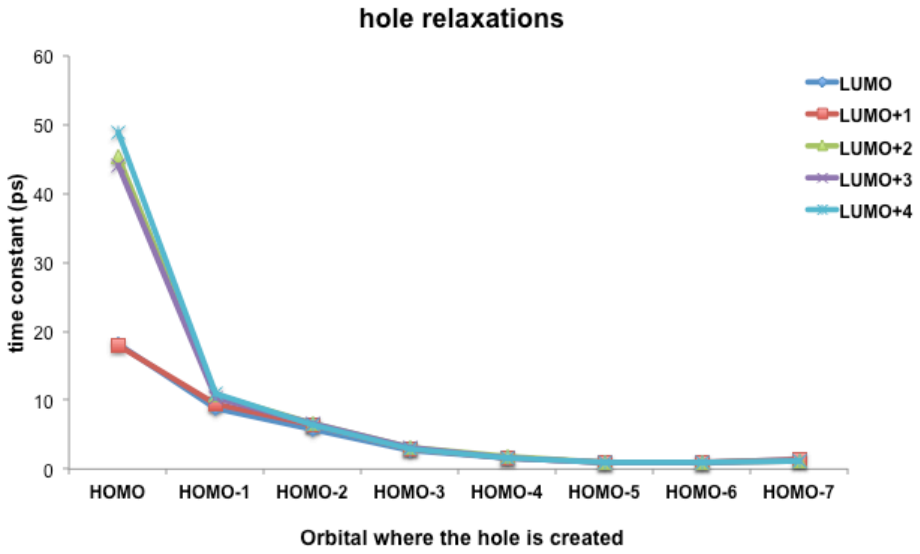

Figure 4.10 Decay constant trend variation among the eight states for each hole relaxation simulation. The legend gives the orbital where the electron is excited into; this excited electron is kept constant throughout each simulation.

The states where the hole is created in HOMO-3 through HOMO-7 have the same time constants regardless of the orbital into which the electron is excited. For the HOMO-3, the population mainly relax into the HOMO-2, HOMO-1, HOMO and some population is also transferred into the HOMO-4 and HOMO-5 as well. For HOMO-4 to HOMO-7, the main decay pathway is the population transfer into the lower HOMOs as they are the nearby intermediate states to relax. Due to this reason, the HOMO-3 decay time constants are slightly longer than those for HOMO-4 to HOMO-7. Thus, the hole relaxation trend for orbitals below the HOMO is decided by their decay into other HOMOs as opposed to decay across the big HOMO-LUMO(+n) gap.

The time constants of states where the hole is created in HOMO are different to each other. That is, S_1 and S_2 can relax to the GS faster while S_3-S_5 do not have intermediate states to relax. The same applies to the time constants of states where the hole is created in HOMO-1 or HOMO-2. However, their time constants do not vary much since all states have nearby intermediate states to relax.

These calculations were repeated a second time and the decay constants and curves did not change appreciably (Tables B.6 and B.7). The study confirms that all separate electron relaxations follow a similar trend while separate hole relaxations also follow a common trend.

It is evident that the hole relaxations when the hole is created in HOMO-3 through HOMO-7 are faster than the electron relaxations when the electron is excited into LUMO+2 through LUMO+4. This occurs because the HOMOs below HOMO-3 are more dense than the LUMO+2, LUMO+3 and LUMO+4 (Figure 4.2). However, the electron relaxations when the electron is excited into LUMO or LUMO+1 are comparable to or faster than the hole relaxations when the hole is created in HOMO, HOMO-1 and HOMO-2.

In order to compare the overall dynamics (Table B.4) with the separate electron and hole relaxations, we divided the overall dynamics into four sections based on the notable energy gaps between the LUMO+1 and LUMO+2, HOMO-2 and HOMO-3 in electronic structure. First, the HOMO-LUMO and HOMO-LUMO+1 overall relaxations are similar to the separate electron relaxations. Also, the relaxations of excitations from HOMO-1 and HOMO-2 to LUMO and LUMO+1 have shorter decay compared to the separate electron or hole relaxations. It suggests that overall dynamics of these states can arise from a mix of electron and hole relaxations. Secondly, relaxations of excitations out of HOMO-HOMO-2 to LUMO+2-LUMO+4 are similar to the respective separate electron relaxations. Next, the relaxations of the excitations out of HOMO-3-HOMO-7 to LUMO-LUMO+1 are similar to the respective separate hole relaxations. Then, the relaxations of the excitations out of HOMO-3-HOMO-7 to LUMO+2-LUMO+4 have shorter decay times compared to the separate electron or hole relaxations. This could be due to the mixed electron hole relaxations for these states.

4.5 Conclusion

The electronic relaxation dynamics in the cluster series, $[Au_{25}(SR)_{18}]^{-1}$ (R = CH_3, C_2H_5, C_3H_7, MPA) [MPA = mercaptopropanoic acid] were investigated using FSSH-TDKS method to understand the ligand effects on dynamics. During the MD simulation, electronic structure of R=MPA showed a smaller energy gap between the LUMO+1 and LUMO+2 compared to the rest of the systems including “SH” moldel. For the core states, the GS growth times of the ligand systems are smaller compared to the “SH” model. All the ligand clusters including “SH” follow a similar trend of decay times and the time constants are in range of 2-19 ps for the core states. Relaxation dynamics on the ligand systems further confirm that the time constants observed experimentally could originate from core-to-core transitions and not from core-to-semiring

transitions. The observed time constants are in picosecond time scale which agree with the experimental time scale.

In the presence of the higher excited states, ligand systems R= CH_3, C_2H_5 and C_3H_7 demonstrate similar relaxations in core states (S_1-S_6) compared to the case we only considered core states. The overall relaxation trend of R= CH_3, C_2H_5, C_3H_7 systems is similar our minimal "SH" model relaxations. In R=MPA, the relaxations of the core states showed slight differences in the presence of the higher states. The shift in the S_1-S_6 states by the energy correction could be more sensitive to the relaxations in R= MPA than in the rest of the systems due to the smaller LUMO+1-LUMO+2 gap in its electronic structure. This could be the reason for the involvement of S_7 state in S_1 and S_2 state relaxations for the R=MPA. However, the S_1 state possess the slowest decay (11-17 ps) while S_7 has a relatively longer decay (8-13 ps) in all ligated clusters.

In $[Au_{25}(SCH_3)_{18}]^{-1}$, the separate electron relaxation trend is decided by their decay into other LUMOs as opposed to decay across the big HOMO(-n)-LUMO gap whereas, separate hole relaxation trend is decided by their decay into other HOMOs as opposed to decay across the big HOMO-LUMO(+n) gap. The relaxations of excitations from lower HOMOs (HOMO-3 and lower) to core orbitals (LUMO, LUMO+1) are dominated by hole relaxations and relaxations of excitations from core orbitals (HOMO-HOMO-2) into higher LUMOs (LUMO+2 and above) are dominated by electron relaxations. Rest of the state relaxations are a mix of both electron and hole relaxations.

4.6 Acknowledgments

This material is based on work supported by Department of Energy under grant DE-SC0012273. The work on the $[Au_{25}(SR)_{18}]^{-1}$ (R = CH_3, C_2H_5, C_3H_7) was performed on the computing for this project was performed on the Beocat Research Cluster at Kansas State University, which is funded in part by NSF grants CHE-1726332, CNS-1006860, EPS-1006860, and EPS-0919443. and Extreme Science and Engineering Discovery Environment (XSEDE),[43] which is supported by National Science Foundation grant number ACI- 1053575. Beocat Application Scientist Dr. Dave Turner provided valuable technical expertise. The work on $[Au_{25}(SR)_{18}]^{-1}$ (R =MPA) used resources of the National Energy Research Scientific Computing Center, DOE Office of Science User Facility supported by the Office of Science of the U.S.

Department of Energy under Contract No. DE-AC02-05CH11231.The authors are grateful to Prof. Alexey V. Akimov for his support and valuable discussions on PYXAID.

4.7 References

1. Stamplecoskie, K. G.; Kamat, P. V., Size-dependent Excited State Behavior of Glutathione-capped Gold Clusters and Their Light-Harvesting Capacity. *J. Am. Chem. Soc.* **2014,** *136* (31), 11093-11099.

2. Stamplecoskie, K. G.; Chen, Y.-S.; Kamat, P. V., Excited-state Behavior of Luminescent Glutathione-Protected Gold Clusters. *J. Phys. Chem. C* **2014,** *118* (2), 1370-1376.

3. Chen, Y.-S.; Choi, H.; Kamat, P. V., Metal-cluster-sensitized Solar Cells. A New Class of Thiolated Gold Sensitizers Delivering Efficiency Greater than 2%. *J. Am. Chem. Soc.* **2013,** *135* (24), 8822-8825.

4. Kogo, A.; Sakai, N.; Tatsuma, T., Photocatalysis of Au_{25}-modified TiO_2 Under Visible and Near Infrared Light. *Electrochem. Commun.* **2010,** *12* (7), 996-999.

5. Kogo, A.; Sakai, N.; Tatsuma, T., Photoelectrochemical Analysis of Size-dependent Electronic Structures of Gold Clusters Supported on TiO_2. *Nanoscale* **2012,** *4* (14), 4217-4221.

6. Yu, C.; Li, G.; Kumar, S.; Kawasaki, H.; Jin, R., Stable $Au_{250}(SR)_{18}/TiO_2$ Composite Nanostructure with Enhanced Visible Light Photocatalytic Activity. *J. Phys. Chem. Lett.* **2013,** *4* (17), 2847-2852.

7. Schaaff, T. G.; Whetten, R. L., Giant Gold−Glutathione Cluster Compounds: Intense Optical Activity in Metal-based Transitions. *The Journal of Physical Chemistry B* **2000,** *104* (12), 2630-2641.

8. Link, S.; Beeby, A.; FitzGerald, S.; El-Sayed, M. A.; Schaaff, T. G.; Whetten, R. L., Visible to Infrared Luminescence from a 28-atom Gold Cluster. *The Journal of Physical Chemistry B* **2002,** *106* (13), 3410-3415.

9. Link, S.; El-Sayed, M. A.; Schaaff, T. G.; Whetten, R. L., Transition from Nanoparticle to Molecular Behavior: A Femtosecond Transient Absorption Study of a Size-Selected 28 Atom Gold Cluster. *Chem. Phys. Lett.* **2002,** *356* (3), 240-246.

10. Lee, D.; Donkers, R. L.; Wang, G.; Harper, A. S.; Murray, R. W., Electrochemistry and optical absorbance and luminescence of molecule-like Au_{38} nanoparticles. *J. Am. Chem. Soc.* **2004,** *126* (19), 6193-6199.

11. Miller, S. A.; Womick, J. M.; Parker, J. F.; Murray, R. W.; Moran, A. M., Femtosecond Relaxation Dynamics of $Au_{25}L_{18}^-$ Monolayer-Protected Clusters. *J. Phys. Chem. C* **2009,** *113* (22), 9440-9444.

12. Heaven, M. W.; Dass, A.; White, P. S.; Holt, K. M.; Murray, R. W., Crystal Structure of the Gold Nanoparticle $[N(C_8H_{17})_4][Au_{25}(SCH_2CH_2Ph)_{18}]$. *J. Am. Chem. Soc.* **2008,** *130* (12), 3754-3755.

13. Zhu, M.; Aikens, C. M.; Hollander, F. J.; Schatz, G. C.; Jin, R., Correlating the Crystal Structure of a Thiol-protected Au_{25} Cluster and Optical Properties. *J. Am. Chem. Soc.* **2008,** *130* (18), 5883-5885.

14. Aikens, C. M., Geometric and electronic structure of $Au_{25}(SPhX)_{18}^-$(X= H, F, Cl, Br, CH_3, and OCH_3). *J. Phys. Chem. Lett.* **2010,** *1* (17), 2594-2599.

15. Parker, J. F.; Kacprzak, K. A.; Lopez-Acevedo, O.; Häkkinen, H.; Murray, R. W., Experimental and Density Functional Theory Analysis of Serial Introductions of Electron-Withdrawing Ligands into the Ligand Shell of a Thiolate-Protected Au_{25} Nanoparticle. *J. Phys. Chem. C* **2010,** *114* (18), 8276-8281.

16. Guo, R.; Murray, R. W., Substituent effects on redox potentials and optical gap energies of molecule-like $Au_{38}(SPhX)_{24}$ nanoparticles. *J. Am. Chem. Soc.* **2005,** *127* (34), 12140-12143.

17. Akola, J.; Kacprzak, K. A.; Lopez-Acevedo, O.; Walter, M.; Grönbeck, H.; Häkkinen, H., Thiolate-protected Au_{25} superatoms as building blocks: dimers and crystals. *J. Phys. Chem. C* **2010,** *114* (38), 15986-15994.

18. Jung, J.; Kang, S.; Han, Y.-K., Ligand Effects on the Stability of Thiol-stabilized Gold Nanoclusters: $Au_{25}(SR)_{18}^-$, $Au_{38}(SR)_{24}$, and $Au_{102}(SR)_{44}$. *Nanoscale* **2012,** *4* (14), 4206-4210.

19. Li, G.; Jiang, D.-e.; Liu, C.; Yu, C.; Jin, R., Oxide-supported atomically precise gold nanocluster for catalyzing Sonogashira cross-coupling. *Journal of catalysis* **2013,** *306*, 177-183.

20. Mathew, A.; Natarajan, G.; Lehtovaara, L.; Häkkinen, H.; Kumar, R. M.; Subramanian, V.; Jaleel, A.; Pradeep, T., Supramolecular Functionalization and Concomitant Enhancement in Properties of Au_{25} Clusters. *ACS Nano* **2013,** *8* (1), 139-152.

21. Jupally, V. R.; Kota, R.; Dornshuld, E. V.; Mattern, D. L.; Tschumper, G. S.; Jiang, D.-e.; Dass, A., Interstaple Dithiol Cross-linking in $Au_{25}(SR)_{18}$ Nanomolecules: A Combined Mass Spectrometric and Computational Study. *J. Am. Chem. Soc.* **2011,** *133* (50), 20258-20266.

22. Dainese, T.; Antonello, S.; Gascón, J. A.; Pan, F.; Perera, N. V.; Ruzzi, M.; Venzo, A.; Zoleo, A.; Rissanen, K.; Maran, F., $Au_{25}(SEt)_{18}$, a Nearly Naked Thiolate-protected Au_{25} cluster: Structural Analysis by Single Crystal X-ray Crystallography and Electron Nuclear Double Resonance. *ACS Nano* **2014,** *8* (4), 3904-3912.

23. Stoll, T.; Sgrò, E.; Jarrett, J. W.; Réhault, J.; Oriana, A.; Sala, L.; Branchi, F.; Cerullo, G.; Knappenberger Jr, K. L., Superatom State-resolved Dynamics of the $Au_{25}(SC_8H_9)_{18}^-$Cluster from Two-dimensional Electronic Spectroscopy. *J. Am. Chem. Soc* **2016,** *138* (6), 1788-1791.

24. Fernando, A.; Weerawardene, K. D. M.; Karimova, N. V.; Aikens, C. M., Quantum Mechanical Studies of Large Metal, Metal Oxide, and Metal Chalcogenide Nanoparticles and Clusters. *Chemical reviews* **2015,** *115* (12), 6112-6216.

25. Jin, R.; Zeng, C.; Zhou, M.; Chen, Y., Atomically Precise Colloidal Metal Nanoclusters and Nanoparticles: Fundamentals and Opportunities. *Chemical reviews* **2016,** *116* (18), 10346-10413.

26. Devadas, M. S.; Kim, J.; Sinn, E.; Lee, D.; Goodson III, T.; Ramakrishna, G., Unique Ultrafast Visible Luminescence in Monolayer-Protected Au_{25} Clusters. *J. Phys. Chem. C* **2010,** *114* (51), 22417-22423.

27. Green, T. D.; Yi, C.; Zeng, C.; Jin, R.; McGill, S.; Knappenberger, K. L., Temperature-Dependent Photoluminescence of Structurally-Precise Quantum-Confined $Au_{25}(SC_8H_9)_{18}$ and $Au_{38}(SC_{12}H_{25})_{24}$ Metal Nanoparticles. *J. Phys. Chem. A* **2014,** *118* (45), 10611-10621.

28. Yau, S. H.; Varnavski, O.; Goodson III, T., An Ultrafast Look at Au Nanoclusters. *Acc. Chem. Res* **2013,** *46* (7), 1506-1516.

29. Yi, C.; Zheng, H.; Herbert, P. J.; Chen, Y.; Jin, R.; Knappenberger Jr, K. L., Ligand-and Solvent-Dependent Electronic Relaxation Dynamics of $Au_{25}(SR)_{18}^{-}$ Monolayer-Protected Clusters. *J. Phys. Chem. C* **2017,** *121* (44), 24894-24902.

30. Senanayake, R. D.; Akimov, A. V.; Aikens, C. M., Theoretical Investigation of Electron and Nuclear Dynamics in the $[Au_{25}(SH)_{18}]^{-1}$ Thiolate-Protected Gold Nanocluster. *J. Phys. Chem. C* **2016,** *121* (20), 10653-10662.

31. Chen, X.; Prezhdo, O. V.; Ma, Z.; Hou, T.; Guo, Z.; Li, Y., Ab initio phonon-coupled nonadiabatic relaxation dynamics of $[Au_{25}(SH)_{18}]^{-}$ clusters. *physica status solidi (b)* **2016,** *253* (3), 458-462.

32. Subramanian, V.; Wolf, E. E.; Kamat, P. V., Catalysis with TiO_2/gold Nanocomposites. Effect of Metal Particle Size on the Fermi Level Equilibration. *J. Am. Chem. Soc.* **2004,** *126* (15), 4943-4950.

33. Tully, J., Mixed Quantum–classical Dynamics. *Faraday Discuss.* **1998,** *110*, 407-419.

34. Craig, C. F.; Duncan, W. R.; Prezhdo, O. V., Trajectory Surface Hopping in the Time-dependent Kohn-Sham Approach for Electron-nuclear Dynamics. *Phys. Rev. Lett.* **2005,** *95* (16), 163001.

35. Jaeger, H. M.; Fischer, S.; Prezhdo, O. V., Decoherence-induced Surface Hopping. *J. Chem. Phys.* **2012,** *137* (22), 22A545.

36. Akimov, A. V.; Prezhdo, O. V., The PYXAID Program for Non-adiabatic Molecular Dynamics in Condensed Matter Systems. *J. Chem. Theory Comput.* **2013,** *9* (11), 4959-4972.

37. Akimov, A. V.; Prezhdo, O. V., Advanced Capabilities of the PYXAID Program: Integration Schemes, Decoherence Effects, Multiexcitonic States, and Field-Matter Interaction. *J. Chem. Theory Comput.* **2014,** *10* (2), 789-804.

38. Perdew, J. P.; Burke, K.; Ernzerhof, M., Generalized Gradient Approximation Made Simple. *Phys. Rev. Lett.* **1996,** *77* (18), 3865.

39. Te Velde, G. t.; Bickelhaupt, F. M.; Baerends, E. J.; Fonseca Guerra, C.; van Gisbergen, S. J.; Snijders, J. G.; Ziegler, T., Chemistry with ADF. *J. Comput. Chem.* **2001,** *22* (9), 931-967.

40. Lenthe, E. v.; Baerends, E.-J.; Snijders, J. G., Relativistic Regular Two-Component Hamiltonians. *J. Chem. Phys.* **1993,** *99* (6), 4597-4610.

41. Kresse, G.; Furthmüller, J., Efficiency of Ab-initio Total Energy Calculations for Metals and Semiconductors Using a Plane-wave Basis Set. *Comput. Mater. Sci* **1996,** *6* (1), 15-50.

42. Kresse, G.; Joubert, D., From Ultrasoft Pseudopotentials to the Projector Augmented-wave Method. *Phys. Rev. B* **1999,** *59* (3), 1758.

43. Towns, J.; Cockerill, T.; Dahan, M.; Foster, I.; Gaither, K.; Grimshaw, A.; Hazlewood, V.; Lathrop, S.; Lifka, D.; Peterson, G. D., XSEDE: Accelerating Scientific Discovery. *Computing in Science & Engineering* **2014,** *16* (5), 62-74.

Chapter 5 - Theoretical Investigation of Relaxation Dynamics in the $Au_{18}(SH)_{14}$ Thiolate-protected Gold Nanocluster

5.1 Abstract

Experimental findings of $Au_{18}(GSH)_{14}$ as a photosensitizer with the highest potential compared to the several other glutathione-protected clusters (Au_{25}, Au_{15}, Au_{10-12}) demand understanding the photo-physics and relaxation dynamics of the $Au_{18}(SR)_{14}$ cluster. To this end, we perform ab initio real-time nonadiabatic molecular dynamics (NA-MD) simulations on the $Au_{18}(SH)_{14}$ to investigate its relaxation dynamics compared to the well-studied $[Au_{25}(SR)_{18}]^{-1}$ relaxation dynamics. In this work, the important excitations covering up to ~ 2.6 eV in the optical absorption spectrum are analyzed to understand the electronic relaxation process of the $Au_{18}(SH)_{14}$ cluster. The GS growth time and decay time constants are not changed significantly with the addition of the 0.3 eV energy correction to the excited states which is used to compensate the underestimation of the DFT band gap. The GS growth times of the $Au_{18}(SH)_{14}$ are several orders of magnitude shorter than the growth times observed for the $[Au_{25}(SH)_{18}]^{-1}$ nanocluster. The S_1(HOMO→LUMO) state gives the slowest decay time (~11 ps) among all the states (S_1-S_{30}) considered similar to Au_{25} cluster. However, the S_1 state in $Au_{18}(SH)_{14}$ is a semiring to core charge transfer state whereas the S_1 in the Au_{25} cluster is a core to core transitions. Rest of the higher states have very short decay time constants less than 1.4 ps except for S_2 which has the second slowest decay of 6.4 ps. The hole relaxations are faster than the electron relaxations in $Au_{18}(SH)_{14}$ cluster due to the closely packed HOMOs in the electronic structure.

5.2 Introduction

Over the past decades, thiolate-protected gold nanoclusters have been of great interest due their applications in chemical sensing,[1] catalysis[2-3] and in bio applications.[4] Unlike larger metal nanoclusters, smaller nanoclusters play an important role due to their size dependent properties.[4-5] Metal nanoclusters with smaller numbers of electrons, such as 2 or 4 free electrons,[6-7] can bridge the link between metal complexes and metal nanoclusters. During the

past few year, various sizes of thiolate-protected gold nanoclusters with different core:ligand ratios have been determined by X-ray crystallography.[8-9] Among them, Au_{25},[10-12] Au_{38}[13] and Au_{20}[14] are some of the small thiolate-protected gold nanoclusters that have been studied extensively.

Among the smallest monolayer-protected nanoclusters, the $Au_{15}(SR)_{13}$ and $Au_{18}(SR)_{14}$ nanoclusters have been identified as the most stable clusters that have 2 and 4 valence electrons respectively.[15-17] The $Au_{18}(SR)_{14}$ nanocluster is the smallest stable member of the "isoelectronic" 4 electron family.[18] Many experimental[19-22] and theoretical[15] studies have been performed to identify the $Au_{18}(SR)_{14}$ nanostructure. Using density functional theory (DFT), Tlahuice and Garzon theoretically predicted a $Au_{18}(SR)_{14}$ structure[15] with prolate bi-tetrahedral Au_8 core protected by two dimer and two trimer [Au(SR)] semiring motifs. However, in 2015, the experimental groups of Jin and Zhu independently crystallized the $Au_{18}(SR)_{14}$ nanocluster.[18, 23] Both experiments obtained a similar geometric structure. Their resolved geometry is a charge neutral cluster that has a face-fused Au_9 bi-octahedral core where the core is protected by semiring motifs consisting of one $Au_4(SR)_5$ tetramer, one $Au_2(SR)_3$ dimer and three $Au(SR)_2$ monomers. This Au_9 core has a +5 charge according to the superatom network model.[24] Here, the core structure can be viewed as a network of tetrahedral Au_4 superatoms. The Au_9 core is larger than the Au_7 and Au_8 cores of $Au_{20}(SR)_{16}$ and $Au_{24}(SR)_{20}$, respectively,[18, 23] where $Au_{20}(SR)_{16}$ and $Au_{24}(SR)_{20}$ are other members of the "isoelectronic" 4e nanocluster family. In $Au_{18}(SR)_{14}$, strong interactions between the core and the rings (strong Au_{core}-$Au_{semiring}$ bonds) have been reported.[18] Zhu and coworkers found that the ligand does not affect the geometric structure of this cluster.[18]

In addition to unique structures, thiolate-protected gold clusters also have size-dependent excited state properties;[11, 15, 25-28] their optical properties such as absorption and emission vary for each cluster. The number of the gold atoms in the core, metal atom-to-thiol ratio, and the oxidation state of the metal core have significant effects on these optical properties.[11, 28-29] Various thiolate-protected gold clusters have been studied for water splitting[30] and solar cell[31-32] applications and these systems demonstrate different photocatalytic activity depending on the size and stoichiometry of the clusters. In 2014, Kamat and coworkers performed ultrafast femtosecond transient absorption spectroscopy and nanosecond transient absorption spectroscopy to explore the excited state behavior of several glutathione-protected clusters.[33]

They demonstrated an increasing photocatalytic reduction yield with decreasing cluster size in the order of $Au_{25}(GSH)_{18}$ < $Au_{18}(GSH)_{14}$ < $Au_{15}(GSH)_{13}$ < $Au_{10\text{-}12}(GSH)_{10\text{-}12}$. According to their investigation, $Au_{18}(GSH)_{14}$ was found to be the photosensitizer with the highest potential based on its good visible light absorption properties and the quantum yield of electron transfer (~4%).[33] They probed the photoinduced electron transfer process using methyl viologen as the electron acceptor. This observation has been further confirmed in a different study by Bang and co-workers where they reported a power conversion efficiency of 3.8% for $Au_{18}(GSH)_{14}$ in a gold nanocluster-sensitized solar cell.[34]

Due to its potential applications, it is important to understand the photo-physics and electronic relaxations of this $Au_{18}(SR)_{14}$ cluster. Comparing the relaxation dynamics of $Au_{18}(SR)_{14}$ with the well-studied $[Au_{25}(SR)_{18}]^{-1}$ relaxation dynamics,[29, 35-37] will provide insights on how dynamics vary based on the nanocluster composition.

Herein, we have performed a systematic theoretical study to understand the electron−nuclear dynamics of the $Au_{18}(SR)_{14}$ nanoparticle, elucidate the physical principles behind the dynamics, and give insights about the mechanism of electron relaxation in comparison to the well-known $[Au_{25}(SR)_{18}]^{-1}$ cluster. Eventually, the relaxation mechanisms of different sized gold clusters will be well tuned for future photocatalytic and light harvesting applications.

5.3 Computational methodology

We have performed ab initio real-time nonadiabatic molecular dynamics (NA-MD) simulations to study the electronic relaxation dynamics in the $Au_{18}(SR)_{14}$ nanocluster The NA-MD simulations were performed using the fewest switches surface hopping (FSSH)[38] algorithm with the classical path approximation and a time-dependent Kohn−Sham description of electronic states (FSSH-TDKS).[39] The overcoherent nature of the FSSH approach is corrected by the decoherence-induced surface hopping (DISH)[40] scheme. The FSSH-TDKS simulations are performed using the PYXAID program.[41-42]

The computational methodology has several steps, which are summarized briefly in this section. $Au_{18}(SR)_{14}$ nanocluster geometry optimization was performed with the PBE[43]/TZP level of theory in the Amsterdam Density Functional (ADF)[44] software package to obtain the relaxed geometry at 0K. The zero-order regular approximation (ZORA)[45] was used to treat the scalar

relativistic effects in gold. Linear response time-dependent density functional theory (TD-DFT) calculations were performed using the same level of theory to get the electronic excitations and the relevant absorption spectra of $Au_{18}(SH)_{14}$. The ADF GUI was used to plot the orbitals.

Then, the 0K systems was thermalized through a temperature ramping calculation performed at 300K in the Vienna Ab initio Simulation Package (VASP).[46] After the temperature ramping, molecular dynamics (MD) simulations were performed. We used projector-augmented wave[47] pseudopotentials, a kinetic energy cutoff value of 402.0 eV, a 24 Å simulation box size, gamma points, and the PBE functional in all of our VASP calculations. A MD trajectory of 5 ps in length was computed with an integration time step of 1 fs.

The nonadiabatic coupling elements were calculated following the same approach we used for the $[Au_{25}(SH)_{18}]^{-1}$ system.[37] The NA-MD calculations were performed considering 3.5 ps length sub-trajectories resulting in 10 different starting geometries. For each NA-MD trajectory, 1000 realizations of the stochastic FSSH/DISH state hopping trajectories were considered.

The important electronic excited states contributing to the optical absorption spectrum of $Au_{18}(SH)_{14}$ in the energy range of 0.00−2.60 eV (visible range) were analyzed. An energy correction was considered for several excited states in order to evaluate the impact of the energy correction for the dynamics as opposed to "without" energy correction. These corrections are used to compensate for underestimation/overestimation in the calculated DFT band gaps compared to the experimental gaps. The decay times of the excited states populations and the ground state population increase times were calculated for the $Au_{18}(SR)_{14}$ nanocluster using the same equations and procedure[37] mentioned in our previous study.

5.4 Results and discussion

The calculated absorption spectrum for the $Au_{18}(SH)_{14}$ nanocluster at the PBE/TZP level of theory is shown in Figure 5.1. The spectrum exhibits significant peaks around 1.82, 2.02, 2.16, 2.37, 2.73 and 3.50 eV in the energy range of 0-3.5 eV. The peak positions are redshifted compared to the peaks observed in the experimental UV-vis absorption spectra of $Au_{18}(SC_6H_{11})_{14}$, which were reported to lie around 1.97, 2.18 and 2.76 eV by Jin and co-workers[23] and at 1.94, 2.14, 2.70 and 3.26 eV by Zhu and co-workers.[18] The first two PBE/TZP peaks are redshifted by a value of ~0.16 eV compared to the experimental peaks. A similar

redshift (0.22 eV) was also previously calculated at the BP86/double-ζ valence plus polarization level of theory.[23] Related DFT calculations (PBE/TZP with ZORA level of theory) reported for the R=CH_3 ligand qualitatively agree with these results, with a similar redshift calculated for the second peak compared to the theoretical spectrum reported here.[18] Overall, a good agreement in the absorption spectrum is achieved for the theoretical calculations compared to experiment considering the typical red-shifts.

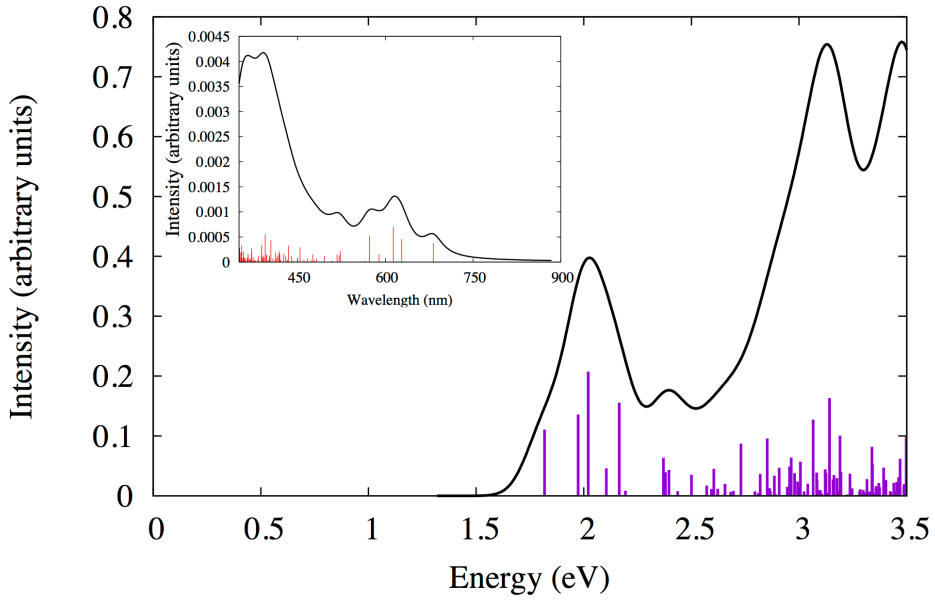

Figure 5.1 Calculated PBE/TZP optical absorption spectrum for $Au_{18}(SH)_{14}$ cluster (in eV). Inset: The absorption spectrum in wavelength (nm).

Table 5.1 Transitions with the highest weights for the prominent excited states arising from the TDDFT calculation for $Au_{18}(SH)_{14}$.

Excited State	Energy (eV)	Oscillator strength	Weight	Most weighted transitions
1	1.82	0.0235	0.8338	HOMO → LUMO
			0.1187	HOMO-1 → LUMO
2	1.97	0.0289	0.5042	HOMO-1 → LUMO
			0.4045	HOMO-2 → LUMO
			0.0425	HOMO → LUMO
			0.0151	HOMO-3 → LUMO
3	2.02	0.0442	0.5503	HOMO-2 → LUMO
			0.2698	HOMO-1 → LUMO
			0.0677	HOMO-3 → LUMO
			0.0476	HOMO → LUMO

			0.0269	HOMO-4 → LUMO
5	2.16	0.0331	0.7262	HOMO-4 → LUMO
			0.1243	HOMO-3 → LUMO
			0.0534	HOMO → LUMO+1
			0.0364	HOMO-1 → LUMO
			0.0142	HOMO-2 → LUMO
			0.0129	HOMO → LUMO
			0.0121	HOMO-5 → LUMO
7	2.37	0.0135	0.7776	HOMO-5 → LUMO
			0.1757	HOMO-6 → LUMO
			0.0121	HOMO-1 → LUMO+1
			0.0062	HOMO-1 → LUMO
			0.0057	HOMO-11 → LUMO
8	2.38	0.0084	0.7948	HOMO → LUMO+2
9	2.40	0.0092	0.6602	HOMO-6 → LUMO
			0.1488	HOMO-5 → LUMO
			0.0877	HOMO → LUMO+2
12	2.50	0.0075	0.418	HOMO-1 → LUMO+1
			0.2837	HOMO-2 → LUMO+1
15	2.60	0.0096	0.3249	HOMO-3 → LUMO+1
			0.2476	HOMO-1 → LUMO+2
21	2.73	0.0186	0.7765	HOMO-2 → LUMO+2
			0.0763	HOMO-3 → LUMO+2
			0.0338	HOMO-12 → LUMO
			0.0163	HOMO-4 → LUMO+2
			0.0109	HOMO → LUMO+5

5.4.1 Relaxation dynamics of the excited state peaks up to ~ 2.6 eV

In this study, we analyze the excitations up to ~ 2.6 eV in the optical absorption spectrum in order to understand the electronic relaxation processes occurring in the $Au_{18}(SH)_{14}$ cluster. The HOMO-6 to LUMO+2 orbitals are mainly involved in the most probable transitions for the excitations covering the 0-2.6 eV energy range (Table 5.1).

The electronic structure of the $Au_{18}(SH)_{14}$ is different from the well-studied $[Au_{25}(SH)_{18}]^{-1}$ cluster. In Au_{25}, it has previously been shown that there is a nearly doubly degenerate LUMO and a nearly triply degenerate HOMO orbital that are involved in the most probable transitions responsible for the first peak (~ 1.52 eV) that appears in the absorption spectrum. These HOMO→LUMO transitions were considered to be core-core transitions due to the localization of the HOMO and LUMO orbitals primarily in the Au_{13} core of $[Au_{25}(SH)_{18}]^{-1}$.[11] However, the $Au_{18}(SH)_{14}$ cluster demonstrates non-degenerate HOMO or LUMO orbitals

(Figure 5.2). The HOMO orbital extends over to the semiring of this cluster, whereas the LUMO is localized on the three layers of the Au_9 core. In $Au_{18}(SH)_{14}$, the single HOMO → LUMO transition (Table 5.1) is the main transition responsible for the peak appearing around 1.82 eV (~1.97 eV experimental peak) which was also observed in previous theoretical calculations.[23] As shown in Figure 5.2, the (HOMO-3, HOMO-4) and (HOMO-8, HOMO-9) sets are nearly doubly degenerate while the HOMO-5, HOMO-6, and HOMO-7 are nearly triply degenerate. The excitations up to ~2.6 eV involve HOMO-6 to LUMO+2 orbitals, and we will consider excited states involving HOMO-9 to LUMO+2 for a better picture of the electron relaxation dynamics.

Table 5.2 gives thirty excited states defined for the FSSH-TDKS calculations to deduce the relaxation dynamics of the $Au_{18}(SH)_{14}$ cluster. It should be noted that the excited states from the TDDFT calculation (Table 5.1) appear slightly different from the states that we define for use in the FSSH-TDKS (Table 5.2). Single Slater determinants are considered for the FSSH-TDKS calculations while TDDFT calculations provide a linear combination of transitions responsible for each excited state.

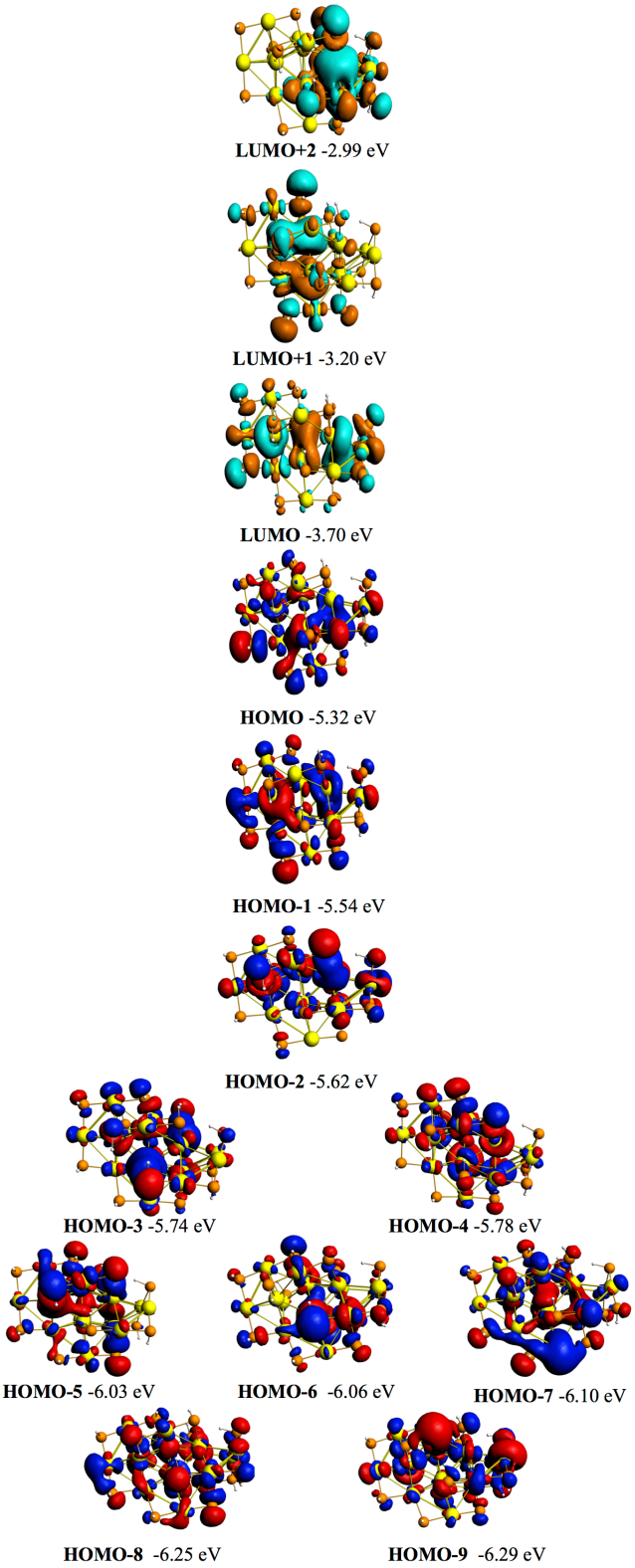

Figure 5.2 PBE/TZP orbitals near the HOMO−LUMO gap and their relative energies (in eV) for the $Au_{18}(SH)_{14}$ cluster.

Table 5.2 Excited states and corresponding transitions used in the FSSH-TDKS calculations.

Excited state	Transitions
S_1	HOMO → LUMO
S_2	HOMO → LUMO+1
S_3	HOMO → LUMO+2
S_4	HOMO-1 → LUMO
S_5	HOMO-1 → LUMO+1
S_6	HOMO-1 → LUMO+2
S_7	HOMO-2 → LUMO
S_8	HOMO-2 → LUMO+1
S_9	HOMO-2 → LUMO+2
S_{10}	HOMO-3 → LUMO
S_{11}	HOMO-3 → LUMO+1
S_{12}	HOMO-3 → LUMO+2
S_{13}	HOMO-4 → LUMO
S_{14}	HOMO-4 → LUMO+1
S_{15}	HOMO-4 → LUMO+2
S_{16}	HOMO-5 → LUMO
S_{17}	HOMO-5 → LUMO+1
S_{18}	HOMO-5 → LUMO+2
S_{19}	HOMO-6 → LUMO
S_{20}	HOMO-6 → LUMO+1
S_{21}	HOMO-6 → LUMO+2
S_{22}	HOMO-7 → LUMO
S_{23}	HOMO-7 → LUMO+1
S_{24}	HOMO-7 → LUMO+2
S_{25}	HOMO-8 → LUMO
S_{26}	HOMO-8 → LUMO+1
S_{27}	HOMO-8 → LUMO+2
S_{28}	HOMO-9 → LUMO
S_{29}	HOMO-9 → LUMO+1
S_{30}	HOMO-9 → LUMO+2

The HOMO-LUMO gap varies around 1.4 eV for the cluster during the MD simulation (Figure 5.3). There is a relatively large gap between the LUMO and LUMO+1 that is also evident in 0K optimized structure (Figure 5.2). The HOMOs are closely packed in energy even though near double and triple degeneracies are apparent. It is an interesting feature of $Au_{18}(SH)_{14}$ compared to other thiolate-protected gold nanoclusters that the HOMO of $Au_{18}(SH)_{14}$ is not

solely localized on the Au_9 core, but is also extended over the semiring motifs.[23] In this study, the HOMO is extended to the $Au_2(SH)_3$ and to one of the $Au(SH)_2$ semirings (Figure 5,2). Jin and coworkers reported a similar observation where the HOMO is extended to the $Au_4(SR)_5$ semiring.[23] The slightly different observations could be due to the different level of theories and the ligand used in the DFT calculations. The ligand R = C_6H_{11} has been used in the DFT study by Jin and coworkers whereas our study uses the smallest model SH. Nonetheless, the LUMO is localized over three layers of the Au_9 core (Figure 5.2) similar to the LUMO orbital reported previously. The HOMO→LUMO transition has been identified as a charge transfer from semiring motifs to Au_9 by Jin and coworkers.[23] The HOMO, HOMO-1, HOMO-2, HOMO-3 and HOMO-4 mainly consist of Au_9 core gold 6*s* orbitals as well as 5*d* gold and 3*p* sulfur orbitals on the $Au_2(SH)_3/Au(SH)_2$ semiring motifs. The HOMO-5, HOMO-6 and HOMO-7 are mainly composed from 5*d* gold and 3*p* sulfur orbitals on the semiring motifs. The HOMO-8 and HOMO-9 mainly consist of 6*s* and 5*d* orbitals of the semiring gold and 3*p* orbitals of sulfur atoms coming from the $Au_4(SH)_5/Au(SH)_2$ semiring motifs.

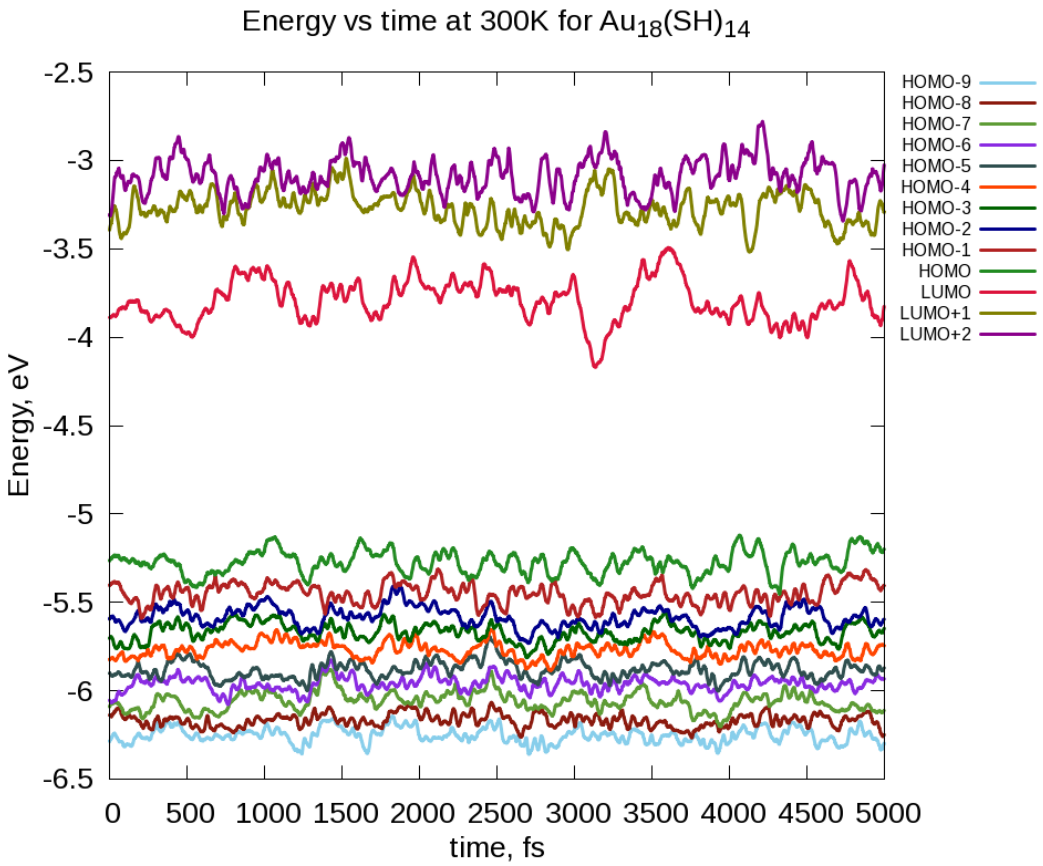

Figure 5.3 Variation of the HOMO−9 to LUMO+2 orbital energies with time.

The 0.3 eV underestimation was obtained by taking the difference between the optical band gap 1.7 eV[23] and the calculated DFT band gap value of 1.4 eV for the $Au_{18}(SH)_{14}$ cluster during the MD simulation. A detailed analysis carried out using an energy correction vs. without an energy correction to the excited states of $[Au_{25}(SH)_{18}]^{-1}$ showed that adding a correction lengthens the ground state growth times, but with minor changes to the overall excited state lifetimes.[37] In the current study, a 0.3 eV correction was added to the S_1-S_4 states only as a test sample (See Appendix C, Figure C.1 and Table C.1). The ground state (GS) growth has decreased with the addition of the correction in all four state relaxations, which is expected, whereas decay time constants have not changed with the correction added. Overall, the GS growth time and decay time constant trends for the S_1-S_4 states are not changed drastically with the addition of the energy correction to the excited states.

To gain more insight on the overall dynamics, the GS growth times and decay constants were calculated for all the thirty states which are tabulated in the Table 5.3. In the presence of

higher states, the S_1 to S_4 GS growth time and the decay time constants (Table 5.3) give similar trend to the trends observed for the case where only had four states (Table C.1).

Table 5.3 The ground state population increase lifetimes and decay times of the excited state population decrease of the S_1-S_{30} excited states "without" the energy correction.

Excited state	GS growth time (ps)	Decay time (ps)
S_1	16	11
S_2	51	6.4
S_3	54	1.4
S_4	20	0.9
S_5	52	0.8
S_6	52	0.6
S_7	24	0.7
S_8	46	0.7
S_9	41	0.6
S_{10}	27	0.8
S_{11}	47	0.8
S_{12}	36	0.6
S_{13}	29	0.8
S_{14}	43	0.7
S_{15}	37	0.6
S_{16}	35	0.7
S_{17}	43	0.6
S_{18}	36	0.5
S_{19}	40	0.7
S_{20}	45	0.6
S_{21}	32	0.5
S_{22}	39	0.6
S_{23}	41	0.5
S_{24}	34	0.5
S_{25}	38	0.6
S_{26}	36	0.5
S_{27}	29	0.5
S_{28}	38	0.6
S_{29}	31	0.5
S_{30}	28	0.4

The GS growth times for the S_1-S_{30} states vary between 16 - 54 ps. The growth times are all shorter than the growth times (73-158 ps) observed for $[Au_{25}(SH)_{18}]^{-1}$.[37] For $Au_{18}(SH)_{14}$, the

S_1 state gives the slowest decay time (10.9 ps) out of all the states; this state is a semiring to core charge transfer state. However in $[Au_{25}(SH)_{18}]^{-1}$, the first peak (~ 1.52 eV) originated from core to core transitions.[11] S_2 also gives a slow decay time constant of 6.4 ps. The rest of the states have ultrafast decay in the range of 0.4 - 1.4 ps. This suggests that there is a notable energy gap between states S_1 and S_2 compared to the rest of the states (Figure 5.3).

The hole relaxations are faster than the electron relaxations in the $Au_{18}(SH)_{14}$, which was not observed in Au_{25}. Figure 5.4 shows a schematic diagram of orbital levels filled with electrons for GS and S_1 to S_9 states. The S_1 population transfers to the GS (Figure C.2a) which is an electron relaxation (Figure 5.4). The S_2 population initially transfers to the S_3 which is then transferred to the S_1 (Figure C.2b). The $S_2 \rightarrow S_3 \rightarrow S_1$ is clearly an electron relaxation (Figure 5.4) where we do not see the movement of the hole among those states. Similarly, the S_3 state population transfers to the S_2 (Figure 5.4) which is also an electron transfer. The calculated decay constants for S_1, S_2 and S_3 states give slow decay constants of 11, 6.4 and 1.4 ps respectively (Table 5.3). In contrast, the decay constants for the rest of the states are shorter (< 1 ps), which give faster relaxations.

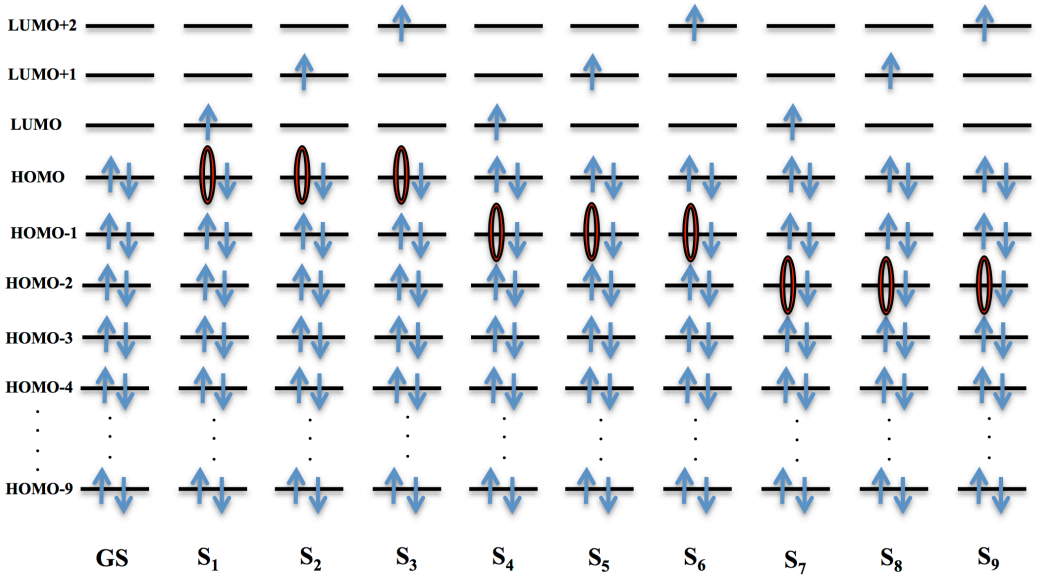

Figure 5.4 A schematic diagram of orbital levels filled with electrons for GS and S_1 to S_9 states.

The S_4 state population rapidly transfers to the S_1 state (Figure C.2d). $S_4 \rightarrow S_1$ is a hole relaxation (Figure 5.4) where only the hole has relaxed while the electron stays constant. This nature is observed in other higher states as well. For example, S_5, S_7 and S_8 states proceed through hole relaxations while S_6 and S_9 states proceed through a mix of hole and electron relaxations (Figure C.3 and Figure 5.4). The faster hole relaxations in the $Au_{18}(SH)_{14}$ cluster could be due to the closely packed HOMOs (Figure 5.3) in the electronic structure compared to the Au_{25} cluster. The decay time constants of states S_6 and S_9 are even shorter than the pure hole relaxations which suggest that mix of hole and electron relaxations leads to faster relaxations.

5.5 Conclusion

Understanding the photo-physics of the $Au_{18}(SR)_{14}$ cluster is important as it has shown to be a promising photosensitizer among glutathione-protected clusters. In this work, the electron−nuclear dynamics of the $Au_{18}(SH)_{14}$ nanoparticle has been investigated theoretically using NA-MD simulations using the FSSH-TDKS method. The important excitations covering up to ~2.6 eV in the optical absorption spectrum were analyzed to understand the electronic relaxation processes in the $Au_{18}(SH)_{14}$ cluster.

The addition of the 0.3 eV energy correction to the excited states slightly increased GS growth times while there were no changes to the decay times. Overall, the GS growth time and decay time constant trends are not changed drastically with the added correction.

The GS growth times obtained for the states covering 0.0-2.6 eV energy were in the range of 16 - 54 ps. Despite the ~1.4 eV HOMO-LUMO gap in $Au_{18}(SH)_{14}$, the GS growth times are several orders of magnitude shorter than the growth times observed for the $[Au_{25}(SH)_{18}]^{-1}$ nanocluster, which only had a ~1.09 eV HOMO-LUMO gap with the PBE level of theory. Similar to the $[Au_{25}(SH)_{18}]^{-1}$ nanocluster dynamics, the S_1 state gives the slowest decay time (~11 ps) among all the states (S_1-S_{30}) considered. However, the S_1 state in $Au_{18}(SH)_{14}$ is a semiring to core charge transfer state, whereas S_1 in the Au_{25} cluster is a core to core transition. S_2 has the second slowest decay time constant (~6.4 ps) while rest of the higher states have very short decay time constants in the energy range of 0.4 - 1.4 ps. A slower decay time constant for S_2 reflects the energy gap between LUMO and LUMO+1 orbitals. The hole relaxations are faster than the electron relaxations in the $Au_{18}(SH)_{14}$ unlike in Au_{25}. The faster hole relaxations in the $Au_{18}(SH)_{14}$ cluster are due to the closely packed HOMOs in the electronic structure.

5.6 Acknowledgments

This material is based on work supported by Department of Energy under grant DE-SC0012273. The work was performed on the computing for this project was performed on the Beocat Research Cluster at Kansas State University, which is funded in part by NSF grants CHE-1726332, CNS-1006860, EPS-1006860, and EPS-0919443. Beocat Application Scientist Dr. Dave Turner provided valuable technical expertise. The authors are grateful to Prof. Alexey V. Akimov for his support and valuable discussions on PYXAID.

5.7 References

1. Sun, J.; Jin, Y., Fluorescent Au Nanoclusters: Recent Progress and Sensing Applications. *J. Mater. Chem. C* **2014,** *2* (38), 8000-8011.

2. Jin, R., Quantum Sized, Thiolate-protected Gold Nanoclusters. *Nanoscale* **2010,** *2* (3), 343-362.

3. Li, G.; Jin, R., Atomically Precise Gold Nanoclusters as New Model Catalysts. *Acc. Chem. Res.* **2013,** *46* (8), 1749-1758.

4. Daniel, M.-C.; Astruc, D., Gold Nanoparticles: Assembly, Supramolecular Chemistry, Quantum-Size-Related Properties, and Applications toward Biology, Catalysis, and Nanotechnology. *Chem. Rev.* **2004,** *104* (1), 293-346.

5. R Kubo; A Kawabata, a.; Kobayashi, S., Electronic Properties of Small Particles. *Annu. Rev. Mater. Sci.* **1984,** *14* (1), 49-66.

6. van der Velden, J. W. A.; Vollenbroek, F. A.; Bour, J. J.; Beurskens, P. T.; Smits, J. M. M.; Bosnian, W. P., Gold Clusters Containing Bidentate Phosphine Ligands. Preparation and X-Ray Structure Investigation of $[Au_5(dppmH)_3(dppm)](NO_3)_2$ and $[Au_{13}(dppmH)_6](NO_3)_n$. *Recl. Trav. Chim. Pays-Bas* **1981,** *100* (4), 148-152.

7. Briant, C. E.; Hall, K. P.; Mingos, D. M. P.; Wheeler, A. C., Synthesis and Structural Characterisation of Hexakis(triphenyl phosphine)hexagold(2+) Nitrate, $[Au_6(PPh_3)_6][NO_3]_2$, and Related Clusters with Edgesharing Bitetrahedral Geometries. *J. Chem. Soc., Dalton Trans.* **1986,** (3), 687-692.

8. Jin, R.; Zeng, C.; Zhou, M.; Chen, Y., Atomically Precise Colloidal Metal Nanoclusters and Nanoparticles: Fundamentals and Opportunities. *Chem. Rev.* **2016,** *116* (18), 10346-10413.

9. Chakraborty, I.; Pradeep, T., Atomically Precise Clusters of Noble Metals: Emerging Link Between Atoms and Nanoparticles. *Chem. Rev.* **2017,** *117* (12), 8208-8271.

10. Heaven, M. W.; Dass, A.; White, P. S.; Holt, K. M.; Murray, R. W., Crystal Structure of the Gold Nanoparticle $[N(C_8H_{17})_4][Au_{25}(SCH_2CH_2Ph)_{18}]$. *J. Am. Chem. Soc.* **2008,** *130* (12), 3754-3755.

11. Zhu, M.; Aikens, C. M.; Hollander, F. J.; Schatz, G. C.; Jin, R., Correlating the Crystal Structure of A Thiol-Protected Au_{25} Cluster and Optical Properties. *J. Am. Chem. Soc.* **2008,** *130* (18), 5883-5885.

12. Zhu, M.; Eckenhoff, W. T.; Pintauer, T.; Jin, R., Conversion of Anionic $[Au_{25}(SCH_2CH_2Ph)_{18}]^-$ Cluster to Charge Neutral Cluster via Air Oxidation. *J. Phys. Chem. C* **2008,** *112* (37), 14221-14224.

13. Qian, H.; Eckenhoff, W. T.; Zhu, Y.; Pintauer, T.; Jin, R., Total Structure Determination of Thiolate-Protected Au_{38} Nanoparticles. *J. Am. Chem. Soc.* **2010,** *132* (24), 8280-8281.

14. Zeng, C.; Liu, C.; Chen, Y.; Rosi, N. L.; Jin, R., Gold–Thiolate Ring as a Protecting Motif in the $Au_{20}(SR)_{16}$ Nanocluster and Implications. *J. Am. Chem. Soc.* **2014,** *136* (34), 11922-11925.

15. Tlahuice, A.; Garzon, I. L., On the structure of the $Au_{18}(SR)_{14}$ cluster. *Phys. Chem. Chem. Phys.* **2012,** *14* (11), 3737-3740.

16. Jiang, D.-e.; Overbury, S. H.; Dai, S., Structure of $Au_{15}(SR)_{13}$ and Its Implication for the Origin of the Nucleus in Thiolated Gold Nanoclusters. *J. Am. Chem. Soc.* **2013,** *135* (24), 8786-8789.

17. Tlahuice-Flores, A.; Jose-Yacaman, M.; Whetten, R. L., On the Structure of the Thiolated Au_{15} Cluster. *Phys. Chem. Chem. Phys.* **2013,** *15* (45), 19557-19560.

18. Chen, S.; Wang, S.; Zhong, J.; Song, Y.; Zhang, J.; Sheng, H.; Pei, Y.; Zhu, M., The Structure and Optical Properties of the $[Au_{18}(SR)_{14}]$ Nanocluster. *Angew. Chem. Int. Ed.* **2015,** *54* (10), 3145-3149.

19. Negishi, Y.; Takasugi, Y.; Sato, S.; Yao, H.; Kimura, K.; Tsukuda, T., Magic-Numbered Au_n Clusters Protected by Glutathione Monolayers (n = 18, 21, 25, 28, 32, 39): Isolation and Spectroscopic Characterization. *J. Am. Chem. Soc.* **2004,** *126* (21), 6518-6519.

20. Ghosh, A.; Udayabhaskararao, T.; Pradeep, T., One-Step Route to Luminescent $Au_{18}SG_{14}$ in the Condensed Phase and Its Closed Shell Molecular Ions in the Gas Phase. *J. Phys. Chem. Lett.* **2012,** *3* (15), 1997-2002.

21. Yao, Q.; Yu, Y.; Yuan, X.; Yu, Y.; Xie, J.; Lee, J. Y., Two-Phase Synthesis of Small Thiolate-Protected Au_{15} and Au_{18} Nanoclusters. *Small* **2013,** *9* (16), 2696-2701.

22. Li, G.; Jiang, D.-e.; Kumar, S.; Chen, Y.; Jin, R., Size Dependence of Atomically Precise Gold Nanoclusters in Chemoselective Hydrogenation and Active Site Structure. *ACS Catal.* **2014,** *4* (8), 2463-2469.

23. Das, A.; Liu, C.; Byun, H. Y.; Nobusada, K.; Zhao, S.; Rosi, N.; Jin, R., Structure Determination of $[Au_{18}(SR)_{14}]$. *Angew. Chem. Int. Ed.* **2015,** *54* (10), 3140-3144.

24. Xu, W. W.; Zhu, B.; Zeng, X. C.; Gao, Y., A Grand Unified Model for Liganded Gold Clusters. *Nat. Commun.* **2016,** *7*, 13574.

25. Yu, Y.; Chen, X.; Yao, Q.; Yu, Y.; Yan, N.; Xie, J., Scalable and Precise Synthesis of Thiolated $Au_{10–12}$, Au_{15}, Au_{18}, and Au_{25} Nanoclusters via pH Controlled CO Reduction. *Chem. Mater.* **2013,** *25* (6), 946-952.

26. Stamplecoskie, K. G.; Chen, Y.-S.; Kamat, P. V., Excited-State Behavior of Luminescent Glutathione-Protected Gold Clusters. *J. Phys. Chem. C* **2014,** *118* (2), 1370-1376.

27. Das, A.; Li, T.; Nobusada, K.; Zeng, C.; Rosi, N. L.; Jin, R., Nonsuperatomic $[Au_{23}(SC_6H_{11})_{16}]^-$ Nanocluster Featuring Bipyramidal Au_{15} Kernel and Trimeric $Au_3(SR)_4$ Motif. *J. Am. Chem. Soc.* **2013,** *135* (49), 18264-18267.

28. Aikens, C. M., Electronic Structure of Ligand-Passivated Gold and Silver Nanoclusters. *J. Phys. Chem. Lett.* **2011,** *2* (2), 99-104.

29. Devadas, M. S.; Kim, J.; Sinn, E.; Lee, D.; Goodson, T.; Ramakrishna, G., Unique Ultrafast Visible Luminescence in Monolayer-Protected Au_{25} Clusters. *J. Phys. Chem. C* **2010,** *114* (51), 22417-22423.

30. Chen, Y.-S.; Kamat, P. V., Glutathione-Capped Gold Nanoclusters as Photosensitizers. Visible Light-Induced Hydrogen Generation in Neutral Water. *J. Am. Chem. Soc.* **2014,** *136* (16), 6075-6082.

31. Chen, Y.-S.; Choi, H.; Kamat, P. V., Metal-Cluster-Sensitized Solar Cells. A New Class of Thiolated Gold Sensitizers Delivering Efficiency Greater Than 2%. *J. Am. Chem. Soc.* **2013,** *135* (24), 8822-8825.

32. Yu, C.; Li, G.; Kumar, S.; Kawasaki, H.; Jin, R., Stable $Au_{25}(SR)_{18}/TiO_2$ Composite Nanostructure with Enhanced Visible Light Photocatalytic Activity. *J. Phys. Chem. Lett.* **2013,** *4* (17), 2847-2852.

33. Stamplecoskie, K. G.; Kamat, P. V., Size-Dependent Excited State Behavior of Glutathione-Capped Gold Clusters and Their Light-Harvesting Capacity. *J. Am. Chem. Soc.* **2014,** *136* (31), 11093-11099.

34. Abbas, M. A.; Kim, T.-Y.; Lee, S. U.; Kang, Y. S.; Bang, J. H., Exploring Interfacial Events in Gold-Nanocluster-Sensitized Solar Cells: Insights into the Effects of the Cluster Size and Electrolyte on Solar Cell Performance. *J. Am. Chem. Soc.* **2015,** *138* (1), 390-401.

35. Link, S.; El-Sayed, M. A.; Gregory Schaaff, T.; Whetten, R. L., Transition from Nanoparticle to Molecular Behavior: a Femtosecond Transient Absorption Study of a Size-selected 28 Atom Gold Custer. *Chem. Phys. Lett.* **2002,** *356* (3), 240-246.

36. Miller, S. A.; Womick, J. M.; Parker, J. F.; Murray, R. W.; Moran, A. M., Femtosecond Relaxation Dynamics of $Au_{25}L_{18}^-$ Monolayer-Protected Clusters. *J. Phys. Chem. C* **2009,** *113* (22), 9440-9444.

37. Senanayake, R. D.; Akimov, A. V.; Aikens, C. M., Theoretical Investigation of Electron and Nuclear Dynamics in the $[Au_{25}(SH)_{18}]^{-1}$ Thiolate-Protected Gold Nanocluster. *J. Phys. Chem. C* **2017,** *121* (20), 10653-10662.

38. C. Tully, J., Mixed quantum-classical dynamics. *Faraday Discuss.* **1998,** *110* (0), 407-419.

39. Craig, C. F.; Duncan, W. R.; Prezhdo, O. V., Trajectory Surface Hopping in the Time-Dependent Kohn-Sham Approach for Electron-Nuclear Dynamics. *Phys. Rev. Lett.* **2005,** *95* (16), 163001.

40. Jaeger, H. M.; Fischer, S.; Prezhdo, O. V., Decoherence-induced Surface Hopping. *J. Chem. Phys.* **2012,** *137* (22), 22A545.

41. Akimov, A. V.; Prezhdo, O. V., The PYXAID Program for Non-Adiabatic Molecular Dynamics in Condensed Matter Systems. *J. Chem. Theory Comput.* **2013,** *9* (11), 4959-4972.

42. Akimov, A. V.; Prezhdo, O. V., Advanced Capabilities of the PYXAID Program: Integration Schemes, Decoherence Effects, Multiexcitonic States, and Field-Matter Interaction. *J. Chem. Theory Comput.* **2014,** *10* (2), 789-804.

43. Perdew, J. P.; Burke, K.; Ernzerhof, M., Generalized Gradient Approximation Made Simple. *Phys. Rev. Lett.* **1996,** *77* (18), 3865-3868.

44. Te Velde, G. t.; Bickelhaupt, F. M.; Baerends, E. J.; Fonseca Guerra, C.; van Gisbergen, S. J.; Snijders, J. G.; Ziegler, T., Chemistry with ADF. *J. Comput. Chem.* **2001,** *22* (9), 931-967.

45. Lenthe, E. v.; Baerends, E.-J.; Snijders, J. G., Relativistic Regular Two-component Hamiltonians. *J. Chem. Phys.* **1993,** *99* (6), 4597-4610.

46. Kresse, G.; Furthmüller, J., Efficiency of Ab-initio Total Energy Calculations for Metals and Semiconductors Using a Plane-Wave Basis Set. *Comput. Mater. Sci.* **1996,** *6* (1), 15-50.

47. Kresse, G.; Joubert, D., From Ultrasoft Pseudopotentials to the Projector Augmented-wave Method. *Phys. Rev. B* **1999,** *59* (3), 1758.

Chapter 6 - Theoretical Investigation of Relaxation Dynamics in $Au_{38}(SH)_{24}$ Thiolate-protected Gold Nanocluster

6.1 Abstract

A subtle change in the electronic structure of thiolate protected noble nanoparticles can result in distinctive energy relaxation dynamics. Corresponding investigations on different sizes and structures of thiolate-protected gold nanoclusters will reveal their physical and chemical properties for further development of catalytic applications. In this work, we performed nonradiative relaxation dynamics simulations of the $Au_{38}(SH)_{24}$ nanocluster to describe electron-vibrational energy exchange. The core and higher excited states involving semiring motifs lying in the energy range of 0.00-2.01 eV are investigated using the time-dependent density functional theory (TDDFT). The surface hopping method with decoherence correction, combined with real-time TDDFT is used to assess the quantum dynamics. The Au_{23} core relaxations were found to occur on a picosecond timescale in the range of 2.0 – 8.2 ps. The higher excited states that consist of core- semiring mixed or semiring states gave ultra-fast decay time constants in the range of 0.6 - 4.9 ps. Our calculations predict that the slowest individual state decay of S_{11} or the slowest combined S_{11}-S_{12}, S_1-S_2-S_6-S_7 and S_4-S_5-S_9-S_{10} decay involves intracore relaxations. The analysis of the phonon spectral densities and the ground state vibrational frequencies suggest that the low frequency (25 cm^{-1}) coherent phonon emission reported experimentally could be the bending of the bi-icosahedral Au_{23} core or the "fan blade twisting" mode of two icosahedral units occurring in a similar frequency range.

6.2 Introduction

Advances in synthesis and isolation of thiolate-protected gold nanoparticles have led to developments in applications such as catalysis and photocatalysis.[1-6] Investigations of energy relaxation dynamics for different sizes and structures of thiolate-protected gold nanoclusters are needed to enable elucidation of the physical and chemical properties underlying these applications.[7-13] Quantum confinement effects become prominent for small gold nanoparticles less than 2 nm in diameter. Thus, the geometric structure of the system plays a role in its

electronic structure,[14-16] and subtle changes in structure can lead to different electron dynamics.[14, 17-18]

Extensive experimental work has examined the electron relaxation dynamics of nanoclusters such as $[Au_{25}(SR)_{18}]^{-1}$, and distinct time scales and relaxation mechanisms have been reported.[19-22] Recent theoretical electron nuclear relaxation studies on $[Au_{25}(SH)_{18}]^{-1}$ nanocluster provided insights into the experimentally proposed relaxation mechanisms.[23-24] The study by Senanayake et al. showed that semiring or other states are not observed at an energy lower than the core-based S_1 state. Moreover, it suggested that the experimentally observed time constants in the several picoseconds range could arise from core-to-core transitions rather than from a core-to-semiring transition. Recently, Jin and co-workers reported an ultrafast relaxation dynamics of $Au_{38}(SC_2H_4Ph)_{24}$ nanoclusters and the effects of structural isomerism.[25] This study found a correlation between the ultrafast relaxation dynamics and the geometric structures of two isomers of thiolate-protected $Au_{38}(SC_2H_4Ph)_{24}$. In another study, Knappenberger and co-workers reported low-frequency vibrations associated with the ligand shell of $Au_{25}(SC_8H_9)_{18}$ and $Au_{38}(SC_{12}H_{25})_{24}$ nanoclusters that mediate the nonradiative relaxation dynamics.[26] The reported modes include Au(I)-S stretching (200 cm^{-1}) and Au(0)−Au(I) stretching (90 cm^{-1}) of the ligand shell.[26]

The $Au_{38}(SR)_{24}$ nanocluster contains a face-fused bi-icosahedral Au_{23} core protected by six -SR-Au-SR-Au-SR- dimeric units often called semirings and three -SR-Au-SR- monomeric semirings, forming a core-shell-like structure.[27-29] This nanocluster has attracted significant research interest in the areas of chirality, doping and catalysis.[26, 30-34] The electronic structure of the lowest energy D_3 isomer of $Au_{38}(SR)_{24}$ can be explained based on a particle-in-a-cylinder (PIC) model due to its nanorod-shaped gold core structure.[28] Thus, the occupied and unoccupied orbitals near the HOMO-LUMO gap can be described by Σ, Π, Δ symmetries. The orbitals can be labeled as M_l, where the azimuthal quantum number M = 0, 1, 2, ... corresponds to Σ, Π, Δ, ... orbitals and l = 1, 2, 3, ... corresponds to the axial quantum number.[28] The core-shell structure of the $Au_{38}(SR)_{24}$ nanocluster can result in interesting optical properties, but careful assignment of core and ligand contributions in optical properties is important. An ultrafast luminescence investigation proposed that the electron dynamics of $Au_{38}(SR)_{24}$ includes core-to-shell relaxations.[25] However, a recent theoretical investigation on the luminescence origin of

$Au_{38}(SR)_{24}$ suggested that the two lowest energy fluorescence bands arise predominantly due to a HOMO → LUMO transition that involves core-based orbitals.[35]

The experimental examination of ultrafast relaxation dynamics performed on the $Au_{38}(SC_2H_4Ph)_{24}$ nanocluster suggests that the isomer with a bi-icosahedral Au_{23} inner core shows rapid decay (1.5 ps) among excited states followed by nanosecond relaxation to the ground state, and that a higher energy structural isomer exhibits similar relaxation processes.[25] They performed the femtosecond experiments on the $Au_{38}(SR)_{24}$ isomer pumped at 490 nm/1050 nm and probed at the visible range (0.0 - 2.3 eV). They proposed a two-state relaxation model[25] similar to a mechanism proposed for the $[Au_{25}(SR)_{18}]^{-1}$.[8, 21] The two-state model assigned to as core-to-shell or electronic rearrangement within the metal core. The picosecond relaxations in both isomers were assigned to core–shell charge transfer or to electronic rearrangement within the metal core;[25] they suggested that the picosecond decay in $Au_{38}(SR)_{24}$ could be an electronic rearrangement within the metal core based on previous experimental and theoretical work on other thiolate-protected gold clusters.[11-12, 36] Assigning the relaxation mechanisms in such complex nanoclusters may need extra caution. For the $Au_{38}(SR)_{24}$ isomer with a bi-icosahedral core, they also reported a coherent phonon emission at 25 cm^{-1} with pumping in the near IR region.[25]

Overall, further experimental and theoretical work is required to fully understand the nonradiative relaxation dynamics of the $Au_{38}(SR)_{24}$ nanocluster. Herein, the focus of this theoretical study is to reveal the electron−nuclear dynamics and give insights into the relaxation mechanism of the thiolate-protected $Au_{38}(SR)_{24}$ nanoparticle. In this study, we use the D_3 isomer of the $Au_{38}(SH)_{24}$ nanocluster for the relaxation dynamics calculations.

6.3 Computational methodology

We have performed ab initio real-time nonadiabatic molecular dynamics (NA-MD) simulations to study the nonadiabatic dynamics in the $Au_{38}(SH)_{24}$ nanocluster. The fewest switches surface hopping (FSSH)[37] algorithm with the classical path approximation and a time-dependent Kohn−Sham description of electronic states (FSSH-TDKS)[38] was used in our calculations. The reported geometrical and electronic structural changes (~0.05 Å) in the $Au_{38}(SH)_{24}$ nanocluster core[35] is less than the reported geometrical and electronic structural changes (~0.33 Å) in the $[Au_{25}(SR)_{18}]^{-1}$ nanocluster upon photoexcitation.[36] Therefore, the

classical path approximation in the NA-MD calculation approach is expected to be suitable to describe the nonradiative relaxation dynamics of the $Au_{38}(SH)_{24}$ nanocluster. The decoherence-induced surface hopping (DISH)[39] scheme is utilized to include decoherence effects. The FSSH simulations in this work are performed using the PYXAID program.[40-41]

The methodology used here is similar to our previous work on $[Au_{25}(SR)_{18}]^{-1}$.[24] The $Au_{38}(SH)_{24}$ nanocluster geometry optimization is performed at the PBE[42]/TZP (frozen core) level of theory in the Amsterdam Density Functional (ADF)[43] software package to obtain the relaxed geometry at 0K. The zero-order regular approximation (ZORA)[44] is used to treat scalar relativistic effects in gold. Linear response time-dependent density functional theory (TD-DFT) calculations were performed using the same level of theory to compute the electronic excitations and the relevant absorption spectrum of $Au_{38}(SR)_{24}$. A ground state vibrational frequency calculation was performed using ADF at the same level of theory to obtain the vibrational modes of the cluster. The ADF GUI was used to plot the orbitals.

The 0K system was thermalized through a temperature ramping calculation performed at 300K. After the temperature ramping, molecular dynamics (MD) simulations were performed through density functional theory (DFT) calculations in the Vienna Ab initio Simulation Package (VASP).[45] We used projector-augmented wave pseudopotentials,[46] a kinetic energy cutoff value of 402.0 eV for the temperature ramping calculation and 301.8 eV energy cutoff value for the MD and NA coupling calculations, a 24 Å simulation box size, gamma points, and the PBE functional in all of our VASP calculations. A MD trajectory of 5 ps in length was computed with a 1 fs integration time step. The nonadiabatic coupling elements were calculated following the same approach we used for the $[Au_{25}(SH)_{18}]^{-1}$ system.

The FSSH calculations employ 3.5 ps length sub-trajectories starting from 10 different initial geometries. For each NA-MD trajectory, 1000 realizations of the stochastic FSSH/DISH state hopping trajectories were considered. We used 100 realizations of the stochastic FSSH/DISH state hopping trajectories for the largest calculation with ninety-eight excited states to reduce the computational cost.

The important electronic excited states contributing to the optical absorption spectrum of $Au_{38}(SH)_{24}$ in the energy range of 0.00−2.01 eV (visible range) were analyzed. The excited state population decay times and the ground state population increase times were calculated for the

$Au_{38}(SH)_{24}$ nanocluster using the same equations and procedure mentioned in our previous study.[24] The phonon spectral density plots were drawn with a resolution of 4.8 cm^{-1}.

6.4 Results and discussion

The experimental optical absorption spectrum for the $Au_{38}(SR)_{24}$ nanocluster displays low energy peaks that lie around 0.9, 1.2, 1.7 and 2.0 eV.[47] The $Au_{38}(SH)_{24}$ spectrum calculated with the PBE level of theory gives similar peaks at 0.99, 1.26, 1.74 and 2.01 eV as shown in Figure 6.1, in good agreement with the experimental spectrum. The calculated spectral peak positions are also in agreement with the PBE/DZ frozen core optical absorption spectrum of the lowest energy D_3 isomer by Aikens and co-workers.[28]

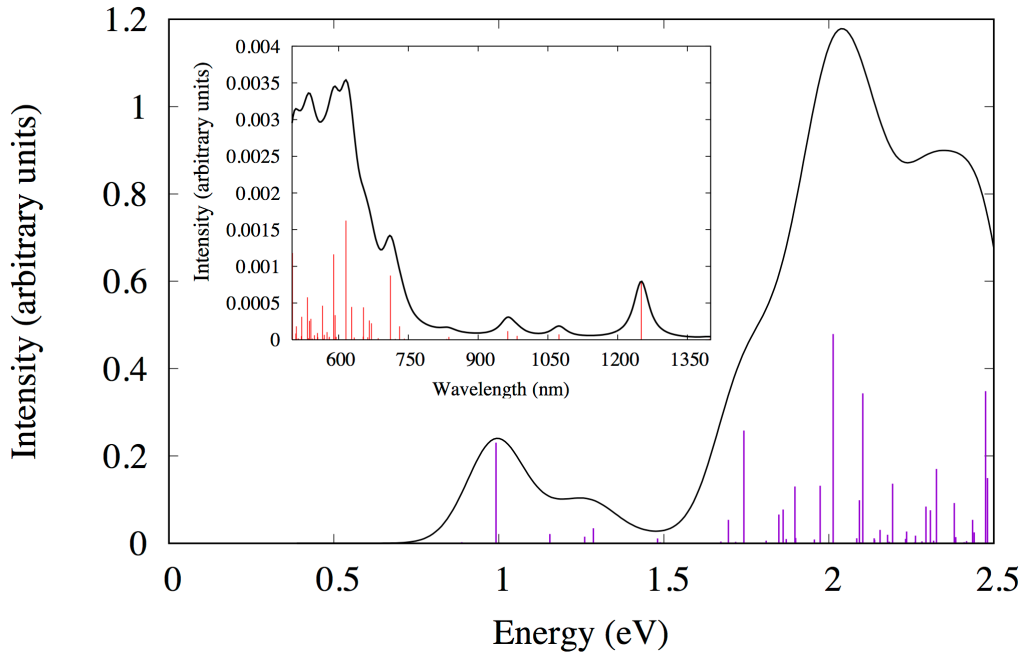

Figure 6.1 Calculated PBE/TZP optical absorption spectrum for $Au_{38}(SH)_{24}$. Inset: The absorption spectrum in wavelength (nm).

6.4.1 Relaxation dynamics of the excited state peaks up to ~ 1.5 eV

The electronic relaxations for the excitations covering the peaks up to approximately 1.5 eV will be analyzed in this section. The calculated orbitals of the $Au_{38}(SH)_{24}$ cluster near the HOMO-LUMO gap (Figure 6.2) can be described using Σ, Π, and Δ symmetries according to the

PIC model. In $Au_{38}(SH)_{24}$, the HOMO-4 to LUMO+4 orbitals arise primarily from gold *sp* atomic orbitals in the bi-icosahedral core (Figure 6.2). The orbital character found in this study is similar to the orbitals shown in the previous work by Aikens and co-workers.[28]

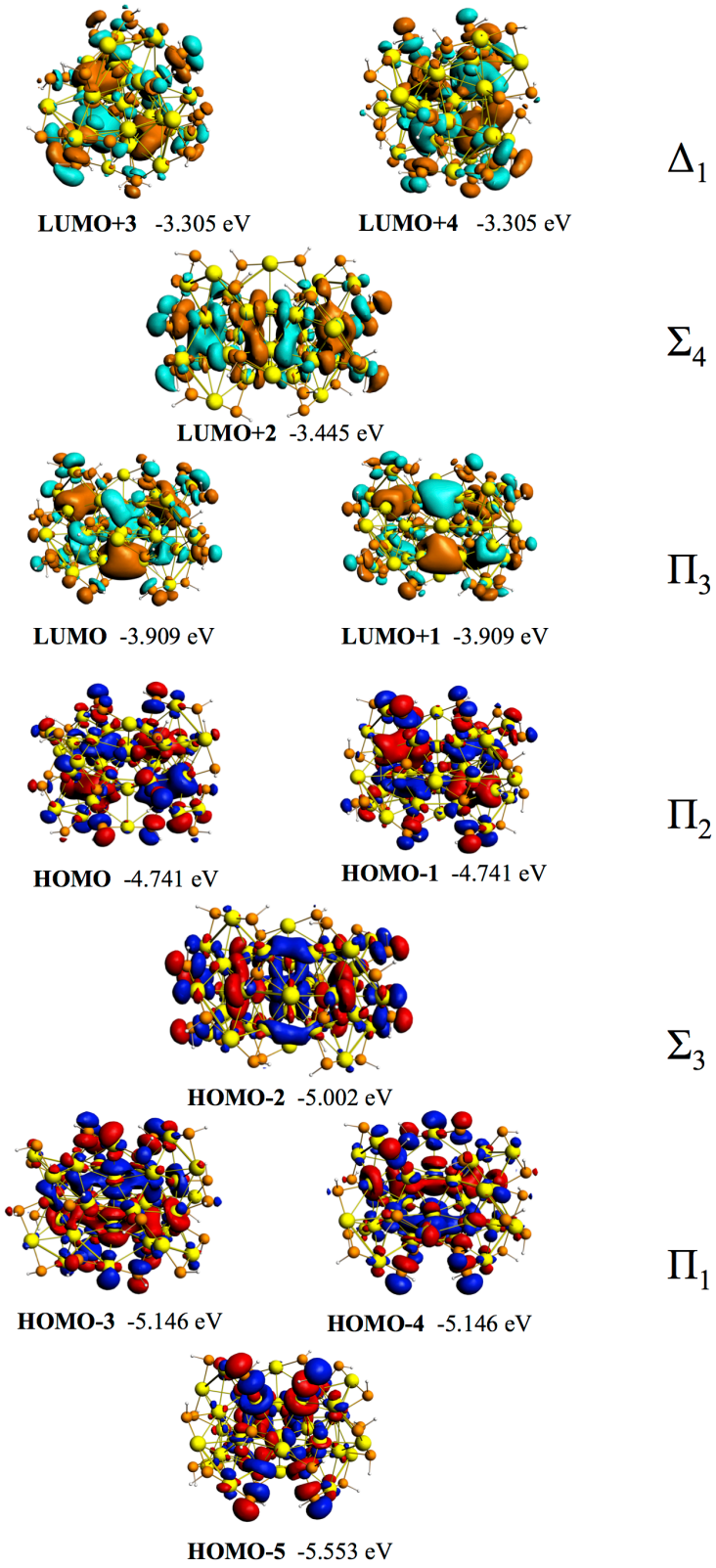

Figure 6.2 PBE/TZP orbitals near the HOMO−LUMO gap and their relative energies (in eV) for $Au_{38}(SH)_{24}$.

The first peak (0.99 eV) arises primarily due to a $\Pi_2 \rightarrow \Pi_3$ transition that has the highest oscillator strength and weight (Table 6.1), in agreement with previous results.[28] In Figure 6.2, the degenerate orbitals are labeled as two different orbitals. For example, HOMO and HOMO-1 are exactly degenerate in the 0 K PBE/TZP optimized structure, but become nondegenerate as the nanocluster vibrates and distorts from its equilibrium structure during the NA-MD calculations. The labeling leads to two transitions that originate from HOMO and HOMO-1 to LUMO and LUMO+1 for the 0.99 eV peak in Table 6.1. This labeling was used in order to define the excited states that will be used in the FSSH-TDKS calculations.

Table 6.1 gives the excitations up to 1.5 eV with the highest oscillator strengths and weights and their respective most probable transitions for the two allowed excited state symmetries A_1 and E_1 for $Au_{38}(SH)_{24}$. The excitations around 1.15-1.29 eV primarily arise from transitions out of the HOMO-2 to LUMO/LUMO+1 ($\Sigma_3 \rightarrow \Pi_3$) and transitions out of HOMO-3/HOMO-4 to LUMO/LUMO+1 ($\Pi_1 \rightarrow \Pi_3$). However, for this peak the $\Sigma_3 \rightarrow \Pi_3$ transition has a small contribution to the oscillator strength and the $\Pi_1 \rightarrow \Pi_3$ transitions have higher contributions to the oscillator strength due to their higher weights. The $\Pi_1 \rightarrow \Pi_3$ transition would be a forbidden transition for a perfectly cylindrical system. Similar observations have been made by Aikens and co-workers.[28] We find that HOMO-4 to LUMO+4 orbitals are involved in the most probable transitions up to the 1.5 eV range (Table 6.1). Therefore, the twenty-five excited states defined for the FSSH-TDKS calculations cover this range. The excited states defined in Table 6.2 represent a single Slater determinant, whereas the TDDFT excitations listed in Table 6.1 are mixed (i.e., linear combinations of several Slater determinants); the Slater determinants defined in Table 6.2 include the Slater determinants present in the TDDFT calculations.

Table 6.1 Transitions with the highest weights for the excited states covering up to 1.5 eV from the TDDFT calculation.

Excitation transitions	Energy (eV)	Oscillator strength	Weight	Most weighted transitions
E_1 symmetry				
1	0.89	0.0006	0.9927	HOMO/HOMO-1 → LUMO/LUMO+1
2	1.15	0.0045	0.9381	HOMO-2 → LUMO/LUMO+1
			0.0452	HOMO-3/HOMO-4 → LUMO/LUMO+1
3	1.29	0.0074	0.9348	HOMO-3/HOMO-4 → LUMO/LUMO+1
			0.0389	HOMO-2 → LUMO/LUMO+1
4	1.33	0.0001	0.9888	HOMO/HOMO-1 → LUMO+2
5	1.49	0.0006	0.9602	HOMO/HOMO-1 → LUMO+3/LUMO+4
A_1 symmetry				
1	0.99	0.0491	0.934	HOMO/HOMO-1 → LUMO/LUMO+1
			0.0427	HOMO-2 → LUMO+2
2	1.26	0.0033	0.9749	HOMO-3/HOMO-4 → LUMO/LUMO+1
			0.0097	HOMO-2 → LUMO+2
3	1.48	0.0024	0.9729	HOMO/HOMO-1 → LUMO+3/LUMO+4
			0.0085	HOMO-2 → LUMO+2

Table 6.2 Excited states and corresponding transitions (covering 0.00-1.50 eV energy range) used in the FSSH-TDKS calculations.

Excited state	Transitions
S_1	HOMO → LUMO
S_2	HOMO → LUMO+1
S_3	HOMO → LUMO+2
S_4	HOMO → LUMO+3
S_5	HOMO → LUMO+4
S_6	HOMO-1 → LUMO
S_7	HOMO-1 → LUMO+1
S_8	HOMO-1 → LUMO+2
S_9	HOMO-1 → LUMO+3
S_{10}	HOMO-1 → LUMO+4
S_{11}	HOMO-2 → LUMO
S_{12}	HOMO-2 → LUMO+1
S_{13}	HOMO-2 → LUMO+2
S_{14}	HOMO-2 → LUMO+3
S_{15}	HOMO-2 → LUMO+4
S_{16}	HOMO-3 → LUMO
S_{17}	HOMO-3 → LUMO+1

S_{18}	HOMO-3 → LUMO+2
S_{19}	HOMO-3 → LUMO+3
S_{20}	HOMO-3 → LUMO+4
S_{21}	HOMO-4 → LUMO
S_{22}	HOMO-4 → LUMO+1
S_{23}	HOMO-4 → LUMO+2
S_{24}	HOMO-4 → LUMO+3
S_{25}	HOMO-4 → LUMO+4

Figure 6.3 demonstrates the variation of the orbital energies with time for the $Au_{38}(SH)_{24}$ cluster as obtained from the MD simulations. The orbital energy variation shows the near-degenerate nature of several sets of the orbitals. For example, the HOMO and HOMO-1 as well as the LUMO and LUMO+1 are nearly degenerate. As mentioned above, the degeneracies of the orbitals shown in Figure 6.2 were obtained by performing a single point calculation on the relaxed geometry at 0K. However, the MD simulation was performed at 300K. During the dynamics, the $Au_{38}(SH)_{24}$ cluster geometry can have distortions in the *x*, *y* and *z* directions that break the perfect D_3 symmetry of the optimized $Au_{38}(SH)_{24}$ geometry. During the MD simulation, the $Au_{38}(SH)_{24}$ has a small HOMO-LUMO gap of approximately ~ 0.75 eV (Figure 6.3).

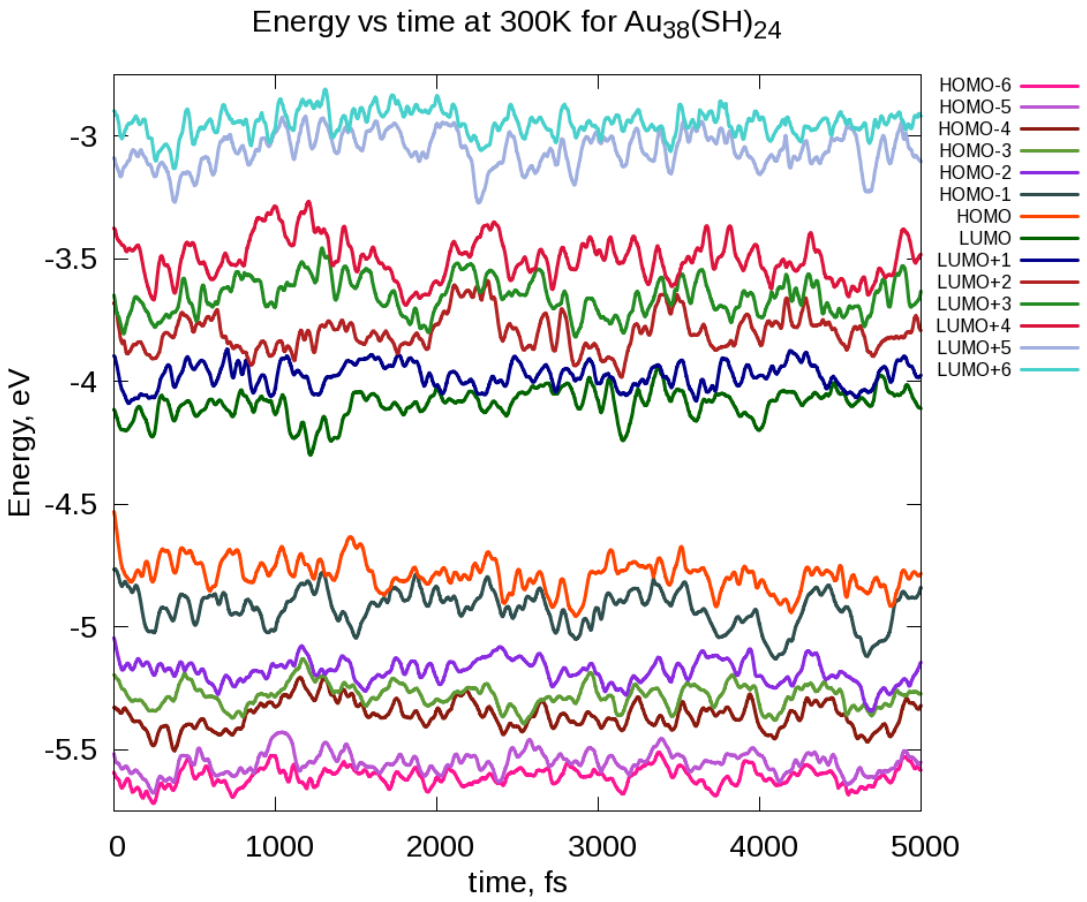

Figure 6.3 Variation of the HOMO−6 to LUMO+6 orbital energies with time.

First, we performed relaxation dynamics only on the S_1, S_2, S_6, and S_7 states as a test case both with and without an energy correction to the excited states. The HOMO-LUMO gap for $Au_{38}(SH)_{24}$ is ~ 0.75 eV during the MD simulation, which is ~ 0.15 eV less than the experimental optical gap of ~ 0.90 eV reported elsewhere.[25, 48] Therefore, a 0.15 eV energy correction is added to the excited states to analyze how the relaxation dynamics will differ with the additional energy correction. Adding an energy correction only lengthens the ground state (GS) growth times (by 16-30%) while the decay time constants are less affected. Overall, the time constants and the relaxation trends of these states do not change significantly with the added correction (see Appendix D, Figure D.1 and Table D.1). Therefore, in this section, the excited state population relaxation dynamics calculations for all twenty-five states (Table 6.2) will be discussed without the correction added. The relaxation dynamics of these twenty-five states will provide insights about the core state (~1.5 eV) relaxations in the $Au_{38}(SH)_{24}$ nanocluster.

The GS growth times and decay times were then calculated for states S_1-S_{25} (Table D.2). In the presence of all twenty-five states, the population evolutions of the S_1, S_2, S_6, and S_7 states (Figure 6.4) follow similar relaxation patterns to the case in which only the S_1, S_2, S_6, and S_7 states were considered (Figure D.1).

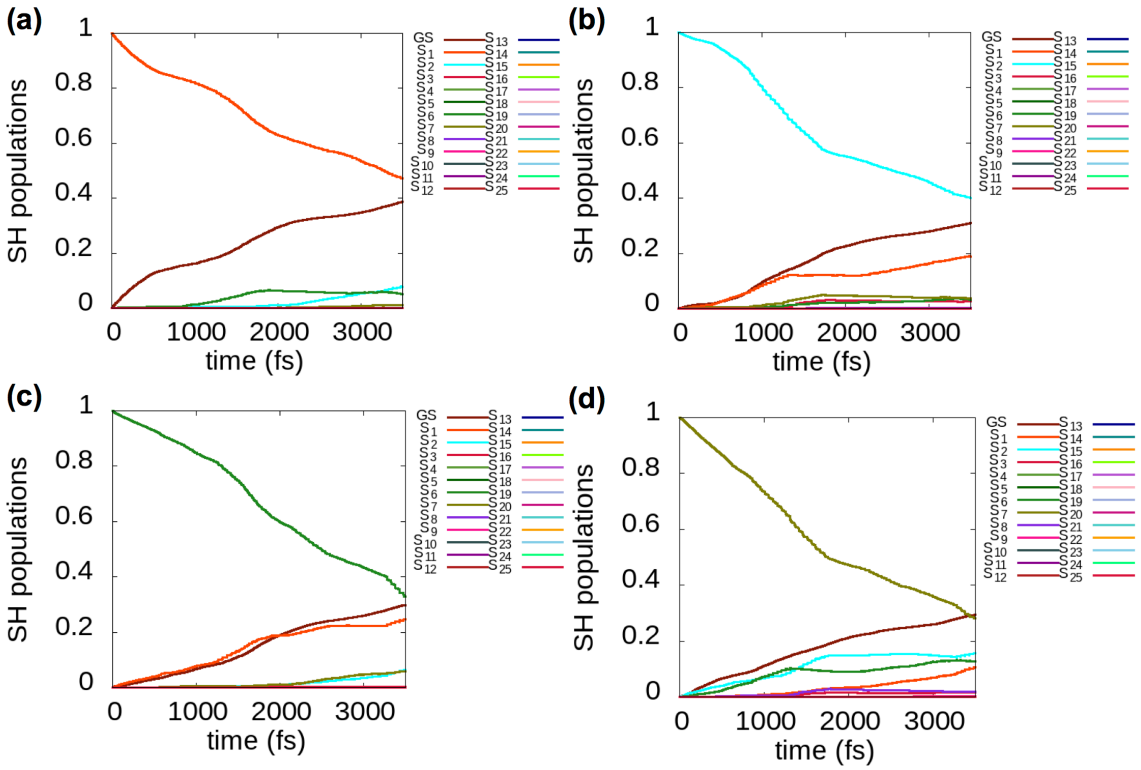

Figure 6.4 Evolution of excited state populations starting in a) S_1, b) S_2, c) S_6, and d) S_7 excited state.

The GS growth times for the S_1-S_{25} states are in the range of 6.4 – 207 ps. The GS growth times are relatively short except for states S_{15}, S_{19}, S_{20}, S_{24} and S_{25}. The overall growth times are shorter by 1-2 orders of magnitude compared to the growth times of $[Au_{25}(SH)_{18}]^{-1}$,[24] which suggests that the identity of the thiolate-protected nanocluster is a critical factor for tuning the lifetimes of the excited electrons.

The S_{11} state (HOMO-2→LUMO) gives the slowest decay time constant (~ 8.2 ps) when its population is fit to an exponential. However, this S_{11} state population has a non-exponential decay after 2000 fs due to population transfer to S_{12} (HOMO-2→LUMO+1) (Figure 6.5a). The S_{12} population mainly transfers back to the S_{11} state (Figure 6.5b). Due to this reason, fitting the

non-exponential S_{11} population decay to an exponential may not result in an accurate decay constant. At 3500 fs, the S_{11} state retains 57% of its initial excited state population (Figure 6.5a). Due to fast population exchange between S_{11} and S_{12}, fitting the total population of S_{11} and S_{12} to one exponential could give a better idea about the decay (Figure 6.5c). The decay constant calculated for the combined S_{11} and S_{12} state population is 9.7 ps. At 3500 fs, the combined S_{11} and S_{12} states retain 67% of the initial excited state population of S_{11}.

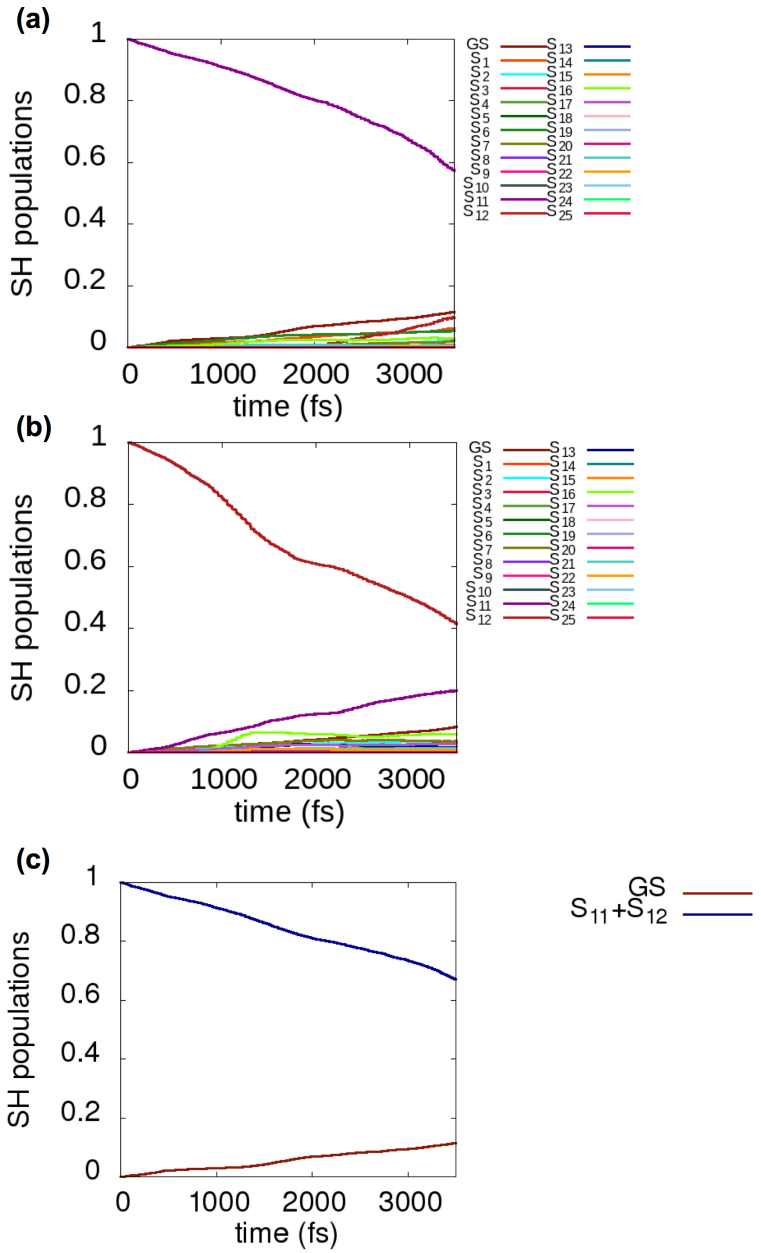

Figure 6.5 (a) Evolution of excited state populations starting in S_{11}. (b) Evolution of excited state populations starting in S_{12}. (c) Evolution of the total population of the S_{11} and S_{12} states when S_{11} is excited. Populations of other states up to S_{25} are not shown for clarity.

The fitting of the combined population of two or more states to an exponential is expected to be reasonable because several states would be probed by the same pump/probe pulse experimentally, and the observed decay will need to factor in more than one state. Therefore, we calculated decay time constants for several other combined state populations. At this point, the core states were grouped based on the orbitals involved and possible population transfers

between the states. For example, S_1, S_2, S_6 and S_7 originate from the HOMO/HOMO-1 → LUMO/LUMO+1 transitions where the HOMO and HOMO-1 as well as the LUMO and LUMO+1 are nearly degenerate. Thus, the population of S_1 can easily transfer its population to S_2, S_6 and S_7 (Figure 6.4a). The total population of S_1, S_2, S_6, and S_7 was fit to an exponential when the S_1, S_2, S_6 and S_7 states were excited separately. Similarly, the other cores states were grouped and their combined population decays were calculated (See Appendix D, Table D.3). The S_1, S_2, S_6, S_7 total population when the S_6 state was excited and the S_4, S_5, S_9, S_{10} total population when the S_5 and S_{10} states were excited gave slower population decay compared to their individual decay constants. The combined S_1-S_2-S_6-S_7 state population decays are in the range of 6.4-10.1 ps and the combined S_4-S_5-S_9-S_{10} state population decays are in the range of 4.1-10.7 ps. These decay time constants are similar to the combined S_{11}-S_{12} population decay time of 9.7 ps.

At this point it is difficult to compare our decay time constants directly with the experimentally observed time constants. The experimental time constants have been observed by using two pump frequencies (490 nm/1050 nm) and a range of probe frequencies. In our calculations, we look at each state relaxation separately rather than pumping the nanocluster system with a specific frequency. The individual state decay constants calculated for $Au_{38}(SR)_{24}$ in our study are in the range of 2.0–8.2 ps, whereas the combined state population decay constants are in the range of 2.0–10.7 ps. They agree with the picosecond time scale observed experimentally. Our calculations show that the slowest decays (the individual decay of S_{11} or the slowest combined S_{11}-S_{12}, S_1-S_2-S_6-S_7 and S_4-S_5-S_9-S_{10} decays) involve HOMO-2→LUMO/LUMO+1, HOMO/HOMO-1→LUMO/LUMO+1 and HOMO/HOMO-1→LUMO+3/LUMO+4 transitions, which are intracore relaxations (Figure 6.2).

6.4.2 Relaxation dynamics of the higher excited states up to ~ 2.01 eV

Jin and co-workers have proposed that the faster 1.5 ps decay observed experimentally could arise from a core-shell relaxation or an intracore relaxation in the lowest energy Au_{38} isomer.[25] They used a probe pulse with the energy covering ~ 0.90-2.33 eV (530 -1300 nm) in their experiments.[25] In this section we analyze the relaxation dynamics of the excited states lying beyond the energy of 1.5 eV in the $Au_{38}(SH)_{24}$ nanocluster optical absorption spectrum (Figure 6.1). The relaxation dynamics of the excited states lying above 1.50 eV is potentially important

in order to understand the involvement of the semiring states, because the 0.00-1.50 eV energy range only covers the gold core states. Here, we have considered the significant excitations appearing in the 0.00-2.01 eV energy range in Figure 6.1.

There are several notable excitations in the energy range of 1.70-2.01 eV (Table D.4). Among them, the excitation around 1.74 eV has a relatively strong oscillator strength value (0.0549) that mainly originates from excitations out of HOMO-6/HOMO-7 orbitals to LUMO/LUMO+1 orbitals (semiring → Π_3) and from the transition out of HOMO-2 to LUMO+2 ($\Sigma_3 \rightarrow \Sigma_4$). HOMO-6 and HOMO-7 are semiring orbitals whereas HOMO-2 and LUMO+2 are gold core-based orbitals. The transition dipole moment components from the $\Sigma_3 \rightarrow \Sigma_4$ transition are large even though the weight of this transition is smaller than some of the others. Thus, the 1.74 eV peak is a combination of excitations involving both gold core and semirings where the $\Sigma_3 \rightarrow \Sigma_4$ transition yields the main contribution due to its high transition dipole moment. The notable excitations around 1.85-2.01 eV have mixed transitions from orbitals involving both gold core and semirings. However, the strongest excitation at 2.01 eV (oscillator strength of 0.1021) is mainly composed from the semiring (HOMO-12/HOMO-13) → LUMO transitions. Comparable findings have been observed by Aikens and co-workers at the PBE/DZ level of theory for $Au_{38}(SR)_{24}$.[28]

Therefore, we considered orbitals ranging from HOMO-13 to LUMO+6 to define the single excitations for the FSSH-TDKS calculations (Table 6.2, Table D.5). The decay times of the excited state population were calculated for all ninety-eight states (Table D.6). In the presence of the higher excited states the relaxation trend of the S_1-S_{25} states is preserved. The S_{11} population transfers its population into the S_{12} state although by a lesser amount (Figure D.2a). Thus, fitting its population decrease to an exponential may suffer less significant error compared to the case involving only twenty-five states. The S_{12} population primarily transfers back to the S_{11} (Figure D.2b). Fitting the S_{11} (HOMO-2→LUMO) population to an exponential give a slower decay time constant of 7.6 ps. At 3500 fs, the S_{11} state retains 58% of its initial excited state population (Figure D.2a). Fitting the total population of the S_{11} and S_{12} states to an exponential gives a time constant of 8.8 ps. At 3500 fs, the combined S_{11}-S_{12} state population retains 66% of the initial S_{11} population (Figure D.2c). The combined state population decay for the core states were calculated again in the presence of higher states. The S_1, S_2, S_6, S_7 total population when S_6 is excited and the S_4, S_5, S_9, S_{10} total population when S_5 and S_{10} are excited

gave slow population decay in the range of 9.7 -10.8 ps, which is similar to the case where only the core states were present.

The higher energy states S_{26}-S_{35} have decay time constants in the range of 1.4 - 4.9 ps. The rest of the higher states (S_{36}-S_{98}) have much shorter time constants in the range of 0.6 -1.7 ps. The S_{36}-S_{98} states are mainly composed of transitions out of the semiring-based orbitals. In general, the decay times of higher energy states are shorter due to the higher density of states at these energies.

6.4.3 Electron−phonon interactions in the $Au_{38}(SH)_{24}$ cluster

Vibrations in the $Au_{38}(SH)_{24}$ nanocluster can lead to nonradiative relaxation of excited states. Therefore, it is important to understand which nuclear vibrational motions couple most strongly with electronic states to understand the dynamics of electronic relaxations in these systems.

In this section we present the phonon spectral densities obtained for core states (S_1-S_{25}) that demonstrate the vibrational modes that are correlated with the nonradiative relaxations (i.e., relevant electron-phonon interactions). The phonon spectral density plots were obtained by taking Fourier transforms of the normalized autocorrelation function of the energy gap fluctuation for a pair of electronic excited states of interest. The pair of electronic excited states could be the GS and an electronic excited state or two different electronic excited states. The analysis of the phonon spectral densities showed intense peaks around 24.2, 33.9, 48.4 and 53.2 cm^{-1} for $Au_{38}(SR)_{24}$ when only the core states (up to ~1.5 eV) were considered in the relaxation dynamics (Figure D.3). Among the prominent peaks, the peak around 24.4 cm^{-1} was found to be the highest in intensity. This peak at 24.4 cm^{-1} was observed when the spectral densities are plotted considering the energy gap fluctuation between the GS-S_{15}, GS-S_{18}, and GS-S_{23} (Figure 6.6). The S_{15} excited state arises from the transition out of HOMO-2 to LUMO+4. The S_{18} and S_{23} states arise from the transitions out of HOMO-3 and HOMO-4 to LUMO+2 respectively.

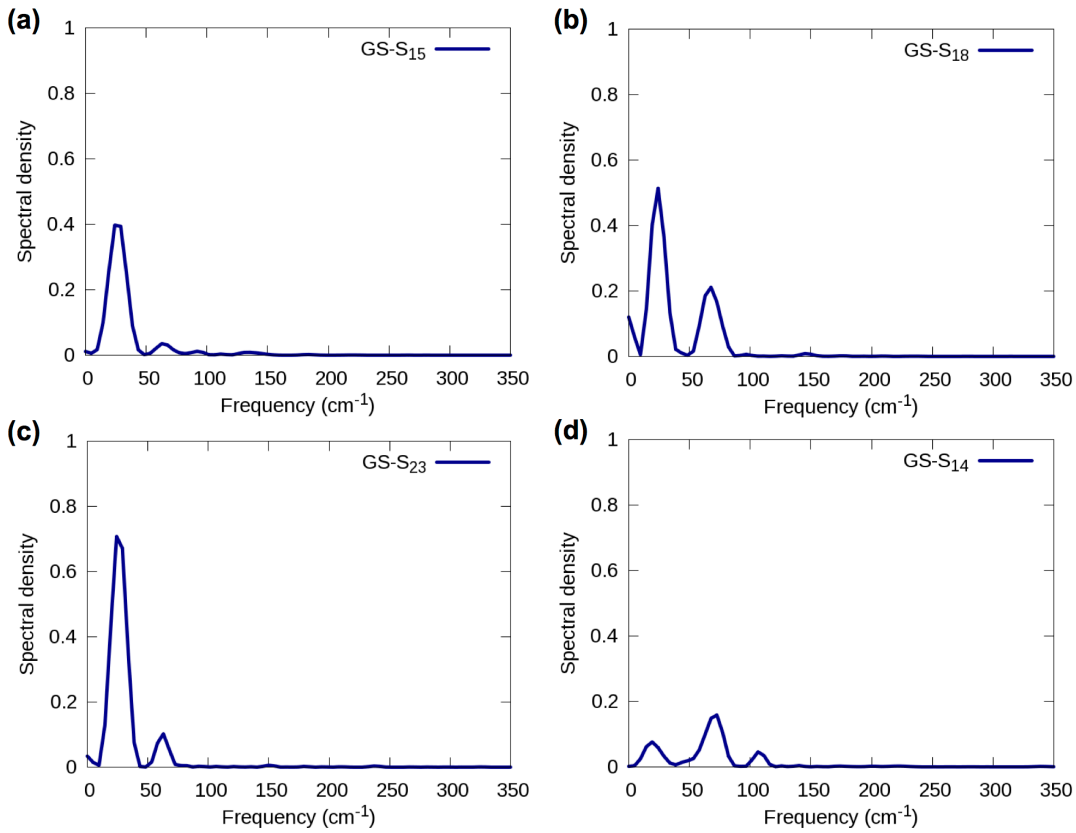

Figure 6.6 Fourier transforms of autocorrelation functions of the fluctuations of the energy gaps (phonon spectral density spectra) between (a) GS-S_{15} (b) GS-S_{18} (c) GS-S_{23} (d) GS-S_{14}.

To correlate the observed vibrational frequencies to the $Au_{38}(SR)_{24}$ cluster geometry, we compared the phonon modes obtained by the NA-MD calculation to the ground state frequency calculation performed with ADF. The ADF frequency calculation gave several interesting vibrational modes arising from the gold core as well as from semiring motifs. A clear "bending mode" of the bi-icosahedral Au_{23} core at its interior 3-fold face was observed at a very low frequency of 23.5 cm^{-1} and a "fan blade twisting" of two icosahedral units was also observed at 25.9 cm^{-1} (Figure 6.7). Several other core, semiring and mixed core-semiring vibrational modes were observed in the low frequency range of 27.4 – 43.5 cm^{-1}. Gold core vibrations were noted in the range of 43.5 – 49.2 cm^{-1} including a core breathing mode around 45.1 cm^{-1}. Frequencies in the range of 90.4 – 96.3 cm^{-1} correspond to semiring bending vibrations. Other prominent gold core vibrations are present at a higher frequency of 104.7 cm^{-1} and in the range of 121.1 – 148.3 cm^{-1}. Vibrational modes found in the range of 219.5 – 293.6 cm^{-1} are primarily the Au(core)-S and Au(I)-S stretching modes.

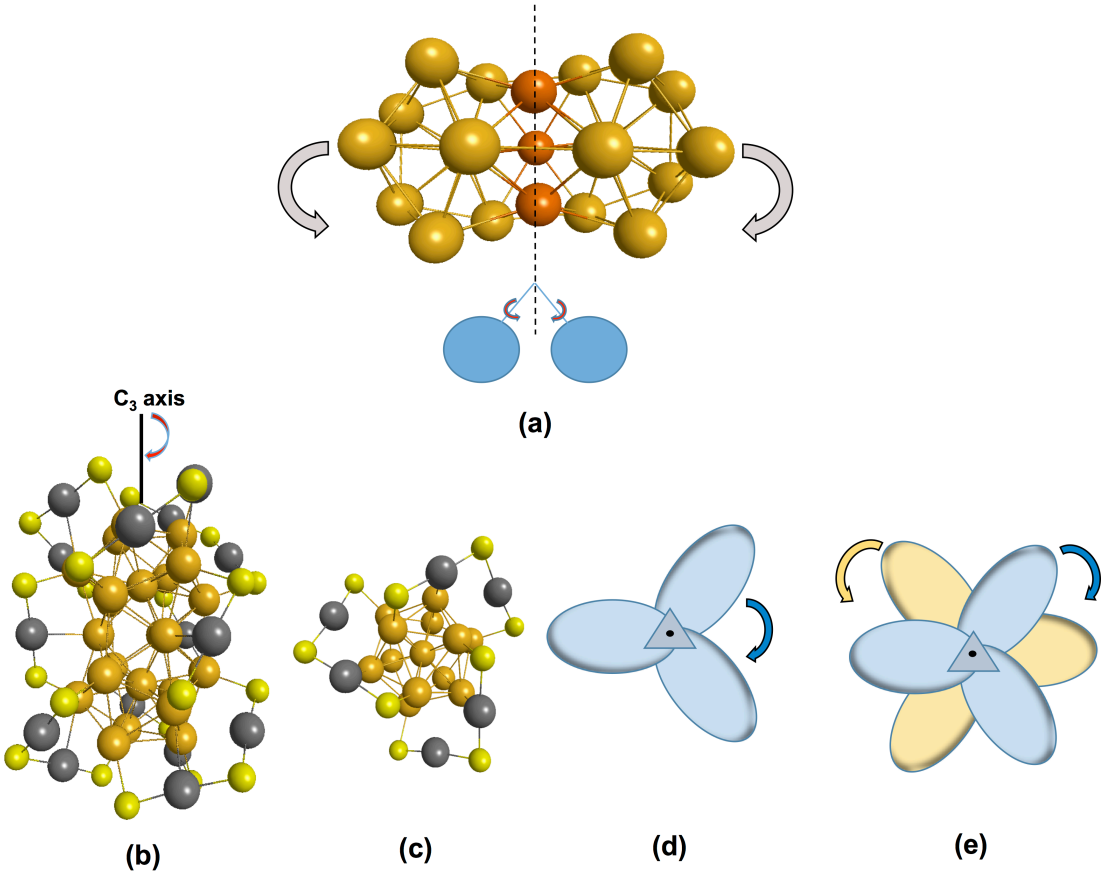

Figure 6.7 (a) "Bending mode" of the bi-icosahedral Au_{23} core at its interior 3-fold face; (b) side view of the $Au_{38}(SR)_{24}$ cluster, with R ligands not shown; (c) geometric model of three $Au_2(SR)_3$ semirings: top view; (d) fan blade resemblance of the three $Au_2(SR)_3$ semirings (e) "fan blade twisting" mode. (core Au-gold, 3-fold face Au-orange, semiring Au-grey, S-yellow).

It is possible that the intense frequency in the phonon spectral density that we observe around 24.4 cm^{-1} from NA-MD calculations is the bending of the bi-icosahedral Au_{23} core or the "fan blade twisting" of two icosahedral units (Figure 6.7), which could largely lead to nonradiative relaxation of the $Au_{38}(SH)_{24}$ nanocluster. Similarly, the low frequency coherent phonon emission reported at 25 cm^{-1} by Jin and co-workers[25] could also be the bending of the bi-icosahedral Au_{23} core or the "fan blade twisting" mode of two icosahedral units. In addition, there is a very small vibrational mode around 106.5 cm^{-1} in Figure 6.6d which could be the gold core breathing vibration appearing around 104.7 cm^{-1} in the ADF frequency calculation.

6.5 Conclusion

TDDFT and a time-dependent Kohn−Sham description of electron-vibrational dynamics (FSSH-TDKS) have been used to understand the nonradiative relaxations in the $Au_{38}(SH)_{24}$ nanocluster. The orbital energy variation during the MD simulation indicated a loss of exact degeneracies in orbitals due to geometrical distortions in the cluster during the dynamics. The $Au_{38}(SH)_{24}$ has a small HOMO-LUMO gap during the MD simulation which is ~ 0.75 eV. The relaxation dynamics performed on the S_1, S_2, S_6, and S_7 states both with and without an energy correction of 0.15 eV showed that the correction lengthens the GS growth times only by 16-30%.

The GS growth times and excited state decay times were calculated for excited states up to ~ 1.5 eV which covers the Au_{23} core states (S_1-S_{25}). The GS growth times of the S_1-S_{25} states were found to be in the range of 6.4 – 207 ps, which are 1-2 orders of magnitude shorter than the growth times reported for the $[Au_{25}(SH)_{18}]^{-1}$ nanocluster. The S_{11} state (HOMO-2→LUMO) gives the slowest decay time constant (~ 8.2 ps). Population transfer was observed between S_{11} and S_{12}. Fitting the total population of the S_{11} and S_{12} to an exponential resulted in a decay constant of 9.7 ps. Initial excitations of the S_5, S_6 and S_{10} states gave slow population decay in the range of 9.6 -10.7 ps, which is similar to that for the initially excited S_{11} state. The slowest state decays involve intracore relaxations.

Relaxation dynamics of the higher excited states covering up to ~ 2.01 eV involve relaxations coming from the core, mixed core-semiring, and semiring states (S_1-S_{98}). The relaxation trends of the S_1-S_{25} states were preserved in the presence of all ninety-eight states. Fitting the S_{11} (HOMO-2→LUMO) population to an exponential gave a relatively slow decay time constant of 7.6 ps. Fitting the total population of S_{11} and S_{12} to an exponential gave a time constant of 8.8 ps. The excitations of the S_5, S_6 and S_{10} states decay gave slow time constants in the range of 9.7-10.8 ps. Higher excited states S_{26}-S_{35} have decay time constants in the range of 1.4 - 4.9 ps. The S_{36}-S_{98} states, which consist of transitions out of the semiring orbitals, have shorter time constants in the range of 0.6 -1.7 ps.

Nonradiative relaxation of the $Au_{38}(SH)_{24}$ excited states are driven by nanocluster vibrations. The analysis of the phonon spectral densities showed peaks around 24.2, 33.9, 48.4 and 53.2 cm^{-1} from the NA-MD calculations. The ADF ground state frequency calculation gave several interesting vibrational modes arising from the gold core as well as from semiring motifs. Among them, the low frequency “bending mode” of the bi-icosahedral Au_{23} core at 23.5 cm^{-1}

and the "fan blade twisting" mode of two icosahedral units observed at 25.9 cm^{-1} were prominent. One or both of these vibrational modes could be the origin of the low frequency coherent phonon emission experimentally reported at 25 cm^{-1}.

6.6 Acknowledgments

This material is based on work supported by Department of Energy under grants DE-SC0012273 to CMA and DE-SC0014429 to OVP. The computing for this project was performed on the computing for this project was performed on the Beocat Research Cluster at Kansas State University, which is funded in part by NSF grants CHE-1726332, CNS-1006860, EPS-1006860, and EPS-0919443. Beocat Application Scientist Dr. Dave Turner provided valuable technical expertise. The authors are grateful to Prof. Alexey V. Akimov for his support and valuable discussions on PYXAID.

6.7 References

1. Herzing, A. A.; Kiely, C. J.; Carley, A. F.; Landon, P.; Hutchings, G. J., Identification of Active Gold Nanoclusters on Iron Oxide Supports for CO Oxidation. *Science* **2008,** *321* (5894), 1331-1335.

2. Yamazoe, S.; Koyasu, K.; Tsukuda, T., Nonscalable Oxidation Catalysis of Gold Clusters. *Acc. Chem. Res.* **2013,** *47* (3), 816-824.

3. Ide, Y.; Matsuoka, M.; Ogawa, M., Efficient Visible-light-induced Photocatalytic Activity on Gold-Nanoparticle-supported Layered Titanate. *J. Am. Chem. Soc.* **2010,** *132* (47), 16762-16764.

4. Sarina, S.; Waclawik, E. R.; Zhu, H., Photocatalysis on Supported Gold and Silver Nanoparticles Under Ultraviolet and Visible Light Irradiation. *Green Chem.* **2013,** *15* (7), 1814-1833.

5. Primo, A.; Corma, A.; García, H., Titania Supported Gold Nanoparticles as Photocatalyst. *Phys. Chem. Chem. Phys.* **2011,** *13* (3), 886-910.

6. Alvaro, M.; Cojocaru, B.; Ismail, A. A.; Petrea, N.; Ferrer, B.; Harraz, F. A.; Parvulescu, V. I.; Garcia, H., Visible-light Photocatalytic Activity of Gold Nanoparticles Supported on Template-synthesized Mesoporous Titania for the Decontamination of the Chemical Warfare Agent Soman. *Appl. Catal., B: Environmental* **2010,** *99* (1-2), 191-197.

7. Yau, S. H.; Varnavski, O.; Goodson III, T., An Ultrafast Look at Au Nanoclusters. *Acc. Chem. Res.* **2013,** *46* (7), 1506-1516.

8. Qian, H.; Sfeir, M. Y.; Jin, R., Ultrafast Relaxation Dynamics of $[Au_{25}(SR)_{18}]^{q}$ Nanoclusters: Effects of Charge State. *J. Phys. Chem. C* **2010,** *114* (47), 19935-19940.

9. Sfeir, M. Y.; Qian, H.; Nobusada, K.; Jin, R., Ultrafast Relaxation Dynamics of Rod-shaped 25-atom Gold Nanoclusters. *J. Phys. Chem. C* **2011,** *115* (14), 6200-6207.

10. Pelton, M.; Tang, Y.; Bakr, O. M.; Stellacci, F., Long-lived Charge-separated States in Ligand-stabilized Silver Clusters. *J. Am. Chem. Soc.* **2012,** *134* (29), 11856-11859.

11. Mustalahti, S.; Myllyperkiö, P.; Lahtinen, T.; Salorinne, K.; Malola, S.; Koivisto, J.; Häkkinen, H.; Pettersson, M., Ultrafast Electronic Relaxation and Vibrational Cooling Dynamics of $Au_{144}(SC_2H_4Ph)_{60}$ Nanocluster Probed by Transient Mid-IR Spectroscopy. *J. Phys. Chem. C* **2014,** *118* (31), 18233-18239.

12. Mustalahti, S.; Myllyperkiö, P.; Lahtinen, T.; Malola, S.; Salorinne, K.; Tero, T.-R.; Koivisto, J.; Häkkinen, H.; Pettersson, M., Photodynamics of a Molecular Water-Soluble Nanocluster Identified as Au_{130}(p MBA)$_{50}$. *J. Phys. Chem. C* **2015,** *119* (34), 20224-20229.

13. Devadas, M. S.; Kwak, K.; Park, J.-W.; Choi, J.-H.; Jun, C.-H.; Sinn, E.; Ramakrishna, G.; Lee, D., Directional Electron Transfer in Chromophore-labeled Quantum-Sized Au_{25} Clusters: Au_{25} as an Electron Donor. *J. Phys. Chem. Lett.* **2010,** *1* (9), 1497-1503.

14. Jin, R.; Zeng, C.; Zhou, M.; Chen, Y., Atomically Precise Colloidal Metal Nanoclusters and Nanoparticles: Fundamentals and Opportunities. *Chem. Rev.* **2016,** *116* (18), 10346-10413.

15. Tian, S.; Li, Y.-Z.; Li, M.-B.; Yuan, J.; Yang, J.; Wu, Z.; Jin, R., Structural Isomerism in Gold Nanoparticles Revealed by X-ray Crystallography. *Nat. Commun.* **2015,** *6*, 8667.

16. Zhu, M.; Aikens, C. M.; Hollander, F. J.; Schatz, G. C.; Jin, R., Correlating the Crystal Structure of a Thiol-protected Au_{25} Cluster and Optical Properties. *J. Am. Chem. Soc.* **2008,** *130* (18), 5883-5885.

17. Zhou, M.; Qian, H.; Sfeir, M. Y.; Nobusada, K.; Jin, R., Effects of Single Atom Doping on the Ultrafast Electron Dynamics of $M_1Au_{24}(SR)_{18}$ (M= Pd, Pt) Nanoclusters. *Nanoscale* **2016,** *8* (13), 7163-7171.

18. Thanthirige, V. D.; Kim, M.; Choi, W.; Kwak, K.; Lee, D.; Ramakrishna, G., Temperature-Dependent Absorption and Ultrafast Exciton Relaxation Dynamics in $MAu_{24}(SR)_{18}$ Clusters (M= Pt, Hg): Role of the Central Metal Atom. *J. Phys. Chem. C* **2016,** *120* (40), 23180-23188.

19. Link, S.; El-Sayed, M. A.; Schaaff, T. G.; Whetten, R. L., Transition From Nanoparticle to Molecular Behavior: A Femtosecond Transient Absorption Study of a Size-Selected 28 Atom Gold Cluster. *Chem. Phys. Lett.* **2002,** *356* (3-4), 240-246.

20. Miller, S. A.; Womick, J. M.; Parker, J. F.; Murray, R. W.; Moran, A. M., Femtosecond Relaxation Dynamics of $Au_{25}L_{18}^{-}$ Monolayer-protected Clusters. *J. Phys. Chem. C* **2009,** *113* (22), 9440-9444.

21. Green, T. D.; Knappenberger, K. L., Relaxation Dynamics of Au_{25} L_{18} Nanoclusters Studied by Femtosecond Time-resolved Near Infrared Transient Absorption Spectroscopy. *Nanoscale* **2012,** *4* (14), 4111-4118.

22. Stamplecoskie, K. G.; Chen, Y.-S.; Kamat, P. V., Excited-state Behavior of Luminescent Glutathione-Protected Gold Clusters. *J. Phys. Chem. C* **2014,** *118* (2), 1370-1376.

23. Chen, X.; Prezhdo, O. V.; Ma, Z.; Hou, T.; Guo, Z.; Li, Y., Ab initio Phonon-coupled Nonadiabatic Relaxation Dynamics of $[Au_{25}(SH)_{18}]^-$ clusters. *physica status solidi (b)* **2016,** *253* (3), 458-462.

24. Senanayake, R. D.; Akimov, A. V.; Aikens, C. M., Theoretical Investigation of Electron and Nuclear Dynamics in the $[Au_{25}(SH)_{18}]^{-1}$ Thiolate-Protected Gold Nanocluster. *J. Phys. Chem. C* **2016,** *121* (20), 10653-10662.

25. Zhou, M.; Tian, S.; Zeng, C.; Sfeir, M. Y.; Wu, Z.; Jin, R., Ultrafast Relaxation Dynamics of $Au_{38}(SC_2H_4Ph)_{24}$ Nanoclusters and Effects of Structural Isomerism. *J. Phys. Chem. C* **2017,** *121* (20), 10686-10693.

26. Green, T. D.; Yi, C.; Zeng, C.; Jin, R.; McGill, S.; Knappenberger Jr, K. L., Temperature-dependent Photoluminescence of Structurally-precise Quantum-Confined $Au_{25}(SC_8H_9)_{18}$ and $Au_{38}(SC_{12}H_{25})_{24}$ metal nanoparticles. *J. Phys. Chem. A* **2014,** *118* (45), 10611-10621.

27. Qian, H.; Eckenhoff, W. T.; Zhu, Y.; Pintauer, T.; Jin, R., Total Structure Determination of Thiolate-protected Au_{38} Nanoparticles. *J. Am. Chem. Soc.* **2010,** *132* (24), 8280-8281.

28. Lopez-Acevedo, O.; Tsunoyama, H.; Tsukuda, T.; Hakkinen, H.; Aikens, C. M., Chirality and Electronic Structure of the Thiolate-protected Au_{38} Nanocluster. *J. Am. Chem. Soc.* **2010,** *132* (23), 8210-8218.

29. Pei, Y.; Gao, Y.; Zeng, X. C., Structural Prediction of Thiolate-protected Au_{38}: a Face-fused bi-icosahedral Au Core. *J. Am. Chem. Soc.* **2008,** *130* (25), 7830-7832.

30. Knoppe, S.; Bürgi, T., Chirality in Thiolate-protected Gold Clusters. *Acc. Chem. Res.* **2014,** *47* (4), 1318-1326.

31. Xu, Q.; Kumar, S.; Jin, S.; Qian, H.; Zhu, M.; Jin, R., Chiral 38-Gold-Atom Nanoclusters: Synthesis and Chiroptical Properties. *Small* **2014,** *10* (5), 1008-1014.

32. Yamazoe, S.; Takano, S.; Kurashige, W.; Yokoyama, T.; Nitta, K.; Negishi, Y.; Tsukuda, T., Hierarchy of Bond Stiffnesses within Icosahedral-based Gold Clusters Protected by Thiolates. *Nat. Commun.* **2016,** *7*, 10414.

33. Negishi, Y.; Igarashi, K.; Munakata, K.; Ohgake, W.; Nobusada, K., Palladium Doping of Magic Gold cluster $Au_{38}(SC_2H_4Ph)_{24}$: Formation of $Pd_2Au_{36}(SC_2H_4$ $Ph)_{24}$ with Higher Stability than $Au_{38}(SC_2H_4Ph)_{24}$. *ChemComm* **2012,** *48* (5), 660-662.

34. Nie, X.; Zeng, C.; Ma, X.; Qian, H.; Ge, Q.; Xu, H.; Jin, R., CeO_2-supported $Au_{38}(SR)_{24}$ Nanocluster Catalyst for CO Oxidation: A Comparison of Ligands-on and -Off Catalysts. *Nanoscale* **2013,** *5*, 5912−5918.

35. Weerawardene, K. D. M.; Guidez, E. B.; Aikens, C. M., Photoluminescence Origin of $Au_{38}(SR)_{24}$ and $Au_{22}(SR)_{18}$ Nanoparticles: A Theoretical Perspective. *J. Phys. Chem. C* **2017,** *121* (28), 15416-15423.

36. Weerawardene, K. D. M.; Aikens, C. M., Theoretical Insights into the Origin of Photoluminescence of $Au_{25}(SR)_{18}$–Nanoparticles. *J. Am. Chem. Soc.* **2016,** *138* (35), 11202-11210.

37. Tully, J., Mixed Quantum–classical Dynamics. *Faraday Discuss.* **1998,** *110*, 407-419.

38. Craig, C. F.; Duncan, W. R.; Prezhdo, O. V., Trajectory Surface Hopping in the Time-dependent Kohn-Sham Approach for Electron-nuclear Dynamics. *Phys. Rev. Lett.* **2005,** *95* (16), 163001.

39. Jaeger, H. M.; Fischer, S.; Prezhdo, O. V., Decoherence-induced Surface Hopping. *J. Chem. Phys.* **2012,** *137* (22), 22A545.

40. Akimov, A. V.; Prezhdo, O. V., The PYXAID Program for Non-Adiabatic Molecular Dynamics in Condensed Matter Systems. *J. Chem. Theory Comput.* **2013,** *9* (11), 4959-4972.

41. Akimov, A. V.; Prezhdo, O. V., Advanced Capabilities of the PYXAID Program: Integration Schemes, Decoherence Effects, Multiexcitonic States, and Field-Matter Interaction. *J. Chem. Theory Comput.* **2014,** *10* (2), 789-804.

42. Perdew, J. P.; Burke, K.; Ernzerhof, M., Generalized Gradient Approximation Made Simple. *Phys. Rev. Lett.* **1996,** *77* (18), 3865.

43. Te Velde, G. t.; Bickelhaupt, F. M.; Baerends, E. J.; Fonseca Guerra, C.; van Gisbergen, S. J.; Snijders, J. G.; Ziegler, T., Chemistry with ADF. *J. Comput. Chem.* **2001,** *22* (9), 931-967.

44. Lenthe, E. v.; Baerends, E.-J.; Snijders, J. G., Relativistic Regular Two-Component Hamiltonians. *J. Chem. Phys.* **1993,** *99* (6), 4597-4610.

45. Kresse, G.; Furthmüller, J., Efficiency of Ab-initio Total Energy Calculations for Metals and Semiconductors using a Plane-wave Basis Set. *Comput. Mater. Sci.* **1996,** *6* (1), 15-50.

46. Kresse, G.; Joubert, D., From Ultrasoft Pseudopotentials to the Projector Augmented-wave Method. *Phys. Rev. B* **1999,** *59* (3), 1758.

47. Tsunoyama, H.; Nickut, P.; Negishi, Y.; Al-Shamery, K.; Matsumoto, Y.; Tsukuda, T., Formation of alkanethiolate-protected gold clusters with unprecedented core sizes in the thiolation of polymer-stabilized gold clusters. *J. Phys. Chem. C* **2007,** *111* (11), 4153-4158.

48. Qian, H.; Zhu, Y.; Jin, R., Size-focusing Synthesis, Optical and Electrochemical Properties of Monodisperse $Au_{38}(SC_2H_4Ph)_{24}$ nanoclusters. *ACS nano* **2009,** *3* (11), 3795-3803.

Chapter 7 - Relaxation Dynamics in the $[Ag_{25}(SR)_{18}]^{-1}$ Thiolate-protected Silver Nanocluster

7.1 Abstract

With the discovery of the "golden" silver nanoparticle $[Ag_{25}(SR)_{18}]^{-1}$, evaluation of its electron nuclear dynamics and relaxation mechanism compared to its well-known gold analog, $[Au_{25}(SR)_{18}]^{-1}$, will be important for future photocatalytic, light harvesting and photoluminescence applications of this system. Relaxation dynamics of the $[Ag_{25}(SR)_{18}]^{-1}$ thiolate-protected silver nanoparticle were investigated using time-dependent density functional theory and surface hopping method with decoherence correction in a real-time DFT approach. The GS recovery times of the S_1-S_6 states in the first excited peak were found to be longer than the corresponding GS recovery times of the Au_{25} nanocluster. The decay time constants were in the range of 2.0-20 ps for the S_1−S_6 states. Both silver and gold clusters follow similar trends in decay times among the first six states S_1−S_6, which are involved in the first excitation peak in their respective optical absorption spectra. In the presence of the higher excited states (with energy up to ~2.30 eV), the S_1−S_6 states had similar decay time constants. Among the higher excited states, S_7 has the slowest decay time constant while S_1 decay is the slowest among all states. Overall, $[Ag_{25}(SH)_{18}]^{-1}$ and $[Au_{25}(SH)_{18}]^{-1}$ both follow common decay time constant trends and relaxation mechanisms due to the similarities in their electronic structures.

7.2 Introduction

Thiolate-protected metal cluster are of great importance due to their potential applications in solar cells, light harvesting and photoluminescence.[1-18] Numerous experimental studies have been performed on thiolate-protected gold nanoclusters to understand their nonradiative relaxation mechanisms[15-17, 19-25] but fewer theoretical studies have been performed.[26-27]

Gold and silver are similar in their atomic sizes, geometric structures, and in their bulk lattices and lattice constants. Irrespective of their similarities in structure, they possess distinct physical and chemical properties. Over the past years, a great number of atomically precise, monolayer protected gold clusters have been characterized using X-ray crystallography,[1, 28-33]

whereas only a few silver clusters have been crystallized.[34-39] After the discovery of the $[Au_{25}(SR)_{18}]^{-1}$ cluster (abbreviated as Au_{25} in the text), Aikens described the electronic structure of an identical Ag_{25} cluster using time dependent density functional method.[40-41] In 2015, Bakr and co-workers crystallized a thiolate-protected silver nanocluster $[Ag_{25}(SR)_{18}]^{-1}$ that is an exact analog of $[Au_{25}(SR)_{18}]^{-1}$ in terms of size, superatom electronic configuration, charge and composition. Thus, this allows researchers to perform direct comparison of properties of thiolate-protected silver and gold nanoclusters. The $[Ag_{25}(SR)_{18}]^{-1}$ cluster consists of an Ag_{13} icosahedral core protected by six V-shaped -S-Ag-S-Ag-S- motifs with an overall quasi-T_h symmetry similar to its gold analog.[42]

Many experimental nonradiative relaxation dynamics investigations on thiolate-protected noble metal nanoclusters have been performed on the $[Au_{25}(SR)_{18}]^{-1}$ nanocluster. [15-17, 19-22] Different research groups have proposed several different mechanisms for the nonradiative relaxation mechanism of $[Au_{25}(SR)_{18}]^{-1}$.[15-17, 19-22] Transient spectroscopy experiments have been done on a ligand-stabilized silver cluster, $[Ag_{44}(SR)_{30}]^{4-}$ to understand the time-dependent optical properties. It has shown a rapid decay of ~1 ps and a slow decay of ~300 ns which has a dependency on the polarity of the solvent used. Experimental work has also been done on a luminescent rod-shaped, silver-doped Ag_xAu_{25-x} clusters to understand the ultrafast relaxation dynamics.[24] They report an ultrafast excited state relaxation (~0.58 ps), which is an internal conversion and a subsequent nuclear relaxation (~20.7 ps) in Ag_xAu_{25-x}. They have observed a faster nuclear relaxation in doped systems compared to that in undoped.

A recent theoretical study using ab initio real-time nonadiabatic molecular dynamics (NA-MD) simulations was performed by our group to understand the electron relaxation dynamics of the Au_{25} cluster.[27] There, we suggested that the time constants observed experimentally[17] could arise from core-to-core transitions rather than from a core-to-semiring transition; no semiring or other states were observed at lower energy than the core-based S_1 state.[27]

As of now, there are no reports of experimental or theoretical work performed to understand the nonradiative relaxation dynamics of thiolate-protected silver nanoclusters which is an exact analog of a thiolate-protected gold nanocluster. With the discovery of the "golden" silver nanoparticle $[Ag_{25}(SR)_{18}]^{-1}$,[42] it will be important to assess the applicability of the relaxation mechanism proposed for the $[Au_{25}(SR)_{18}]^{-1}$ nanocluster to its silver analog. Herein, we

perform electron nuclear dynamics to reveal the relaxation mechanism for excited electrons in the "golden" silver nanoparticle $[Ag_{25}(SR)_{18}]^{-1}$.

7.3 Computational methodology

We have performed ab initio real-time nonadiabatic molecular dynamics (NA-MD) simulations to study the nonadiabatic dynamics in the $[Ag_{25}(SR)_{18}]^{-1}$ nanocluster. The procedure used is similar to our previous study of $[Au_{25}(SR)_{18}]^{-1}$ relaxation dynamics.[27]

The NA-MD simulations were performed using a fewest switches surface hopping (FSSH)[43] algorithm with the classical path approximation and a time-dependent Kohn−Sham description of electronic states (FSSH-TDKS).[44] The decoherence-induced surface hopping (DISH)[45] scheme is utilized to include decoherence effects. The FSSH simulations are performed using the PYXAID program.[46-47]

The $[Ag_{25}(SR)_{18}]^{-1}$ nanocluster geometry optimization was performed with the PBE[48]/TZP level of theory in the Amsterdam Density Functional (ADF)[49] software package to obtain the relaxed geometry at 0K. The zero-order regular approximation (ZORA)[50] was used to treat the scalar relativistic effects in silver. Linear response time-dependent density functional theory (TD-DFT) calculations were performed using the same level of theory to calculate the electronic excited states and the relevant absorption spectra of $[Ag_{25}(SR)_{18}]^{-1}$.

Then, the 0K system was thermalized through a temperature ramping calculation performed at 300K. After the temperature ramping, molecular dynamics (MD) simulations were performed using density functional theory (DFT) calculations with the Vienna Ab initio Simulation Package (VASP).[51] We used projector-augmented wave (PAW)[52] pseudopotentials, a kinetic energy cutoff value of 402.0 eV for the temperature ramping calculation and 301.8 eV energy cutoff value for the MD and NA coupling calculations, a 24 Å simulation box size, gamma points, and the PBE functional in our all VASP calculations. The MD trajectory of 5 ps in length was computed with a 1 fs integration time step.

The nonadiabatic coupling elements were calculated following the same approach we used for the $[Au_{25}(SH)_{18}]^{-1}$ system.[27] The NA-MD calculations were performed considering 3.5 ps length sub-trajectories resulting in 10 different starting geometries. For each NA-MD trajectory, 1000 realizations of the stochastic FSSH/DISH state hopping trajectories were considered.

The important electronic excited states contributing to the optical absorption spectrum of $[Ag_{25}(SR)_{18}]^{-1}$ in the energy range of 0.00−2.30 eV (visible range) were analyzed. An energy correction was considered for several excited states in order to evaluate impact of the energy correction on the dynamics. These corrections are used to compensate for underestimation/overestimation in the calculated DFT band gaps compared to the experimental gaps. The decay times of the excited states populations and the ground state population increase times were calculated for the $[Ag_{25}(SR)_{18}]^{-1}$ nanocluster using the same equations and procedure mentioned in our previous study.

7.4 Results and discussion

The $[Ag_{25}(SH)_{18}]^{-1}$ theoretical absorption spectrum (Figure 7.1) calculated at the PBE/TZP level of theory gives strong peaks around 1.66, 2.25, 2.47 and 2.75 eV. The first peak at 1.66 eV is blueshifted compared to the 1.41 eV peak of Au_{25}, whereas the second peak at 2.25 eV is redshifted compared to the 2.50 eV peak of Au_{25} at the same level of theory.[27] This behavior is also shown in experimental spectra.[42] The peak positions obtained in the current study are similar to the peak positions obtained for $[Ag_{25}(SH)_{18}]^{-1}$ using SAOP/TZP level of theory by Aikens.[41] Also, the theoretical peak positions are redshifted compared to the significant peaks 1.84, 2.53 and 3.18 observed experimentally.[42] The redshifting of the theoretical peaks compared to experiment has also been observed for the well-known Au_{25} cluster.[28] However, the redshifting of the first peak in the silver cluster is less than that of the gold cluster. According to Aikens, the first peak of the $[Ag_{25}(SH)_{18}]^{-1}$ originates from the HOMO→ LUMO transition where the HOMO is nearly triply degenerate and LUMO is nearly doubly degenerate similar to the Au_{25} analog.[41] The HOMO and LUMO of $[Ag_{25}(SH)_{18}]^{-1}$ are both silver core based orbitals.[41]

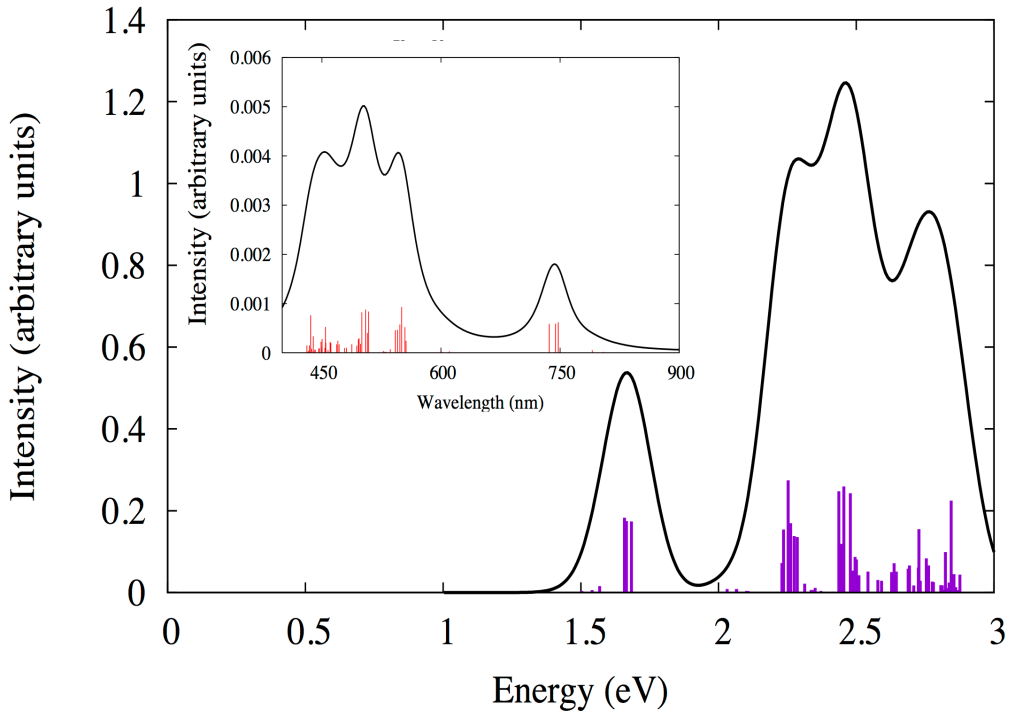

Figure 7.1 Calculated PBE/TZP optical absorption spectrum for $[Ag_{25}(SH)_{18}]^{-1}$. Inset: The absorption spectrum in wavelength (nm).

7.4.1 Relaxation dynamics of the first excited state peak

In the following sections, the electronic relaxations of the $[Ag_{25}(SH)_{18}]^{-1}$ cluster are analyzed. First, the 1.66 eV peak is examined in order to understand its relaxations. Table 7.1 shows the important excitations involved in the first peak at 1.66 eV based on their oscillator strengths and weights. Because the $[Ag_{25}(SH)_{18}]^{-1}$ cluster has similar electronic structure to its gold analog, similarities in their excitations can be noted. Three main excitations involving the HOMO-2 to LUMO+1 orbitals in the most probable transitions give rise to the 1.66 eV peak (Table 7.1), which was also the case for the Au_{25} cluster.

Table 7.1 TDDFT transitions with the highest weights for prominent excited states for $[Ag_{25}(SH)_{18}]^{-1}$.

Excited state	Energy (eV)	Oscillator strength	Weight	Most weighted transitions
4	1.66	0.0389	0.3386	HOMO-2 → LUMO
			0.2451	HOMO-2 → LUMO+1
			0.145	HOMO → LUMO
			0.1026	HOMO-1 → LUMO
5	1.67	0.0372	0.2869	HOMO → LUMO+1
			0.2217	HOMO-2 → LUMO
			0.1525	HOMO-2 → LUMO+1
			0.1252	HOMO-1 → LUMO+1
			0.1236	HOMO-1 → LUMO
6	1.68	0.0370	0.5256	HOMO-1 → LUMO+1
			0.2674	HOMO → LUMO+1
			0.0624	HOMO-2 → LUMO
			0.0611	HOMO-2 → LUMO+1

Even though the HOMO, HOMO-1, and HOMO-2 are nearly triply degenerate and the LUMO and LUMO+1 are nearly doubly degenerate. Therefore, we can use the same FSSH-TDKS defined excited states (S_1 - S_6) as in our previous Au_{25} simulations.[36] The HOMO-2 to LUMO+1 orbitals are all silver core-based orbitals. The silver core-based orbitals are primarily composed of the 5s orbitals of silver with some contribution from the silver 4d atomic orbitals.[41]

The orbital energy variation in $[Ag_{25}(SH)_{18}]^{-1}$ obtained during the MD simulation is shown in Figure 7.2. The near degeneracies of the HOMO, HOMO-1, HOMO-2 and LUMO, LUMO+1 are apparent, similar to the Au_{25} analog. The HOMO-LUMO gap of the silver cluster varies around 1.15 eV during the MD simulation. This gap is ~0.33 eV smaller than the optical gap of ~1.48 eV (~840 nm) found from the experimental optical absorption spectrum reported by Bakr and co-workers.[42] Therefore, it is important to add a correction to the excited states to compensate for the underestimation in the calculated DFT optical band gap compared to the experimental. Our previous relaxation dynamics calculations on the Au_{25} analog showed that the inclusion of the correction lengthens the ground state growth times, but had minor effects on the overall excited state lifetimes.[27] In our current work, a 0.33 eV energy correction is employed in our calculations on $[Ag_{25}(SH)_{18}]^{-1}$.

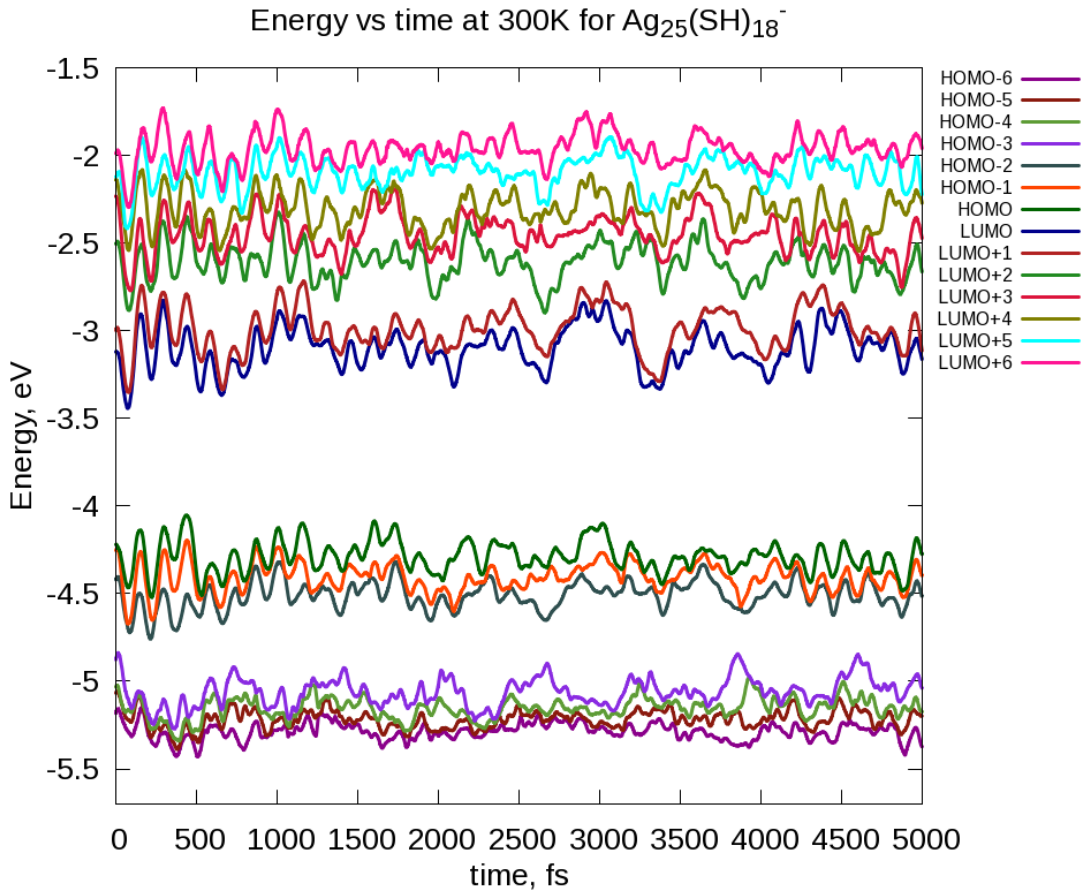

Figure 7.2 Variation of the HOMO−6 to LUMO+6 orbital energies with time.

We performed two different calculation sets, one considering the original energy gaps and another including the 0.33 eV energy correction on the S_1-S_6 excited states.

Figure 7.3 shows the computed population dynamics for the S_1-S_6 states. The population dynamics performed with the energy correction are shown in Figure E.1 due to their similar relaxation patterns. Both the excited state population decays and the GS population increase times are determined for S_1-S_6 states. The population relaxation curves for S_1-S_6 states show "step relaxation" behavior where the population of a state transfers rapidly to another state. For example, the S_2(HOMO → LUMO+1) state quickly transfers its population to the S_1(HOMO → LUMO) state during the 2700-3200 fs time frame in Figure 7.3b. There are rapid population transfers from S_5(HOMO → 2-LUMO) to S_3(HOMO-1 → LUMO) (Figure 7.3e) and S_6(HOMO-2 → LUMO+1) to S_4(HOMO-1 → LUMO+1) (Figure 7.3f) during the 1000-2000 fs time frames. A rapid population transfer could arise due to near-degeneracies that arise in the orbitals that are involved in these states during the MD simulation. During the ~ 2600-3400 fs time frame

from the MD simulations, near-degeneracy can be observed in the LUMO and LUMO+1 orbitals. During that time frame, the S_2 and S_1 states have close energies which promote a rapid population transfer among these states. Similar explanations can be given to population transfers between S_5 to S_3 and S_6 to S_4. During the ~1100-2100 fs time frame, the HOMO-1 and HOMO-2 orbitals show degeneracies which will stimulate the S_5 to S_3 and S_6 to S_4 population transfers. The relaxation patterns of states S_1 and S_2 are similar to that of the Au_{25} cluster whereas the states S_3-S_6 demonstrate slight differences. For example, the S_5 state rapidly transfers its population to the S_3 state (Figure 7.3e) and the S_6 state relaxes to S_4 (Figure 7.3f), which are hole relaxations.

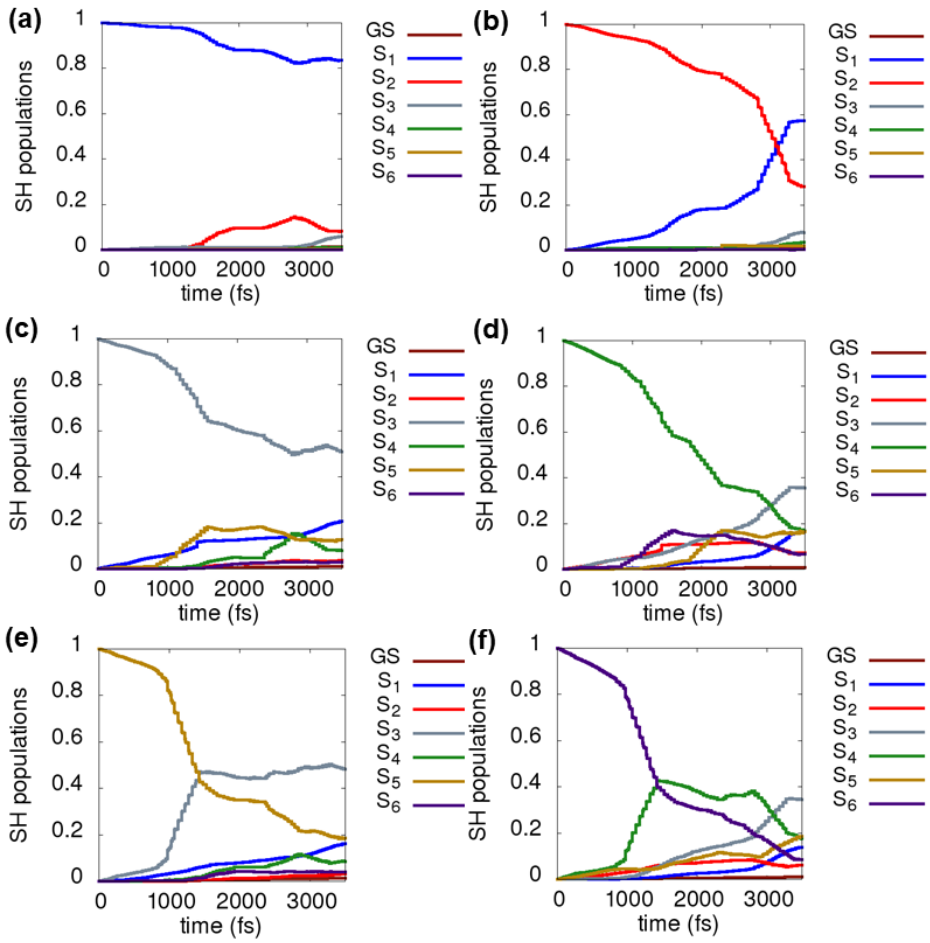

Figure 7.3 Evolution of the populations of S_1, S_2, S_3, S_4, S_5, S_6 states. Panels a−f are relaxations from S_1 to S_6, respectively, without the energy correction.

Even without considering the correction, the GS growth times (Table 7.2) of the $[Ag_{25}(SH)_{18}]^{-1}$ are much longer than the corresponding growth times (73-158 ps)[27] of the Au_{25} cluster. A reason could be that the underestimation of the DFT HOMO-LUMO gap of silver is smaller (0.33 eV) than the underestimation in the gold cluster (0.55 eV). Also, the LUMO and LUMO+1, HOMO to HOMO-2 orbitals in Ag_{25} are closer in energy (Figure 7.2) than in Au_{25} cluster. Because of this, there can be rapid population transfers in-between the core states in Ag_{25} than in Au_{25} which makes the repopulation of the GS harder. For example, the S_1 state population transfers into the S_2 and then the S_2 population is transferred back to the S_1 (Figure 7.3a,b) much faster than in Au_{25}. During the MD simulation, the average HOMO-LUMO gap of the Ag_{25} cluster is around ~1.19 eV, whereas the Au_{25} cluster had a slightly lower gap of ~1.09

eV. This could be another reason to have longer growth times for Ag_{25}. There is a significant increase in the growth times with the addition of the correction while retaining the growth time decay pattern. Both the gold and silver cluster GS growth times have a similar trend except for the S_4 state. Generally, the higher initial excitation leads to slower repopulation of the ground state due to the gap between that state and the GS and the relaxation friction caused by the intermediate states. However, state S_4 gives the slowest GS growth time for the silver cluster while the S_6 state had the slowest growth time for the gold cluster. The S_4 transfer its population to higher states S_6 and S_5 before relaxing into lower states (Figure 7.3d), which could slow down the repopulation of the GS. This is again due to the close energies of the core orbitals in silver cluster as mentioned earlier. The S_6 has a faster growth time compared to S_4 as S_6 relaxes into lower states instead of going into higher states. In Au_{25}, the S_4 only relaxed into lower states.

Table 7.2 Ground state population increase lifetimes after excitation of the six excited states contributing to the 1.66 eV peak.

Excited state	GS growth time (ps) without considering the energy correction	GS growth time (ps) with the energy correction
S_1	251	447
S_2	317	659
S_3	334	751
S_4	411	1926
S_5	270	890
S_6	371	1405

The decay time constants of the first six states (Table 7.3) are ultrafast compared to the GS growth times obtained. The added correction has no notable impact on the decay time constants and their trend is preserved. The decay times calculated for the S_1-S_6 may underestimated or overestimated due to the error involved in fitting step relaxation curves to an exponential.

Table 7.3 Decay times of the excited state population decrease of the six excited states contributing to the 1.66 eV peak.

Excited state	Decay time (ps) without considering the energy correction	Decay time (ps) with the energy correction
S_1	18	20
S_2	6.1	6.0
S_3	4.6	4.7
S_4	2.8	2.8
S_5	2.2	2.2
S_6	2.0	2.0

Figure 7.4 displays how the decay time constant trend varies among the first six states for both silver and gold clusters. It is clear that $[Ag_{25}(SH)_{18}]^{-1}$ and $[Au_{25}(SH)_{18}]^{-1}$ follow a similar trend among the first six states. However, the $[Ag_{25}(SH)_{18}]^{-1}$ decay times are slightly slower than the decay times of Au_{25}.

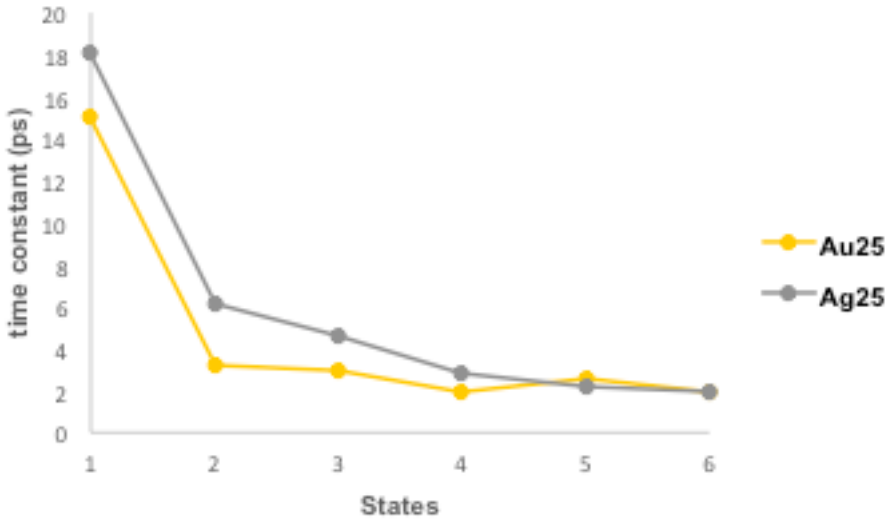

Figure 7.4 The decay time constant variations with six excited states (without the corrections to the excited states) for $[Ag_{25}(SH)_{18}]^{-1}$ and $[Au_{25}(SH)_{18}]^{-1}$.

The ground state repopulation time after excitation of the S_1 state is much larger than the decay times of the S_1 state (251 ps vs. 18 ps). This nature is similar to what observed in the gold cluster. Thus, the S_2 and S_3 states could play an important role in the S_1 state relaxation in sliver as well.

7.4.2 Relaxation dynamics of higher excited state peaks up to ~2.30 eV

In this section, the relaxation dynamics of the higher excited states will be analyzed. Forty-two higher excited states were included in the calculations which account for peaks up to ~2.30 eV in energy. According to the calculated theoretical absorption spectrum (Figure 7.1) no significant peaks appear around the 1.70-2.20 eV range. The HOMO-6 to LUMO+5 orbitals are the orbitals involved in the most probable transitions based on their high oscillator strengths and transition dipole moments (Table E.1). Hence, all possible single particle transitions were considered for orbitals between HOMO−6 and LUMO+5 in the FSSH-TDKS calculations (Table 7.4). The S_7-S_{35} transitions have the same definition as in Au_{25} higher excited states to facilitate comparison between Au_{25} and Ag_{25}. S_1−S_6 have the same definitions as in our previous Au_{25} and Ag_{25} first peak relaxations (Table 7.4).

Table 7.4 Transitions considered for higher excited states.

Excited state	Transition	Excited state	Transition
S_1	HOMO → LUMO	S_{22}	HOMO-4 → LUMO+1
S_2	HOMO → LUMO+1	S_{23}	HOMO-4 → LUMO+2
S_3	HOMO-1 → LUMO	S_{24}	HOMO → 4-LUMO+3
S_4	HOMO-1 → LUMO+1	S_{25}	HOMO-4 → LUMO+4
S_5	HOMO-2 → LUMO	S_{26}	HOMO-5 → LUMO
S_6	HOMO-2 → LUMO+1	S_{27}	HOMO-5 → LUMO+1
S_7	HOMO →LUMO+2	S_{28}	HOMO-5 → LUMO+2
S_8	HOMO → LUMO+3	S_{29}	HOMO-5 → LUMO+3
S_9	HOMO → LUMO+4	S_{30}	HOMO-5 → LUMO+4
S_{10}	HOMO-1 → LUMO+2	S_{31}	HOMO-6 → LUMO
S_{11}	HOMO-1 → LUMO+3	S_{32}	HOMO-6 → LUMO+1
S_{12}	HOMO-1 → LUMO+4	S_{33}	HOMO-6 → LUMO+2
S_{13}	HOMO-2 → LUMO+2	S_{34}	HOMO-6 → LUMO+3
S_{14}	HOMO-2 → LUMO+3	S_{35}	HOMO-6 → LUMO+4
S_{15}	HOMO-2 → LUMO+4	S_{36}	HOMO → LUMO+5
S_{16}	HOMO-3 → LUMO	S_{37}	HOMO-1 → LUMO+5
S_{17}	HOMO-3 → LUMO+1	S_{38}	HOMO-2 → LUMO+5
S_{18}	HOMO-3 → LUMO+2	S_{39}	HOMO-3 → LUMO+5
S_{19}	HOMO-3 → LUMO+3	S_{40}	HOMO-4 → LUMO+5
S_{20}	HOMO-3 → LUMO+4	S_{41}	HOMO-5 → LUMO+5

S_{21}	HOMO-4 → LUMO	**S_{42}**	HOMO-6 → LUMO+5

The relaxation dynamics of the first peak showed no difference in decay time constants compared to the constants calculated considering the correction. In Au_{25} cluster, with the PBE level of theory, the first excitation peak was underestimated by around 0.55 eV compared to the experimental first peak and the second peak had a smaller underestimation. Therefore, the 0.55 eV correction was only added to the S_1-S_6 states and not for the higher excited states. In Ag_{25}, the underestimation of the gap (~0.33 eV) is less than that in Au_{25} (0.55 eV). In order to have the Ag_{25} relaxation calculations in consistent with the Au_{25}, the 0.33 eV correction was only added to the S_1-S_6 states in Ag_{25}. We also performed a calculation without considering an energy correction to the S_1-S_6 states to see how relaxations can differ. The decoherence correction was included in all calculations.

The S_1 state has the slowest decay time constant out of all the states considered in this study. The S_1 decay was obtained as 17 ps, 18 ps for "without" correction, "with" correction added in S_1-S_6 states respectively (Table E.2). The S_1-S_6 decay constant trend in the presence of higher states (Figure E.2) is also similar to the decay constant trend observed when only the S_1-S_6 states considered (Table 7.3).

Among the higher excited states, S_7 has a longer decay time of 11 ps for both "with" and "without" energy gap correction to the S_1−S_6 states (Table E.2). The longer lifetimes in S_7 compared to the other higher states could be due to the large energy gap between the S_7 and S_6 states in Ag_{25} which makes the population transfer difficult. The gap between the LUMO+1 and LUMO+2 orbitals in the Ag_{25} electronic structure results the energy gap between the S_6 and S_7. This gap is smaller in Ag_{25} (Figure 7.2) compared to the Au_{25}. The S_7 decay for the Au_{25} was 9.9 ps. However, in both the silver and gold clusters, the S_7 population transfers mainly to the S_8 state and at 3.5 ps the S_7 state retains 75% of its initial population. Thus, the differences in the S_7 decay time constant in silver and gold clusters could be due to the variations in the shape of the population curves in fitting to the exponential. The HOMO-LUMO energy gap (~1.19 eV) of Ag_{25} (Figure 7.2) is slightly larger than the HOMO-LUMO gap of Au_{25} (~1.09 eV) in MD simulations.[36]

Faster decay times for S_7 may observed due to geometrical relaxations of S_7 that will reduce the S_6-S_7 gap.[53] The decay time constants calculated for the Ag_{25} are slightly slower than the respective Au_{25} time constants except for some higher states (Table E.2). This behavior was

also observed in the relaxation dynamics in the first peak (S_1-S_6 states only) in Ag_{25}. Overall, the decay time constant trend in Ag_{25} is similar to Au_{25}. Similar electronic structures in both clusters Ag_{25} and Au_{25} result in similar relaxation dynamics. The previous work on $[Au_{25}(SH)_{18}]^{-1}$ by our group[27-28, 53] suggested that the first excited peak relaxations are due to gold core-to-core transitions rather than a core-to-semiring transition that was proposed experimentally.[17] Our current study proposes an equivalent relaxation mechanism for $[Ag_{25}(SH)_{18}]^{-1}$, where no semiring or other states are observed at lower energy other than the core-based S_1 state.

7.5 Conclusion

The electron-nuclear dynamics of the $[Ag_{25}(SR)_{18}]^{-1}$ thiolate-protected silver nanoparticle have been investigated using TDDFT and FSSH-TDKS approach. The relaxation dynamics of the $[Ag_{25}(SR)_{18}]^{-1}$ nanocluster have been compared with the relaxations of its exact gold analog, the well-known $[Au_{25}(SR)_{18}]^{-1}$ nanocluster. The time scales for the GS recovery were found to be up to 2 orders of magnitude larger than the relaxation time scales of the S_1−S_6 excited states, which was also the case in $[Au_{25}(SR)_{18}]^{-1}$. The GS recovery times are slower for the S_2-S_6 states compared to S_1, suggesting recovery of the GS population is impeded by the effective "friction" due to the presence of intermediate electronic states. State S_4 gives the slowest GS growth time for the silver cluster while the S_6 state had the slowest growth time for the gold cluster. The GS recovery times of the S_1-S_6 states were found to be longer than the corresponding GS recovery times of Au_{25} even without the energy gap correction. This could be due to several reasons such as, smaller underestimation (0.33 eV) of the DFT HOMO-LUMO gap compared to the experimental optical gap for the $[Ag_{25}(SR)_{18}]^{-1}$ nanocluster, the core states of Ag_{25} which are closer in energies than in Au_{25} and the slightly larger HOMO-LUMO gap of Ag_{25}. The $[Au_{25}(SR)_{18}]^{-1}$ cluster had a 0.55 eV HOMO-LUMO gap underestimation compared to experiment. The addition of the energy gap correction increased the GS growth times by a factor of 1.8-4.7. Faster relaxation time constants in the range of 2.0-20 ps were observed for the S_1−S_6 excited state population decay. Faster decay time constants are observed for the S_1−S_6 states because population can transfer to other excited states in addition to the GS. The calculated decay times of Ag_{25} are slightly slower for S_1-S_4 states than the corresponding times of Au_{25}. Nevertheless, both silver and gold clusters conserve a similar trend in decay times among all the states including the first six states.

The relaxation dynamics of higher excited states with energy up to ~2.30 eV preserved the relaxation trends observed for the S_1−S_6 states. Among the higher excited states, S_7 has a comparatively longer 11 ps decay time both "with" and "without" the energy gap correction to the S_1−S_6 states. The energy gap between the S_6 and S_7 state may result in the longer S_7 decay, which was also the case in Au_{25} cluster. S_7 population relaxation is similar in both gold and silver clusters. The S_1 state population demonstrates the slowest decay. Overall, the decay time constant trends in Ag_{25} are similar to the Au_{25} nanocluster. Therefore, $[Ag_{25}(SH)_{18}]^{-1}$ follows a relaxation mechanism equivalent to the $[Au_{25}(SR)_{18}]^{-1}$ nanocluster where no semiring or other states are observed at lower energy other than the core-based S_1 state. We hope the theoretical insights given on $[Ag_{25}(SH)_{18}]^{-1}$ nonradiative relaxations will serve as a model platform for experimentalists to use $[Ag_{25}(SH)_{18}]^{-1}$ as a substitute for $[Au_{25}(SH)_{18}]^{-1}$ in future photocatalytic applications.

7.6 Acknowledgments

This material is based on work supported by Department of Energy under grants DE-SC0012273. The computing for this project was performed on the computing for this project was performed on the Beocat Research Cluster at Kansas State University, which is funded in part by NSF grants CHE-1726332, CNS-1006860, EPS-1006860, and EPS-0919443 and Extreme Science and Engineering Discovery Environment (XSEDE),[54] which is supported by National Science Foundation grant number ACI- 1053575. Beocat Application Scientist Dr. Dave Turner provided valuable technical expertise. The authors are grateful to Prof. Alexey V. Akimov for his support and valuable discussions on PYXAID.

7.7 References

1. Jin, R., Atomically Precise Metal Nanoclusters: Stable Sizes and Optical Properties. *Nanoscale* **2015,** *7* (5), 1549-1565.

2. Valden, M.; Lai, X.; Goodman, D. W., Onset of Catalytic Activity of Gold Clusters on Titania with the Appearance of Nonmetallic Properties. *Science* **1998,** *281* (5383), 1647-1650.

3. Zhu, Y.; Qian, H.; Drake, B. A.; Jin, R., Atomically Precise $Au_{25}(SR)_{18}$ Nanoparticles as Catalysts for the Selective Hydrogenation of α,β-Unsaturated Ketones and Aldehydes. *Angew. Chem. Int. Ed.* **2010,** *49* (7), 1295-1298.

4. Ramakrishna, G.; Varnavski, O.; Kim, J.; Lee, D.; Goodson, T., Quantum-Sized Gold Clusters as Efficient Two-Photon Absorbers. *J. Am. Chem. Soc.* **2008,** *130* (15), 5032-5033.

5. Ramakrishna, G.; Varnavski, O.; Kim, J.; Lee, D.; Goodson, T. In *Nonlinear Optical Properties of Quantum Sized Gold Clusters*, Photonic Devices + Applications, SPIE: 2008; p 12.

6. Stamplecoskie, K. G.; Kamat, P. V., Size-Dependent Excited State Behavior of Glutathione-Capped Gold Clusters and Their Light-Harvesting Capacity. *J. Am. Chem. Soc.* **2014,** *136* (31), 11093-11099.

7. Chen, Y.-S.; Choi, H.; Kamat, P. V., Metal-Cluster-Sensitized Solar Cells. A New Class of Thiolated Gold Sensitizers Delivering Efficiency Greater Than 2%. *J. Am. Chem. Soc.* **2013,** *135* (24), 8822-8825.

8. Kogo, A.; Sakai, N.; Tatsuma, T., Photocatalysis of Au_{25}-modified TiO_2 Under Visible and Near Infrared Light. *Electrochem. Commun.* **2010,** *12* (7), 996-999.

9. Kogo, A.; Sakai, N.; Tatsuma, T., Photoelectrochemical Analysis of Size-dependent Electronic Structures of Gold Clusters Supported on TiO_2. *Nanoscale* **2012,** *4* (14), 4217-4221.

10. Yu, C.; Li, G.; Kumar, S.; Kawasaki, H.; Jin, R., Stable $Au_{25}(SR)_{18}/TiO_2$ Composite Nanostructure with Enhanced Visible Light Photocatalytic Activity. *J. Phys. Chem. Lett.* **2013,** *4* (17), 2847-2852.

11. Subramanian, V.; Wolf, E. E.; Kamat, P. V., Catalysis with TiO_2/gold Nanocomposites. Effect of Metal Particle Size on the Fermi Level Equilibration. *J. Am. Chem. Soc.* **2004,** *126* (15), 4943-4950.

12. Qian, K.; Sweeny, B. C.; Johnston-Peck, A. C.; Niu, W.; Graham, J. O.; DuChene, J. S.; Qiu, J.; Wang, Y.-C.; Engelhard, M. H.; Su, D., Surface Plasmon-driven Water Reduction: Gold Nanoparticle Size Matters. *J. Am. Chem. Soc.* **2014,** *136* (28), 9842-9845.

13. Gomes Silva, C. u.; Juárez, R.; Marino, T.; Molinari, R.; García, H., Influence of Excitation Wavelength (UV or visible light) on the Photocatalytic Activity of Titania Containing Gold Nanoparticles for the Generation of Hydrogen or Oxygen from Water. *J. Am. Chem. Soc.* **2010,** *133* (3), 595-602.

14. Primo, A.; Marino, T.; Corma, A.; Molinari, R.; Garcia, H., Efficient Visible-light Photocatalytic Water Splitting by Minute Amounts of Gold Supported on Nanoparticulate CeO_2 Obtained by a Biopolymer Templating Method. *J. Am. Chem. Soc.* **2011,** *133* (18), 6930-6933.

15. Stamplecoskie, K. G.; Chen, Y.-S.; Kamat, P. V., Excited-state Behavior of Luminescent Glutathione-Protected Gold Clusters. *J. Phys. Chem. C* **2014,** *118* (2), 1370-1376.

16. Link, S.; El-Sayed, M. A.; Schaaff, T. G.; Whetten, R. L., Transition from Nanoparticle to Molecular Behavior: a Femtosecond Transient Absorption Study of a Size-Selected 28 Atom Gold Cluster. *Chem. Phys. Lett.* **2002,** *356* (3-4), 240-246.

17. Miller, S. A.; Womick, J. M.; Parker, J. F.; Murray, R. W.; Moran, A. M., Femtosecond Relaxation Dynamics of $Au_{25}L_{18}^-$ Monolayer-protected Clusters. *J. Phys. Chem. C* **2009,** *113* (22), 9440-9444.

18. Lee, D.; Donkers, R. L.; Wang, G.; Harper, A. S.; Murray, R. W., Electrochemistry and Optical Absorbance and Luminescence of Molecule-like Au_{38} Nanoparticles. *J. Am. Chem. Soc.* **2004,** *126* (19), 6193-6199.

19. Devadas, M. S.; Kim, J.; Sinn, E.; Lee, D.; Goodson III, T.; Ramakrishna, G., Unique Ultrafast Visible Luminescence in Monolayer-Protected Au_{25} Clusters. *J. Phys. Chem. C* **2010,** *114* (51), 22417-22423.

20. Green, T. D.; Knappenberger, K. L., Relaxation Dynamics of $Au_{25}L_{18}$ Nanoclusters Studied by Femtosecond Time-resolved Near Infrared Transient Absorption Spectroscopy. *Nanoscale* **2012,** *4* (14), 4111-4118.

21. Yau, S. H.; Varnavski, O.; Goodson III, T., An Ultrafast Look at Au Nanoclusters. *Acc. Chem. Res.* **2013,** *46* (7), 1506-1516.

22. Stoll, T.; Sgrò, E.; Jarrett, J. W.; Réhault, J.; Oriana, A.; Sala, L.; Branchi, F.; Cerullo, G.; Knappenberger Jr, K. L., Superatom State-resolved Dynamics of the $Au_{25}(SC_8H_9)_{18}^-$Cluster from Two-dimensional Electronic Spectroscopy. *J. Am. Chem. Soc.* **2016,** *138* (6), 1788-1791.

23. Zhou, M.; Tian, S.; Zeng, C.; Sfeir, M. Y.; Wu, Z.; Jin, R., Ultrafast Relaxation Dynamics of $Au_{38}(SC_2H_4Ph)_{24}$ Nanoclusters and Effects of Structural Isomerism. *J. Phys. Chem. C* **2017,** *121* (20), 10686-10693.

24. Zhou, M.; Zhong, J.; Wang, S.; Guo, Q.; Zhu, M.; Pei, Y.; Xia, A., Ultrafast Relaxation Dynamics of Luminescent Rod-Shaped, Silver-Doped Ag_xAu_{25-x} Clusters. *J. Phys. Chem. C* **2015,** *119* (32), 18790-18797.

25. Sfeir, M. Y.; Qian, H.; Nobusada, K.; Jin, R., Ultrafast Relaxation Dynamics of Rod-Shaped 25-Atom Gold Nanoclusters. *J. Phys. Chem. C* **2011,** *115* (14), 6200-6207.

26. Chen, X.; Prezhdo, O. V.; Ma, Z.; Hou, T.; Guo, Z.; Li, Y., Ab initio Phonon-coupled Nonadiabatic Relaxation Dynamics of $[Au_{25}(SH)_{18}]^-$ Clusters. *physica status solidi (b)* **2016,** *253* (3), 458-462.

27. Senanayake, R. D.; Akimov, A. V.; Aikens, C. M., Theoretical Investigation of Electron and Nuclear Dynamics in the $[Au_{25}(SH)_{18}]^{-1}$ Thiolate-Protected Gold Nanocluster. *J. Phys. Chem. C* **2016,** *121* (20), 10653-10662.

28. Zhu, M.; Aikens, C. M.; Hollander, F. J.; Schatz, G. C.; Jin, R., Correlating the Crystal Structure of a Thiol-protected Au_{25} Cluster and Optical Properties. *J. Am. Chem. Soc.* **2008,** *130* (18), 5883-5885.

29. Negishi, Y.; Nobusada, K.; Tsukuda, T., Glutathione-protected Gold Clusters Revisited: Bridging the Gap Between Gold (I)− thiolate Complexes and Thiolate-protected Gold Nanocrystals. *J. Am. Chem. Soc.* **2005,** *127* (14), 5261-5270.

30. Lopez-Acevedo, O.; Tsunoyama, H.; Tsukuda, T.; Hakkinen, H.; Aikens, C. M., Chirality and Electronic Structure of the Thiolate-protected Au_{38} Nanocluster. *J. Am. Chem. Soc.* **2010,** *132* (23), 8210-8218.

31. Jadzinsky, P. D.; Calero, G.; Ackerson, C. J.; Bushnell, D. A.; Kornberg, R. D., Structure of a Thiol Monolayer-Protected Gold Nanoparticle at 1.1 Å Resolution. *Science* **2007,** *318* (5849), 430-433.

32. Zeng, C.; Chen, Y.; Kirschbaum, K.; Appavoo, K.; Sfeir, M. Y.; Jin, R., Structural Patterns at All Scales in a Nonmetallic Chiral $Au_{133}(SR)_{52}$ Nanoparticle. *Sci. Adv.* **2015,** *1* (2), e1500045.

33. Dass, A.; Theivendran, S.; Nimmala, P. R.; Kumara, C.; Jupally, V. R.; Fortunelli, A.; Sementa, L.; Barcaro, G.; Zuo, X.; Noll, B. C., $Au_{133}(SPh\text{-}t\ Bu)_{52}$ Nanomolecules: X-ray Crystallography, Optical, Electrochemical, and Theoretical Analysis. *J. Am. Chem. Soc.* **2015,** *137* (14), 4610-4613.

34. Desireddy, A.; Conn, B. E.; Guo, J.; Yoon, B.; Barnett, R. N.; Monahan, B. M.; Kirschbaum, K.; Griffith, W. P.; Whetten, R. L.; Landman, U., Ultrastable Silver Nanoparticles. *Nature* **2013,** *501* (7467), 399.

35. Yang, H.; Wang, Y.; Huang, H.; Gell, L.; Lehtovaara, L.; Malola, S.; Häkkinen, H.; Zheng, N., All-thiol-stabilized Ag_{44} and $Au_{12}Ag_{32}$ Nanoparticles with Single-crystal Structures. *Nat. Commun.* **2013,** *4*, 2422.

36. Yang, H.; Wang, Y.; Zheng, N., Stabilizing Subnanometer Ag (0) Nanoclusters by Thiolate and Diphosphine Ligands and their Crystal structures. *Nanoscale* **2013,** *5* (7), 2674-2677.

37. AbdulHalim, L. G.; Bootharaju, M. S.; Tang, Q.; Del Gobbo, S.; AbdulHalim, R. G.; Eddaoudi, M.; Jiang, D.-e.; Bakr, O. M., $Ag_{29}(BDT)_{12}(TPP)_4$: A Tetravalent Nanocluster. *J. Am. Chem. Soc.* **2015,** *137* (37), 11970-11975.

38. Dhayal, R. S.; Liao, J. H.; Liu, Y. C.; Chiang, M. H.; Kahlal, S.; Saillard, J. Y.; Liu, C., $[Ag_{21}\{S_2P(OiPr)_2\}_{12}]^+$: An Eight-Electron Superatom. *Angew. Chem. Int. Ed.* **2015,** *54* (12), 3702-3706.

39. Yang, H.; Lei, J.; Wu, B.; Wang, Y.; Zhou, M.; Xia, A.; Zheng, L.; Zheng, N., Crystal Structure of a Luminescent Thiolated Ag Nanocluster with an Octahedral Ag_{64}^+ Core. *ChemComm* **2013,** *49* (3), 300-302.

40. Bakr, O. M.; Amendola, V.; Aikens, C. M.; Wenseleers, W.; Li, R.; Dal Negro, L.; Schatz, G. C.; Stellacci, F., Silver Nanoparticles with Broad Multiband Linear Optical Absorption. *Angew. Chem. Int. Ed.* **2009,** *121* (32), 6035-6040.

41. Aikens, C. M., Origin of Discrete Optical Absorption Spectra of $M_{25}(SH)_{18}^-$ Nanoparticles (M= Au, Ag). *J. Phys. Chem. C* **2008,** *112* (50), 19797-19800.

42. Joshi, C. P.; Bootharaju, M. S.; Alhilaly, M. J.; Bakr, O. M., $[Ag_{25}(SR)_{18}]^-$: The "golden" Silver Nanoparticle. *J. Am. Chem. Soc.* **2015,** *137* (36), 11578-11581.

43. Tully, J., Mixed Quantum–classical Dynamics. *Faraday Discuss.* **1998,** *110*, 407-419.

44. Craig, C. F.; Duncan, W. R.; Prezhdo, O. V., Trajectory Surface hopping in the Time-dependent Kohn-Sham Approach for electron-nuclear Dynamics. *Phys. Rev. Lett.* **2005,** *95* (16), 163001.

45. Jaeger, H. M.; Fischer, S.; Prezhdo, O. V., Decoherence-induced Surface Hopping. *J. Chem. Phys.* **2012,** *137* (22), 22A545.

46. Akimov, A. V.; Prezhdo, O. V., The PYXAID Program For Non-adiabatic Molecular Dynamics in Condensed Matter Systems. *J. Chem. Theory Comput.* **2013,** *9* (11), 4959-4972.

47. Akimov, A. V.; Prezhdo, O. V., Advanced Capabilities of the PYXAID Program: Integration Schemes, Decoherence Effects, Multiexcitonic States, and Field-Matter Interaction. *J. Chem. Theory Comput.* **2014,** *10* (2), 789-804.

48. Perdew, J. P.; Burke, K.; Ernzerhof, M., Generalized Gradient Approximation Made Simple. *Phys. Rev. Lett.* **1996,** *77* (18), 3865.

49. Te Velde, G. t.; Bickelhaupt, F. M.; Baerends, E. J.; Fonseca Guerra, C.; van Gisbergen, S. J.; Snijders, J. G.; Ziegler, T., Chemistry with ADF. *J. Comput. Chem.* **2001,** *22* (9), 931-967.

50. Lenthe, E. v.; Baerends, E.-J.; Snijders, J. G., Relativistic Regular Two-Component Hamiltonians. *J. Chem. Phys.* **1993,** *99* (6), 4597-4610.

51. Kresse, G.; Furthmüller, J., Efficiency of Ab-initio Total Energy Calculations for Metals and Semiconductors using a Plane-wave Basis Set. *Comput. Mater. Sci.* **1996,** *6* (1), 15-50.

52. Kresse, G.; Joubert, D., From Ultrasoft Pseudopotentials to the Projector Augmented-wave Method. *Phys. Rev. B* **1999,** *59* (3), 1758.

53. Weerawardene, K. D. M.; Aikens, C. M., Theoretical Insights into the Origin of Photoluminescence of $Au_{25}(SR)_{18}^-$Nanoparticles. *J. Am. Chem. Soc.* **2016,** *138* (35), 11202-11210.

54. Towns, J.; Cockerill, T.; Dahan, M.; Foster, I.; Gaither, K.; Grimshaw, A.; Hazlewood, V.; Lathrop, S.; Lifka, D.; Peterson, G. D., XSEDE: Accelerating Scientific Discovery. *Computing in Science & Engineering* **2014,** *16* (5), 62-74.

Chapter 8 - Real-time TDDFT Investigation of Optical Absorption in Gold Nanowires

8.1 Abstract

Using a real-time TDDFT method, a set of linear gold nanowires Au_m (m = 4, 6, 8, 10, 12) is investigated to understand the plasmon-like behavior that results from resonant excitation of a superposition of single-electron transitions. These characteristic excitations of gold nanowires have been previously investigated via linear response TDDFT calculations, and the results from these two approaches are compared; real-time TDDFT is shown to provide complementary information about the excitations in these systems. This study also investigates the relationship between the d-band transitions and the plasmon-like states in gold nanowires. In this work, the longitudinal and transverse absorption peaks are studied after dipolar excitation, and the effects of changing the length of the nanowire are examined. The time evolution of the single particle transitions and the interplay between different transitions involved in the plasmon-like excitations of model gold nanowires are also investigated. The longitudinal mode occurs around 1-2 eV in the optical absorption spectra, and it redshifts with increasing nanowire length. A splitting in the longitudinal peak is present due to the involvement of interband transitions. The frequency of the transverse mode, which lies around 6-7 eV in the absorption spectra, tends to stay constant as the nanowire length increases. The time-dependent occupation numbers and their Fourier transformed spectra reveal that a dominant single particle transition ($\Sigma_n \rightarrow \Sigma_{n+1}$) can be identified in the longitudinal peaks which is coupled with less probable d-band transitions (d $\rightarrow \Sigma$). In contrast, the transverse modes are constructed from a coupling of two or more single particle transitions with $\Sigma_n \rightarrow \Pi_n$ character.

8.2 Introduction

Noble metal nanoparticles composed of silver and gold are of interest due their important applications in sensing,[1-9] catalysis,[10] biomedicine,[11-14] energy conversion and energy storage.[15-16] Gold nanorods and nanowires can be used in photothermal cancer therapy applications.[12, 17] Noble metal nanoparticles in the size range of 10 – 100 nm give one or more strong absorption peaks in the visible to near IR region which is an important characteristic of those nanoparticles called the surface plasmon resonance (SPR).[18-22] The SPR phenomenon in gold and silver

nanoparticles has been widely studied experimentally[23-26] and theoretically[27-32] because their applications rely on this property. The absorption peaks can be tuned by changing the size,[33] shape[34-35] and the environment[36] of the nanoparticles.

Among the various shapes of nanoparticles available, nanorods and nanowires have drawn significant attention due the high sensitivity of their optical properties to their aspect ratios.[20, 37-38] The two main plasmon resonances present in alkali metal and noble metal nanowires are the longitudinal and transverse modes.[6, 36, 39-42] The longitudinal mode is obtained by applying an electric field polarized along the main axis (*z* direction) of the nanowire. A change in the nanowire length can result in a change in the energy and the intensity of the longitudinal mode.[43] The transverse mode is obtained by applying the field in a direction polarized perpendicular to the main axis such as the *x* direction. Previous investigations on nanorods/nanowires have shown that the longitudinal peak in the optical absorption spectrum tends to redshift in energy with increasing aspect ratio while the transverse mode does not greatly change in energy with increasing aspect ratio.[36, 39-42]

Time dependent density functional theory (TDDFT) has been used to understand the origin of the optical absorption spectra of these noble metal nanoparticles.[28, 41-51] The absorption spectra of small nanoclusters exhibit one or more intense peaks that are similar to the plasmon resonance of larger nanoparticles.[46, 52] Linear response time dependent density functional theory (LR-TDDFT) calculations demonstrate that dipolar plasmon modes in the noble metal nanoclusters can be recognized through the concept of constructive addition of single electron transitions. This is expected to be applicable for both large nanoparticles that are several hundred nanometers in size and smaller nanoparticles with diameters less than 2 nm.[42, 46, 53-55] A different method for identifying single particle transitions and plasmons that relies on the different behavior of plasmon and single particle transition energies upon scaling of the electron-electron interactions has also been suggested by Jacob and coworkers.[47]

The TDDFT method has been widely used to study model systems of noble metal nanowires.[43, 47-51] The plasmon excitations in small nanowires have often been investigated using the frequency domain LR-TDDFT method.[43] Although extremely useful for calculating absorption spectra and determining the transitions responsible, LR-TDDFT calculations do not reveal the dynamical nature of the interplay between the electronic excited states which is vital to understanding the plasmon modes present in nanoclusters. Therefore, the real time TDDFT (RT-

TDDFT) method has recently attracted attention as a prominent method to understand the time evolution of molecular systems in the presence of an external perturbation.

Real-time TDDFT (RT-TDDFT) has been used to study the end and central plasmon modes in linear sodium and silver chains by Gao and coworkers.[49-50] Later, Luo et al.[51] investigated the size dependence of electronic excitations in copper, silver and gold chains up to 26 atoms. Recently, the coherent plasmonic behavior of silver nanowires Ag_m (m= 4, 6, 8, 10, 12) was studied by Li and coworkers[56] using a RT-TDDFT method. In the latter study, the interplay between the time evolution of the superposition of the single particle transitions and the plasmonic excitations was investigated. It was shown that the transverse transitions in silver nanowires are collective in nature and oscillate in phase with respect to each other.

A LR-TDDFT investigation on silver nanowires showed that the longitudinal peak of the silver nanowires corresponds to the HOMO → LUMO transition, which is a Σ → Σ transition (the delocalized frontier orbitals of nanowires can be referenced by the irreducible representations of the $D_{\infty h}$ point group (Σ, Π, Δ, etc.) due to their approximate cylindrical symmetry), whereas the transverse peak is a superposition of several single particle transitions (Σ → Π) adding constructively.[43] This behavior was also observed in similar RT-TDDFT calculations.[56] Until now, there has been no RT-TDDFT investigation performed on the gold nanowires to understand the dynamical nature of the superposition of single particle transitions involved. Furthermore, the plasmon resonance in noble metal nanoparticles can be affected by transitions from the d band. This effect is profound in gold nanoparticles due to relativistic effects that lead to a smaller splitting between the d and sp bands compared to silver and alkali metal nanoparticles.[41, 48, 57] In this work, our aim is to understand how the plasmon-like excitations in gold nanowires differ compared to those of silver nanowires using the RT-TDDFT approach. We also aim to understand to what extent transitions out of the d band play a role in determining the character of plasmon-like states in gold nanowires. Moreover, we show how the RT-TDDFT method can provide complementary information to the LR-TDDFT approach.

8.3 Computational methodology

The current work uses the RT-TDDFT approach to study the interplay between the time evolution of the superposition of the single particle transitions and the plasmonic excitations in

the model gold nanowires Au_m (m= 4, 6, 8, 10, 12). A step function electric field[58] is utilized as the perturbation to probe the dipole response of the longitudinal and transverse modes upon changing the nanowire length. The step function electric field can be described as follows.

$$E(t) = E_0 \text{ for } t < 0 \quad (t = \text{time})$$

$$E(t) = 0 \text{ for } t > 0$$

In practice this is done by preparing the initial electron density for the system with a self-consistent field calculation performed in the presence of a static electric field E_0. Then, the field is turned off and the electronic system is propagated using the RT-TDDFT approach.[56] Similar to the previous silver nanowire study by Li and coworkers,[56] the nature of the plasmon excitation as a superposition of single particle transitions is analyzed through the time evolution of the molecular orbital occupation numbers. The collective oscillation of single particle orbital occupations that are in-phase and coherent will help to identify the collective nature of the plasmon resonance.

RT-TDDFT calculations were performed on a series of linear gold chains having 4, 6, 8, 10 and 12 atoms. A development version of the GAUSSIAN series of programs[59] was used to carry out the real time simulations. The RT-TDDFT calculations are described elsewhere.[56] The real time formalization utilizes an approach similar to a full time dependent Hartree-Fock (TDHF) approach developed by Schlegel and coworkers.[60] That method was previously used to understand the effects of a time dependent electric field on the dipole moments, charge distribution and the frontier orbital population in linear polyenes.[61-62]

In this work, the BP86[63-64] exchange-correlation functional and the LanL2DZ[65-67] effective core potential basis set were used in all calculations. A simulation time of 120 fs was performed for the longitudinal mode and 480 fs for the transverse mode with an integration step size of 1.2 as. The longer simulation time for the transverse mode was performed to check convergence; it was found that a good convergence in the optical absorption spectrum of the system can be achieved with a simulation time of 120 fs. An external static field was used with a strength of 0.001 au. A 150 au damping factor was used during Fourier transformation of the time-dependent dipole moments to obtain the dipole strength function which is proportional to the optical absorption spectrum. The damping factor is used to account for the experimental broadening. The time-dependent dipole moment $\mu(t)$ is calculated at each time step using the equation,

$$\mu(t) = \mathrm{Tr}[\mathbf{DP}(t)] \quad \textbf{(8.1)}$$

In the orthonormal basis, the dipole matrix is given by **D** and the density matrix is given by **P**. Then, the dipole strength function *S(ω)* is given by,[68]

$$S(\omega) = \frac{4\pi\omega\, Tr[\mathrm{Im}\alpha(\omega)]}{3c} \quad \textbf{(8.2)}$$

where *α(ω)* is the polarizability in the frequency domain, which can be obtained by the Fourier transform of the dipole moment $\mu_i(\omega)$ and step electric field $E_i(\omega)$ relation as shown:

$$\mu_i(\omega) = \alpha_{ii}(\omega)E_i(\omega) \quad \textbf{(8.3)}$$

where *i* indicates the *x, y, z* Cartesian coordinates.

Coordinates for the gold nanowires were obtained from an optimization at the BP86/TZP level of theory with scalar relativistic effects treated by ZORA[69] using the ADF[70] software. The nanowires are positioned so that their coordinates lie along the *z*-axis. LR-TDDFT calculations were performed on the same series of gold nanowires with the BP86/LanL2DZ level of theory to compare with the RT-TDDFT results.

8.4 Results and discussion

8.4.1 Dipole strength functions of the longitudinal and transverse modes

The dipole strength functions (optical absorption spectra) that result from applying a step function electric field to five gold nanowires are shown in Figure 8.1. The electric field perturbation is applied along the longitudinal (*z* direction) and transverse (*x* direction) directions. Due to the symmetry of the system, results for an electric field in the *y* direction (not shown) are the same as the *x* direction. The main peaks in the energy range of 0-8 eV are analyzed for both longitudinal and transverse modes. Unlike in a similar series of silver nanowires[56] where the longitudinal mode appears as a single sharp peak in the energy range of 1-2 eV, several peaks in the optical absorption plots for the gold nanowires indicate that several longitudinal excitations are present. Despite some differences due to the level of theory used, most of the findings in this RT-TDDFT study are consistent with the previous LR-TDDFT study on gold nanowires performed by Guidez and Aikens.[43] For example, the LR-TDDFT spectra of gold nanowires display a redshift and several longitudinal excitations at ~ 2 eV[43] comparable to that observed for

the peaks in the energy range of 2-6 eV in Figure 8.1a - e. The Au_4 nanowire exhibits a small peak around 2 eV that redshifts with the increasing number of atoms in the nanowire up to Au_{12}. The peak intensity grows and the peak displays a splitting with increasing length. In the energy range of 3-7 eV, a few low intensity peaks and a high intensity peak are present for Au_4 which also redshift for longer nanowires. The intensities of the peaks around 3 eV significantly increase with length, while the peaks in the 4-7 eV range increase less dramatically in intensity for longer systems. The splitting of the peaks in longer nanowires are due to the transitions originating from the d band, which was shown in the previous LR-TDDFT study on gold nanowires.[43] Redshifting of the longitudinal peak has also been observed for silver nanowires.[56] Similar to the silver nanowire case,[56] the energy of the transverse peak (6-7 eV) is essentially constant although a small blueshift is apparent as the nanowire length increases. Unlike in silver, the gold nanowires exhibit several transverse peaks as well as several longitudinal excitations. For both excitation modes, the dipole strength increases as the nanowire length grows. This has also been observed for other elongated systems such as pentagonal nanorods.[42]

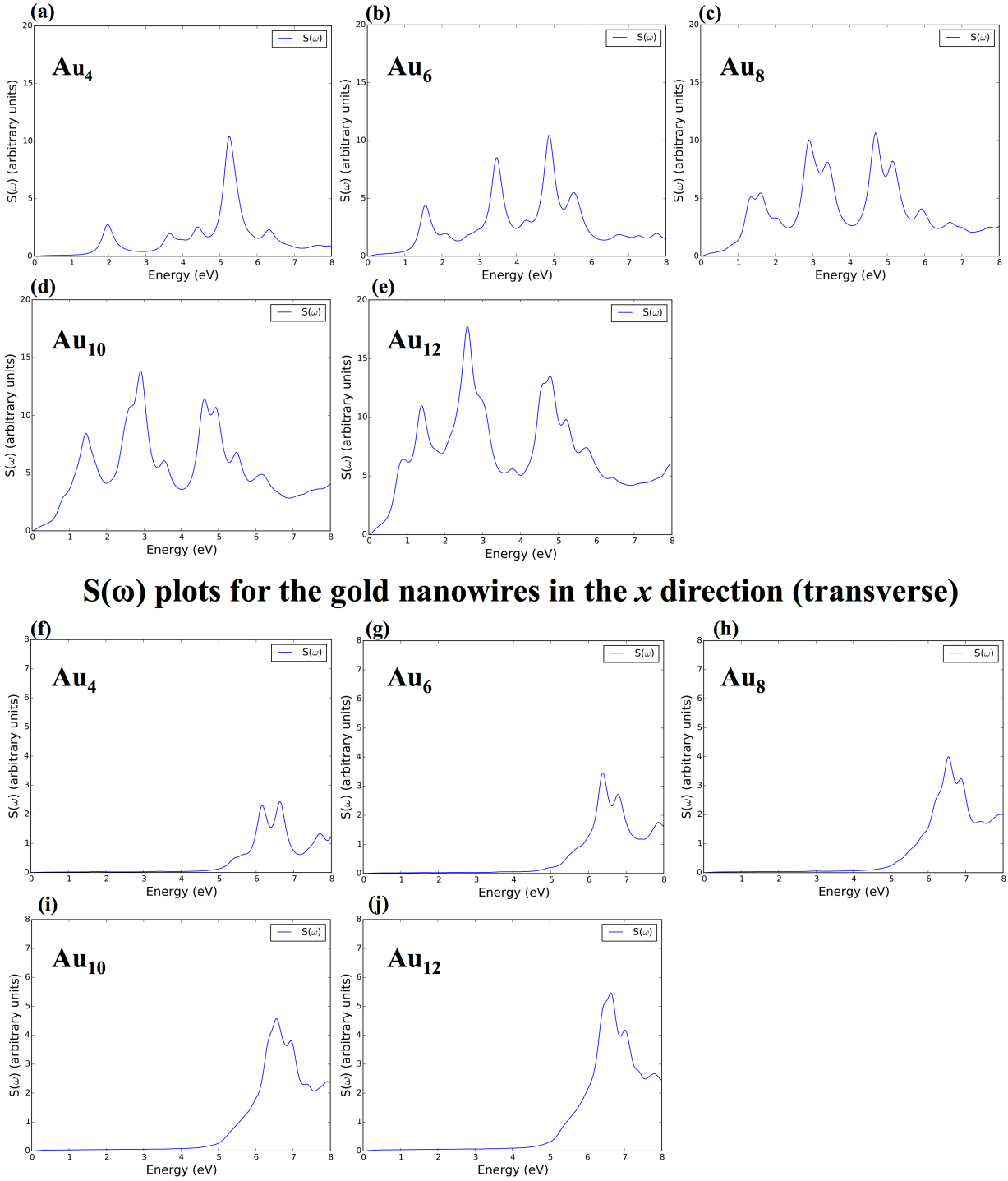

Figure 8.1 Optical absorption spectra for the longitudinal and transverse modes in the nanowires Au_m (m= 4, 6, 8, 10, 12).

8.4.2 Longitudinal mode excitations

In gold, the 5d orbital energies are much closer to the energy of the 6s orbital compared to the 4d-5s difference in silver. Therefore, developing an understanding of interband transitions originating from the d band of the gold nanowires is crucial because of the coupling of these transitions with intraband transitions and their combined effects on the longitudinal and transverse mode frequencies and intensities.[43] The longitudinal mode in our small gold nanowires can be explained by a single particle transition as discussed in detail below.

As in the previous real-time study on related silver nanowires by Li and coworkers,[56] the time dependent occupation numbers of the relevant orbitals are obtained through analyzing the evolution of the electron density by projecting to the ground state molecular orbital space. This approach is useful to understand the nature of the interplay between the single particle transitions involved in plasmon modes. This analysis is carried out for the longitudinal mode to recognize the orbitals involved in the important transitions contributing to the longitudinal peak. The respective orbital occupation number variations and their Fourier transformed spectra are shown in Figure 8.2; we present pairs of orbitals that can be identified as strongly correlated transitions for the given longitudinal mode. Less strongly correlated transitions are shown in the SI in Appendix F. The constructive and destructive nature of the electronic transitions can be obtained by the phase relationship between the time evolution of the orbital occupation numbers. If the orbital occupation number variations are in phase with the same frequency, they can constructively or destructively interact to give rise to several peaks in the optical absorption spectrum. A similar approach has been utilized in analyzing silver nanowire transverse modes to identity the orbitals responsible for the main peaks appearing in their optical absorption spectra.[56] In the longitudinal mode of the current gold nanowire study, we observe a coupling of sp delocalized orbital transitions ($S_n \rightarrow S_{n+1}$; n is the axial quantum number) with the interband transitions ($d \rightarrow S_{n+1}$) as explained in more detail below.

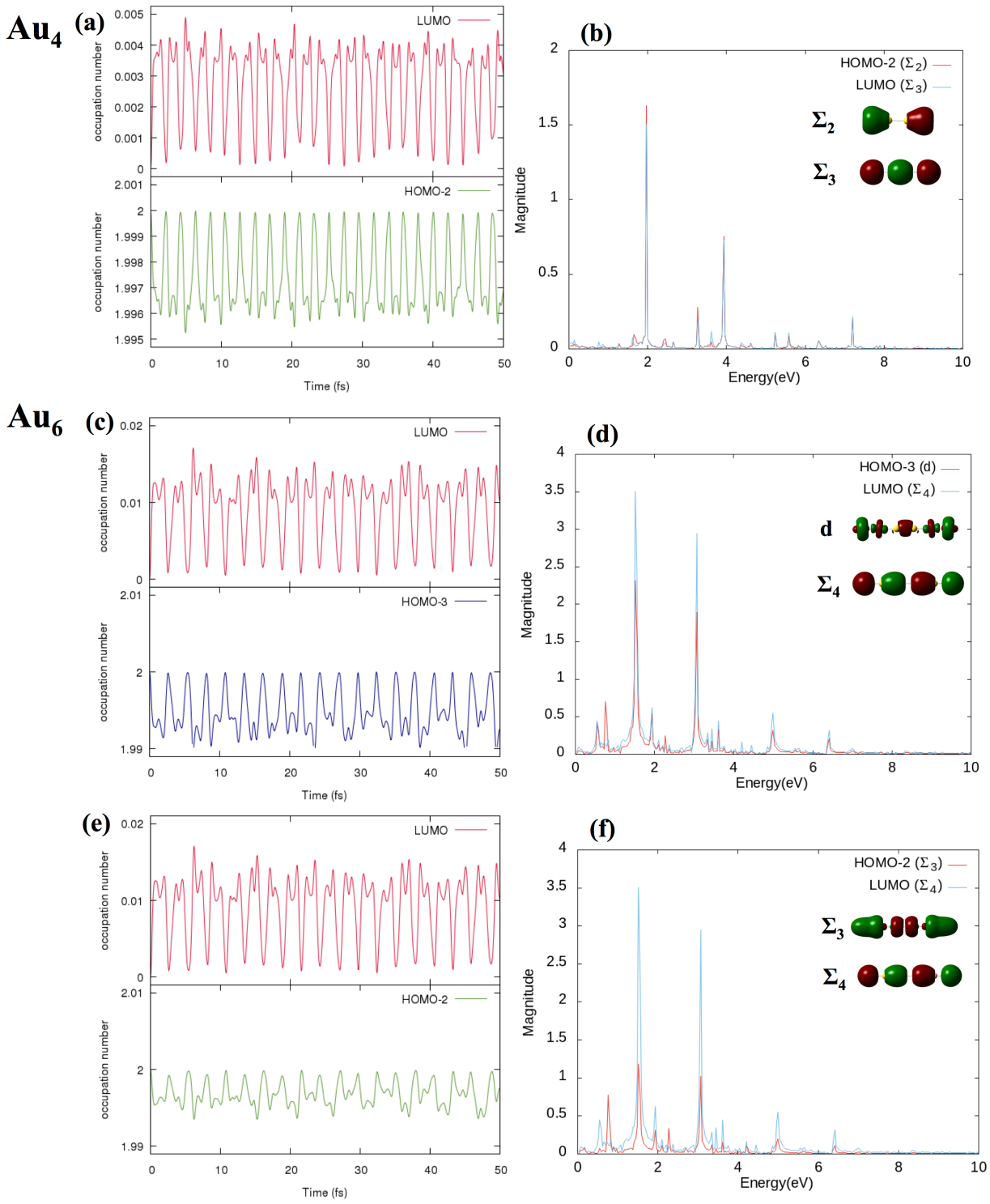

Figure 8.2 Variations in orbital occupation numbers with time and their Fourier transformed spectra for strongly coupled orbital pairs in the longitudinal mode of Au_m (m = 4, 6) nanowires. For Au_4, (a) shows the orbital occupation number variations for the two orbitals most responsible for the longitudinal mode and (b) shows their Fourier transformed spectra. Likewise, the c, d, e and f plots represent the orbital occupation number variations and their Fourier transformed spectra and for Au_6. The strongest

occupied-to-unoccupied transition is d → Σ_4 in plots c and d, and the e and f plots are for a less probable transition (Σ_3 → Σ_4).

Table 8.1 Single particle transitions involved in the longitudinal mode of gold nanowires determined by RT-TDDFT calculations.

Nanowire	Single particle transition	Symmetries
Au_4	HOMO-2 → LUMO	$\Sigma_2 \rightarrow \Sigma_3$
Au_6	HOMO-2 → LUMO HOMO-3 → LUMO	$\Sigma_3 \rightarrow \Sigma_4$ $d \rightarrow \Sigma_4$
Au_8	HOMO-2 → LUMO HOMO-3 → LUMO	$d \rightarrow \Sigma_5$ $\Sigma_4 \rightarrow \Sigma_5$
Au_{10}	HOMO-3 → LUMO HOMO-4 → LUMO	$d \rightarrow \Sigma_6$ $\Sigma_5 \rightarrow \Sigma_6$
Au_{12}	HOMO-3 → LUMO HOMO-4 → LUMO HOMO-5 → LUMO	$d \rightarrow \Sigma_7$ $\Sigma_6 \rightarrow \Sigma_7$ $d \rightarrow \Sigma_7$

In analyzing the real-time simulations of the longitudinal mode, this excitation is mainly constructed by one dominant single particle transition with a small contribution from one or two other single particle transitions as shown in Table 8.1. This was not the case for the longitudinal mode obtained by the LR-TDDFT method using LB94/DZ, where it was dominated by the single particle HOMO → LUMO transition.[43] Differences in the level of theory used and how the relativistic effects have been treated in the LR and RT methods could be the reason for the different results observed from the two approaches. The LR-TDDFT calculations were also performed with the same level of theory as the RT-TDDFT calculations to compare the excitations from the two methods directly. Both LR and RT calculations used the relativistic effects incorporated into the LanL2DZ basis set in the Gaussian software. The absorption spectra obtained by LR-TDDFT method are shown in the supporting information Figure F.1 in Appendix. The excitations were calculated only up to 7 eV. The peak positions and the relative intensities of the absorption spectra obtained by LR and RT match well with each other.

Even though the orbital numberings are different in the two studies, the symmetries of the longitudinal mode are similar (i.e., $\Sigma_n \rightarrow \Sigma_{n+1}$). The Kohn-Sham orbital energy diagram of the Au_4 nanowire obtained using the BP86/LanL2DZ level of theory is shown in Figure 8.3. At this level of theory, the overlap of the d band with the sp-based Σ orbitals is clearly evident, which is the case for gold systems.

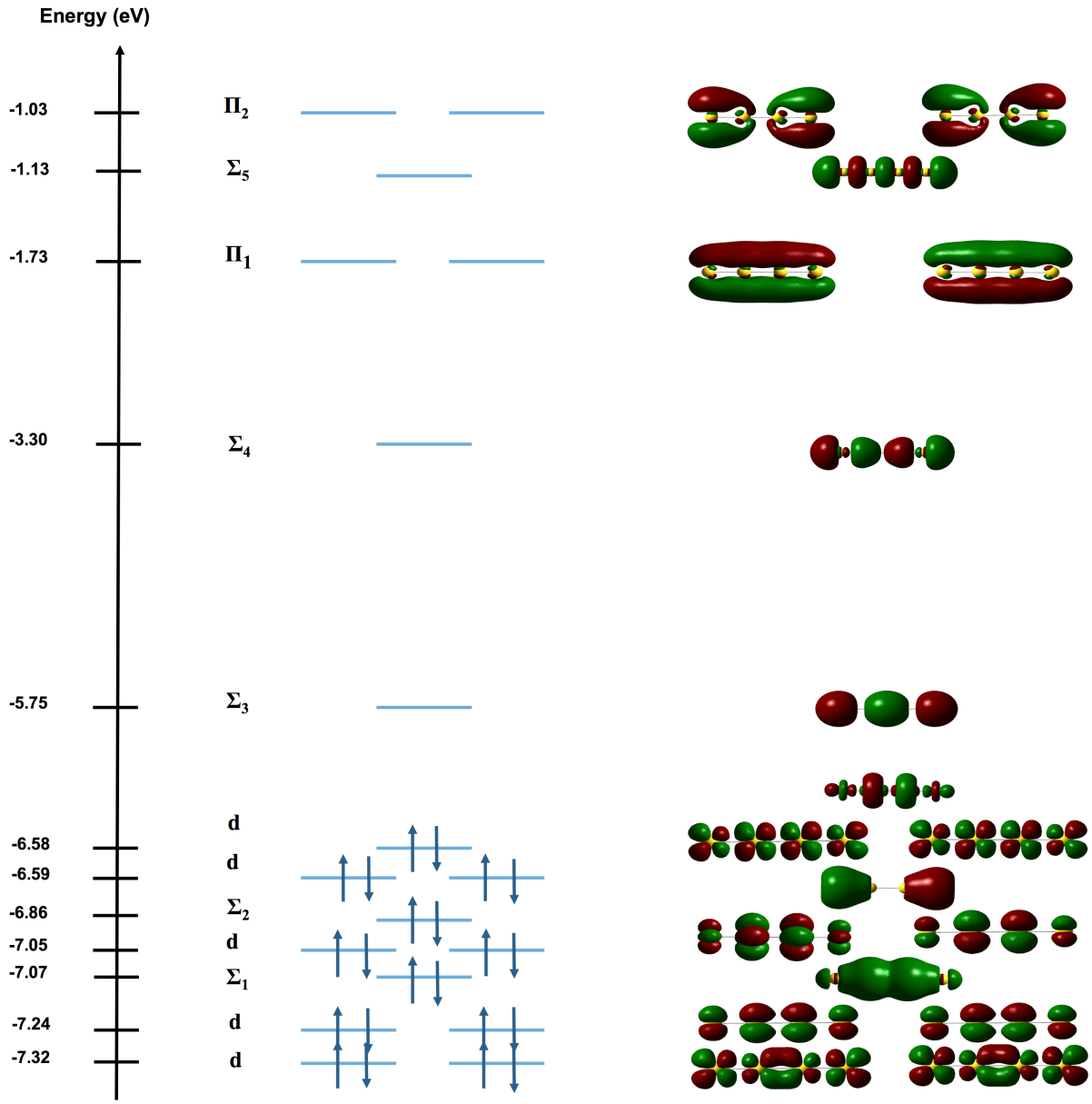

Figure 8.3 Kohn-Sham orbital energy diagram of Au_4.

In the Au_4 nanowire, the HOMO-2 → LUMO transition corresponds to a Σ_2 → Σ_3 transition (Table 8.1). For the corresponding silver case, the strong excitation in Ag_4 also arises from a Σ_2 → Σ_3 transition, although this corresponds to a HOMO → LUMO transition.[56] As shown in Figure 8.2a, the orbital occupation numbers of the HOMO-2 and LUMO vary in phase and with the same frequency. They are strongly related and give rise to two intense peaks around 2 and 4 eV in the Fourier transformed spectrum that agree with the peaks arising in the same energy range in the optical absorption spectrum. Therefore, it is evident that the HOMO-2 →

LUMO transition ($\Sigma_2 \rightarrow \Sigma_3$) plays an important role in these two peaks of the longitudinal mode in the Au_4 nanowire.

For comparison, the contributions of different single particle transitions can be determined from the eigenvectors in the LR-TDDFT calculations that provide the weights of each individual transition. Table 8.2 shows the LR-TDDFT excitation energies, oscillator strengths, single particle transitions, and the weights of each transition for both longitudinal and transverse modes for this nanowire. For the longitudinal mode, the HOMO-2 → LUMO transition possesses a high weight in the peak around 1.98 eV, which agrees with our assessment from the RT-TDDFT calculations. In the real time simulation of the Au_4 nanowire we observe additional prominent peaks around 3.6, 4.4 and 5.2 eV in the longitudinal mode of the optical absorption spectrum (Figure 8.1a-e). The LR-TDDFT transitions in Table 8.2 indicate that there are peaks around 3.67, 4.43, and 5.29 eV. The 3.67 eV, 4.43 eV and 5.29 eV peaks are comparable with the real time simulation peaks around the same energies. The RT-TDDFT peak positions differ slightly compared to the LR-TDDFT calculations due to error associated in reading off the peak positions from the dipole strength function in the RT approach, whereas the LR approach determines the excitation energies from eigenvalues of the Casida equation.

The peak at 5.2 eV has the highest intensity in the real time simulation of the Au_4 longitudinal mode (Figure 8.1) which is also reflected in the LR-TDDFT calculation of a 5.29 eV peak with a high oscillator strength (f=1.35) in Table 8.2. To understand the origin of this peak, the transitions involved in the 5.29 eV peak (Table 8.2) were further analyzed from the Fourier transformed spectra of the orbital occupation numbers in the RT-TDDFT calculations. The respective Fourier transformed spectra of the orbital occupation numbers are shown in the supporting information. As shown in Figure F.2, it is evident that the HOMO-12 → LUMO, HOMO-7 → LUMO+1, HOMO-2 → LUMO+3, HOMO-1 → LUMO+2, HOMO-1 → LUMO+2 and HOMO → LUMO+3 transitions from the RT-TDDFT calculation are the single particle transitions giving rise to the peak around 5.2 eV in the Fourier transformed spectra. These are also the transitions that contribute to the peak around 5.29 eV according to the LR-TDDFT calculations (Table 8.2). However, the magnitudes of the peaks around 5.2 eV are very small compared to the magnitude of the ~1.9 eV peak (HOMO-12 → LUMO) in the Fourier transformed spectra of the orbital occupation numbers (Figure F.2).

Table 8.2 The LR-TDDFT excitation energies, oscillator strengths, single particle transitions and weights of each transition for longitudinal (L) and transverse (T) modes of Au_4 at the BP86/LanL2DZ level of theory. The "→/←" signs in the Transitions column indicate the excitations/de-excitations.

Peak	Energy (eV)	Oscillator strength	Transitions	Weight
L	1.98	0.39	HOMO-12 → LUMO	-0.161
			HOMO-2 → LUMO	0.712
			HOMO-2 ← LUMO	-0.201
	3.67	0.23	HOMO-12 → LUMO	0.623
			HOMO-7 → LUMO+1	0.27
			HOMO-4 → LUMO+1	-0.136
			HOMO-2 → LUMO	0.121
	4.43	0.27	HOMO-12 → LUMO	-0.214
			HOMO-7 → LUMO+1	0.57
			HOMO-4 → LUMO+1	-0.136
			HOMO-1 → LUMO+2	0.228
			HOMO-1 → LUMO+2	0.227
	5.29	1.35	HOMO-12 → LUMO	0.177
			HOMO-7 → LUMO+1	-0.217
			HOMO-2 → LUMO	0.138
			HOMO-2 → LUMO+3	0.136
			HOMO-1 → LUMO+2	0.413
			HOMO-1 → LUMO+2	0.413
			HOMO → LUMO+3	0.194
T	5.49	0.24	HOMO-1 → LUMO+2	-0.115
			HOMO-1 → LUMO+2	-0.115
			HOMO → LUMO+3	0.675
	6.2	0.25	HOMO-9 → LUMO +2	0.18
			HOMO-9 → LUMO+2	-0.179
			HOMO-8 → LUMO+5	-0.197
			HOMO-8 → LUMO+4	0.197
			HOMO-7 → LUMO+1	-0.124
			HOMO-6 → LUMO+3	-0.259
			HOMO-4 → LUMO+2	-0.217
			HOMO-3 → LUMO+4	-0.13
			HOMO-3 → LUMO+5	0.13
			HOMO-2 → LUMO+4	0.389
	6.38	0.22	HOMO-10 → LUMO+2	-0.134

			HOMO-10 → LUMO+2	-0.134
			HOMO-6 → LUMO+4	0.473
			HOMO-6 → LUMO+5	0.473
	6.7	0.3	HOMO-11 → LUMO+3	0.116
			HOMO-8 → LUMO+4	0.415
			HOMO-8 → LUMO+5	0.415
			HOMO-6 → LUMO+3	0.109
			HOMO-4 → LUMO+2	-0.114
			HOMO-2 → LUMO+5	0.243

For Au_6, the HOMO-3 is strongly correlated with the LUMO while the HOMO-2 is less strongly correlated with the LUMO (Figure 8.2). The Fourier transformed spectrum of the orbital occupation numbers of the HOMO-3 has peaks of similar magnitude to those of the LUMO, whereas the HOMO-2 has peaks with a smaller magnitude although they fall in the same frequency range of 1.5 – 4 eV. The orbital occupation number variation also shows that the HOMO-3 orbital occupation numbers vary in a larger range than for the HOMO-2. Therefore, the HOMO-3 → LUMO transition (d → Σ transition) appears to be the main transition involved in the longitudinal mode of Au_6, while HOMO-2 → LUMO (which has $\Sigma_n \rightarrow \Sigma_{n+1}$ character) contributes to a lesser extent. LR-TDDFT calculations show that these two transitions can constructively add together to give rise to a strong peak, and this constructive interaction is identified by the hallmark of in-phase oscillations in the RT-TDDFT calculations.

The Au_8, Au_{10}, and Au_{12} nanowires have HOMO-3 → LUMO, HOMO-4 → LUMO, and HOMO-4 → LUMO, respectively, as the most probable transitions. Each of these transitions has $\Sigma_n \rightarrow \Sigma_{n+1}$ character. The d → Σ transitions are less probable transitions that contribute to the longitudinal mode (Table 8.1). Real time dynamics illustrating the transitions contributing to the longitudinal mode of Au_8, Au_{10} and Au_{12} are shown in Figures F.3, F.4 and F.5 respectively in Appendix F.

8.4.3 Transverse mode excitations

Figure 8.1f – j shows that the transverse modes of the gold nanowires display a band of several peaks in the energy range of 6-7 eV, which was also observed in previous LR-TDDFT calculations.[43] The transverse mode in the energy range of 6-7 eV displays two peaks where the

peak closer to 6 eV grows in intensity significantly while the peak closer to the 7 eV grows in intensity less noticeably as the nanowire length increases from Au_4 to Au_{12}. Overall, the transverse peak intensity increases with the nanowire length.

In contrast to the longitudinal mode, the transverse modes in gold nanowires are constructed from a coupling of two or more single particle transitions with $\Sigma_n \rightarrow \Pi_n$ character (Figure 8.4). The single particle transitions involved in the transverse mode of the gold nanowires are shown in Table 8.3. The involvement of two or more $\Sigma_n \rightarrow \Pi_n$ type single particle transitions in the transverse modes has also been observed in real time simulations in similar silver nanowires.[56] In the silver nanowire case, the strong transverse peak has been identified as arising from a superposition of $\Sigma_n \rightarrow \Pi_n$ single particle transitions. Their orbital occupation number variations are in phase with the same frequency and they constructively/destructively interact to give rise to several peaks in the transverse mode, which is supported by a configuration interaction (CI) picture arising from LR-TDDFT calculations.[56]

Table 8.3 The single particle transitions involved in the transverse mode of gold nanowires obtained by RT-TDDFT calculations.

Nanowire	Single particle transition	Symmetries
Au_4	HOMO-2 → LUMO+4 HOMO-4 → LUMO+2	$\Sigma_2 \rightarrow \Pi_2$ $\Sigma_1 \rightarrow \Pi_1$
Au_6	HOMO-6 →LUMO+4 HOMO-9 → LUMO+3	$\Sigma_2 \rightarrow \Pi_2$ $\Sigma_1 \rightarrow \Pi_1$
Au_8	HOMO-4 → LUMO+8 HOMO-9 → LUMO+5 HOMO-10 →LUMO+4	$\Sigma_3 \rightarrow \Pi_3$ $\Sigma_2 \rightarrow \Pi_2$ $\Sigma_1 \rightarrow \Pi_1$
Au_{10}	HOMO-9 → LUMO+9 HOMO-13 → LUMO+7 HOMO-16 → LUMO+6	$\Sigma_3 \rightarrow \Pi_3$ $\Sigma_2 \rightarrow \Pi_2$ $\Sigma_1 \rightarrow \Pi_1$
Au_{12}	HOMO-15 → LUMO+9 HOMO-17 → LUMO+7 HOMO-19 → LUMO+5	$\Sigma_3 \rightarrow \Pi_3$ $\Sigma_2 \rightarrow \Pi_2$ $\Sigma_1 \rightarrow \Pi_1$

Figure 8.4 shows the orbital occupation number variation and the respective Fourier transformed spectra for the strongly correlated transitions for the transverse mode of Au_4. The data for Au_4 clearly indicates that the HOMO-2 → LUMO+4 and HOMO-4 → LUMO+2 transitions are the most probable due to the strong relationships between the respective orbital occupation number variations as shown in Figures 8.4c and f. The two transitions have $\Sigma_2 \rightarrow \Pi_2$

and $\Sigma_1 \rightarrow \Pi_1$ symmetries. The HOMO-2 and LUMO+4 orbital occupation numbers vary in phase and with the same frequency which is the same case as HOMO-4 and LUMO+2. As explained for the longitudinal mode, the Fourier transformed spectra of the respective orbital occupation numbers (Figure 8.4a, b, d and e) demonstrate peaks with a high magnitude around the 6–7 eV energy range, which supports the idea that those transitions are responsible for the transverse peak (two main peaks) that appear in the 6–7 eV range in the optical absorption spectrum of Au_4.

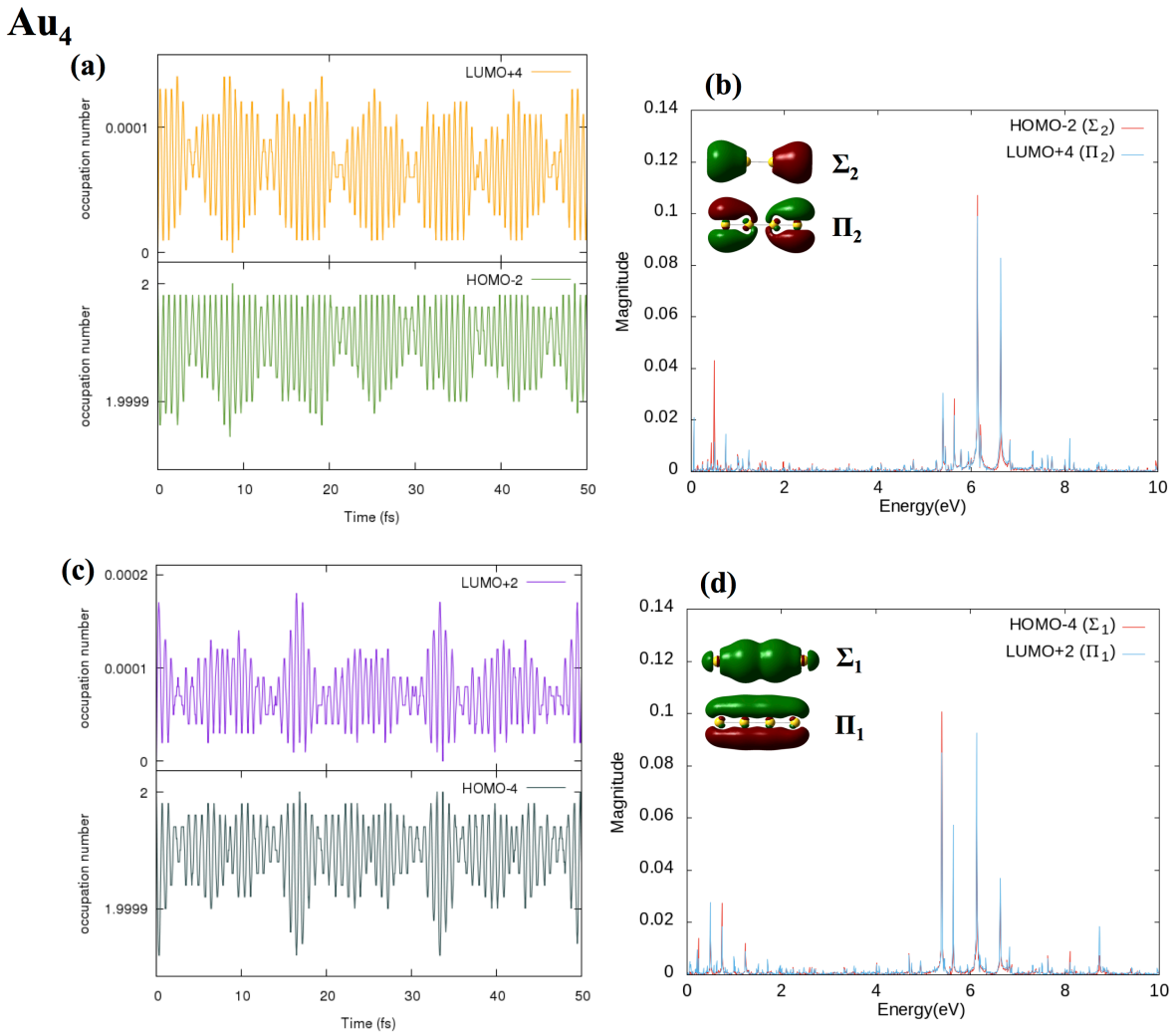

Figure 8.4 The orbital occupation number variation [a and c] and the respective Fourier transformed spectra [b and d] for strongly correlated transitions responsible for the transverse mode of Au_4.

Table 8.2 also collects the energies, oscillator strengths, transitions and weights of the transitions involved in the Au_4 transverse mode from the LR-TDDFT calculations. It indicates three main peaks around 5.49, 6.20, 6.38 and 6.70 eV which are comparable to the main peaks around 5.4, 6.1 and 6.6 eV in the Au_4 optical absorption spectrum (Figure 8.1f). The two main transitions HOMO-4 → LUMO+2 and HOMO-2 → LUMO+4 obtained from real time simulations are also visible in the LR-TDDFT calculation as transitions with high oscillator strength values. However, their weights are not as high as those of the other transitions. The remaining transitions (Table 8.2) involved in the LR-TDDFT transverse mode are also visible from the real time calculations, which is evident from the Fourier transformed spectra of their orbital occupation numbers. However, the Fourier transformed spectrum of these orbital occupations exhibit low magnitude peaks around the 6 – 7 eV energy range compared to the peaks related to the primary orbitals mentioned above. This supports the idea that the transverse mode of the gold nanowires is mainly constructed with $\Sigma_n \rightarrow \Pi_n$ type transitions while other transitions contribute to a lesser extent. Their orbital occupation numbers vary in phase with same frequency which is evident from the real-time calculations.

Further analysis of the real-time simulation with excitation in the *x* direction reveals that there is a relatively intense peak arising around the ~1.8 eV region in the orbital occupation number Fourier transformed spectra of the HOMO-6 and LUMO orbitals as shown in Figure 8.5a and b. This could suggest a transition between HOMO-6 to LUMO which is a $d\Pi \rightarrow \Sigma$ transition. The $d\Pi$ orbital is an orbital with mixed Au d band and sp-based Π character. It is interesting to note that the longitudinal peak of Au_4 arises around 1.98 eV, which is close to the same energy as the energy (~1.8 eV) of the peak arising from the HOMO-6 → LUMO ($d\Pi \rightarrow \Sigma$) transition. Therefore, it is a characteristic that is visible in the Fourier transformed spectra of the orbitals when the system is excited in *z* direction but also visible in the Fourier transformed spectra of orbitals when it is excited in *x* direction. However, the orbital occupation number variation for those two orbitals is very small (Figure 8.5c) and could be the reason that a peak is not visible around 1.8 eV in the *x*-polarized optical absorption spectrum for Au_4. This behavior was not present in the silver nanowire case.

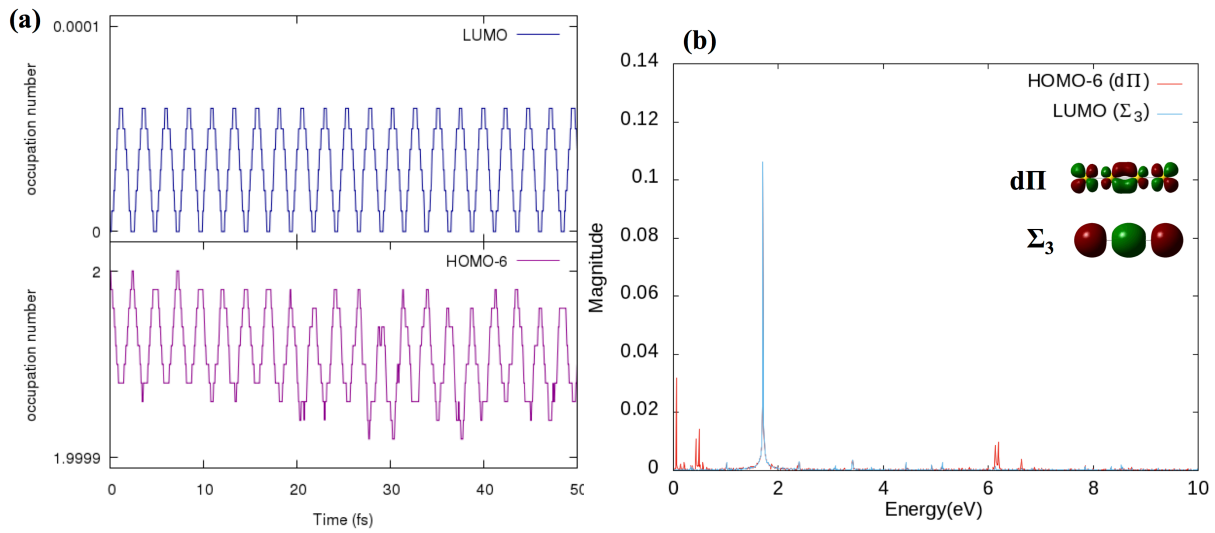

Figure 8.5 The orbital occupation number variations and their Fourier transformed spectra of two orbitals HOMO-6 and LUMO of Au_4 excited by excitation in the *x* direction.

Similar behavior can be observed in the rest of the nanowires which is also shown in Table 8.3. Their orbital occupation number variations and the Fourier transformed spectra for the strongly correlated transitions are shown in Figure F.6, F.7, F.8 and F.9 in Appendix F.

Overall, the RT-TDDFT calculations on gold nanowires using the Gaussian software have reasonably produced similar plasmon like characteristics as in the LR-TDDFT calculations performed on the similar gold nanowires using both ADF and Gaussian software. This study further confirms that the RT-TDDFT method can reproduce results similar to the LR method for the small gold systems (nanowires) in the weak perturbation regime which has been shown for the silver systems previously. Therefore, the findings from this study will be an initiative to investigate stronger field perturbations on the gold/silver systems to understand their plasmon character. Modeling plasmons in a stronger field regime can provide insights for the experimental observations.

8.5 Conclusion

A series of linear gold nanowires having 4, 6, 8, 10 and 12 atoms were investigated using a RT-TDDFT method with a step function electric field perturbation. The dipolar response of the longitudinal and transverse modes upon changing the nanowire length was probed. The aim of this work is to understand the differences in the plasmon-like character in gold nanowires

compared to silver nanowires using the RT-TDDFT method and to investigate how the d band transitions play a role in determining the character of plasmon-like states in gold nanowires. Therefore, we studied the time evolution of the single particle transitions and examined the interplay between different transitions involved in the plasmonic excitations of model gold nanowires Au_m (m= 4, 6, 8, 10, 12).

The dipole strength functions (optical absorption spectra) were obtained for both longitudinal and transverse modes of the nanowires. It was evident that the longitudinal mode appears in the energy range of 1-2 eV and redshifts with increasing nanowire length similar to previous LR-TDDFT calculations on gold nanowires as well as RT and LR calculations on silver nanowires. A splitting is evident in the longitudinal peak with increasing nanowire length. The transitions originating from the d band are the reason for the observed splitting in the longitudinal mode in gold nanowires. The transverse mode is present around the 6-7 eV energy range of the optical absorption spectrum, which is constant as the length of the nanowire increases. In both modes, the dipole strength increases as the nanowire length increases from Au_4 to Au_{12}.

The time-dependent occupation numbers and their Fourier transformed spectra are used to understand the nature of the interplay between the single particle transitions involved in both of the plasmon modes. This analysis recognized the orbitals responsible for the important transitions contributing to both the longitudinal and transverse modes. The single particle transitions can constructively/destructively interact with each other, as observed through orbital occupation number variations that are in phase with the same frequency. This will give rise to several peaks in the optical absorption spectrum.

A dominant single particle transition ($\Sigma_n \rightarrow \Sigma_{n+1}$) can be identified in the longitudinal mode of gold nanowires similar to the previous silver nanowire study. We also observe a coupling of the dominant single particle transition with the less probable d-band transitions that have $d \rightarrow \Sigma$ character. This behavior was true for all the gold nanowires considered in this study except for the Au_6 nanowire which gives $d \rightarrow \Sigma$ as the most dominant single particle transition.

The transverse modes in gold nanowires are constructed from a coupling of two or more single particle transitions with $\Sigma_n \rightarrow \Pi_n$ character, which was also seen in the previous silver nanowire study. The analysis of the x-polarized transitions also revealed a relatively intense peak with $d\Pi \rightarrow \Sigma$ character arising around the 1.8 eV region in the orbital occupation number Fourier

transformed spectra; this is in the same energy range as the longitudinal peak. However, this peak is not visible around 1.8 eV in the *x*-polarized optical absorption spectrum. This could be due to the very small orbital occupation number variations in those two orbitals.

8.6 Acknowledgements

This material is based on work supported by the Department of Energy under grant DE-SC0012273. The computing for this project was performed on the computing for this project was performed on the Beocat Research Cluster at Kansas State University, which is funded in part by NSF grants CHE-1726332, CNS-1006860, EPS-1006860, and EPS-0919443. The development of the first-principles electronic dynamics is supported by the US Department of Energy (DE-SC0006863 to XL). The development of linear response TDDFT method for computational spectroscopy was supported by the National Science Foundation (CHE-1565520 to XL).

8.7 References

1. Haes, A. J.; Haynes, C. L.; McFarland, A. D.; Schatz, G. C.; Van Duyne, R. P.; Zou, S., Plasmonic Materials for Surface-enhanced Sensing and Spectroscopy. *MRS Bull* **2005,** *30* (05), 368-375.

2. Kneipp, K.; Wang, Y.; Kneipp, H.; Perelman, L. T.; Itzkan, I.; Dasari, R. R.; Feld, M. S., Single Molecule Detection using Surface-Enhanced Raman scattering (SERS). *Phys. Rev. Lett.* **1997,** *78* (9), 1667.

3. Nie, S.; Emory, S. R., Probing Single Molecules and Single Nanoparticles by Surface-enhanced Raman Scattering. *science* **1997,** *275* (5303), 1102-1106.

4. Michaels, A. M.; Nirmal, M.; Brus, L., Surface Enhanced Raman Spectroscopy of Individual Rhodamine 6G Molecules on Large Ag Nanocrystals. *J. Am. Chem. Soc.* **1999,** *121* (43), 9932-9939.

5. Hutter, E.; Fendler, J. H., Exploitation of Localized Surface Plasmon Resonance. *Adv. Mater.* **2004,** *16* (19), 1685-1706.

6. Mullin, J.; Valley, N.; Blaber, M. G.; Schatz, G. C., Combined Quantum Mechanics (TDDFT) and Classical Electrodynamics (Mie theory) Methods for Calculating Surface Enhanced Raman and Hyper-Raman Spectra. *J. Phys. Chem. A* **2012,** *116* (38), 9574-9581.

7. Saha, K.; Agasti, S. S.; Kim, C.; Li, X.; Rotello, V. M., Gold Nanoparticles in Chemical and Biological Sensing. *Chem. Rev.* **2012,** *112* (5), 2739-2779.

8. Tagar, Z. A.; Memon, N.; Agheem, M. H.; Junejo, Y.; Hassan, S. S.; Kalwar, N. H.; Khattak, M. I., Selective, Simple and Economical Lead Sensor based on Ibuprofen Derived Silver Nanoparticles. *Sens. Actuator B-Chem.* **2011,** *157* (2), 430-437.

9. Jiang, S.; Win, K. Y.; Liu, S.; Teng, C. P.; Zheng, Y.; Han, M.-Y., Surface-functionalized Nanoparticles for Biosensing and Imaging-guided Therapeutics. *Nanoscale* **2013,** *5* (8), 3127-3148.

10. Sun, Y., Conversion of Ag Nanowires to AgCl Nanowires Decorated with Au Nanoparticles and Their Photocatalytic Activity. *J. Phys. Chem. C* **2010,** *114* (5), 2127-2133.

11. Huang, X.; Neretina, S.; El-Sayed, M. A., Gold Nanorods: From Synthesis and Properties to Biological and Biomedical Applications. *Adv. Mater.* **2009,** *21* (48), 4880-4910.

12. Huang, X.; El-Sayed, I. H.; Qian, W.; El-Sayed, M. A., Cancer Cell Imaging and Photothermal Therapy in the Near-infrared Region by Using Gold Nanorods. *J. Am. Chem. Soc.* **2006,** *128* (6), 2115-2120.

13. Zhang, J. Z., Biomedical Applications of Shape-controlled Plasmonic Nanostructures: A Case Study of Hollow Gold Nanospheres for Photothermal Ablation Therapy of Cancer. *J. Phys. Chem. Lett.* **2010,** *1* (4), 686-695.

14. Parab, H. J.; Chen, H. M.; Lai, T.-C.; Huang, J. H.; Chen, P. H.; Liu, R.-S.; Hsiao, M.; Chen, C.-H.; Tsai, D.-P.; Hwu, Y.-K., Biosensing, Cytotoxicity, and Cellular Uptake Studies of Surface-modified Gold Nanorods. *J. Phys. Chem. C* **2009,** *113* (18), 7574-7578.

15. Hirakawa, T.; Kamat, P. V., Photoinduced Electron Storage and Surface Plasmon Modulation in Ag@ TiO_2 Clusters. *Langmuir* **2004,** *20* (14), 5645-5647.

16. Chen, Y.-S.; Choi, H.; Kamat, P. V., Metal-cluster-sensitized Solar Cells. A New Class of Thiolated Gold Sensitizers Delivering Efficiency Greater than 2%. *J. Am. Chem. Soc.* **2013,** *135* (24), 8822-8825.

17. El-Sayed, I. H.; Huang, X.; El-Sayed, M. A., Surface Plasmon Resonance Scattering and Absorption of Anti-EGFR Antibody Conjugated Gold Nanoparticles in Cancer Diagnostics: Applications in Oral Cancer. *Nano Lett.* **2005,** *5* (5), 829-834.

18. Jin, R.; Cao, Y.; Mirkin, C. A.; Kelly, K.; Schatz, G. C.; Zheng, J., Photoinduced Conversion of Silver Nanospheres to Nanoprisms. *Science* **2001,** *294* (5548), 1901-1903.

19. Fedrigo, S.; Harbich, W.; Buttet, J., Collective Dipole Oscillations in Small Silver Clusters Embedded in Rare-gas Matrices. *Phys. Rev. B* **1993,** *47* (16), 10706.

20. Schmucker, A. L.; Harris, N.; Banholzer, M. J.; Blaber, M. G.; Osberg, K. D.; Schatz, G. C.; Mirkin, C. A., Correlating Nanorod Structure with Experimentally Measured and Theoretically Predicted Surface Plasmon Resonance. *ACS nano* **2010,** *4* (9), 5453-5463.

21. Köller, L.; Schumacher, M.; Köhn, J.; Teuber, S.; Tiggesbäumker, J.; Meiwes-Broer, K., Plasmon-enhanced Multi-ionization of Small Metal Clusters in Strong Femtosecond Laser Fields. *Phys. Rev. Lett.* **1999,** *82* (19), 3783.

22. Jain, P. K.; El-Sayed, M. A., Plasmonic Coupling in Noble Metal Nanostructures. *Chem. Phys. Lett.* **2010,** *487* (4), 153-164.

23. Mahmoud, M. A.; El-Sayed, M. A., Different Plasmon Sensing Behavior of Silver and Gold Nanorods. *J. Phys. Chem. Lett.* **2013,** *4* (9), 1541-1545.

24. Okamoto, H.; Imura, K., Visualizing the Optical Field Structures in Metal Nanostructures. *J. Phys. Chem. Lett.* **2013,** *4* (13), 2230-2241.

25. Chen, H.; Shao, L.; Li, Q.; Wang, J., Gold Nanorods and their Plasmonic Properties. *Chem. Soc. Rev.* **2013,** *42* (7), 2679-2724.

26. Polavarapu, L.; Liz-Marzán, L. M., Towards Low-cost Flexible Substrates for Nanoplasmonic Sensing. *Phys. Chem. Chem. Phys.* **2013,** *15* (15), 5288-5300.

27. Kelly, K. L.; Coronado, E.; Zhao, L. L.; Schatz, G. C., The Optical Properties of Metal Nanoparticles: The Influence of Size, Shape, and Dielectric Environment. *J. Phys. Chem. B* **2003,** *107* (3), 668-677.

28. Aikens, C. M., Electronic Structure of Ligand-passivated Gold and Silver Nanoclusters. *J. Phys. Chem. Lett.* **2010,** *2* (2), 99-104.

29. Morton, S. M.; Silverstein, D. W.; Jensen, L., Theoretical Studies of Plasmonics using Electronic Structure Methods. *Chem. Rev.* **2011,** *111* (6), 3962-3994.

30. Nordlander, P.; Prodan, E., Plasmon Hybridization in Nanoparticles Near Metallic Surfaces. *Nano Lett.* **2004,** *4* (11), 2209-2213.

31. Nordlander, P.; Oubre, C.; Prodan, E.; Li, K.; Stockman, M., Plasmon Hybridization in Nanoparticle Dimers. *Nano Lett.* **2004,** *4* (5), 899-903.

32. Jain, P. K.; El-Sayed, M. A., Surface Plasmon Resonance Sensitivity of Metal Nanostructures: Physical Basis and Universal Scaling in Metal Nanoshells. *J. Phys. Chem. C* **2007,** *111* (47), 17451-17454.

33. Link, S.; El-Sayed, M. A., Size and Temperature Dependence of the Plasmon Absorption of Colloidal Gold Nanoparticles. *J. Phys. Chem. B* **1999,** *103* (21), 4212-4217.

34. Gonzalez, A.; Noguez, C.; Ortiz, G.; Rodriguez-Gattorno, G., Optical Absorbance of Colloidal Suspensions of Silver Polyhedral Nanoparticles. *J. Phys. Chem. B* **2005,** *109* (37), 17512-17517.

35. Wiley, B. J.; Im, S. H.; Li, Z.-Y.; McLellan, J.; Siekkinen, A.; Xia, Y., Maneuvering the Surface Plasmon Resonance of Silver Nanostructures through Shape-Controlled Synthesis. *J. Phys. Chem. B* **2006,** *110* (32), 15666-15675.

36. Link, S.; Mohamed, M.; El-Sayed, M., Simulation of the Optical Absorption Spectra of Gold Nanorods as a Function of their Aspect Ratio and the Effect of the Medium Dielectric Constant. *J. Phys. Chem. B* **1999,** *103* (16), 3073-3077.

37. Al-Sherbini, E.-S. A., UV–visible Light Reshaping of Gold Nanorods. *Mater. Chem. Phys.* **2010,** *121* (1), 349-353.

38. Ni, W.; Ambjornsson, T.; Apell, S. P.; Chen, H.; Wang, J., Observing Plasmonic−molecular Resonance Coupling on Single Gold Nanorods. *Nano Lett.* **2009,** *10* (1), 77-84.

39. Yu, Y.-Y.; Chang, S.-S.; Lee, C.-L.; Wang, C. C., Gold Nanorods: Electrochemical Synthesis and Optical Properties. *J. Phys. Chem. B* **1997,** *101* (34), 6661-6664.

40. Pietrobon, B.; McEachran, M.; Kitaev, V., Synthesis of Size-controlled Faceted Pentagonal Silver Nanorods with Tunable Plasmonic Properties and Self-assembly of these Nanorods. *ACS nano* **2008,** *3* (1), 21-26.

41. Liao, M.-S.; Bonifassi, P.; Leszczynski, J.; Ray, P. C.; Huang, M.-J.; Watts, J. D., Structure, Bonding, and Linear Optical Properties of a Series of Silver and Gold Nanorod Clusters: DFT/TDDFT Studies. *J. Phys. Chem. A* **2010,** *114* (48), 12701-12708.

42. Johnson, H. E.; Aikens, C. M., Electronic Structure and TDDFT Optical Absorption Spectra of Silver Nanorods. *J. Phys. Chem. A* **2009,** *113* (16), 4445-4450.

43. Guidez, E. B.; Aikens, C. M., Theoretical Analysis of the Optical Excitation Spectra of Silver and Gold Nanowires. *Nanoscale* **2012,** *4* (14), 4190-4198.

44. Khan, S. A.; Senapati, D.; Senapati, T.; Bonifassi, P.; Fan, Z.; Singh, A. K.; Neeley, A.; Hill, G.; Ray, P. C., Size Dependent Nonlinear Optical Properties of Silver Quantum Clusters. *Chem. Phys. Lett.* **2011,** *512* (1), 92-95.

45. Koponen, L.; Tunturivuori, L. O.; Puska, M. J.; Hancock, Y., Tunability of the Optical Absorption in Small Silver Cluster-polymer Hybrid Systems. *J. Chem. Phys.* **2010,** *132* (21), 214301.

46. Aikens, C. M.; Li, S.; Schatz, G. C., From Discrete Electronic States to Plasmons: TDDFT Optical Absorption Properties of Ag_n (n= 10, 20, 35, 56, 84, 120) Tetrahedral Clusters. *J. Phys. Chem. C* **2008,** *112* (30), 11272-11279.

47. Bernadotte, S.; Evers, F.; Jacob, C. R., Plasmons in Molecules. *J. Phys. Chem. C* **2013,** *117* (4), 1863-1878.

48. Lian, K.-Y.; Sałek, P.; Jin, M.; Ding, D., Density-functional Studies of Plasmons in Small Metal Clusters. *J. Chem. Phys.* **2009,** *130* (17), 174701.

49. Yan, J.; Yuan, Z.; Gao, S., End and Central Plasmon Resonances in Linear Atomic Chains. *Phys. Rev. Lett.* **2007,** *98* (21), 216602.

50. Yan, J.; Gao, S., Plasmon Resonances in Linear Atomic Chains: Free-electron Behavior and Anisotropic Screening of d Electrons. *Phys. Rev. B* **2008,** *78* (23), 235413.

51. Gao, B.; Ruud, K.; Luo, Y., Plasmon Resonances in Linear Noble-metal Chains. *J. Chem. Phys.* **2012,** *137* (19), 194307.

52. Harb, M.; Rabilloud, F.; Simon, D.; Rydlo, A.; Lecoultre, S.; Conus, F.; Rodrigues, V.; Félix, C., Optical Absorption of Small Silver Clusters: Ag_n,(n= 4–22). *J. Chem. Phys.* **2008,** *129* (19), 194108.

53. Kümmel, S.; Andrae, K.; Reinhard, P.-G., Collectivity in the Optical Response. of Small Metal Clusters. *Appl. Phys. B* **2001,** *73* (4), 293-297.

54. Bae, G.-T.; Aikens, C. M., Time-dependent Density Functional Theory Studies of Optical Properties of Ag Nanoparticles: Octahedra, Truncated Octahedra, and Icosahedra. *J. Phys. Chem. C* **2012,** *116* (18), 10356-10367.

55. Guidez, E. B.; Aikens, C. M., Diameter Dependence of the Excitation Spectra of Silver and Gold Nanorods. *J. Phys. Chem. C* **2013,** *117* (23), 12325-12336.

56. Ding, F.; Guidez, E. B.; Aikens, C. M.; Li, X., Quantum Coherent Plasmon in Silver Nanowires: A Real-time TDDFT Study. *J. Chem. Phys.* **2014,** *140* (24), 244705.

57. Kresin, V. V., Collective Resonances in Silver Clusters: Role of d Electrons and the Polarization-free Surface Layer. *Phys. Rev. B* **1995,** *51* (3), 1844.

58. Yabana, K.; Nakatsukasa, T.; Iwata, J. I.; Bertsch, G., Real-time, Real-space Implementation of the Linear Response Time-dependent Density-Functional Theory. *Phys. Status Solidi B* **2006,** *243* (5), 1121-1138.

59. Frisch, M.; Trucks, G.; Schlegel, H. B.; Scuseria, G.; Robb, M.; Cheeseman, J.; Scalmani, G.; Barone, V.; Mennucci, B.; Petersson, G., Gaussian 09, revision D. 01. Gaussian, Inc., Wallingford CT: 2009.

60. Li, X.; Smith, S. M.; Markevitch, A. N.; Romanov, D. A.; Levis, R. J.; Schlegel, H. B., A time-dependent Hartree–Fock Approach for Studying the Electronic Optical Response of Molecules in Intense Fields. *Phys. Chem. Chem. Phys.* **2005,** *7* (2), 233-239.

61. Smith, S. M.; Li, X.; Markevitch, A. N.; Romanov, D. A.; Levis, R. J.; Schlegel, H. B., A Numerical Simulation of Nonadiabatic Electron Excitation in the Strong Field Regime: Linear Polyenes. *J. Phys. Chem. A* **2005,** *109* (23), 5176-5185.

62. Smith, S. M.; Li, X.; Markevitch, A. N.; Romanov, D. A.; Levis, R. J.; Schlegel, H. B., Numerical Simulation of Nonadiabatic Electron Excitation in the Strong Field Regime. 2. Linear Polyene Cations. *J. Phys. Chem. A* **2005,** *109* (46), 10527-10534.

63. Becke, A. D., Density-functional Exchange-energy Approximation with Correct Asymptotic Behavior. *Phys. Rev. A* **1988,** *38* (6), 3098-3100.

64. Perdew, J. P., Density-functional Approximation for the Correlation Energy of the Inhomogeneous Electron Gas. *Phys. Rev. B* **1986,** *33* (12), 8822-8824.

65. Hay, P. J.; Wadt, W. R., Ab initio Effective Core Potentials for Molecular Calculations. Potentials for K to Au Including the Outermost Core Orbitals. *J. Chem. Phys.* **1985,** *82* (1), 299-310.

66. Hay, P. J.; Wadt, W. R., Ab initio Effective Core Potentials for Molecular Calculations. Potentials for the Transition Metal Atoms Sc to Hg. *J. Chem. Phys.* **1985,** *82* (1), 270-283.

67. Wadt, W. R.; Hay, P. J., Ab initio Effective Core Potentials for Molecular Calculations. Potentials for Main Group Elements Na to Bi. *J. Chem. Phys.* **1985,** *82* (1), 284-298.

68. Martin, R. M., *Electronic Structure: Basic Theory and Practical Methods*. Cambridge university press: 2004.

69. Lenthe, E. v.; Baerends, E.-J.; Snijders, J. G., Relativistic Regular Two-component Hamiltonians. *J. Chem. Phys.* **1993,** *99* (6), 4597-4610.

70. Te Velde, G. t.; Bickelhaupt, F. M.; Baerends, E. J.; Fonseca Guerra, C.; van Gisbergen, S. J.; Snijders, J. G.; Ziegler, T., Chemistry with ADF. *J. Comput. Chem.* **2001,** *22* (9), 931-967.

Chapter 9 - Conclusions

Thiolate-protected noble metal nanoparticles in ~2 nm size regime are efficient solar photon harvesters, due to their favorable absorption spectrum that spans throughout the visible region. The traditional non-plasmonic noble metal clusters can also enhance photocatalytic yields upon visible irradiation. Clear mechanistic insights and photo-physics of excited state dynamics in thiolate-protected noble metal nanoclusters are important for developing photocatalytic applications. Relaxation dynamics on different structures and sizes of thiolate-protected noble metal nanoclusters reveal their physical and chemical properties for further development of light harvesting, photocatalytic and photoluminescence applications. In our work, the core and higher excited states lying in the visible range are investigated using TDDFT. We performed NA-MD simulations using the fewest switches surface hopping method with decoherence correction with a Kohn-Sham description of electronic states (FSSH-TDKS) to study the electronic relaxation dynamics.

Experimental studies on the nonradiative relaxation dynamics of the $[Au_{25}(SR)_{18}]^{-1}$ thiolate-protected gold nanocluster reported very distinct time constants which span from the femtosecond to nanosecond scale. Our calculations on $[Au_{25}(SH)_{18}]^{-1}$ showed that population transfer from the S_1(HOMO → LUMO) state to the ground state (GS) occurs on the several hundred picoseconds time scale. Relaxation between excited states that arise from core-to-core transitions occurs on a shorter time scale (2−18 ps). No semiring or other states were observed at an energy lower than the core-based S_1 state. This observation suggested that the several picosecond time constants observed by Moran and co-workers could arise from core-to-core transitions rather than from a core-to-semiring transition. A relatively slow decay time was observed for S_7. The S_1 state population decrease is the slowest decay due to the large energy gap to the ground state.

We investigated the electronic relaxation dynamics in the cluster series, $[Au_{25}(SR)_{18}]^{-1}$ (R = CH_3, C_2H_5, C_3H_7, MPA) [MPA = mercaptopropanoic acid] to understand the ligand effects on dynamics. The GS growth times of the ligand systems are smaller compared to the growth times in the “SH” model. All the ligand clusters including the “SH” model follow a similar trend in decay for the core states. The current study further confirms that the time constants observed by Moran and co-workers could originate from core-to-core transitions and not from core-to-

semiring transitions. The observed time constants are in the picosecond time scale (2-19 ps), which agrees with the experimental time scale. In the presence of the higher excited states, R= H, CH_3, C_2H_5, and C_3H_7 demonstrate similar relaxations trends whereas R=MPA shows a slightly different relaxation of the core states due to the smaller LUMO+1-LUMO+2 gap in its electronic structure. However, the S_1(HOMO → LUMO) state gave the slowest decay in all ligated clusters. S_7 has a relatively long decay. Separate electron and hole relaxations were performed on the $[Au_{25}(SCH_3)_{18}]^{-1}$ nanocluster to understand how the independent electron and hole relaxations contribute to the overall relaxation dynamics.

The thiolate-protected gold cluster $Au_{18}(GSH)_{14}$ has been identified as a photosensitizer with the highest potential compared to the several other glutathione-protected clusters (Au_{25}, Au_{15}, Au_{10-12}). We investigated the relaxation dynamics of $Au_{18}(SH)_{14}$ compared to the well-studied $[Au_{25}(SR)_{18}]^{-1}$. The GS growth times of $Au_{18}(SH)_{14}$ are several orders of magnitude shorter than the growth times observed for the Au_{25} nanocluster. The S_1 state gives the slowest decay time (~11 ps) among all the states. The S_1 state in Au_{18} is a semiring-to-core charge transfer state whereas the S_1 in the Au_{25} cluster is a core-to-core transitions. The higher states have short decay times (<1.4 ps). S_2 has the second slowest decay of 6.4 ps. The hole relaxations are faster than the electron relaxations due to the closely packed HOMOs in the Au_{18} electronic structure.

A subtle change in the electronic structure of thiolate-protected noble nanoparticles can result in distinctive relaxation dynamics. We performed nonradiative relaxation dynamics of the $Au_{38}(SH)_{24}$ nanocluster to describe electron relaxation dynamics. The Au_{23} core relaxations are on the picosecond timescale in the range of 2.0 – 9.7 ps. The higher excited states, including core-semiring mixed or semiring states, gave ultrafast decay times in the range of 0.6 - 4.9 ps. Our calculations predicted that the slowest decay, the decay of S_{11} or the combined S_{11}-S_{12}, S_1-S_2-S_6-S_7 and S_4-S_5-S_9-S_{10} decay, involves intracore relaxations. The phonon spectral densities and the ground state vibrational frequencies suggested that the low frequency (25 cm^{-1}) coherent phonon emission reported experimentally could be the bending of the bi-icosahedral Au_{23} core or the "fan blade twisting" mode of two icosahedral units.

The relaxation dynamics of the "golden" silver nanoparticle $[Ag_{25}(SR)_{18}]^{-1}$, showed that both silver and its exact gold analog follow a similar trend in decay times among the core states (S_1-S_6). The GS recovery times of the core states are longer than the corresponding GS recovery

times of the Au_{25} nanocluster. Among the higher excited states, S_7 has the slowest decay. The S_1 decay is the slowest among all states. Overall, $[Ag_{25}(SH)_{18}]^{-1}$ and $[Au_{25}(SH)_{18}]^{-1}$ follow a common decay trend and a relaxation mechanism due to their similar electronic structures.

The real-time TDDFT method is gaining attention as a prominent method to understand the time evolution of molecular systems in the presence of an external perturbation. We performed a real-time TDDFT investigation on a set of linear gold nanowires Au_m (m = 4, 6, 8, 10, 12) to understand the plasmon-like behavior that results from resonant excitation of a superposition of single-electron transitions. The longitudinal peak redshifts with increasing nanowire length and splitting was observed due to the interband transitions involvement. The transverse peak stays constant as the nanowire length increases. The time-dependent occupation numbers and their Fourier transformed spectra revealed that a dominant single particle transition ($\Sigma_n \rightarrow \Sigma_{n+1}$) is responsible for the longitudinal peaks, which is coupled with less probable d-band transitions ($d \rightarrow \Sigma$). The transverse modes are constructed from a coupling of two or more single particle transitions with $\Sigma_n \rightarrow \Pi_n$ character.

As future work, the relaxation dynamics of the $[Au_{25}(SR)_{18}]^{-1}$ with an experimentally used ligand (e.g. R=CH_2CH_2Ph) needs to be assessed to fully understand the importance of the ligand effect on dynamics. Slight difference in the electronic structure of R=MPA compared to the rest of the ligand systems considered in this thesis questions whether there are any notable geometrical changes that occur during the dynamics. Therefore, the geometrical changes during the dynamics can be evaluated in systems with R=MPA and CH_2CH_2Ph to understand the differences in relaxation patterns. Experimental relaxation dynamics on $Au_{25}(SR)_{18}$ have shown that the charge state and the dopants can give different relaxation mechanisms. Thus, charge and dopant effects on dynamics can be evaluated based on the $[Au_{25}(SR)_{18}]^q$ (q=+1,0,-1) and $[MAu_{24}(SR)_{18}]^{-1}$ (M=Pt, Pd, Hg) systems. Furthermore, complex population relaxations in thiolate-protected gold/silver nanoparticles demand a kinetic model to precisely calculate the decay constants. A simple kinetic model developed for small number of states would offer a better picture of the decay into intermediate states. Further, the possibilities of two exponential fitting of the populations could be evaluated for the complex population decay. The FSSH-TDKS method used in this thesis is constructed based on single Slater determinant approach which is unable to capture the plasmonic type excitations. Hence, a theoretical method with multiple

Slater determinants can be developed as opposed to the single Slater determinant approach to capture the plasmonic excitations in the noble metal systems.

Appendix A - Supporting Information for "Theoretical Investigation of Electron and Nuclear Dynamics in the $Au_{25}(SH)_{18}^{-1}$ Thiolate-protected Gold Nanocluster"

Table A.1 The most probable transitions with highest oscillator strengths and their weights that contribute to the peak around 2.20 eV.

Excitation transitions	Energy (eV)	Oscillator strength	Weight	Most weighted transitions
7	2.07	0.0044	0.6354	HOMO → LUMO+2
			0.2366	HOMO → LUMO+3
			0.0479	HOMO-2 → LUMO+3
			0.0300	HOMO-1 → LUMO+3
			0.0129	HOMO-2 → LUMO+4
			0.0115	HOMO-6 → LUMO+1
8	2.10	0.0053	0.4393	HOMO → LUMO+3
			0.2957	HOMO-1 → LUMO+2
			0.1222	HOMO → LUMO+2
			0.0345	HOMO-2 → LUMO+2
			0.0330	HOMO-1 → LUMO+4
			0.0236	HOMO-6 → LUMO
			0.0151	HOMO-5 → LUMO+1
9	2.13	0.0019	0.5248	HOMO-1 → LUMO+2
			0.1450	HOMO → LUMO+3
			0.0802	HOMO-5 → LUMO
			0.0556	HOMO → LUMO+2
			0.0443	HOMO-1 → LUMO+3
			0.0436	HOMO-2 → LUMO+3
			0.0376	HOMO-6 → LUMO
			0.0274	HOMO-2 → LUMO+2
			0.0136	HOMO-6 → LUMO+1
10	2.15	0.0001	0.5018	HOMO-1 → LUMO+3
			0.1977	HOMO-6 → LUMO
			0.1977	HOMO-2 → LUMO+2
			0.0814	HOMO-2 → LUMO+3
11	2.18	0.0002	0.2332	HOMO-2 → LUMO+2
			0.1915	HOMO-5 → LUMO
			0.1753	HOMO-5 → LUMO+1
			0.1441	HOMO-2 → LUMO+3
			0.1405	HOMO → LUMO+4
			0.0435	HOMO-6 → LUMO+1

			0.0306	HOMO-1 → LUMO+2
			0.0306	HOMO-1 → LUMO+3
12	2.18	0.0037	0.3061	HOMO-5 → LUMO
			0.2424	HOMO-6 → LUMO
			0.1628	HOMO-2 → LUMO+2
			0.1171	HOMO-2 → LUMO+3
			0.0841	HOMO-5 → LUMO+1
			0.0234	HOMO-1 → LUMO+3
			0.0214	HOMO-1 → LUMO+2
			0.0148	HOMO-6 → LUMO+1
13	2.20	0.0020	0.3455	HOMO-6 → LUMO+1
			0.2543	HOMO-5 → LUMO+1
			0.1286	HOMO → LUMO+4
			0.1237	HOMO-5 → LUMO
			0.0790	HOMO-2 → LUMO+3
			0.0250	HOMO-7 → LUMO
14	2.22	0.0089	0.2681	HOMO → LUMO+4
			0.2423	HOMO-6 → LUMO+1
			0.1408	HOMO-6 → LUMO
			0.0638	HOMO-2 → LUMO+3
			0.0548	HOMO-7 → LUMO
			0.0501	HOMO-1 → LUMO+3
			0.0498	HOMO-1 → LUMO+4
			0.0360	HOMO-1 → LUMO+2
			0.0236	HOMO-5 → LUMO
			0.0167	HOMO-5 → LUMO+1
			0.0138	HOMO → LUMO+3
			0.0136	HOMO-10 → LUMO
15	2.23	0.0033	0.2869	HOMO-7 → LUMO
			0.2162	HOMO-6 → LUMO
			0.1253	HOMO-5 → LUMO
			0.0633	HOMO → LUMO+4
			0.0517	HOMO-1 → LUMO+3
			0.0508	HOMO-1 → LUMO+4
			0.0503	HOMO-5 → LUMO+1
			0.0476	HOMO → LUMO+3
			0.0237	HOMO-6 → LUMO+1
			0.0218	HOMO-1 → LUMO+2
			0.0145	HOMO-2 → LUMO+3
			0.0115	HOMO-7 → LUMO+1
16	2.25	0.0028	0.4561	HOMO-7 → LUMO

			0.2036	HOMO-5 → LUMO+1
			0.1296	HOMO-1 → LUMO+4
			0.0716	HOMO-2 → LUMO+2
			0.0593	HOMO-6 → LUMO+1
			0.0137	HOMO → LUMO+4
			0.0112	HOMO → LUMO+3
			0.0102	HOMO-5 → LUMO
			0.0102	HOMO-6 → LUMO
17	2.26	0.0039	0.8223	HOMO-7 → LUMO+1
			0.0465	HOMO-6 → LUMO+1
			0.0240	HOMO-1 → LUMO+3
			0.0198	HOMO-2 → LUMO+3
			0.0170	HOMO → LUMO+5
			0.0135	HOMO-2 → LUMO+4
			0.0130	HOMO-2 → LUMO+4
			0.0111	HOMO-5 → LUMO
18	2.28	0.0160	0.3576	HOMO-2 → LUMO+4
			0.1476	HOMO-2 → LUMO+3
			0.0923	HOMO-6 → LUMO+1
			0.0868	HOMO → LUMO+5
			0.0710	HOMO-1 → LUMO+3
			0.0555	HOMO-7 → LUMO+1
			0.0487	HOMO-5 → LUMO
			0.0367	HOMO → LUMO+2
			0.0280	HOMO-5 → LUMO+1
			0.0159	HOMO-1 → LUMO+4
			0.0152	HOMO-6 → LUMO
			0.0113	HOMO-10 → LUMO+1
19	2.35	0.0017	0.7619	HOMO → LUMO+5
			0.1022	HOMO-2 → LUMO+4
			0.0398	HOMO-10 → LUMO+1
			0.0311	HOMO-1 → LUMO+4
			0.0163	HOMO-1 → LUMO+3
			0.0129	HOMO-7 → LUMO+1
20	2.38	0.0218	0.3433	HOMO-1 → LUMO+5
			0.1332	HOMO → LUMO+4
			0.1313	HOMO-2 → LUMO+2
			0.1146	HOMO-1 → LUMO+4
			0.0796	HOMO-5 → LUMO+1
			0.0472	HOMO-2 → LUMO+3
			0.0270	HOMO-7 → LUMO

			0.0179	HOMO-2 → LUMO+5
			0.0163	HOMO-6 → LUMO+1
			0.0123	HOMO-1 → LUMO+3
			0.0101	HOMO-13 → LUMO

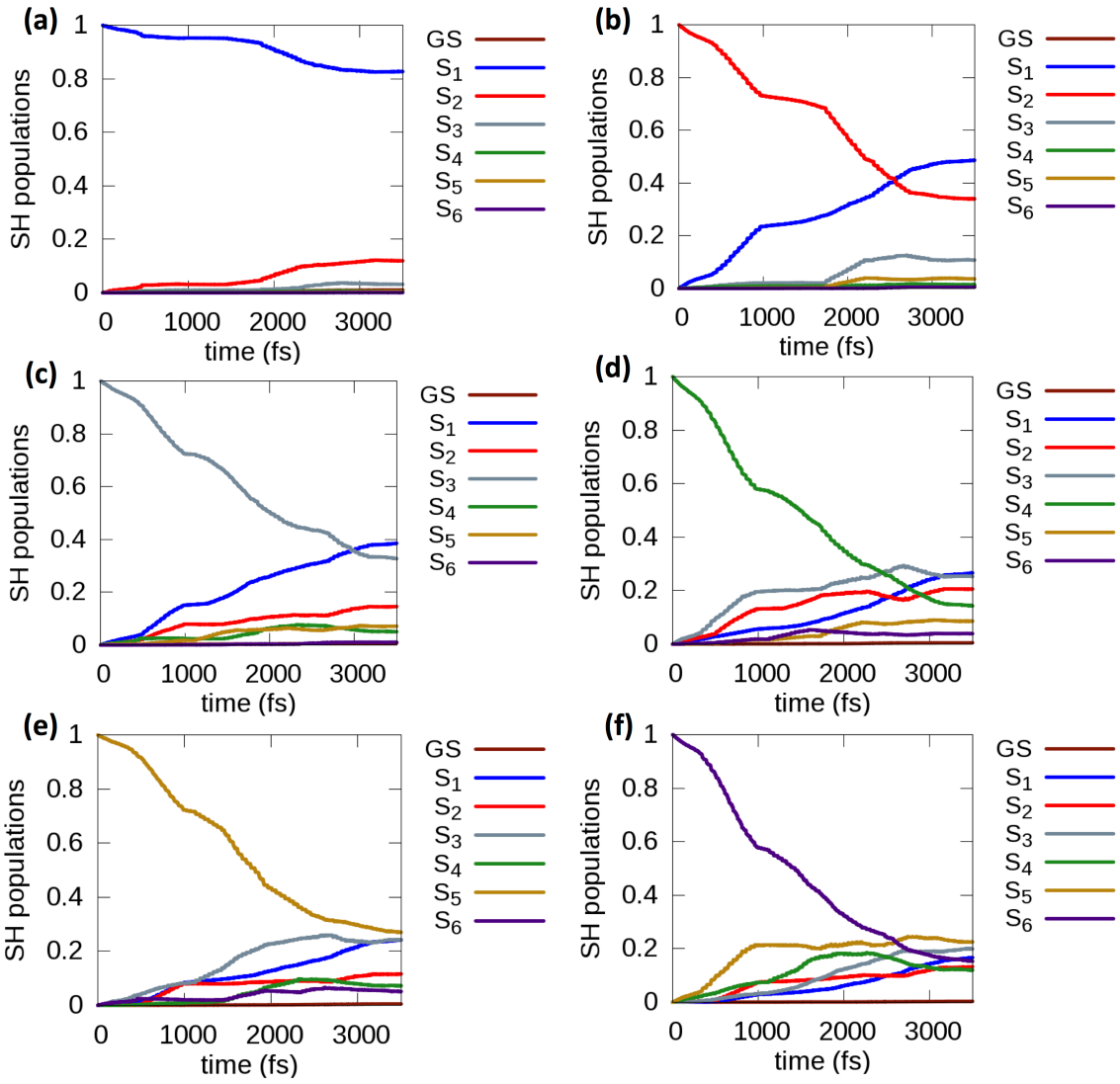

Figure A.1 Evolution of the populations of S_1, S_2, S_3, S_4, S_5, S_6 states. Parts (a) to (f) represent relaxations from S_1-S_6, respectively, with energy correction.

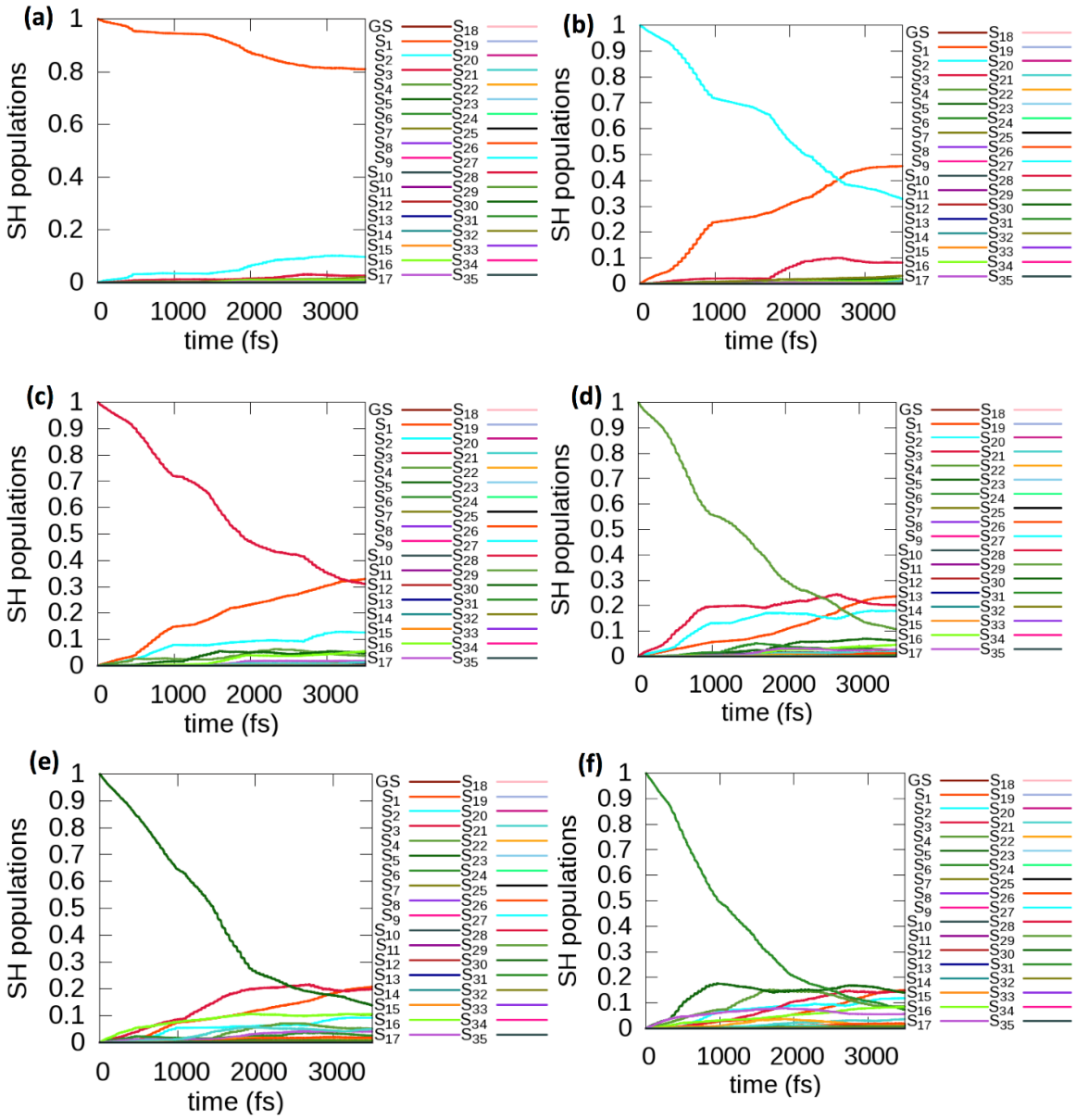

Figure A.2 Population relaxations of S_1, S_2, S_3, S_4, S_5, S_6 states with the energy correction in the presence of higher energy states. Parts (a) to (f) represent S_1-S_6 respectively.

Table A.2 The decay times of the excited state population decrease of the six excited states in the presence of higher excited states with the inclusion of the energy correction.

Excited state	Decay time (ps)
S_1	15
S_2	3.3
S_3	3.0
S_4	1.7

S_5	1.8
S_6	1.4

Table A.3 The decay times of the excited state population decrease of the S_7-S_{35} higher excited states with the inclusion of the energy correction.

Excited state	Decay time (ps)
S_7	9.9
S_8	2.8
S_9	1.5
S_{10}	3.1
S_{11}	1.6
S_{12}	1.2
S_{13}	2.3
S_{14}	1.5
S_{15}	1.2
S_{16}	2.9
S_{17}	1.7
S_{18}	2.8
S_{19}	1.5
S_{20}	1.0
S_{21}	1.8
S_{22}	1.2
S_{23}	1.7
S_{24}	1.1
S_{25}	0.9
S_{26}	1.4
S_{27}	1.0
S_{28}	1.3
S_{29}	0.9
S_{30}	0.7
S_{31}	1.3
S_{32}	0.9
S_{33}	1.1
S_{34}	0.9
S_{35}	0.8

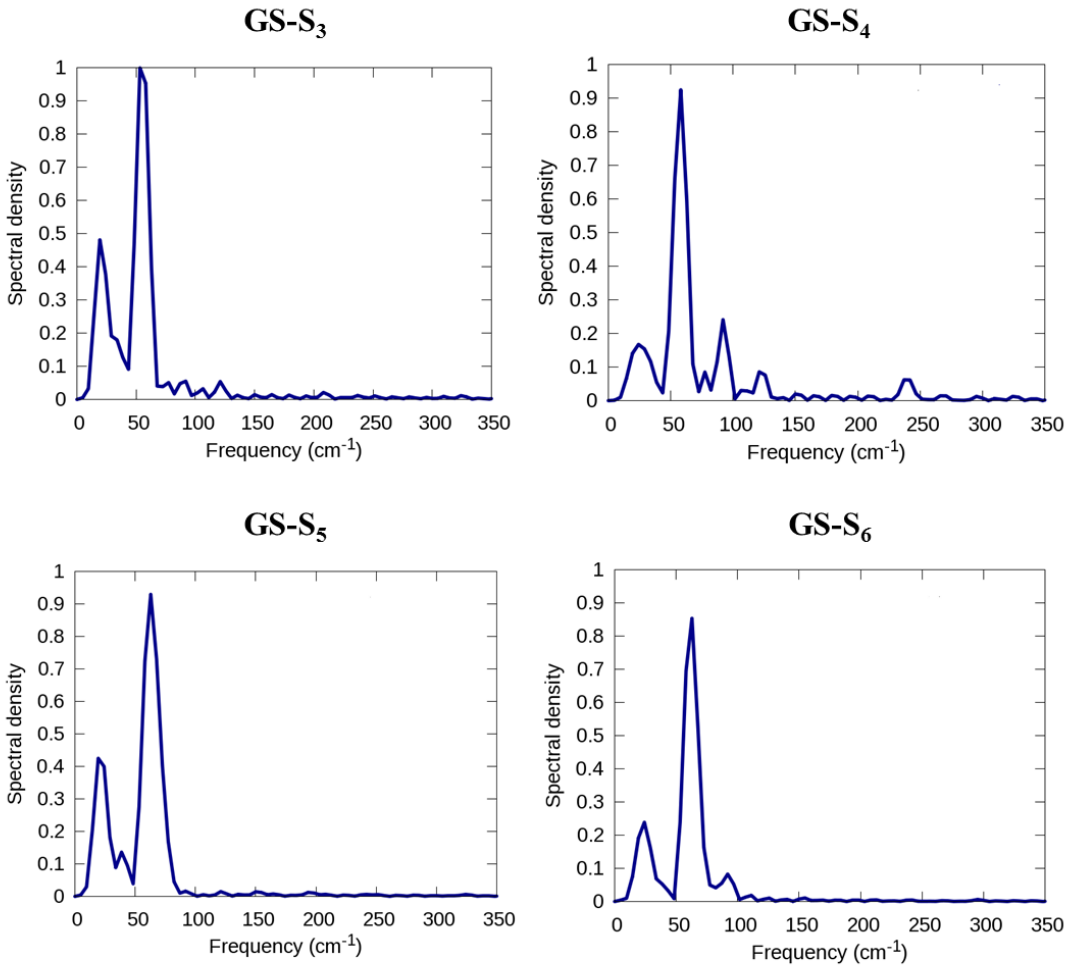

Figure A.3 Fourier transform of autocorrelation functions of the fluctuations of the energy gaps (phonon spectral density spectra) between the GS-S_3, GS-S_4, GS-S_5, GS-S_6.

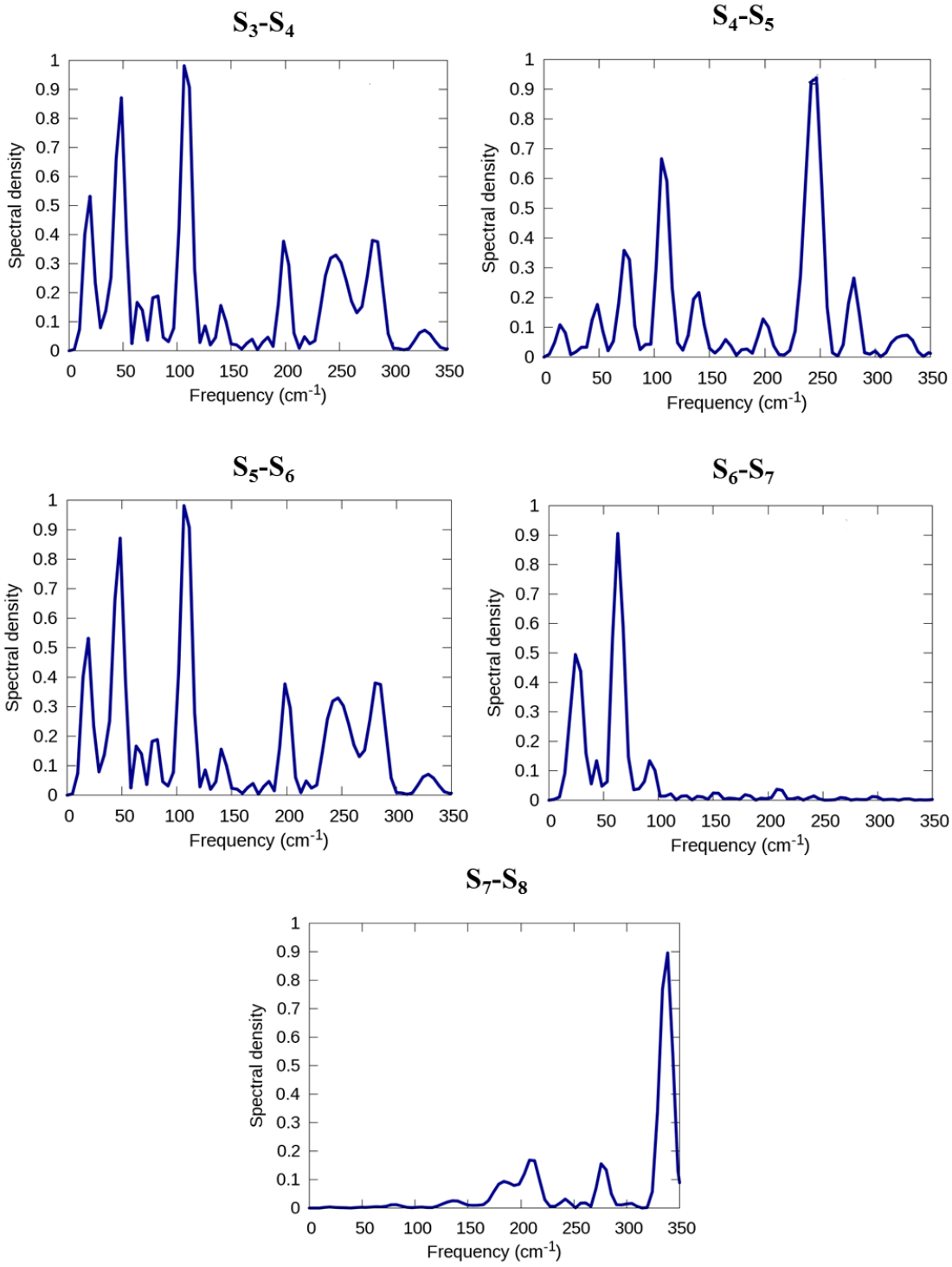

Figure A.4 Fourier transform of autocorrelation functions of the fluctuations of the energy gaps (phonon spectral density spectra) between the S_3-S_4, S_4-S_5, S_5-S_6, S_6-S_7, S_7-S_8.

Appendix B - Supporting Information for "The Electronic Relaxation Dynamics in $[Au_{25}(SR)_{18}]^{-1}$ (R = CH_3, C_2H_5, C_3H_7, MPA) [MPA = mercaptopropionic acid ligand] Thiolate-protected Nanocluster Series: Ligand Effects and Separate Electron and Hole Relaxation Dynamics in the $[Au_{25}(SCH_3)_{18}]^{-1}$ Nanocluster"

Table B.1 The TDDFT excitations, energy, oscillator strength, weights and most weighted transitions involved in the 1.35 eV peak of the $[Au_{25}(SR)_{18}]^{-1}$ (R = CH_3, C_2H_5, C_3H_7, MPA) clusters.

Excitation transitions for R= CH_3	Energy (eV)	Oscillator strength	Weight	Most weighted transitions
4	1.34	0.0217	0.5339	HOMO → LUMO+1
			0.1832	HOMO-1 → LUMO
			0.1519	HOMO-2 → LUMO
			0.0943	HOMO → LUMO
			0.0122	HOMO-1 → LUMO+1
5	1.35	0.0230	0.6838	HOMO-1 → LUMO
			0.2163	HOMO → LUMO+1
			0.0418	HOMO-1 → LUMO+1
			0.027	HOMO → LUMO
6	1.37	0.0228	0.8776	HOMO-2 → LUMO+1
			0.0544	HOMO → LUMO
			0.0251	HOMO-2 → LUMO
			0.0101	HOMO → LUMO+1

Excitation transitions for R= C_2H_5	Energy (eV)	Oscillator strength	Weight	Most weighted transitions
4	1.36	0.0235	0.5041	HOMO → LUMO+1
			0.2451	HOMO-2 → LUMO
			0.1611	HOMO → LUMO
			0.0345	HOMO-1 → LUMO+1
			0.0249	HOMO-1 → LUMO
5	1.37	0.0245	0.4358	HOMO-1 → LUMO
			0.2659	HOMO-2 → LUMO
			0.2327	HOMO → LUMO+1
			0.0234	HOMO-1 → LUMO+1
			0.0144	HOMO → LUMO
6	1.39	0.0252	0.6122	HOMO-2 → LUMO+1
			0.2615	HOMO-1 → LUMO+1
			0.0586	HOMO → LUMO
			0.0329	HOMO-2 → LUMO

Excitation transitions for R= C_3H_7	Energy (eV)	Oscillator strength	Weight	Most weighted transitions
4	1.35	0.0244	0.4485	HOMO → LUMO+1
			0.2191	HOMO → LUMO

			0.2174	HOMO-2 → LUMO
5	1.36	0.0261	0.3531	HOMO-1 → LUMO
			0.3345	HOMO-2 → LUMO
			0.2366	HOMO → LUMO+1
6	1.38	0.0269	0.6256	HOMO-2 → LUMO+1
			0.2556	HOMO-1 → LUMO+1

Excitation transitions for R= MPA	**Energy (eV)**	**Oscillator strength**	**Weight**	**Most weighted transitions**
1	1.13	0.0131	0.8587	HOMO → LUMO
			0.0699	HOMO → LUMO+1
			0.0222	HOMO-2 → LUMO
			0.0172	HOMO-1 → LUMO
			0.0137	HOMO-1 → LUMO+1
4	1.27	0.0220	0.9412	HOMO-1 → LUMO+1
			0.0162	HOMO-1 → LUMO
			0.0116	HOMO → LUMO
			0.0071	HOMO-2 → LUMO
			0.0044	HOMO-2 → LUMO+2
5	1.31	0.0177	0.9194	HOMO-2 → LUMO
			0.032	HOMO-2 → LUMO+1
			0.0143	HOMO → LUMO

			0.0097	HOMO-1 → LUMO+1
6	1.38	0.0176	0.9279	HOMO-2 → LUMO+1
			0.0301	HOMO-2 → LUMO

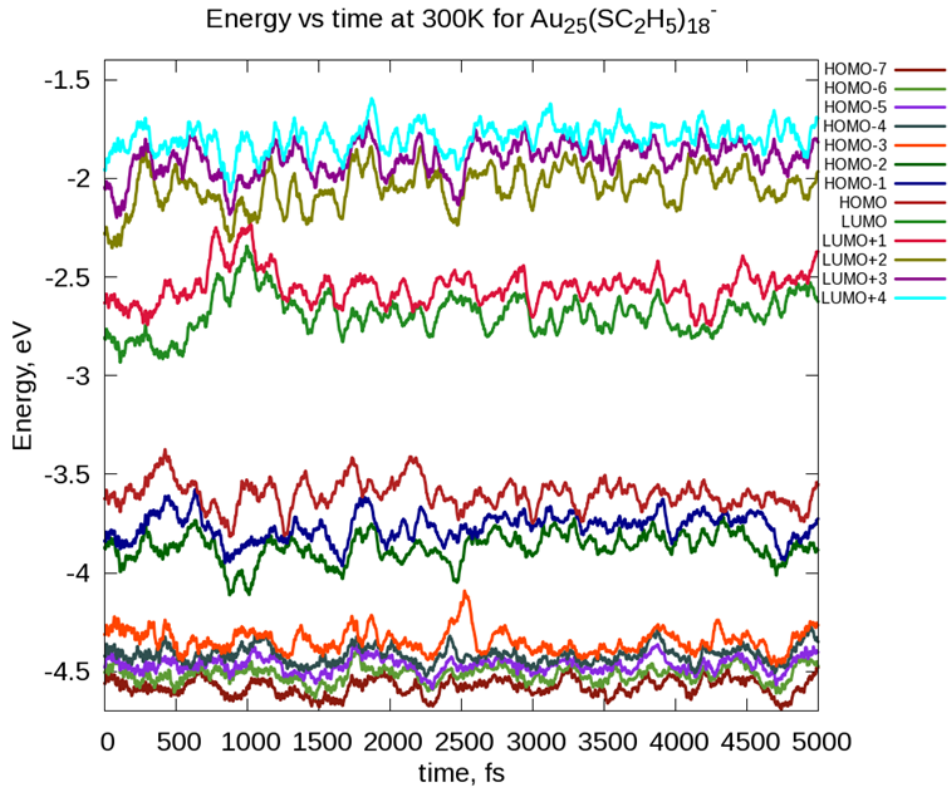

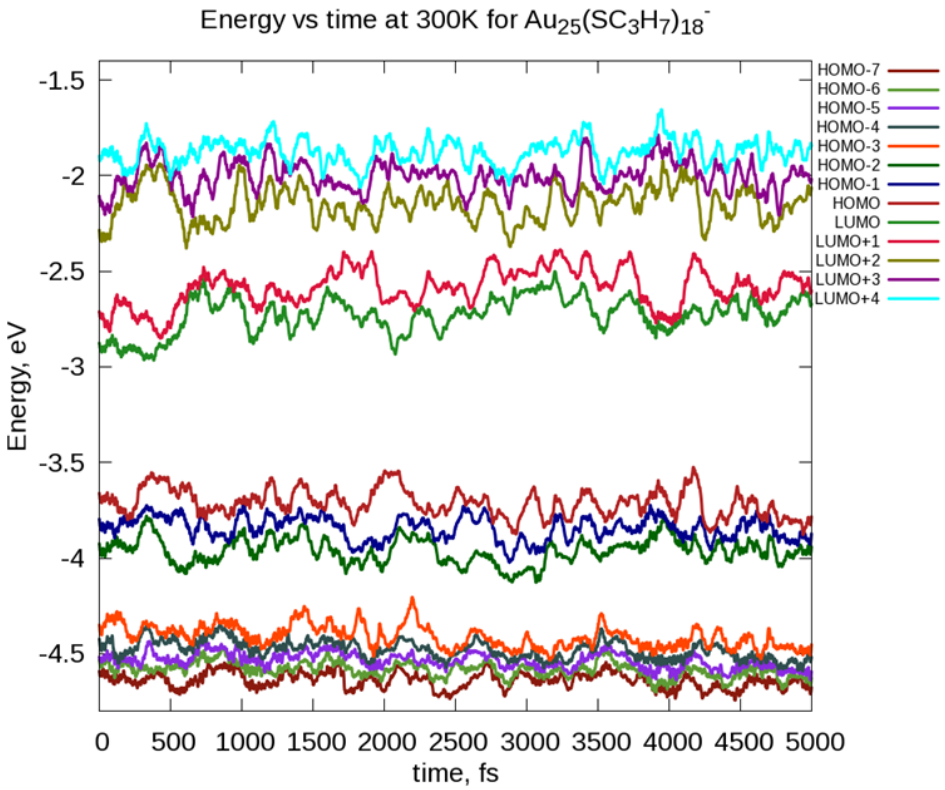

Figure B.1 Orbital energy variation with time during the MD simulation for $[Au_{25}(SR)_{18}]^{-1}$ (R= C_2H_5, C_3H_7).

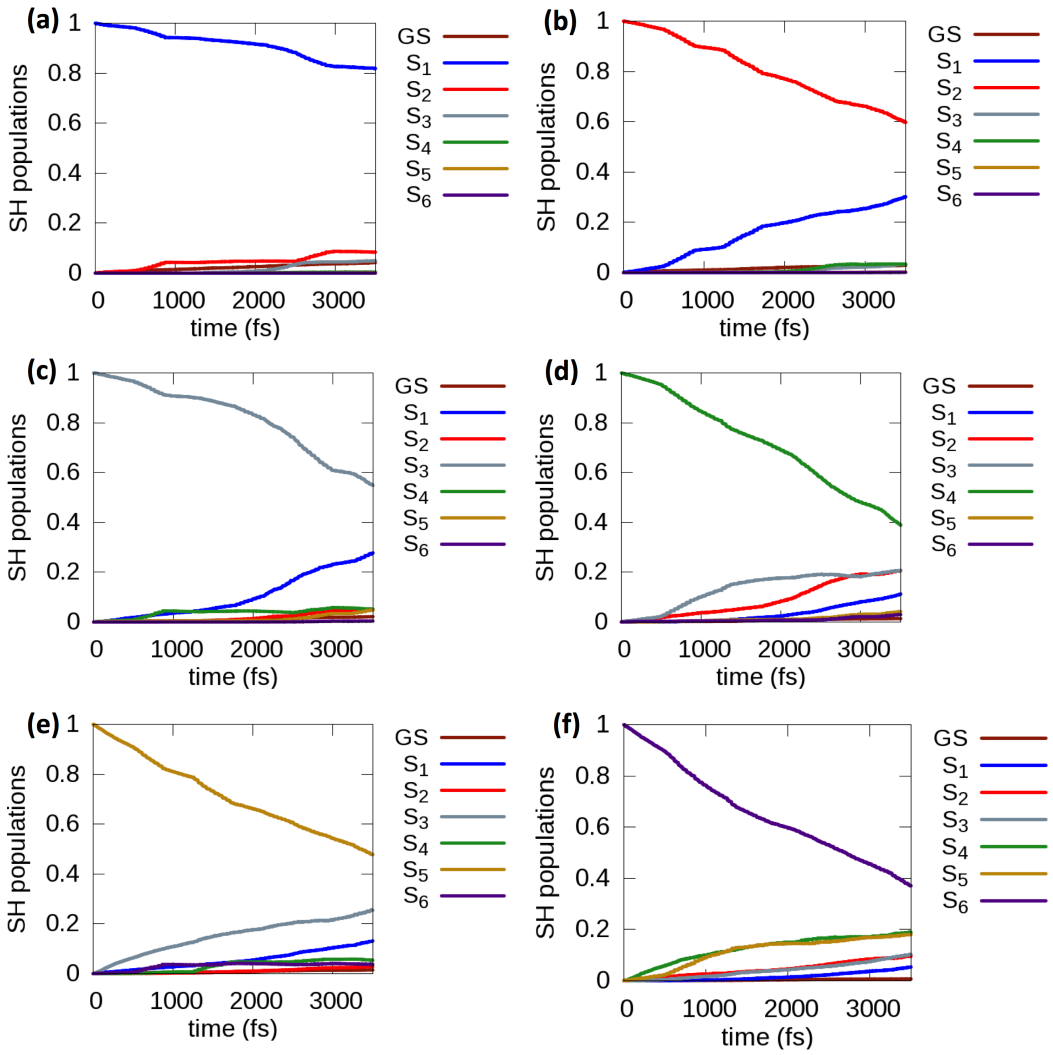

Figure B.2 Evolution of the populations of S_1, S_2, S_3, S_4, S_5, S_6 states. Panels a−f are relaxations from S_1 to S_6, respectively, with the energy correction for the $[Au_{25}(SCH_3)_{18}]^{-1}$.

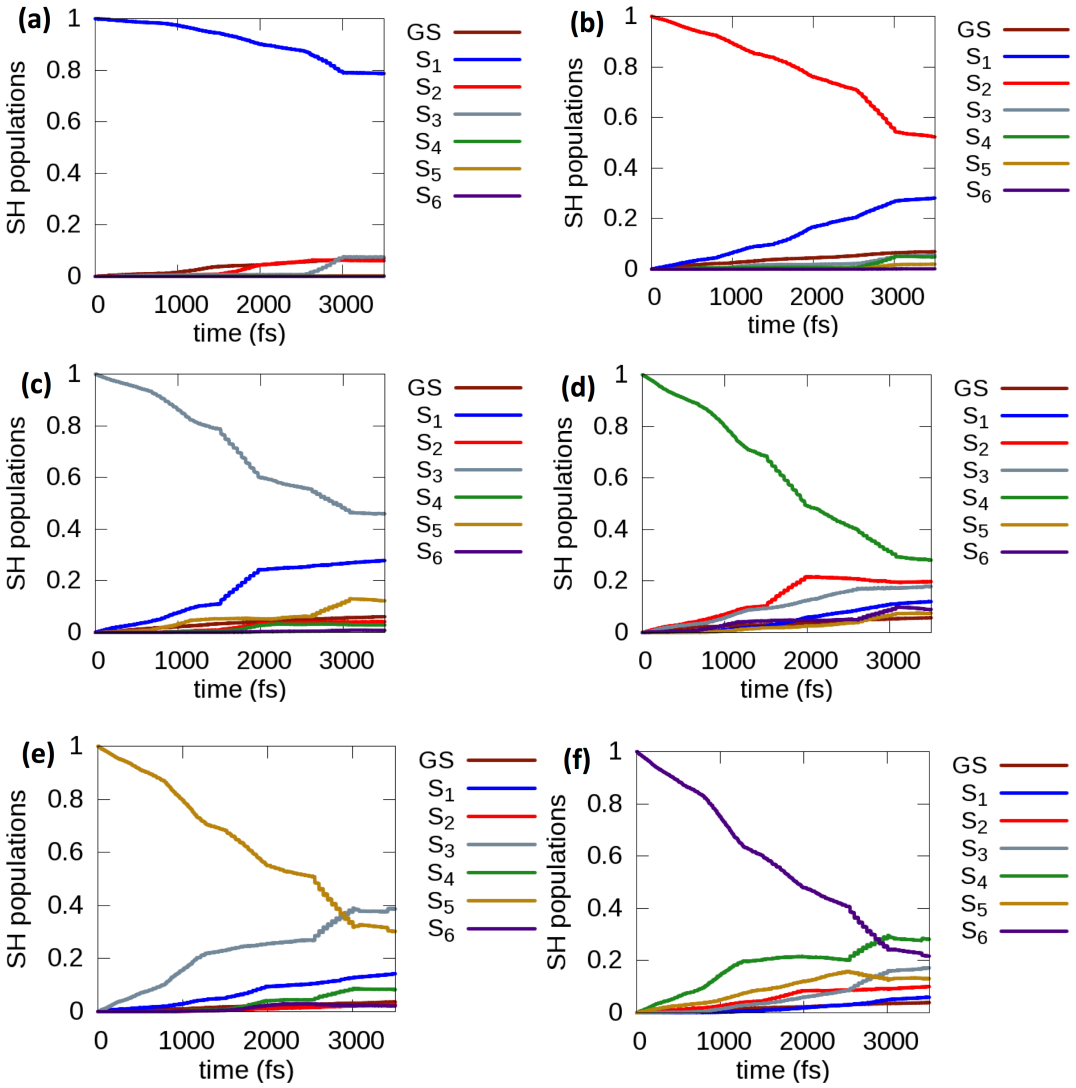

Figure B.3 Evolution of the populations of S_1, S_2, S_3, S_4, S_5, S_6 states. Panels a−f are relaxations from S_1 to S_6, respectively, without the energy correction for the $[Au_{25}(SC_2H_5)_{18}]^{-1}$.

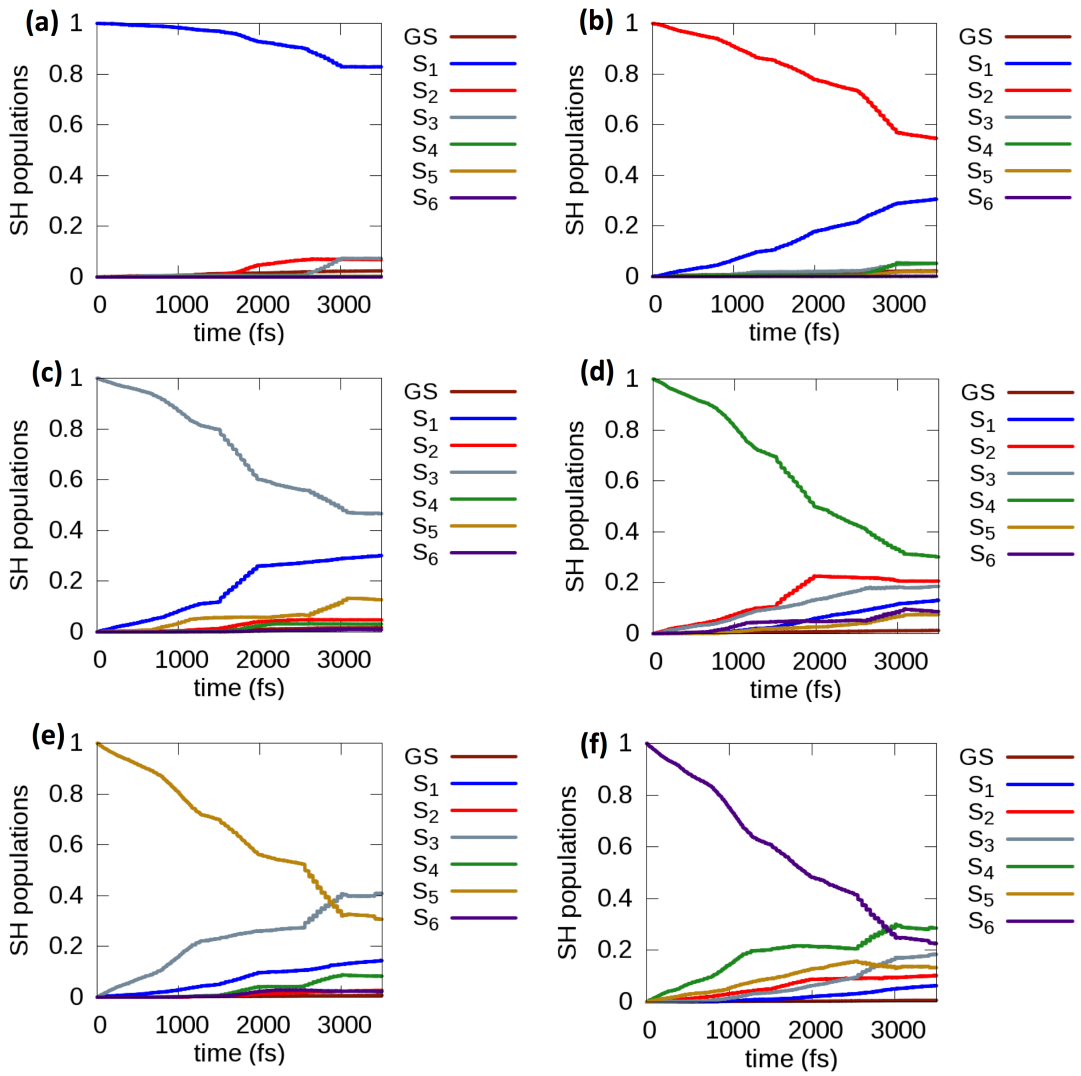

Figure B.4 Evolution of the populations of S_1, S_2, S_3, S_4, S_5, S_6 states. Panels a−f are relaxations from S_1 to S_6, respectively, with the energy correction for the $[Au_{25}(SC_2H_5)_{18}]^{-1}$.

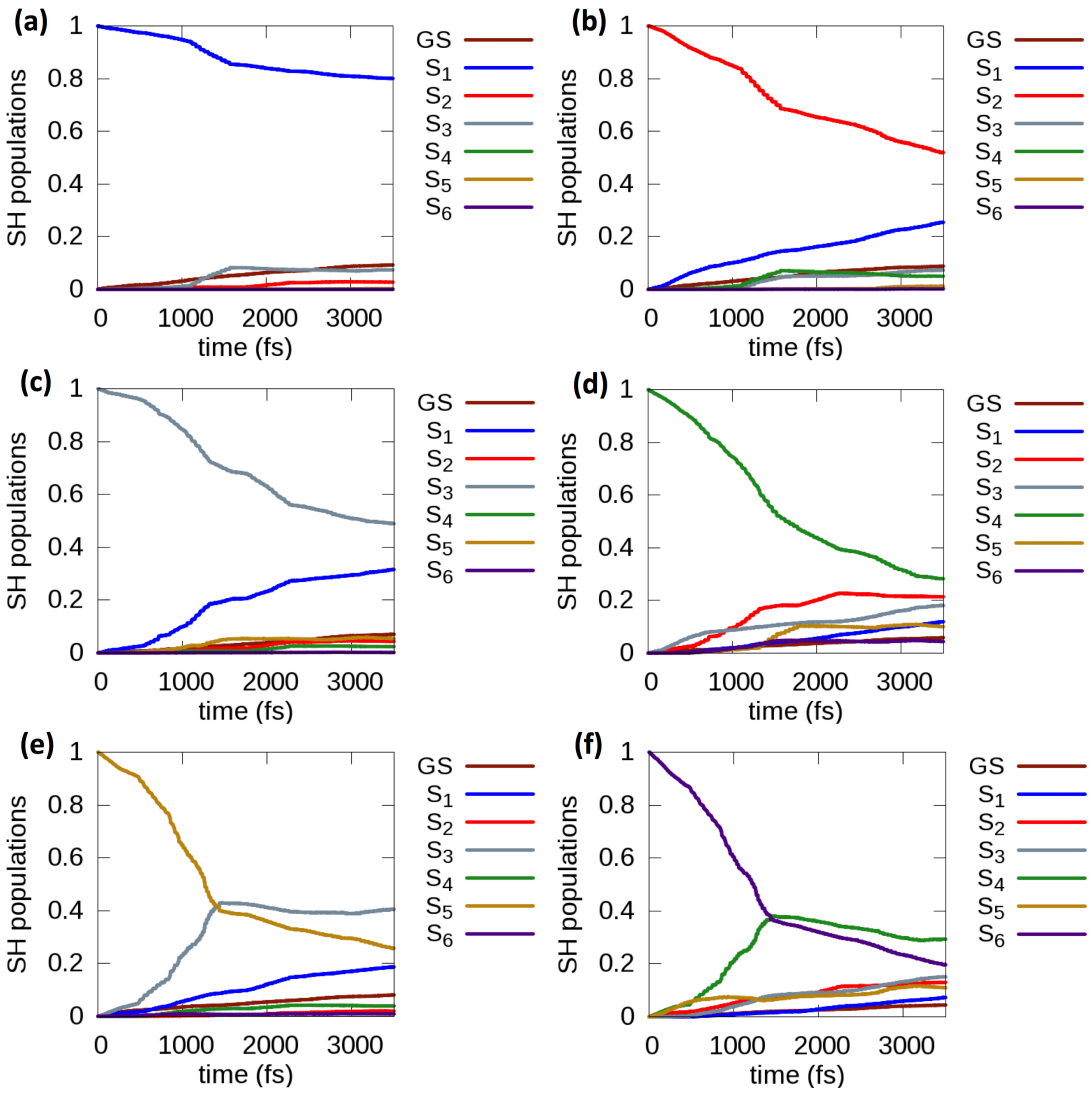

Figure B.5 Evolution of the populations of S_1, S_2, S_3, S_4, S_5, S_6 states. Panels a−f are relaxations from S_1 to S_6, respectively, without the energy correction for the $[Au_{25}(SC_3H_7)_{18}]^{-1}$.

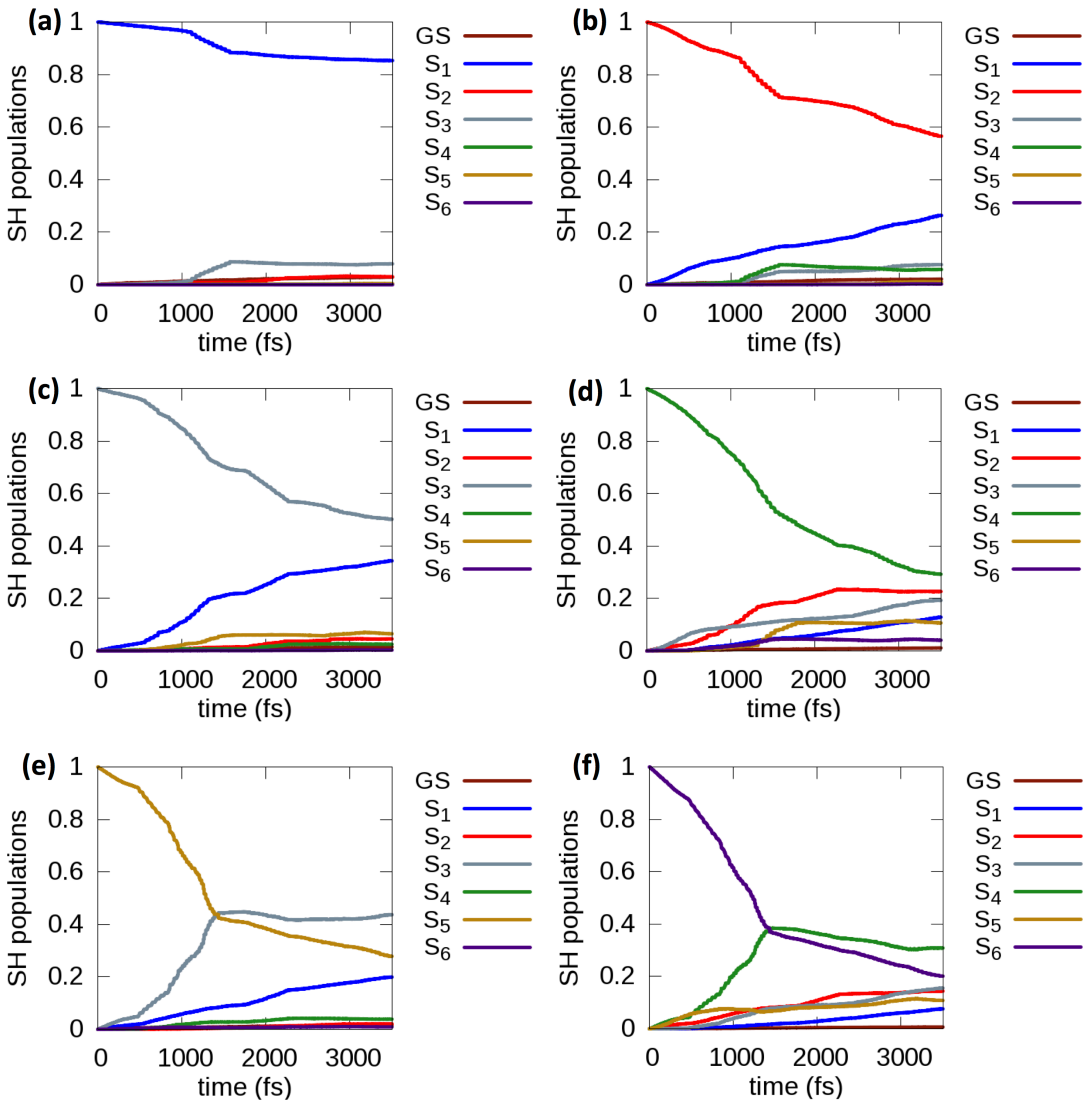

Figure B.6 Evolution of the populations of S_1, S_2, S_3, S_4, S_5, S_6 states. Panels a−f are relaxations from S_1 to S_6, respectively, with the energy correction for the $[Au_{25}(SC_3H_7)_{18}]^{-1}$.

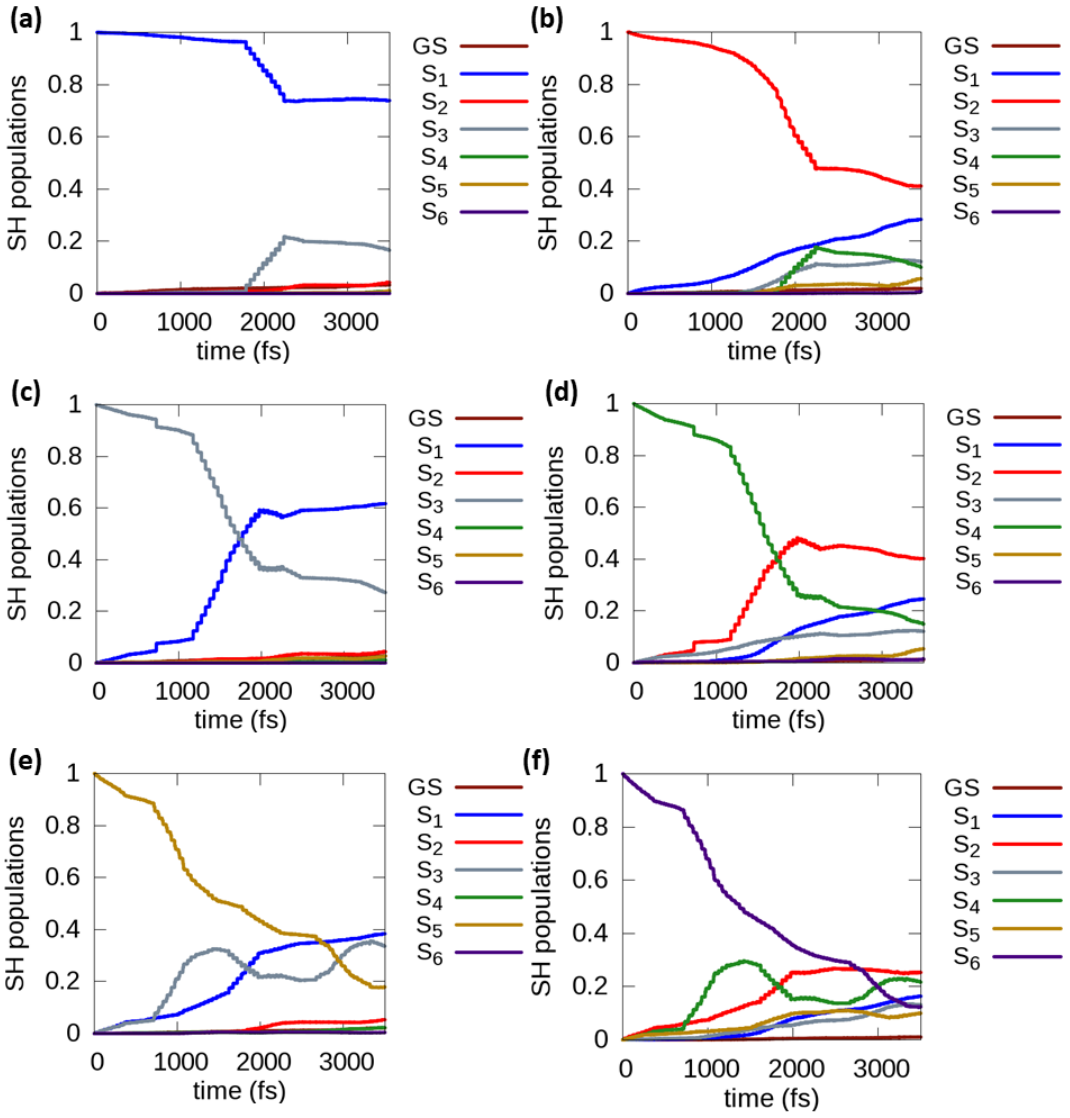

Figure B.7 Evolution of the populations of S_1, S_2, S_3, S_4, S_5, S_6 states. Panels a−f are relaxations from S_1 to S_6, respectively, with the energy correction for the $[Au_{25}(MPA)_{18}]^{-1}$.

Table B.2 GS growth times calculated for ligated clusters with the 0.55 eV energy correction.

Excited state	GS growth times(ps) with correction				
	H	CH_3	C_2H_5	C_3H_7	MPA
S_1	313	77	129	102	99
S_2	365	105	136	139	175
S_3	441	168	184	207	128
S_4	690	258	257	277	298
S_5	750	215	476	184	188

S_6	1429	477	566	473	395

Table B.3 Decay times calculated for ligated clusters with the 0.55 eV energy correction.

Excited state	Decay times (ps) with correction				
	H	CH_3	C_2H_5	C_3H_7	MPA
S_1	18	18	22	18	12
S_2	3.3	7.4	7.0	5.9	4.5
S_3	3.1	7.8	4.6	4.6	2.9
S_4	1.9	4.7	3.2	2.7	2.2
S_5	2.6	4.9	3.5	2.3	2.4
S_6	1.9	3.8	2.7	1.9	2.1

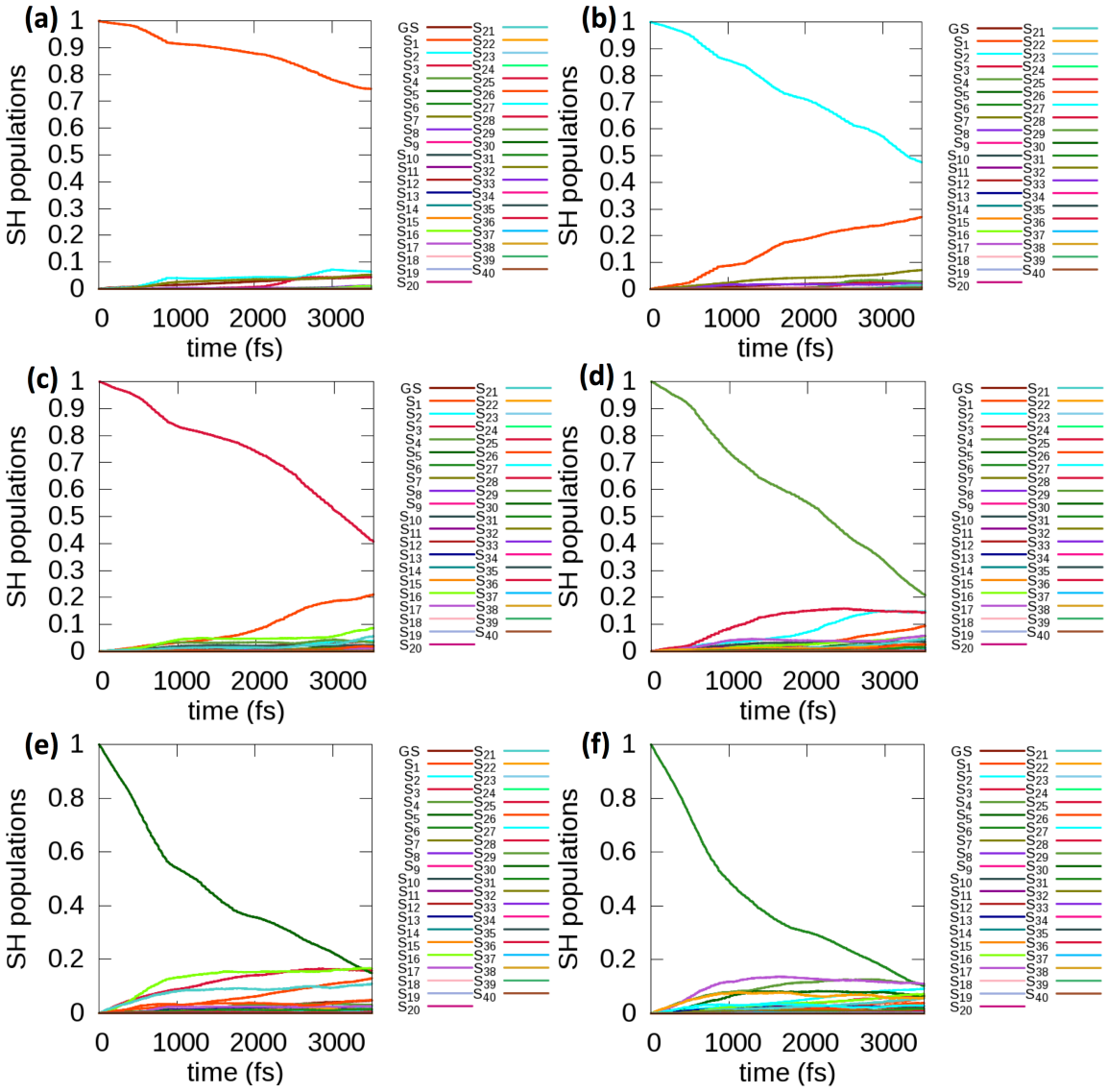

Figure B.8 Evolution of the populations of states initially excited into S_1, S_2, S_3, S_4, S_5, S_6 (a-f, respectively) for $[Au_{25}(SCH_3)_{18}]^{-1}$ with the 0.55 eV energy correction in the presence of higher excited states.

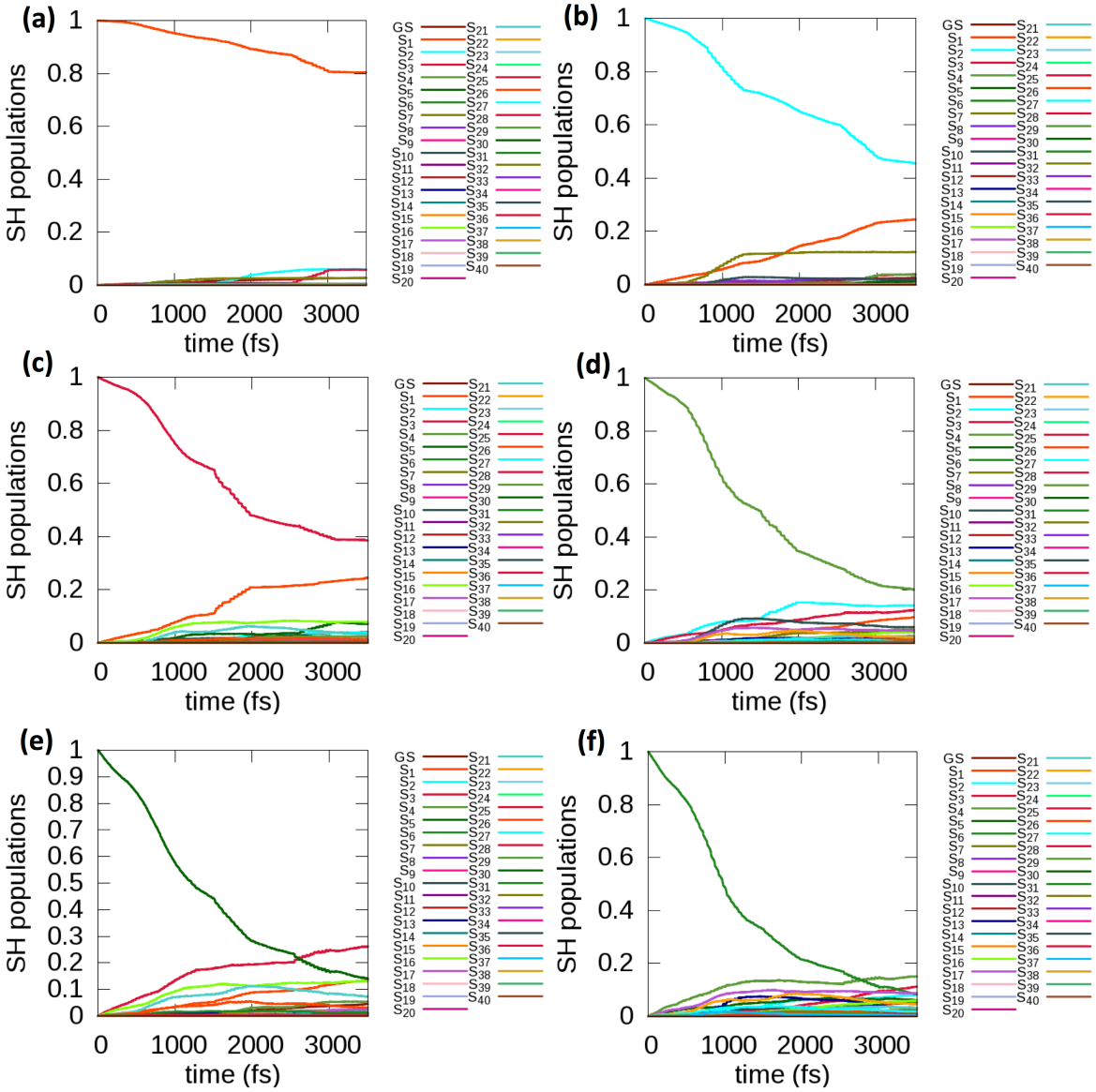

Figure B.9 Evolution of the populations of states initially excited into S_1, S_2, S_3, S_4, S_5, S_6 (a-f, respectively) for $[Au_{25}(SC_2H_5)_{18}]^{-1}$ with the 0.55 eV energy correction in the presence of higher excited states.

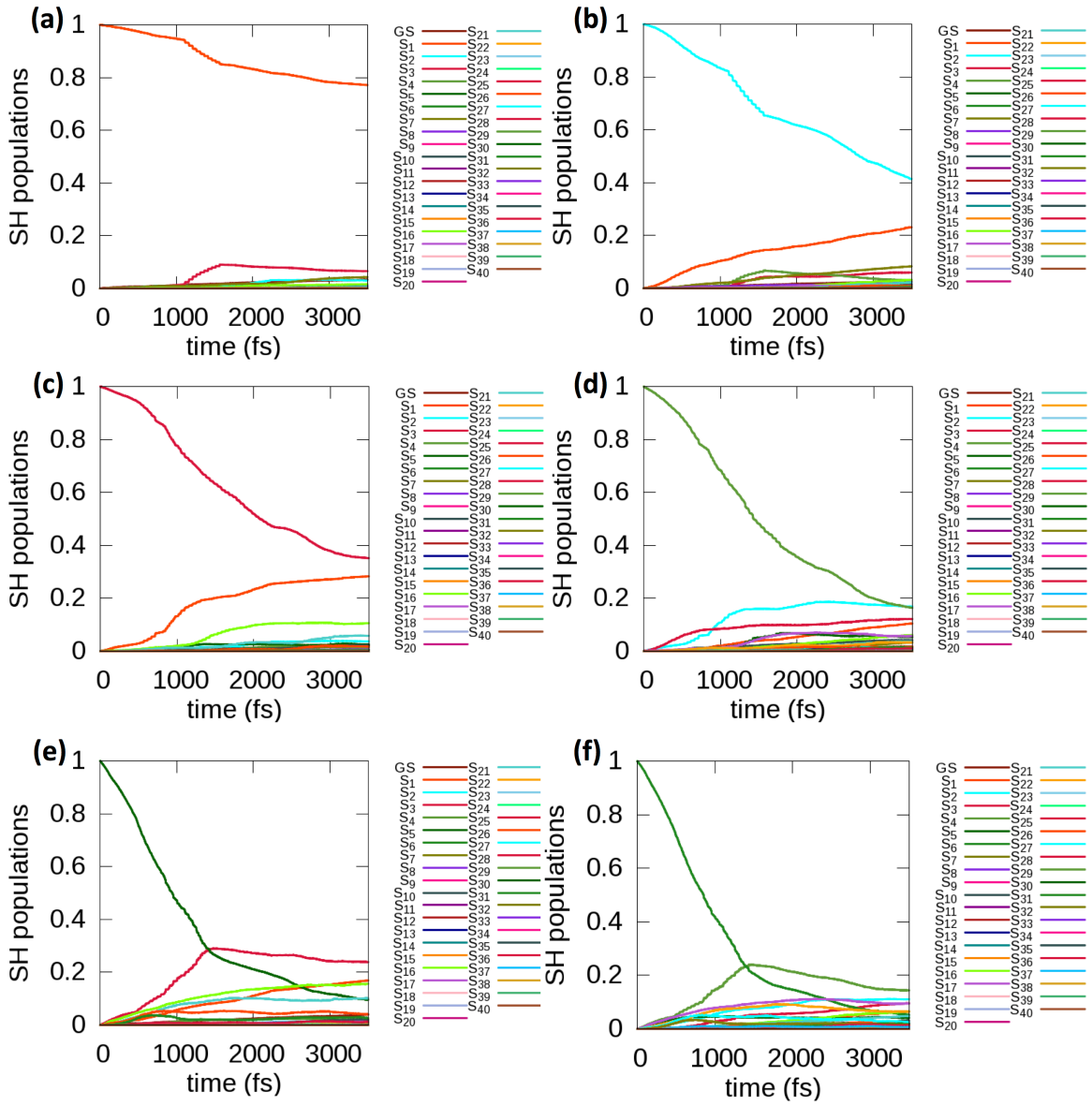

Figure B.10 Evolution of the populations of states initially excited into S_1, S_2, S_3, S_4, S_5, S_6 (a-f, respectively) for $[Au_{25}(SC_3H_7)_{18}]^{-1}$ with the 0.55 eV energy correction in the presence of higher excited states.

Table B.4 Decay time constants obtained for $[Au_{25}(SR)_{18}]^{-1}$ (R = CH_3, C_2H_5, C_3H_7, MPA) nanoclusters for S_1-S_{40} states.

Decay time (ps)				
Excited state	**methyl**	**ethyl**	**propyl**	**MPA**
S_1	13.5	16.6	12.1	10.7
S_2	5.6	4.6	4.2	2.8
S_3	5.8	3.2	3.3	2.0

S_4	3.1	2.1	2.1	1.5
S_5	1.9	1.8	1.3	1.0
S_6	1.6	1.4	1.1	0.9
S_7	8.0	13.1	10.8	8.6
S_8	1.6	2.0	2.0	1.9
S_9	1.4	1.6	1.4	1.1
S_{10}	3.7	3.7	3.8	2.3
S_{11}	1.4	1.3	1.4	1.3
S_{12}	1.5	1.2	1.1	0.9
S_{13}	3.7	3.3	2.3	1.5
S_{14}	1.5	1.5	1.2	0.8
S_{15}	1.5	1.1	1.0	0.7
S_{16}	3.5	2.4	3.9	4.1
S_{17}	2.3	2.2	2.7	2.3
S_{18}	2.2	2.1	2.6	2.2
S_{19}	1.0	1.0	1.3	0.9
S_{20}	1.1	0.9	1.0	0.7
S_{21}	1.8	1.3	1.6	1.4
S_{22}	1.3	1.3	1.3	1.2
S_{23}	1.4	1.2	1.5	0.9
S_{24}	0.7	0.6	0.8	0.6
S_{25}	0.8	0.6	0.6	0.5
S_{26}	1.0	1.0	1.0	1.1
S_{27}	0.8	0.9	0.9	0.9
S_{28}	0.9	1.0	0.9	0.9
S_{29}	0.6	0.6	0.6	0.6
S_{30}	0.7	0.6	0.5	0.5
S_{31}	0.9	1.0	0.8	0.9
S_{32}	0.8	1.1	0.8	0.9
S_{33}	0.8	1.0	0.8	0.7
S_{34}	0.6	0.6	0.6	0.5
S_{35}	0.7	0.6	0.5	0.4
S_{36}	1.2	1.0	1.0	0.7
S_{37}	1.1	0.9	0.9	0.7
S_{38}	1.2	0.9	0.9	0.6
S_{39}	0.8	0.6	0.7	0.4
S_{40}	0.9	0.6	0.6	0.4

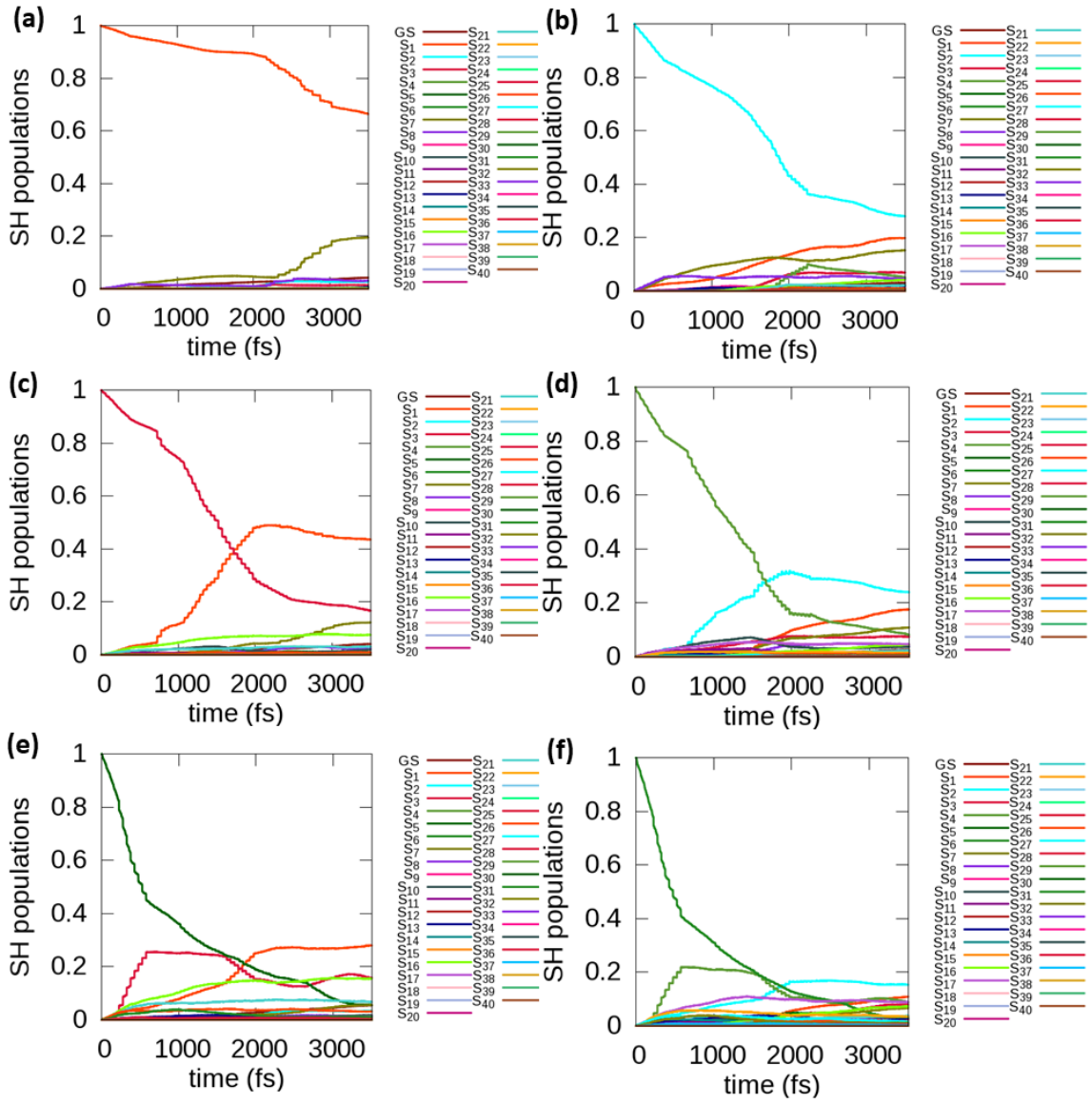

Figure B.11 Evolution of the populations of states initially excited into S_1, S_2, S_3, S_4, S_5, S_6 (a-f, respectively) for $[Au_{25}(MPA)_{18}]^{-1}$ with the 0.55 eV energy correction in the presence of higher excited states.

Table B.5 Excited states considered during separate electron and hole relaxations.

Excited state	Transition	Excited state	Transition
S_1	HOMO → LUMO	S_{21}	HOMO-4 → LUMO
S_2	HOMO → LUMO+1	S_{22}	HOMO-4 → LUMO+1
S_3	HOMO → LUMO+2	S_{23}	HOMO-4 → LUMO+2
S_4	HOMO → LUMO+3	S_{24}	HOMO-4 → LUMO+3
S_5	HOMO → LUMO+4	S_{25}	HOMO-4 → LUMO+4
S_6	HOMO → 1-LUMO	S_{26}	HOMO-5 → LUMO
S_7	HOMO-1 → LUMO+1	S_{27}	HOMO-5 → LUMO+1
S_8	HOMO-1 → LUMO+2	S_{28}	HOMO-5 → LUMO+2
S_9	HOMO-1 → LUMO+3	S_{29}	HOMO-5 → LUMO+3
S_{10}	HOMO-1 → LUMO+4	S_{30}	HOMO-5 → LUMO+4
S_{11}	HOMO-2 → LUMO	S_{31}	HOMO-6 → LUMO
S_{12}	HOMO-2 → LUMO+1	S_{32}	HOMO-6 → LUMO+1
S_{13}	HOMO-2 → LUMO+2	S_{33}	HOMO-6 → LUMO+2
S_{14}	HOMO-2 → LUMO+3	S_{34}	HOMO-6 → LUMO+3
S_{15}	HOMO-2 → LUMO+4	S_{35}	HOMO-6 → LUMO+4
S_{16}	HOMO-3 → LUMO	S_{36}	HOMO-7 → LUMO
S_{17}	HOMO-3 → LUMO+1	S_{37}	HOMO-7 → LUMO+1
S_{18}	HOMO-3 → LUMO+2	S_{38}	HOMO-7 → LUMO+2
S_{19}	HOMO-3 → LUMO+3	S_{39}	HOMO-7 → LUMO+3
S_{20}	HOMO-3 → LUMO+4	S_{40}	HOMO-7 → LUMO+4

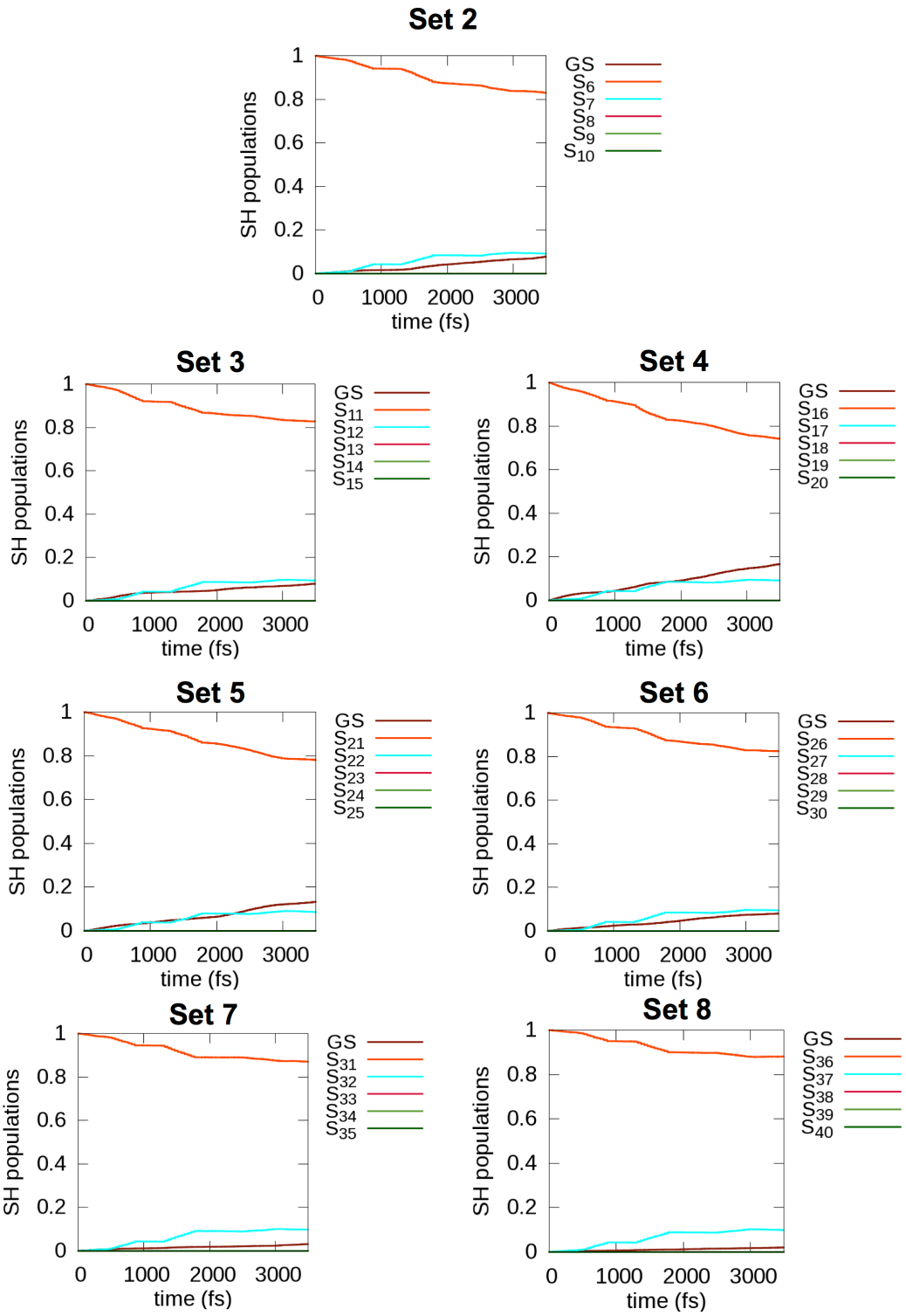

Figure B.12 Evolution of the populations of S_6, S_{11}, S_{16}, S_{21}, S_{26}, S_{31}, S_{36} states from the set 2 to set 8 electron relaxations respectively in $[Au_{25}(SCH_3)_{18}]^{-1}$.

Table B.6 Calculated decay time constants for the eight electron relaxation sets.

Excited state	Transition	Decay time (ps) -Trial 1	Decay time (ps) -Trial 2
set 1 (hole created in HOMO)			
S_1	HOMO → LUMO	13.4	13.4
S_2	HOMO → LUMO+1	6.9	7.1
S_3	HOMO → LUMO+2	6.9	6.7
S_4	HOMO → LUMO+3	1.7	1.7
S_5	HOMO → LUMO+4	1.8	1.8
set 2 (hole created in HOMO-1)			
S_6	HOMO-1 → LUMO	16.9	17.0
S_7	HOMO-1 → LUMO+1	8.6	8.6
S_8	HOMO-1 → LUMO+2	6.9	6.7
S_9	HOMO-1 → LUMO+3	1.7	1.7
S_{10}	HOMO-1 → LUMO+4	1.8	1.8
set 3 (hole created in HOMO-2)			
S_{11}	HOMO-2 → LUMO	15.6	16.2
S_{12}	HOMO-2 → LUMO+1	8.7	8.7
S_{13}	HOMO-2 → LUMO+2	6.9	6.9
S_{14}	HOMO-2 → LUMO+3	1.7	1.7
S_{15}	HOMO-2 → LUMO+4	1.8	1.8
set 4 (hole created in HOMO-3)			
S_{16}	HOMO-3 → LUMO	10.9	11.4
S_{17}	HOMO-3 → LUMO+1	7.9	7.7
S_{18}	HOMO-3 → LUMO+2	6.7	6.8
S_{19}	HOMO-3 → LUMO+3	1.7	1.7
S_{20}	HOMO-3 → LUMO+4	1.7	1.7
set 5 (hole created in HOMO-4)			
S_{21}	HOMO-4 → LUMO	13.1	12.5
S_{22}	HOMO-4 → LUMO+1	8.7	8.5
S_{23}	HOMO-4 → LUMO+2	6.6	6.5
S_{24}	HOMO-4 → LUMO+3	1.7	1.7
S_{25}	HOMO-4 → LUMO+4	1.8	1.7
set 6 (hole created in HOMO-5)			
S_{26}	HOMO-5 → LUMO	15.9	15.8
S_{27}	HOMO-5 → LUMO+1	9.2	9.5
S_{28}	HOMO-5 → LUMO+2	6.4	6.6
S_{29}	HOMO-5 → LUMO+3	1.7	1.7
S_{30}	HOMO-5 → LUMO+4	1.7	1.7
set 7 (hole created in HOMO-6)			
S_{31}	HOMO-6 → LUMO	21.0	20.7

S_{32}	HOMO-6 → LUMO+1	9.5	9.6
S_{33}	HOMO-6 → LUMO+2	6.5	6.5
S_{34}	HOMO-6 → LUMO+3	1.6	1.6
S_{35}	HOMO-6 → LUMO+4	1.7	1.7
set 8 (hole created in HOMO-7)			
S_{36}	HOMO-7 → LUMO	22.6	23.2
S_{37}	HOMO-7 → LUMO+1	9.8	10.0
S_{38}	HOMO-7 → LUMO+2	6.1	6.2
S_{39}	HOMO-7 → LUMO+3	1.6	1.6
S_{40}	HOMO-7 → LUMO+4	1.7	1.7

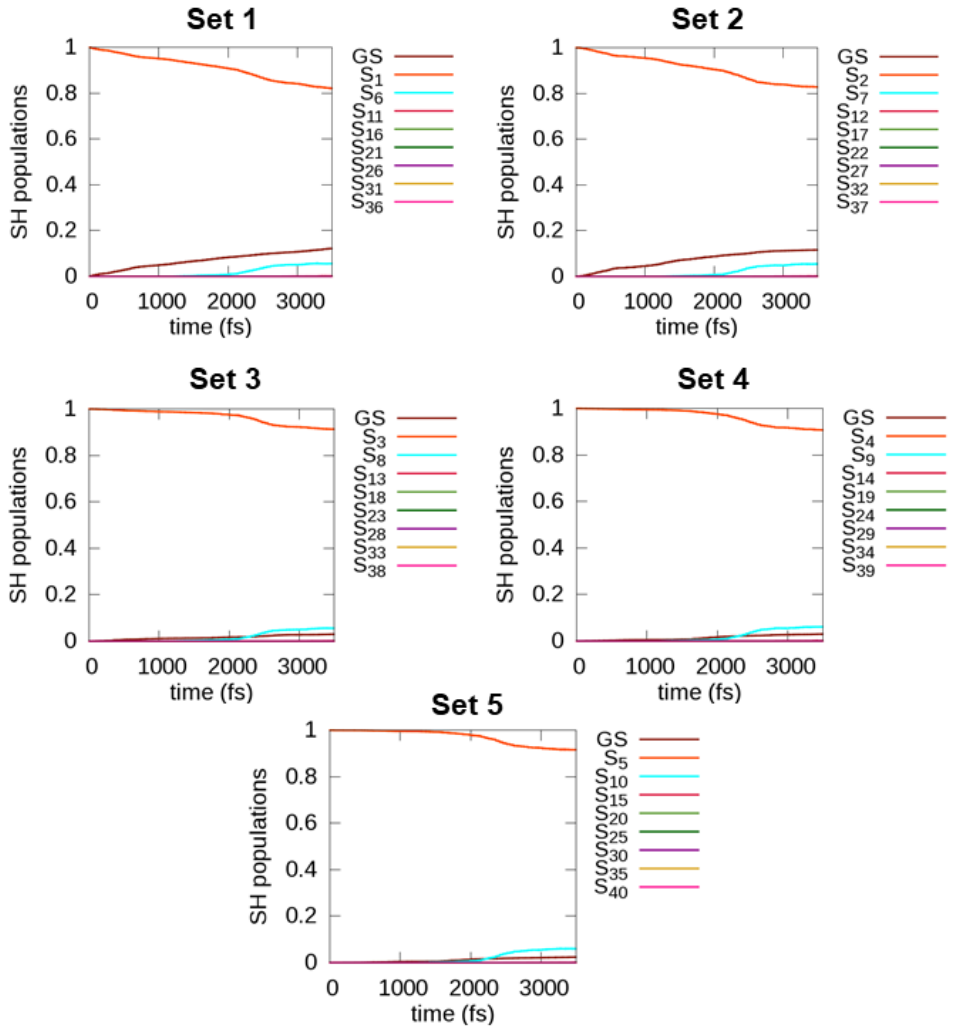

Figure B.13 Evolution of the populations of S_1, S_2, S_3, S_4, S_5 states from the set 1 to set 5 hole relaxations respectively in $[Au_{25}(SCH_3)_{18}]^{-1}$.

Table B.7 Calculated decay time constants for the five hole relaxation sets.

Excited state	Transition	Decay time (ps)-Trial 1	Decay time (ps) -Trial 2
set 1 (electron excited into LUMO)			
S_1	HOMO → LUMO	18.2	19.8
S_6	HOMO-1 → LUMO	8.9	8.7
S_{11}	HOMO-2 → LUMO	5.7	5.6
S_{16}	HOMO-3 → LUMO	2.7	2.7
S_{21}	HOMO-4 → LUMO	1.6	1.6
S_{26}	HOMO-5 → LUMO	1.0	1.0
S_{31}	HOMO-6 → LUMO	1.0	1.0
S_{36}	HOMO-7 → LUMO	1.3	1.3
set 2 (electron excited into LUMO+1)			
S_2	HOMO → LUMO+1	18.0	17.3
S_7	HOMO-1 → LUMO+1	9.5	9.4
S_{12}	HOMO-2 → LUMO+1	6.3	6.1
S_{17}	HOMO-3 → LUMO+1	3.0	2.9
S_{22}	HOMO-4 → LUMO+1	1.7	1.7
S_{27}	HOMO-5 → LUMO+1	1.0	1.0
S_{32}	HOMO-6 → LUMO+1	1.0	1.0
S_{37}	HOMO-7 → LUMO+1	1.3	1.3
set 3 (electron excited into LUMO+2)			
S_3	HOMO → LUMO+2	45.5	44.5
S_8	HOMO-1 → LUMO+2	10.8	10.5
S_{13}	HOMO-2 → LUMO+2	6.5	6.4
S_{18}	HOMO-3 → LUMO+2	3.1	3.0
S_{23}	HOMO-4 → LUMO+2	1.8	1.7
S_{28}	HOMO-5 → LUMO+2	1.0	1.0
S_{33}	HOMO-6 → LUMO+2	1.0	1.0
S_{38}	HOMO-7 → LUMO+2	1.3	1.3
set 4 (electron excited into LUMO+3)			
S_4	HOMO → LUMO+3	44.1	42.2
S_8	HOMO-1 → LUMO+3	10.3	10.8
S_{14}	HOMO-2 → LUMO+3	6.7	6.6
S_{18}	HOMO-3 → LUMO+3	3.0	3.0
S_{24}	HOMO-4 → LUMO+3	1.7	1.7
S_{28}	HOMO-5 → LUMO+3	1.0	1.0
S_{34}	HOMO-6 → LUMO+3	1.0	0.9
S_{38}	HOMO-7 → LUMO+3	1.2	1.3
set 5 (electron excited into LUMO+4)			
S_5	HOMO → LUMO+4	48.8	47.7

S_{10}	HOMO-1 → LUMO+4	10.9	10.7
S_{15}	HOMO-2 → LUMO+4	6.4	6.5
S_{20}	HOMO-3 → LUMO+4	2.9	2.9
S_{25}	HOMO-4 → LUMO+4	1.6	1.7
S_{30}	HOMO-5 → LUMO+4	1.0	1.0
S_{35}	HOMO-6 → LUMO+4	1.0	1.0
S_{40}	HOMO-7 → LUMO+4	1.2	1.2

Appendix C - Supporting Information for "Theoretical Investigation of Relaxation Dynamics in the $Au_{18}(SH)_{14}$ Thiolate-protected Gold Nanocluster"

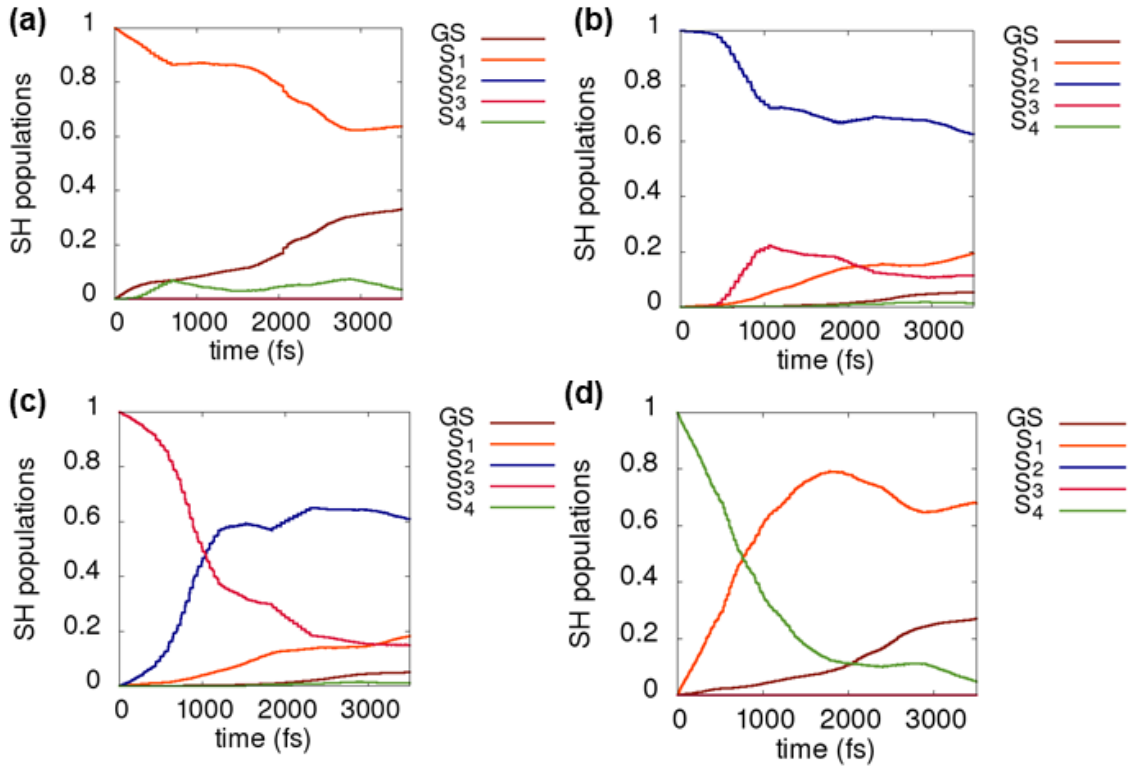

Figure C.1. Evolution of the populations of S_1, S_2, S_3, S_4 states. Panels a−d are relaxations from S_1 to S_4, respectively, without the energy correction. The decay with the correction (0.30 eV) is not shown here, because these calculations exhibit similar relaxation trends although with slightly increased GS growth times.

Table C.1. Ground state population increase lifetimes and excited state population decay times after excitation of the S_1, S_2, S_3, and S_4 states. Lifetimes are presented both without and with a 0.3 eV correction to the excited state energies.

Excited state	Without energy correction	With 0.3 eV energy correction
GS growth times (ps)		
S_1	9	27
S_2	80	80
S_3	90	73
S_4	13	48
Decay times (ps)		
S_1	7.2	15.6
S_2	6.0	5.9
S_3	1.6	1.5
S_4	1.0	1.1

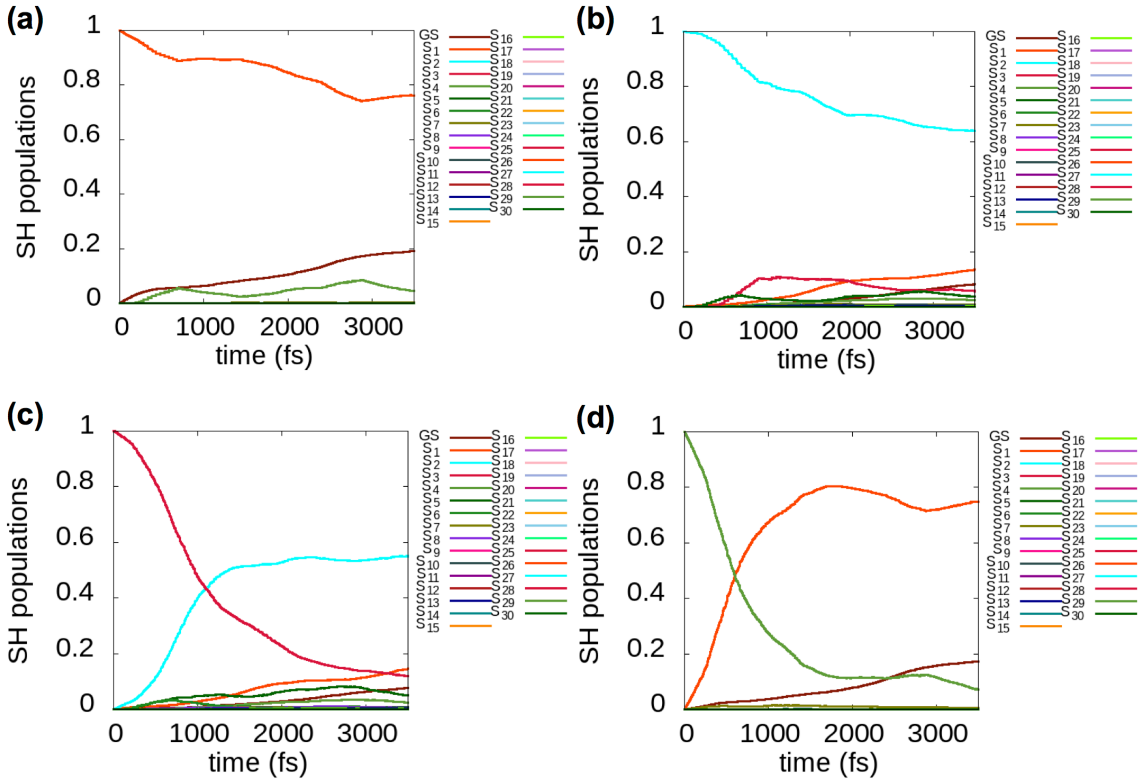

Figure C.2. Evolution of the populations of S_1, S_2, S_3, S_4 states in the presence of the higher excited states. Panels a−d are relaxations from S_1 to S_4, respectively, without the energy correction.

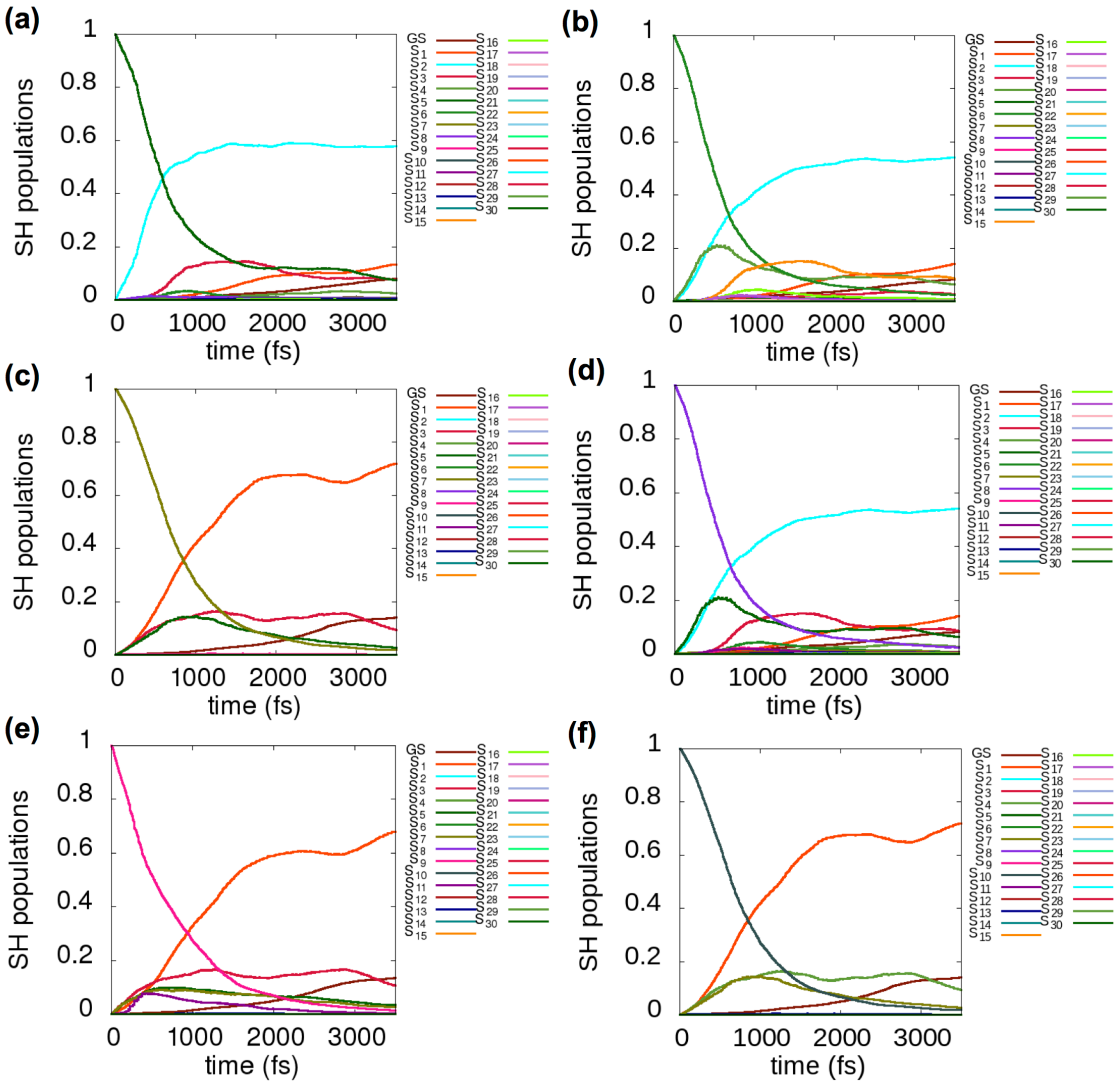

Figure C.3. Evolution of the populations of S_5, S_6, S_7, S_8, S_9, S_{10} states in the presence of the higher excited states. Panels a−f are relaxations from S_5 to S_{10}, respectively, without the energy correction.

Appendix D - Supporting Information for "Theoretical Investigation of Relaxation Dynamics in $Au_{38}(SH)_{24}$ Thiolate-protected Gold Nanocluster"

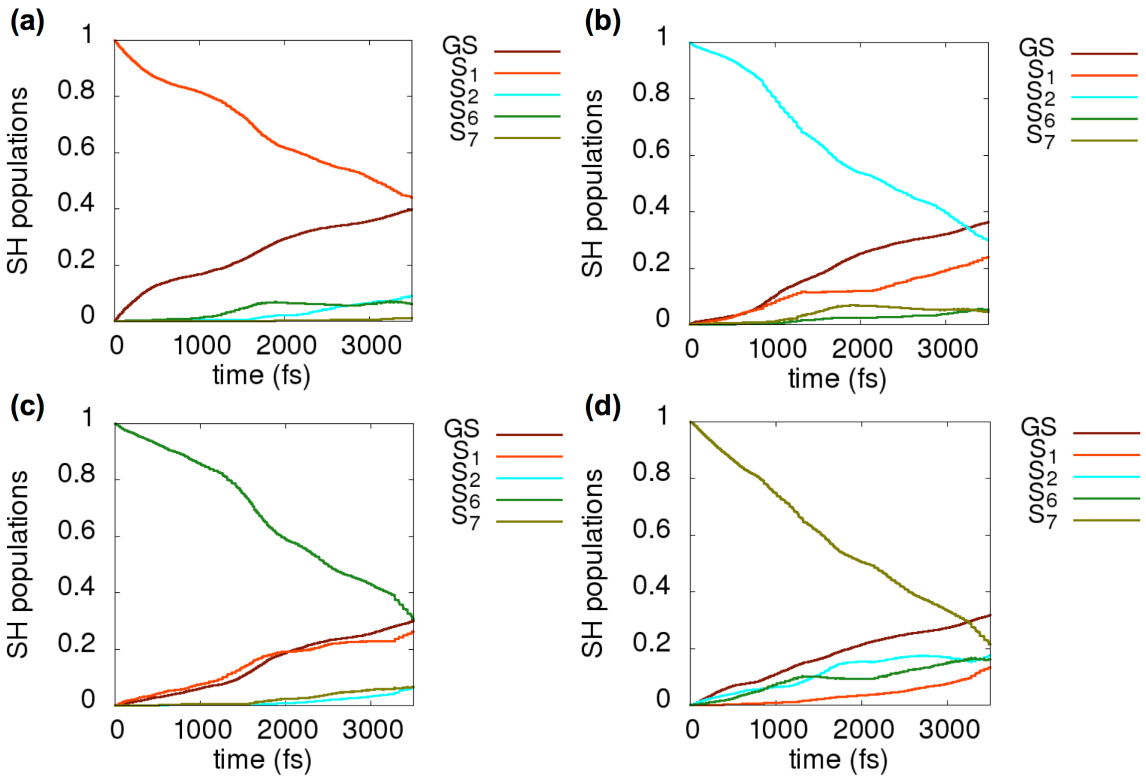

Figure D.1. Evolution of excited state populations starting in a) S_1, b) S_2, c) S_6, and d) S_7 excited state, without the energy correction. The decay with the correction is not shown here, because these calculations exhibit similar relaxation trends although with slightly increased GS growth times.

Table D.1. Ground state population increase lifetimes and excited state population decay times after excitation of the S_1, S_2, S_6, and S_7 states. Lifetimes are presented both without and with a 0.15 eV correction to the excited state energies.

Excited state	Without energy correction	With 0.15 eV energy correction
GS growth times (ps)		
S_1	6.2	7.2
S_2	7.6	9.1
S_6	10.4	12.1
S_7	8.9	11.4
Decay times (ps)		
S_1	4.4	4.9
S_2	3.4	3.8
S_6	3.9	4.1
S_7	2.9	3.1

Table D.2. Ground state population increase lifetimes and excited state population decay times of the S_1-S_{25} excited states. No energy correction was employed.

Excited state	GS growth time (ps)	Decay time (ps)
S_1	6.4	4.7
S_2	8.8	3.7
S_3	17	3.2
S_4	31	3.5
S_5	46	4.1
S_6	10	4.0
S_7	9.2	2.9
S_8	18	2.5
S_9	33	2.6
S_{10}	64	3.2
S_{11}	30	8.2
S_{12}	46	4.3
S_{13}	80	2.9
S_{14}	93	3.3
S_{15}	152	3.3
S_{16}	29	3.1

S_{17}	47	2.5
S_{18}	83	2.0
S_{19}	108	2.0
S_{20}	200	2.2
S_{21}	19	3.0
S_{22}	43	2.6
S_{23}	65	2.0
S_{24}	107	2.1
S_{25}	207	2.4

Table D.3. Decay constants calculated for the combined state populations. The notation S_a+S_b+S_c+S_d_fromS_a denotes that the S_a, S_b, S_c, S_d state populations are combined when the S_a state is excited.

Combined state group	Decay time (ps)	Combined state group	Decay time (ps)
S_1+S_2+S_6+S_7_fromS_1	6.4	S_{11}+S_{12}_fromS_{11}	9.7
S_1+S_2+S_6+S_7_fromS_2	7.7	S_{11}+S_{12}_fromS_{12}	7.2
S_1+S_2+S_6+S_7_fromS_6	10.1	S_{16}+S_{17}+S_{21}+S_{22}_fromS_{16}	3.9
S_1+S_2+S_6+S_7_fromS_7	7.8	S_{16}+S_{17}+S_{21}+S_{22}_fromS_{17}	3.8
S_1+S_2_fromS_1	5.1	S_{16}+S_{17}+S_{21}+S_{22}_fromS_{21}	5.9
S_1+S_2_fromS_2	6.0	S_{16}+S_{17}+S_{21}+S_{22}_fromS_{22}	6.3
S_6+S_7_fromS_6	4.3	S_{16}+S_{17}_fromS_{16}	3.3
S_6+S_7_fromS_7	3.9	S_{16}+S_{17}_fromS_{17}	3.2
S_4+S_5+S_9+S_{10}_fromS_4	4.1	S_{21}+S_{22}_fromS_{21}	3.2
S_4+S_5+S_9+S_{10}_fromS_5	9.6	S_{21}+S_{22}_fromS_{22}	3.4
S_4+S_5+S_9+S_{10}_fromS_9	4.2	S_{18}+S_{23}_fromS_{18}	2.1
S_4+S_5+S_9+S_{10}_fromS_{10}	10.7	S_{18}+S_{23}_fromS_{23}	2.7
S_4+S_5_fromS_4	3.6	S_{19}+S_{20}+S_{24}+S_{25}_fromS_{19}	2.2
S_4+S_5_fromS_5	6.4	S_{19}+S_{20}+S_{24}+S_{25}_fromS_{20}	3.3
S_9+S_{10}_fromS_9	2.7	S_{19}+S_{20}+S_{24}+S_{25}_fromS_{24}	2.9
S_9+S_{10}_fromS_{10}	4.4	S_{19}+S_{20}+S_{24}+S_{25}_fromS_{25}	5.0
S_3+S_8_fromS_3	3.6	S_{19}+S_{20}_fromS_{19}	2.0
S_3+S_8_fromS_8	3.6	S_{19}+S_{20}_fromS_{20}	2.7
S_{14}+S_{15}_fromS_{14}	3.4	S_{24}+S_{25}_fromS_{24}	2.1
S_{14}+S_{15}_fromS_{15}	4.6	S_{24}+S_{25}_fromS_{25}	3.1

Table D.4. Transitions involved in the TDDFT excited states from 1.50-2.01 eV

Excitation transitions	Energy (eV)	Oscillator strength	Weight	Most weighted transitions
E_1 symmetry				
10	1.81	0.0013	0.9317	HOMO-8/HOMO-9 → LUMO/LUMO+1
			0.0128	HOMO-10 → LUMO/LUMO+1
11	1.87	0.0021	0.6797	HOMO/HOMO-1 → LUMO+5/LUMO+6
			0.2671	HOMO-3/HOMO-4 → LUMO+3/LUMO+4
12	1.90	0.0026	0.827	HOMO-10 → LUMO/LUMO+1
			0.0861	HOMO-3/HOMO-4 → LUMO+3/LUMO+4
			0.0559	HOMO/HOMO-1 → LUMO+5/LUMO+6
14	1.96	0.0019	0.6507	HOMO-12/HOMO-13 → LUMO/LUMO+1
			0.2291	HOMO-3/HOMO-4 → LUMO+3/LUMO+4
			0.0375	HOMO-10 → LUMO/LUMO+1
			0.0291	HOMO/HOMO-1 → LUMO+5/LUMO+6
15	1.97	0.0281	0.2945	HOMO-12/HOMO-13 → LUMO/LUMO+1
			0.2938	HOMO-3/HOMO-4 → LUMO+3/LUMO+4
			0.0966	HOMO-10 → LUMO/LUMO+1
			0.1415	HOMO/HOMO-1 → LUMO+5/LUMO+6
A_1 symmetry				
4	1.70	0.0114	0.3679	HOMO-2 → LUMO+2
			0.452	HOMO-6/HOMO-7 → LUMO/LUMO+1
			0.1109	HOMO-8/HOMO-9 → LUMO/LUMO+1
5	1.74	0.0549	0.27	HOMO-2 → LUMO+2
			0.5272	HOMO-6/HOMO-7 → LUMO/LUMO+1
			0.0989	HOMO-8/HOMO-9 → LUMO/LUMO+1
6	1.85	0.0140	0.4888	HOMO-8/HOMO-9 → LUMO/LUMO+1
			0.4278	HOMO/HOMO-1 → LUMO+5/LUMO+6
			0.0195	HOMO-2 → LUMO+2
7	1.86	0.0165	0.5885	HOMO-3/HOMO-4 → LUMO+3/LUMO+4
			0.2584	HOMO/HOMO-1 → LUMO+5/LUMO+6
			0.0935	HOMO-8/HOMO-9 → LUMO/LUMO+1
8	1.90	0.0277	0.3569	HOMO-12/HOMO-13 → LUMO/LUMO+1
			0.3266	HOMO-3/HOMO-4 → LUMO+3/LUMO+4
			0.1827	HOMO/HOMO-1 → LUMO+5/LUMO+6
			0.0409	HOMO-2 → LUMO+2
9	2.01	0.1021	0.4535	HOMO-12/HOMO-13 → LUMO/LUMO+1
			0.2161	HOMO014/HOMO-15 → LUMO/LUMO+1
			0.0935	HOMO-2 → LUMO+2

Table D.5. Transitions considered for higher excited states up to 2.01 eV

Excited state	Transition	Excited state	Transition
S_{26}	HOMO → LUMO+5	S_{63}	HOMO-8 → LUMO+6
S_{27}	HOMO→ LUMO+6	S_{64}	HOMO-9 → LUMO
S_{28}	HOMO-1 → LUMO+5	S_{65}	HOMO-9 → LUMO+1
S_{29}	HOMO-1 → LUMO+6	S_{66}	HOMO-9 → LUMO+2
S_{30}	HOMO-2 → LUMO+5	S_{67}	HOMO-9 → LUMO+3
S_{31}	HOMO-2 → LUMO+6	S_{68}	HOMO-9 → LUMO+4
S_{32}	HOMO-3 → LUMO+5	S_{69}	HOMO-9 → LUMO+5
S_{33}	HOMO-3 →LUMO+6	S_{70}	HOMO-9 → LUMO+6
S_{34}	HOMO-4 → LUMO+5	S_{71}	HOMO-10 → LUMO
S_{35}	HOMO-4 → LUMO+6	S_{72}	HOMO-10 → LUMO+1
S_{36}	HOMO-5 → LUMO	S_{73}	HOMO-10 → LUMO+2
S_{37}	HOMO-5 → LUMO+1	S_{74}	HOMO-10 → LUMO+3
S_{38}	HOMO-5 → LUMO+2	S_{75}	HOMO-10 → LUMO+4
S_{39}	HOMO-5 → LUMO+3	S_{76}	HOMO-10 → LUMO+5
S_{40}	HOMO-5 → LUMO+4	S_{77}	HOMO-10 → LUMO+6
S_{41}	HOMO-5 → LUMO+5	S_{78}	HOMO-11 → LUMO
S_{42}	HOMO-5 → LUMO+6	S_{79}	HOMO-11 → LUMO+1
S_{43}	HOMO-6 → LUMO	S_{80}	HOMO-11 → LUMO+2
S_{44}	HOMO-6 → LUMO+1	S_{81}	HOMO-11 → LUMO+3
S_{45}	HOMO-6 → LUMO+2	S_{82}	HOMO-11 → LUMO+4
S_{46}	HOMO-6 → LUMO+3	S_{83}	HOMO-11 → LUMO+5
S_{47}	HOMO-6 → LUMO+4	S_{84}	HOMO-11 → LUMO+6
S_{48}	HOMO-6 → LUMO+5	S_{85}	HOMO-12 → LUMO
S_{49}	HOMO-6 → LUMO+6	S_{86}	HOMO-12 → LUMO+1
S_{50}	HOMO-7 → LUMO	S_{87}	HOMO-12 → LUMO+2
S_{51}	HOMO-7 → LUMO+1	S_{88}	HOMO-12 → LUMO+3
S_{52}	HOMO-7 → LUMO+2	S_{89}	HOMO-12 → LUMO+4
S_{53}	HOMO-7 → LUMO+3	S_{90}	HOMO-12 → LUMO+5
S_{54}	HOMO-7 → LUMO+4	S_{91}	HOMO-12 → LUMO+6
S_{55}	HOMO-7 → LUMO+5	S_{92}	HOMO-13 → LUMO
S_{56}	HOMO-7 → LUMO+6	S_{93}	HOMO-13 → LUMO+1
S_{57}	HOMO-8 → LUMO	S_{94}	HOMO-13 → LUMO+2
S_{58}	HOMO-8 → LUMO+1	S_{95}	HOMO-13 → LUMO+3
S_{59}	HOMO-8 → LUMO+2	S_{96}	HOMO-13 → LUMO+4
S_{60}	HOMO-8 → LUMO+3	S_{97}	HOMO-13 → LUMO+5
S_{61}	HOMO-8 → LUMO+4	S_{98}	HOMO-13 → LUMO+6
S_{62}	HOMO-8 → LUMO+5		

Table D.6. Decay times of the excited state population decrease for the S_1-S_{98} states. No energy correction is employed.

Excited state	Decay time (ps)	Excited state	Decay time (ps)	Excited state	Decay time (ps)	Excited state	Decay time (ps)
S_1	4.8	S_{26}	4.9	S_{51}	1.3	S_{76}	0.9
S_2	4.0	S_{27}	2.0	S_{52}	1.2	S_{77}	0.8
S_3	3.5	S_{28}	2.5	S_{53}	1.1	S_{78}	1.0
S_4	3.7	S_{29}	1.7	S_{54}	1.1	S_{79}	0.9
S_5	4.1	S_{30}	3.3	S_{55}	1.2	S_{80}	0.9
S_6	3.9	S_{31}	2.0	S_{56}	0.9	S_{81}	0.8
S_7	3.1	S_{32}	2.2	S_{57}	1.0	S_{82}	0.9
S_8	2.6	S_{33}	1.4	S_{58}	0.9	S_{83}	0.9
S_9	2.5	S_{34}	1.8	S_{59}	0.9	S_{84}	0.7
S_{10}	3.2	S_{35}	1.4	S_{60}	0.8	S_{85}	1.1
S_{11}	7.6	S_{36}	1.5	S_{61}	0.8	S_{86}	0.9
S_{12}	4.5	S_{37}	1.5	S_{62}	0.9	S_{87}	0.8
S_{13}	2.8	S_{38}	1.3	S_{63}	0.7	S_{88}	0.8
S_{14}	3.2	S_{39}	1.3	S_{64}	1.0	S_{89}	0.8
S_{15}	3.5	S_{40}	1.3	S_{65}	0.9	S_{90}	0.9
S_{16}	3.0	S_{41}	1.3	S_{66}	0.8	S_{91}	0.7
S_{17}	2.4	S_{42}	1.1	S_{67}	0.7	S_{92}	0.7
S_{18}	2.0	S_{43}	1.7	S_{68}	0.7	S_{93}	0.7
S_{19}	1.9	S_{44}	1.6	S_{69}	0.8	S_{94}	0.7
S_{20}	2.2	S_{45}	1.3	S_{70}	0.7	S_{95}	0.6
S_{21}	2.9	S_{46}	1.3	S_{71}	1.1	S_{96}	0.7
S_{22}	2.4	S_{47}	1.4	S_{72}	1.0	S_{97}	0.6
S_{23}	1.9	S_{48}	1.4	S_{73}	0.9	S_{98}	0.6
S_{24}	1.9	S_{49}	1.0	S_{74}	0.9		
S_{25}	2.2	S_{50}	1.5	S_{75}	0.9		

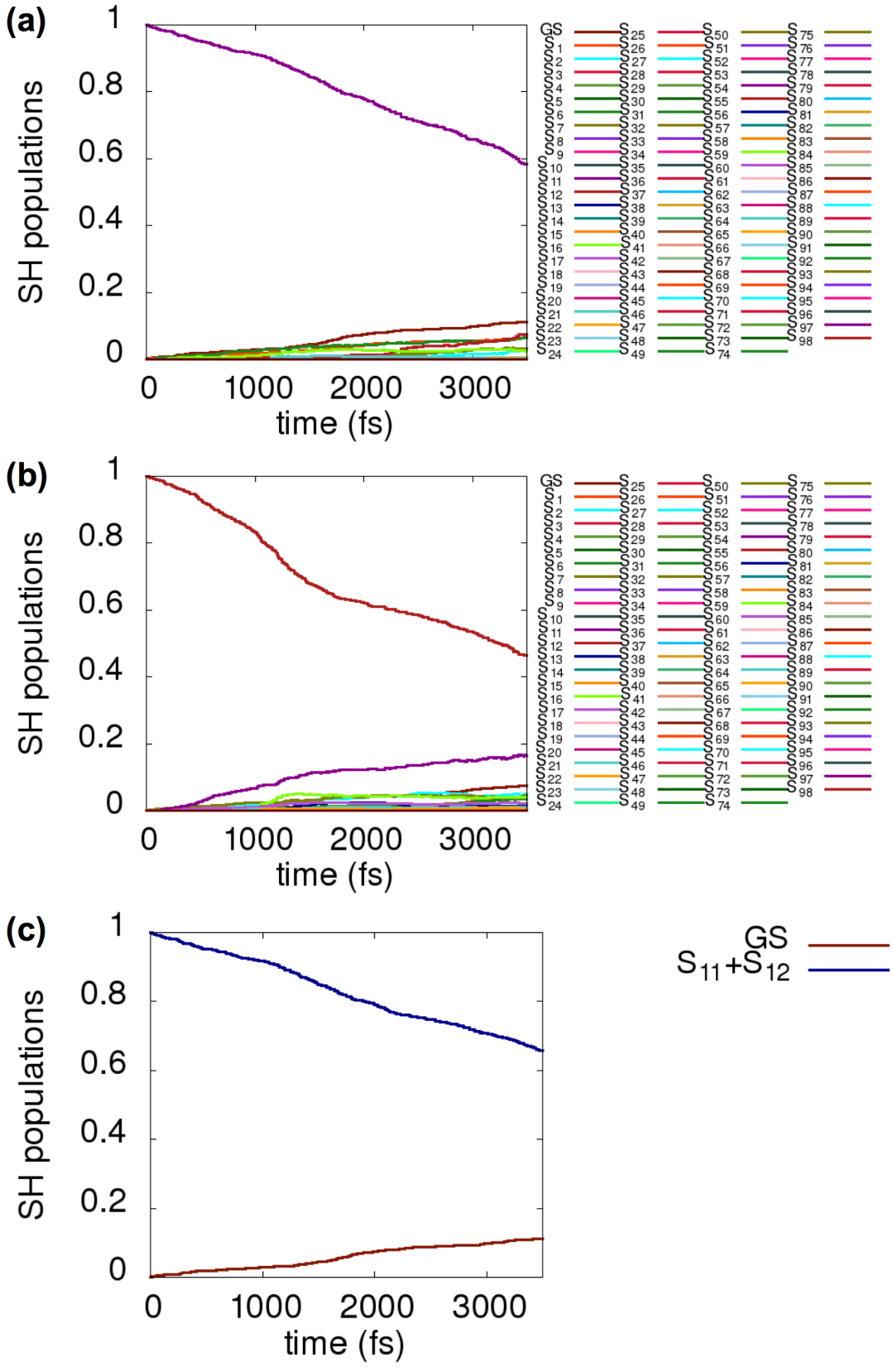
(a)
SH populations
time (fs)
(b)
SH populations
time (fs)
(c)
SH populations
time (fs)
GS
S11+S12

Figure D.2. (a) Evolution of excited state populations starting in S_{11}. (b) Evolution of excited state populations starting in S_{12}. (c) Evolution of the total population of the S_{11} and S_{12} states when S_{11} is excited in the presence of higher excited states up to S_{98}. Populations of other states up to S_{25} are not shown for clarity.

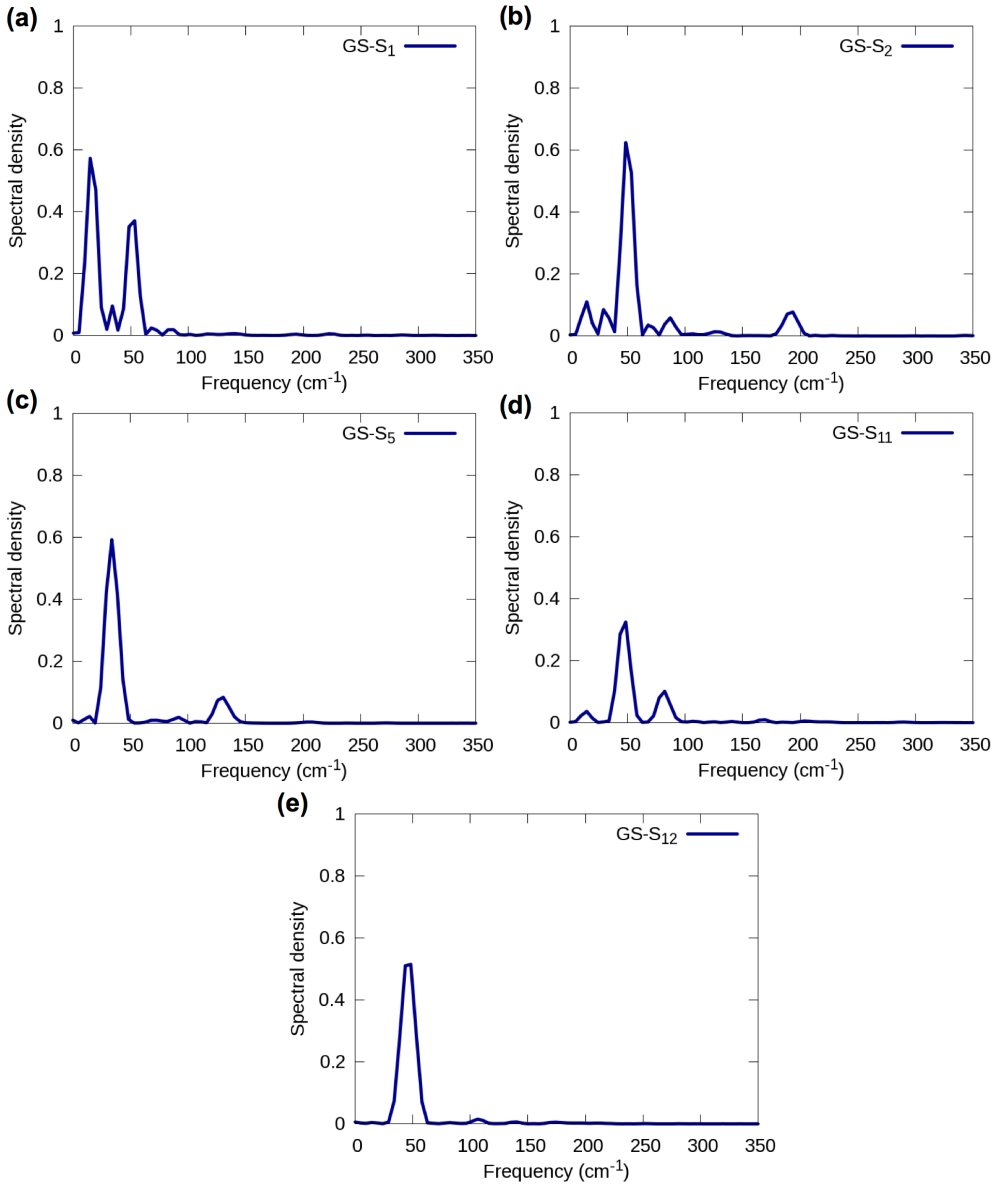

Figure D.3. Fourier transform of autocorrelation functions of the fluctuations of the energy gaps (phonon spectral density spectra) between (a) GS-S_1 (b) GS-S_2 (c) GS-S_5 (d) GS-S_{11} (d). GS-S_{12}.

Appendix E - Supporting Information for "Relaxation Dynamics in the $[Ag_{25}(SR)_{18}]^{-1}$ Thiolate-protected Silver Nanocluster"

Table E.1 The most probable transitions with highest oscillator strengths and their weights that contribute to the peak around 2.30 eV.

Excitation transitions	Energy (eV)	Oscillator strength	Weight	Most weighted transitions
13	2.23	0.0153	0.5862	HOMO-3 → LUMO
			0.1145	HOMO-5 → LUMO
			0.1005	HOMO-2 → LUMO+4
			0.0824	HOMO-1 → LUMO+3
			0.0259	HOMO-2 → LUMO+2
			0.0163	HOMO-1 → LUMO+5
			0.0117	HOMO → LUMO+4
14	2.24	0.0328	0.2139	HOMO-4 → LUMO
			0.1076	HOMO-1 → LUMO+3
			0.0845	HOMO-4 → LUMO+1
			0.0831	HOMO-2 → LUMO+2
			0.0825	HOMO-2 → LUMO+4
			0.0572	HOMO → LUMO+3
			0.0492	HOMO-5 → LUMO
			0.0462	HOMO → LUMO+2
			0.0408	HOMO-3 → LUMO+1
			0.0393	HOMO-2 → LUMO+3
			0.0325	HOMO → LUMO+4
			0.0304	HOMO-1 → LUMO+5
			0.0258	HOMO → LUMO+5
15	2.25	0.0585	0.2997	HOMO → LUMO+4
			0.1651	HOMO-4 → LUMO
			0.1113	HOMO-1 → LUMO+2
			0.0487	HOMO-6 → LUMO+1
			0.0472	HOMO-2 → LUMO+4
			0.0462	HOMO-1 → LUMO+3
			0.0415	HOMO-2 → LUMO+5
			0.0387	HOMO-6 → LUMO
			0.0339	HOMO → LUMO+5
16	2.26	0.0361	0.2067	HOMO-2 → LUMO+4
			0.186	HOMO-3 → LUMO
			0.1672	HOMO-4 → LUMO
			0.1036	HOMO-5 → LUMO

			0.0709	HOMO → LUMO+5
			0.0613	HOMO-2 → LUMO+5
			0.0535	HOMO → LUMO+3
			0.0379	HOMO-2 → LUMO+3
17	2.27	0.0294	0.3133	HOMO-4 → LUMO
			0.1222	HOMO-3 → LUMO
			0.1084	HOMO-6 → LUMO
			0.0786	HOMO-5 → LUMO
			0.0774	HOMO-1 → LUMO+3
			0.0585	HOMO-2 → LUMO+2
			0.0458	HOMO → LUMO+4
			0.035	HOMO-1 → LUMO+5
18	2.29	0.0289	0.5026	HOMO-5 → LUMO
			0.1204	HOMO-1 → LUMO+3
			0.0572	HOMO-1 → LUMO+5
			0.0492	HOMO-2 → LUMO+2
			0.0461	HOMO-3 → LUMO+1
			0.0454	HOMO → LUMO+5

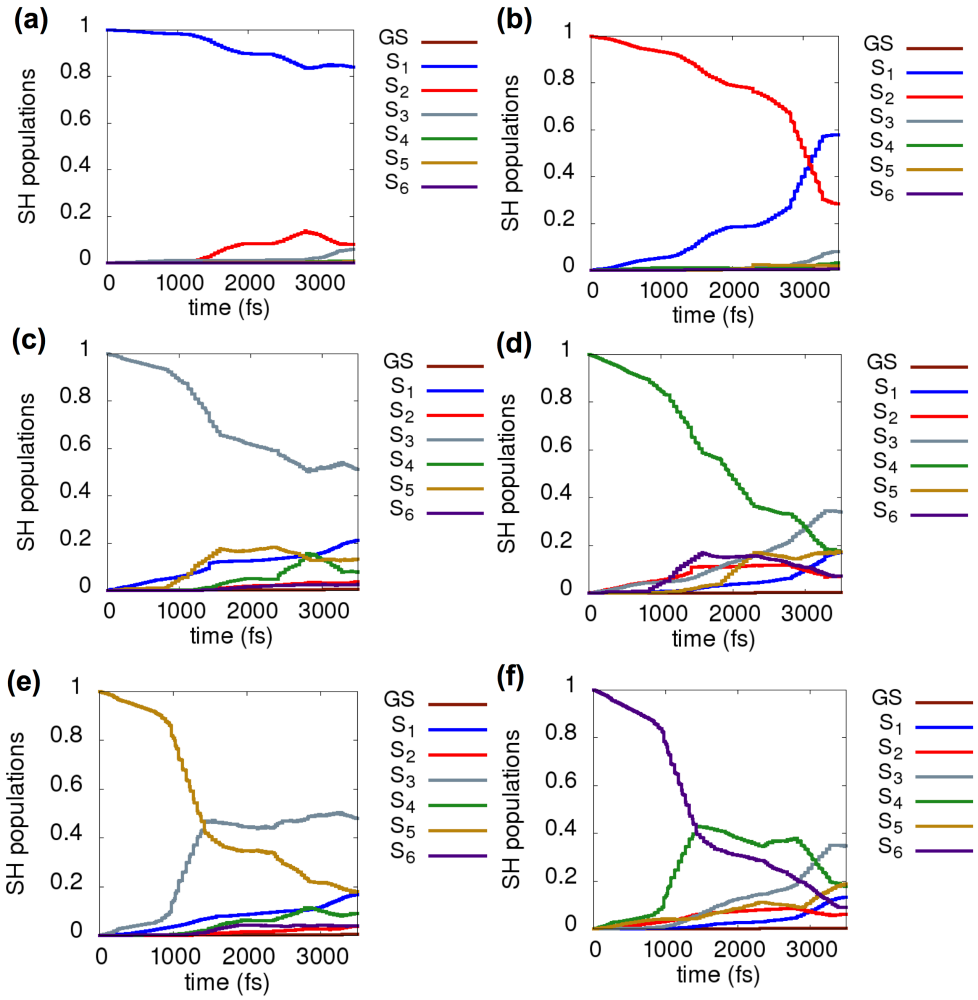

Figure E.1 Evolution of the populations of S_1, S_2, S_3, S_4, S_5, S_6 states. Parts (a) to (f) represent relaxations from S_1-S_6, respectively, with energy correction.

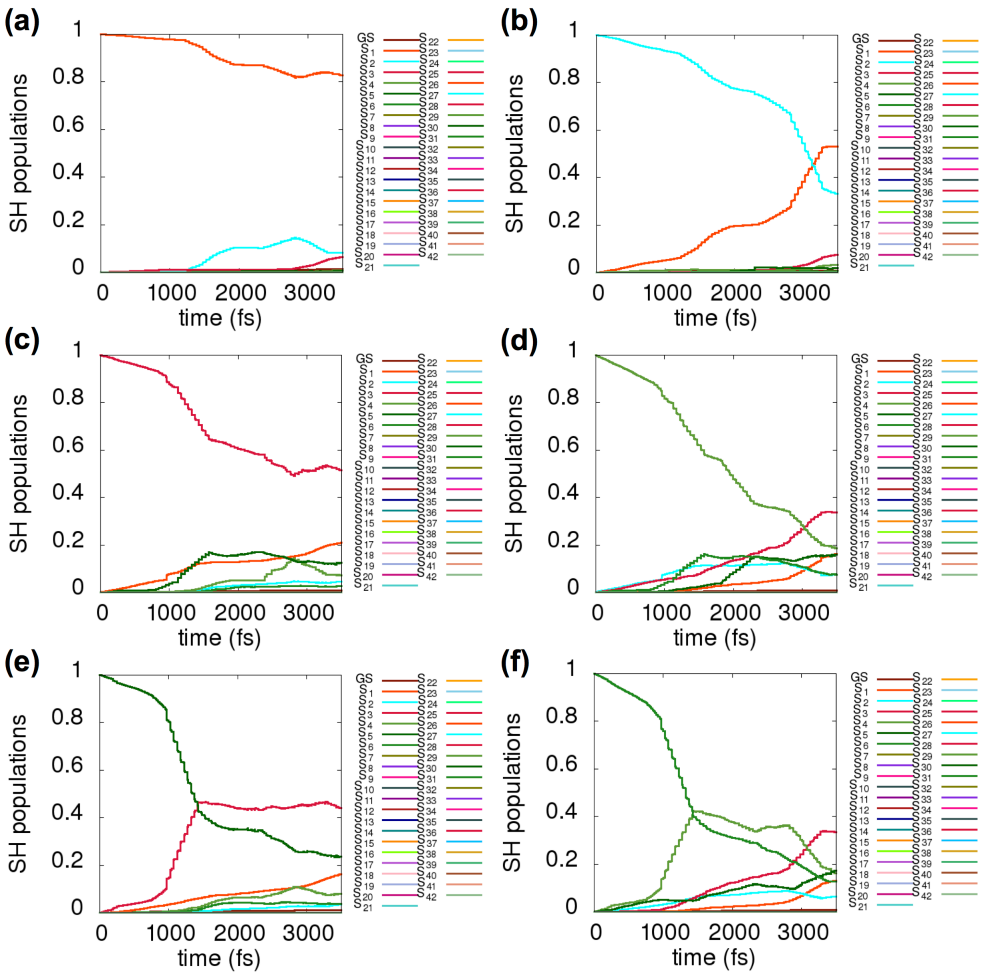

Figure E.2 Population relaxations of S_1, S_2, S_3, S_4, S_5, S_6 states with the energy correction in the presence of higher energy states. Parts (a) to (f) represent S_1-S_6 respectively.

Table E.2 The decay time constants obtained for $[Ag_{25}(SH)_{18}]^{-1}$ nanoclusters for the higher excited states including the S_1-S_6 states. The decay time constants are given when no correction is added and when the 0.33 eV correction added to the S_1-S_6 states. The decay time constants obtained for $[Au_{25}(SH)_{18}]^{-1}$ nanocluster[1] are also shown here.

Excited state	Decay time (ps) without the correction to the first six states (Ag_{25})	Decay time (ps) with the 0.33 eV correction to the first six states (Ag_{25})	Decay time (ps) with the 0.55 eV correction to the first six state (Au_{25})
S_1	17	18	15
S_2	6.2	6.2	3.3
S_3	4.6	4.9	2.9
S_4	2.8	3.0	1.7

S_5	2.3	2.3	1.8
S_6	2.0	2.0	1.4
S_7	11	11	9.9
S_8	2.9	2.8	2.7
S_9	2.9	2.9	1.5
S_{10}	5.2	5.4	3.3
S_{11}	2.1	2.1	1.6
S_{12}	1.8	1.8	1.2
S_{13}	2.1	2.1	2.3
S_{14}	1.3	1.3	1.5
S_{15}	1.4	1.4	1.2
S_{16}	2.5	2.3	2.9
S_{17}	1.9	1.8	1.7
S_{18}	2.4	2.4	2.7
S_{19}	1.6	1.5	1.4
S_{20}	1.4	1.4	1.0
S_{21}	1.5	1.4	1.8
S_{22}	1.3	1.2	1.2
S_{23}	1.4	1.4	1.7
S_{24}	1.0	1.0	1.1
S_{25}	1.0	1.0	0.9
S_{26}	1.0	0.9	1.5
S_{27}	0.9	0.9	1.0
S_{28}	1.0	1.0	1.3
S_{29}	0.7	0.7	0.9
S_{30}	0.8	0.8	0.7
S_{31}	1.1	1.1	1.3
S_{32}	1.0	1.0	1.0
S_{33}	1.0	1.0	1.2
S_{34}	0.8	0.8	0.9
S_{35}	0.8	0.8	0.8
S_{36}	2.5	2.6	N/A
S_{37}	1.9	1.9	N/A
S_{38}	1.4	1.4	N/A
S_{39}	1.3	1.3	N/A
S_{40}	0.9	0.9	N/A
S_{41}	0.7	0.7	N/A
S_{42}	0.8	0.8	N/A

References

1. Senanayake, R. D.; Akimov, A. V.; Aikens, C. M., Theoretical Investigation of Electron and Nuclear Dynamics in the $[Au_{25}(SH)_{18}]^{-1}$ Thiolate-Protected Gold Nanocluster. *J. Phys. Chem. C* **2016,** *121* (20), 10653-10662.

Appendix F - Supporting Information for "Real-time TDDFT Investigation of Plasmon Resonance Analogs in Gold Nanowires"

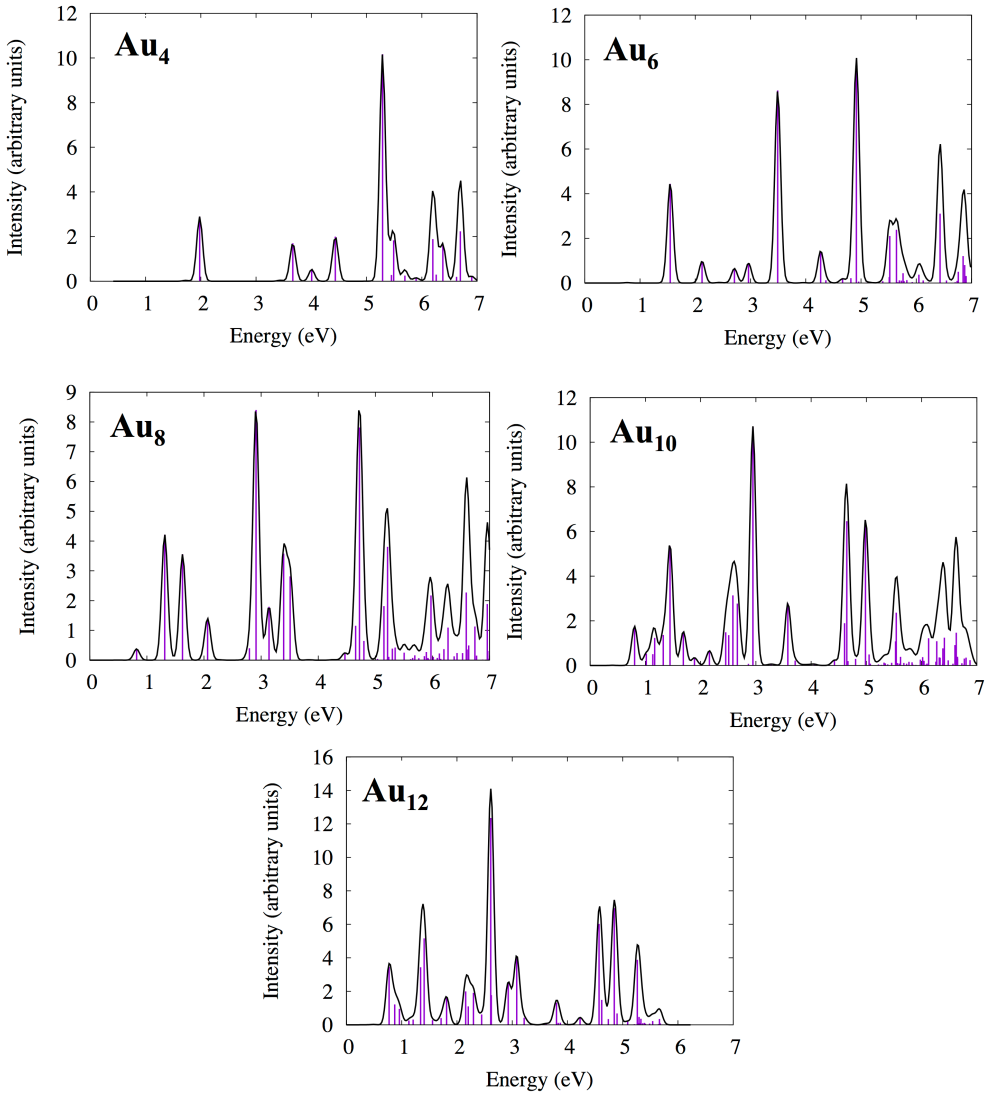

Figure F.1 The absorption spectra obtained by LR-TDDFT method using Gaussian software. Gaussian fitting was used with a FWHM value of 0.125. The spectra for Au_{12} was only calculated up to 5.7 eV due to the calculation resource limitations.

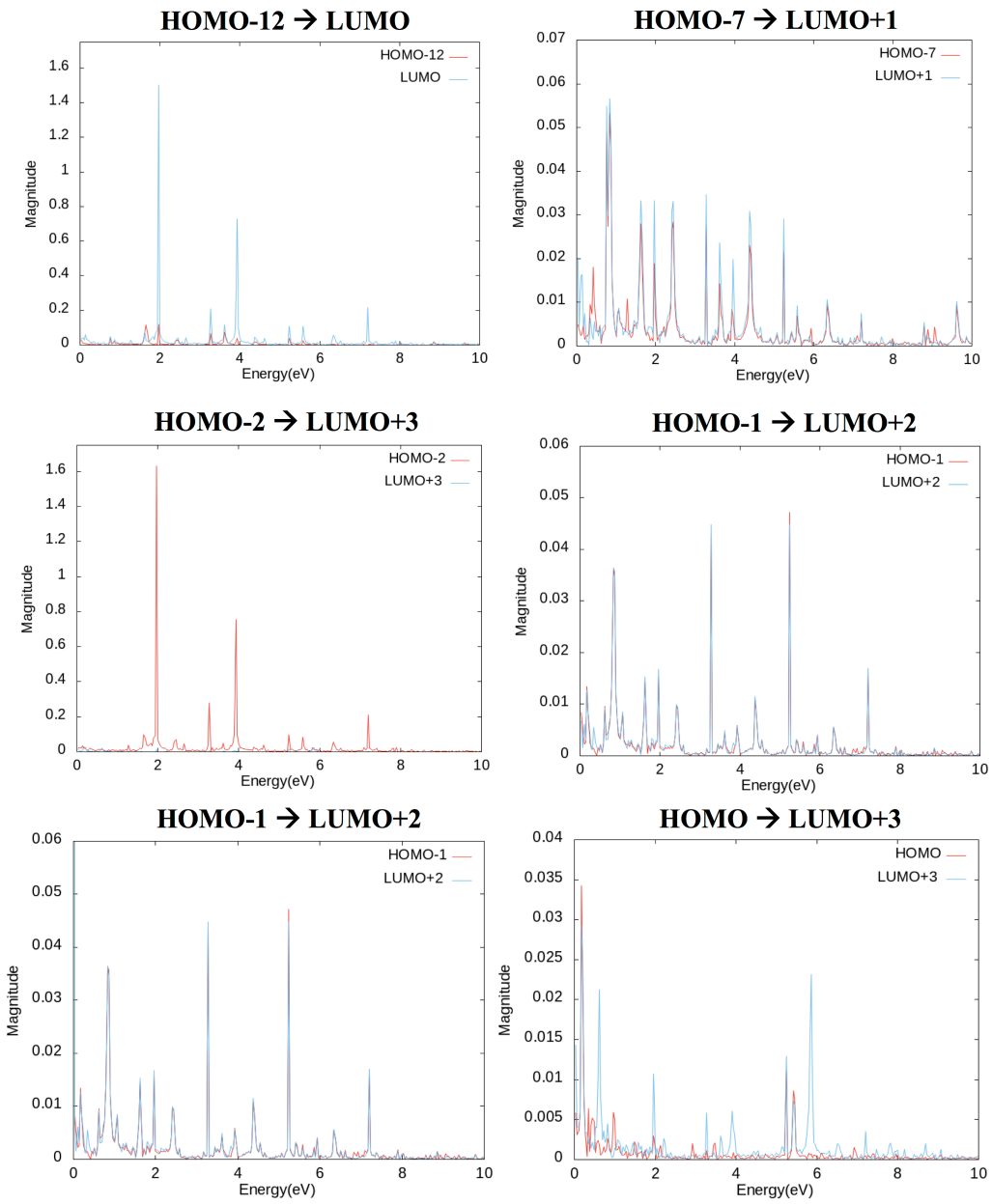

Figure F.2 The Fourier transformed spectra of the orbital occupation number variations for the peak around ~5.2 eV in the longitudinal mode of Au_4.

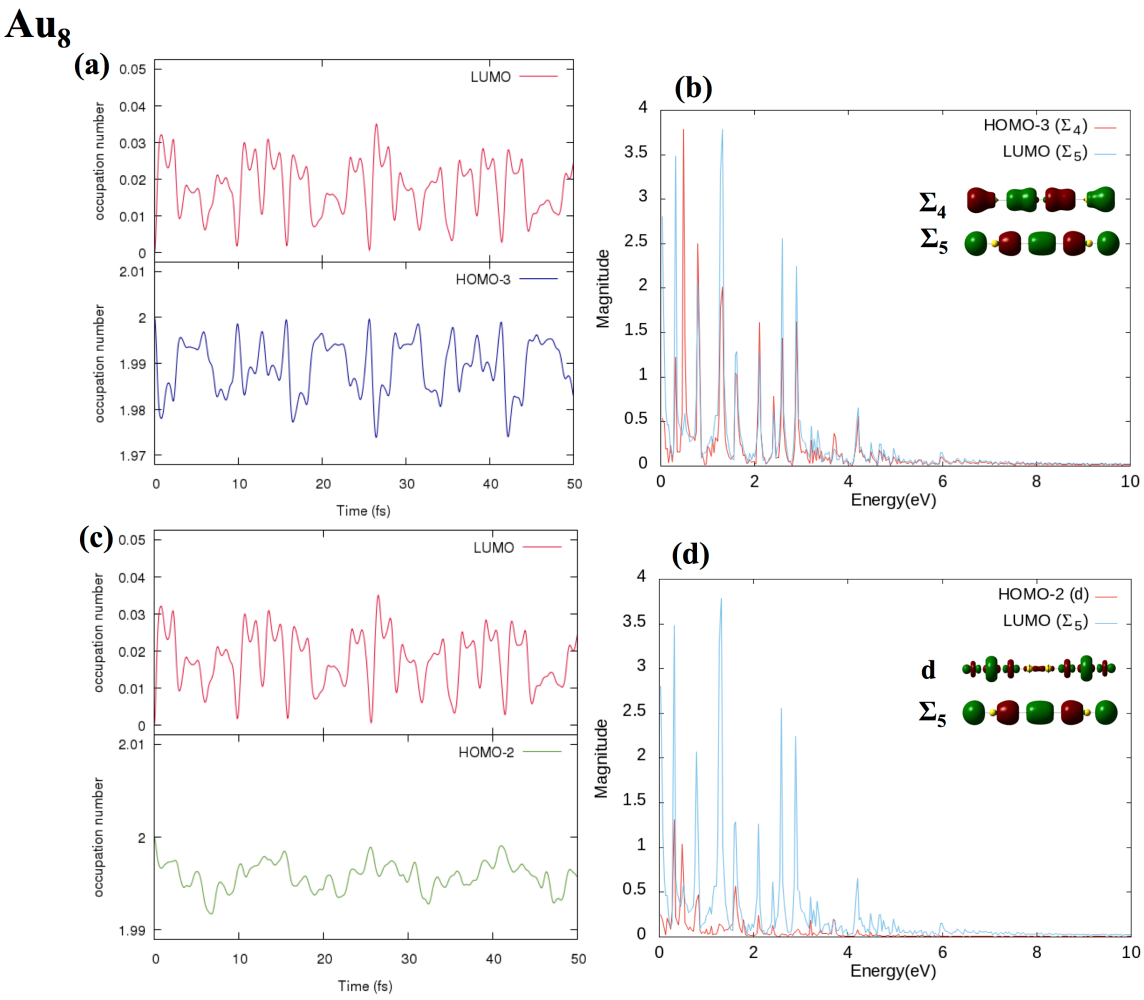

Figure F.3 Variations in orbital occupation numbers with time and their Fourier transformed spectra for strongly coupled orbital pairs in the longitudinal mode of Au_m (m = 8) nanowire. The a and b plots are shown for the most probable transition ($\Sigma_4 \rightarrow \Sigma_5$) in Au_8 while the c and d plots are shown for the less probable transition (d $\rightarrow \Sigma_5$).

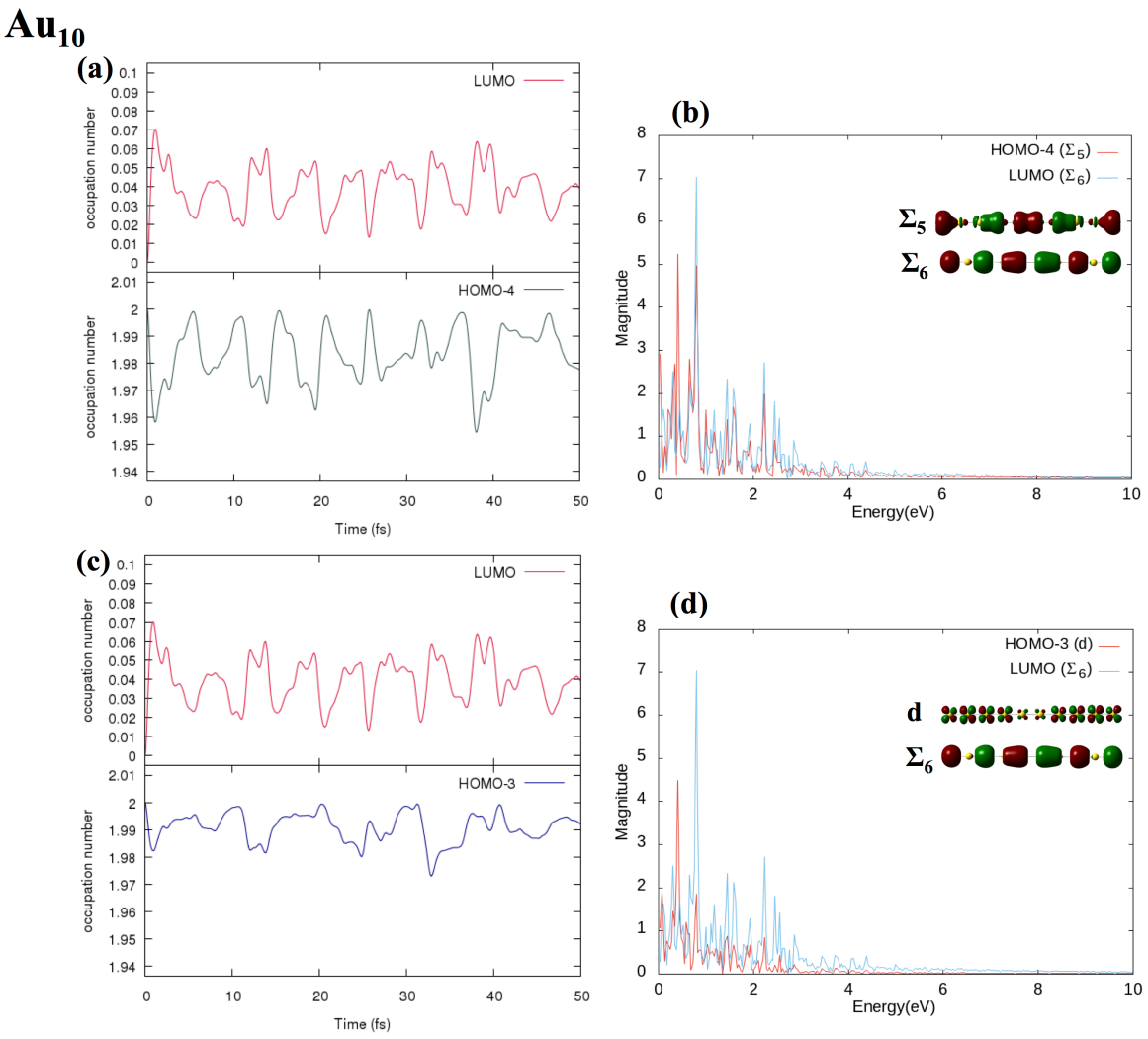

Figure F.4 Variations in orbital occupation numbers with time and their Fourier transformed spectra for strongly coupled orbital pairs in the longitudinal mode of Au_m (m = 10) nanowire. The a and b plots are shown for the most probable transition ($\Sigma_5 \rightarrow \Sigma_6$) in Au_{10} while the c and d plots are shown for the less probable transition (d $\rightarrow \Sigma_6$).

Au_{12}

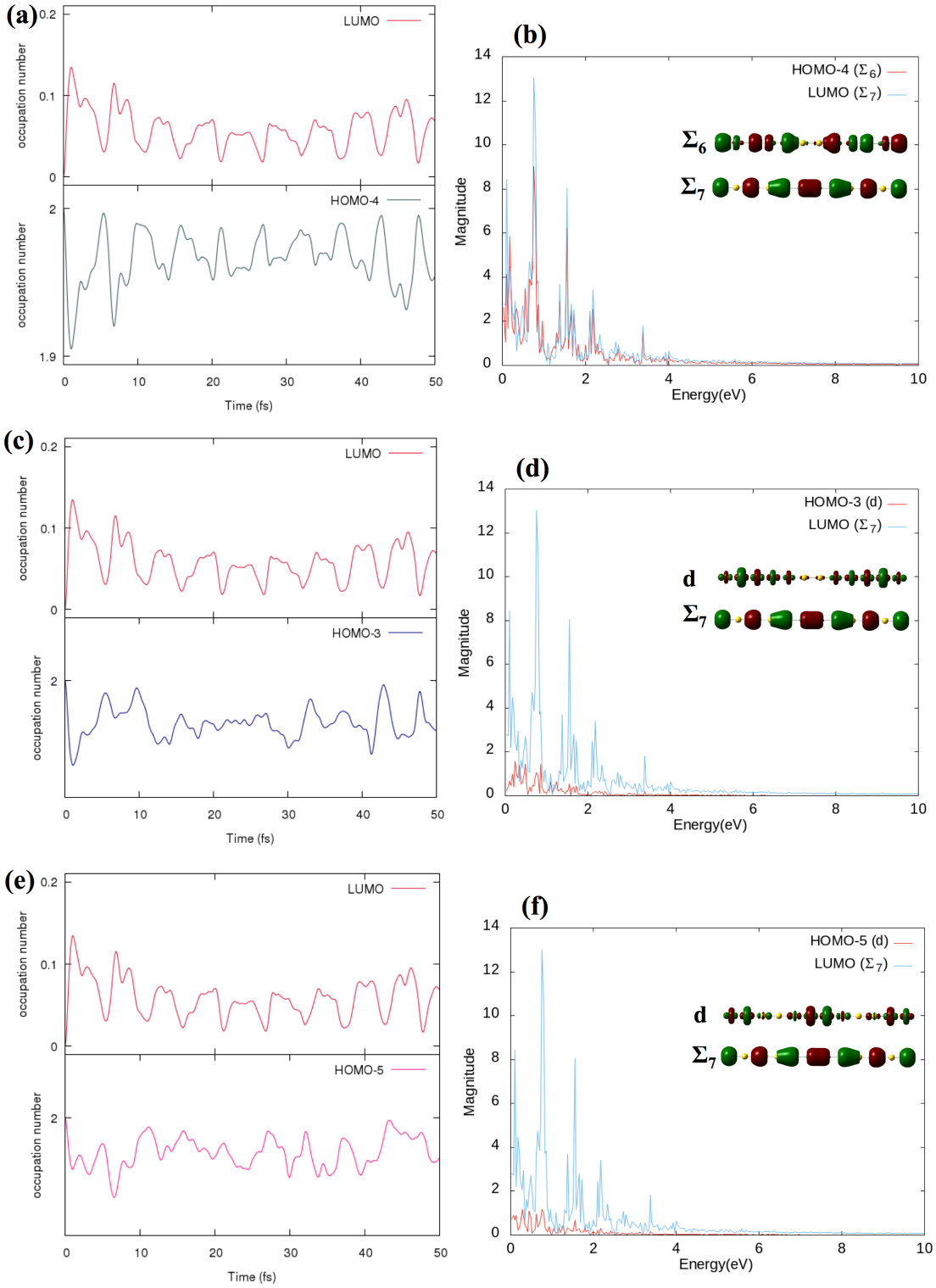

Figure F.5 Variations in orbital occupation numbers with time and their Fourier transformed spectra for strongly coupled orbital pairs in the longitudinal mode of Au_m (*m*

= 12) nanowire. The a and b plots are shown for the most probable transition ($S_6 \rightarrow S_7$) in Au_{12} while the c and d, e and f plots are shown for the two less probable transitions (d $\rightarrow$ S_7).

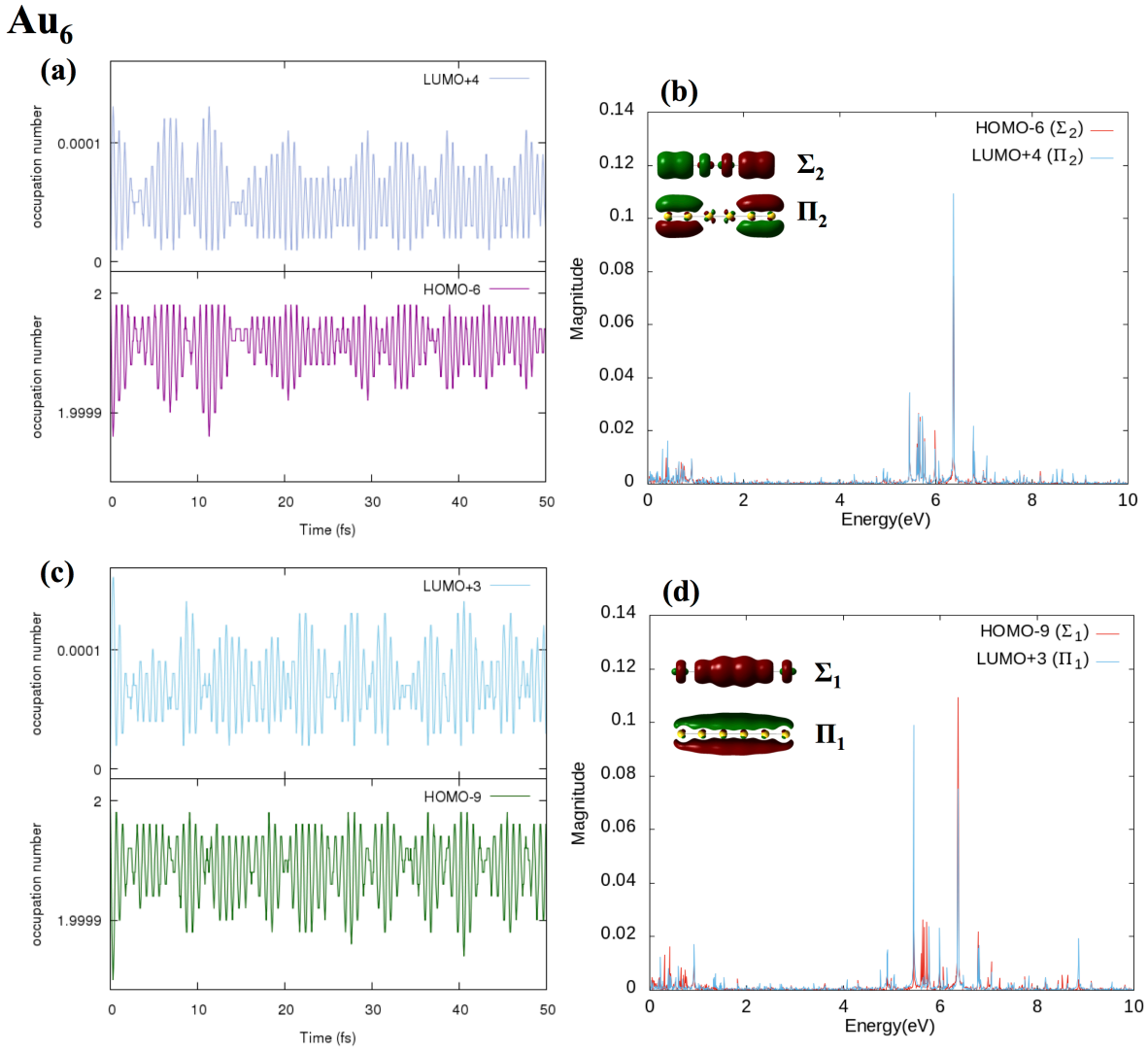

Figure F.6 The orbital occupation number variation [a and b] and the respective Fourier transformed spectra [c and d] for strongly correlated transitions ($S_2 \rightarrow \Pi_2$, $S_1 \rightarrow \Pi_1$) responsible for the transverse mode of Au_m (m = 6) nanowire.

Au_8

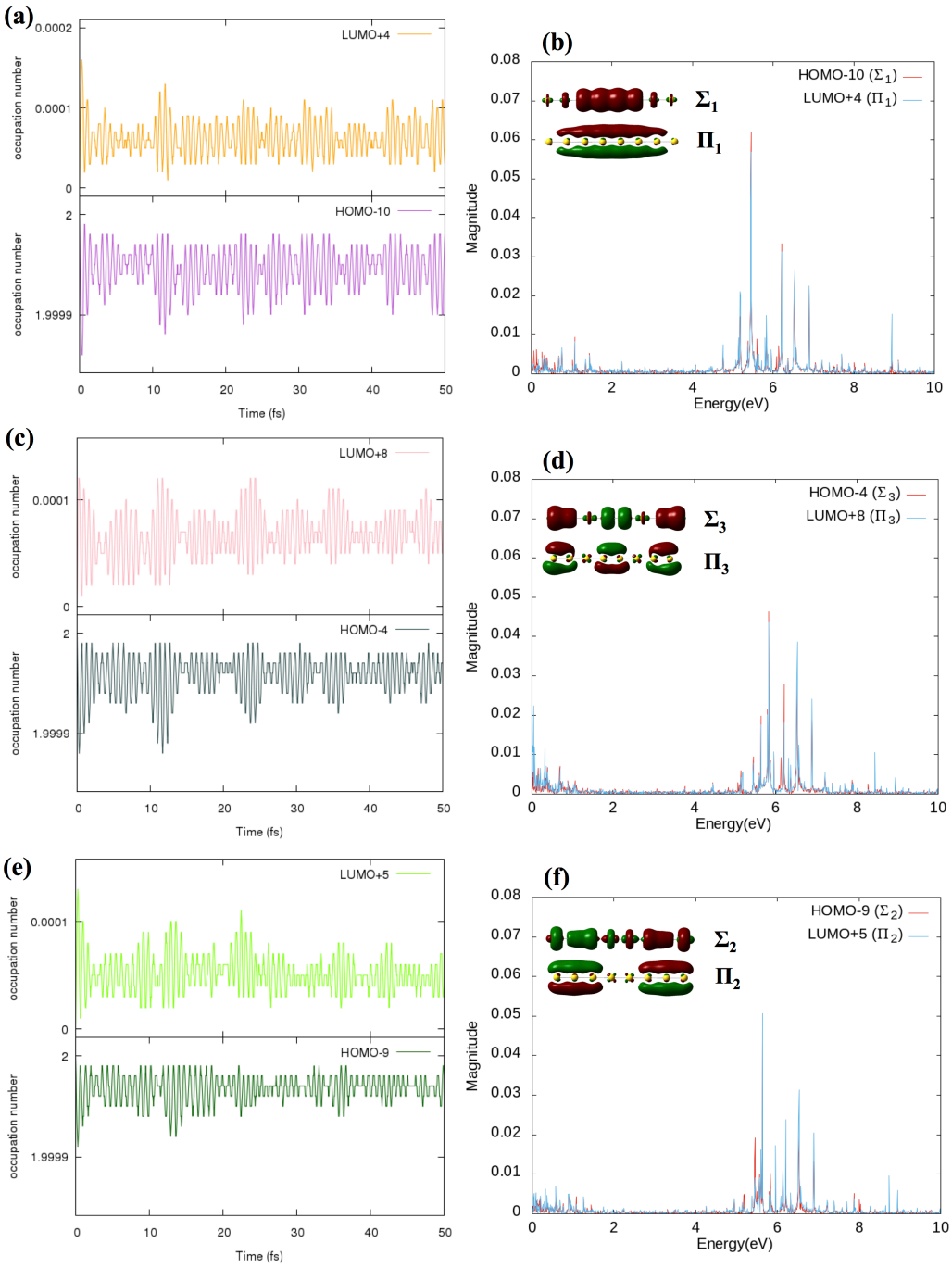

Figure F.7 The orbital occupation number variation [a, c and e] and the respective Fourier transformed spectra [b, d and f] for strongly correlated transitions ($S_1 \rightarrow \Pi_1$, $S_3 \rightarrow \Pi_3$, $S_2 \rightarrow \Pi_2$) responsible for the transverse mode of Au_m ($m = 8$) nanowire.

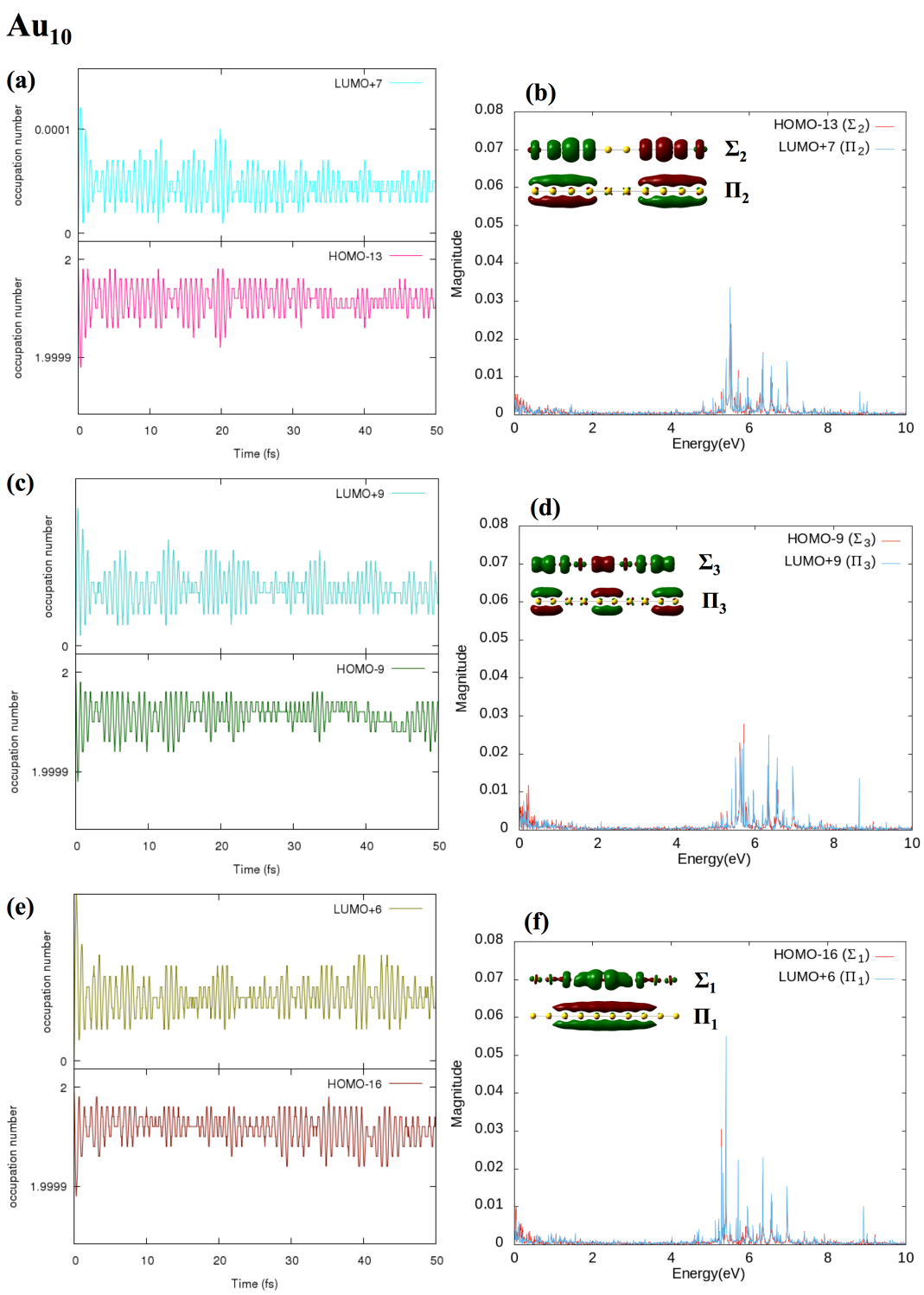

Figure F.8 The orbital occupation number variation [a, c and e] and the respective Fourier transformed spectra [b, d and f] for strongly correlated transitions ($S_2 \rightarrow \Pi_2$, $S_3 \rightarrow \Pi_3$, $S_1 \rightarrow \Pi_1$) responsible for the transverse mode of Au_m (m = 10) nanowire.

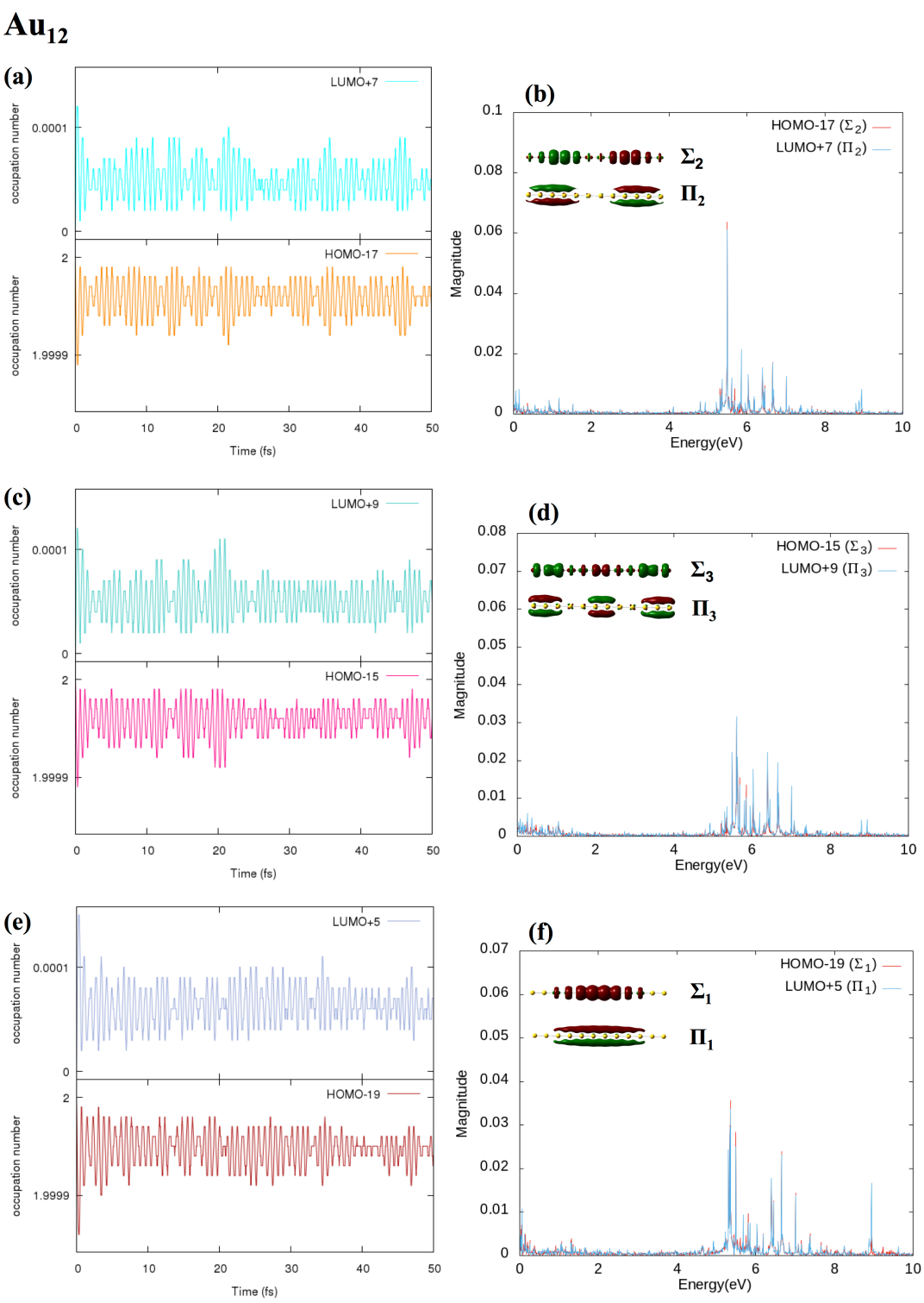

Figure F.9 The orbital occupation number variation [a, c and e] and the respective Fourier transformed spectra [b, d and f] for strongly correlated transitions ($S_2 \rightarrow \Pi_2$, $S_3 \rightarrow \Pi_3$, $S_1 \rightarrow \Pi_1$) responsible for the transverse mode of Au_m (m = 12) nanowire.